Exploring fundamental physics with gravitational waves

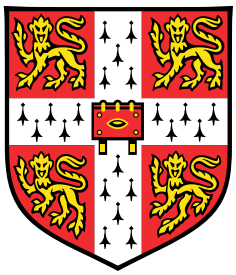
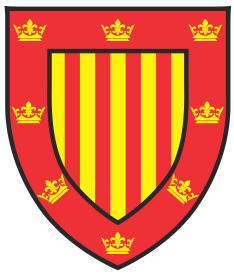

Deyan Petrov MIHAYLOV

Supervisors:
Prof. Gerard GILMORE
Prof. Anthony LASENBY
Prof. Jonathan GAIR

Institute of Astronomy, Department of Physics
University of Cambridge

This dissertation is submitted for the degree of
Doctor of Philosophy

Peterhouse September 2018

Declaration

This dissertation is the result of my own work and includes nothing which is the outcome of work done in collaboration except as declared in the Preface and specified in the text. It is not substantially the same as any that I have submitted, or, is being concurrently submitted for a degree or diploma or other qualification at the University of Cambridge or any other University or similar institution except as declared in the Preface and specified in the text. I further state that no substantial part of my dissertation has already been submitted, or, is being concurrently submitted for any such degree, diploma or other qualification at the University of Cambridge or any other University of similar institution except as declared in the Preface and specified in the text. All concepts, results and data obtained by others are properly referenced. Any use of "we" in the main text reflects my stylistic preference and nothing more. Some of the results presented in the dissertation have been published previously. Part I of the thesis consists of the following two publications:

- C. J. Moore, **Deyan P. Mihaylov**, A. Lasenby, G. Gilmore
  An astrometric search method for individually resolvable gravitational wave sources with Gaia
  Physical Review Letters, **119**, 261102, 2017

- **Deyan P. Mihaylov**, C. J. Moore, J. Gair, A. Lasenby, G. Gilmore
  Astrometric effects of gravitational wave backgrounds with non-Einsteinian polarizations
  Physical Review D, **97**, 124058, 2018

The following article is currently being prepared for submission to a journal and therefore has only been included as part of my prospective work on the topic relating to Part I of the dissertation:

- **Deyan P. Mihaylov**, C. J. Moore, J. Gair, A. Lasenby, G. Gilmore
  An astrometric method for constraining the speed of gravitational waves

These largely constitute the contents of Chapters 2, 3, and 4 of my thesis.

Part II of my dissertation consists of the following publication:

- **Deyan P. Mihaylov**, J. Gair
  Transition of EMRIs through resonance: corrections to higher order in the on-resonance flux modification
  Journal of Mathematical Physics, **58**, 112501, 2017

This largely constitutes the contents of Chapter 5 of my thesis.

Explicit citation to any of these papers indicates work done in collaboration. This is done in Chapter 3, where the current version of the numerical pipeline was developed by Christopher Moore; I developed a parallel version of the pipeline while working on this project, which is no longer maintained. I have also contributed to the version of the pipeline which was used to produce the results in Chapter 3.

This dissertation is less than 60000 words in length, including abstract, tables, footnotes and appendices, but excluding table of contents, photographs, diagrams, figure captions, list of figures, bibliography and acknowledgements.

Deyan P. Mihaylov
September 2018

Acknowledgements

Completing a doctoral degree has proven to be a demanding and challenging endeavour, but overall an interesting and rewarding experience. I would like to thank the people who helped, supported, and encouraged me over the past few years.

First and foremost, I would like to sincerely thank my supervisors, Professors Gerry Gilmore, Anthony Lasenby, and Jonathan Gair. They have all shown great patience in helping me launch my career as a physicist, and over the past few years have taught me not only everything I know about gravitational waves, but also a great deal about how to be a researcher, and how to develop an intuition for asking the right questions in science.

I ought to thank a great number of people at the Institute of Astronomy, with whom I have shared office space, discussed science, and enjoyed amusing conversations over coffee. In particular I would like to thank Christopher Moore, who has helped me immensely by guiding me in choosing my research questions, proof-reading my papers, and engaging in long discussions about gravitational waves. Among my fellow graduate students I would like to thank, in no particular order, Adam Jermyn, Alvin Chua, Bjoern Soergel, Cameron Lemon, Clare Wethers, Dominika Boneberg, Lindsay Oldham, and Sarah Bosman.

During my time in Cambridge I have had the distinct pleasure of meeting and interacting with many faculty members who have left an impression on me. I would like to thank the late Donald Lynden-Bell for the innumerable discussions about General Relativity, Anthony Challinor for useful discussions related to cosmology, and Ulrich Sperhake for his help with my membership in LIGO. I am also grateful for the help of the administrative teams in the Institute of Astronomy and Peterhouse. Particular thanks should go to Debbie Peterson and Margaret Harding for their ever supportive efforts, and to Vasily Belokurov and Paul Hewett for helping me navigate some of the challenging moments of my tenure.

Abstract

In this dissertation I explore several topics in the field of gravitational wave astronomy. By means of introduction, I review the historical evolution of humanity's understanding of the mechanics of gravity, and the events which eventually led to the first ever detection of gravitational waves in 2015.

The first half of the thesis is dedicated to the effect which gravitational waves have on the apparent position of stars on the sky. The astrometric shift caused by a gravitational wave signal can be quantified, and precise astrometric measurements (from *Gaia*) can provide a new method for searching for low-frequency GWs. This method is applied to searches for signals from individually resolvable supermassive black hole binaries. The main obstacle to performing efficient searches is the large size of the data sets, which consist of more than one billion stars. A near-lossless compression which reduces the size of the data set by a factor of 10^6 is discussed and implemented. Mock data sets are generated to simulate detections of gravitational waves using this method, and the frequency and directional sensitivities of the full-term *Gaia* mission are calculated. Parallels are drawn with the field of pulsar timing searches for GWs. This knowledge of the astrometric response is used to address the problem of searching for low frequency gravitational wave backgrounds using astrometric measurements. The astrometric deflections due to a stochastic GW background form a correlated vector field on the sphere (sky). Using a convenient decomposition of the correlation matrix, the 2-point correlation functions are calculated and compared to the redshift correlation in pulsar timing literature (and the Hellings-Downs curve). The correlation between redshift and astrometric deflections is also considered.

The second part of the dissertation focuses on the problem of resonances in extreme mass-ratio in-spirals (EMRIs). These events are prime candidates for GW detection in the millihertz band (by detectors like LISA), and involve a stellar mass black hole (or a similar compact object) merging with a supermassive black hole. Properties of the trajectory of the lighter body are well known, however little is known about the behaviour of such systems during resonance of the radial and polar motions. Two existing models for this behaviour are described: the instantaneous frequency approach (developed by Gair, Bender, and Yunes) and

the two timescales approach (proposed by Flanagan and Hinderer). Both methods depend on exact treatment of the gravitational self-force, which is currently not available. The results of Gair, Bender, and Yunes are extended to higher-order in the on-resonance flux modification, and the instantaneous frequency approach is confirmed to be a valid treatment of this problem. The algorithm for finding higher-order solutions is described, and further directions for extending this research are proposed.

Table of contents

List of figures

List of tables

1

Introduction

The ancient Greek philosopher Aristotle famously claimed that there is no motion without a cause. Instead of postulating a universal force which commands the motion of bodies, he and his contemporaries believed in the power of the four classical elements: earth, water, air, and fire. The earthen masses were pulled by their "gravitas" towards the terrestrial centre of the Cosmos, while fire, possessing less gravity, moved upwards [2]. While Aristotle believed in a geo-centric universe, the Platonic-Pythagorean school of thought advocated that the Earth was cube-shaped, and other forms rested flatly on its faces. According to them, as well as the Chinese school of thought, the Cosmos was spherical with a cube – the Earth – in the middle, and gravity was not the underlying cause for this world order, but rather an unavoidable consequence of the structural shape of the earth element. The Roman scholars took Aristotle's idea further, believing that gravity depended on the inherent "nature" of each substance. In summary, ancient thinkers theorised that the earth held together the entire world, but disagreed with each other as to how exactly this mechanism worked, i.e., they had diverging theories for the origin of gravity [3].

1.1 Newton's theory

Centuries later, of course, these ancient beliefs were all found out to be false. This revolution of thought arrived with the wave of Renaissance scholars and philosophers, who cast new light on humanity's understanding of the shape of the world and the mechanisms of gravity. In the sixteenth century, Nicolas Copernicus formulated a new model of the Universe, putting the Sun at its centre instead of the Earth. Galileo proposed the idea of universal gravitational acceleration in the seventeenth century (as opposed to the ancient view that gravity depends on the substance) [4]. The German astronomer and mathematician Johannes Kepler refined

the work of Copernicus by carefully studying the orbit of Mars over an extended period of time, and concluded that it was not a circle, but in fact an ellipse, and the Sun was not at the centre, but rather resided at one of the foci of the ellipse (the same was later demonstrated for the other known planets too) [5]. Kepler made another interesting discovery about the motion of planets around the Sun: by observation he deduced that planets do not move at a constant speed along their orbits, but rather in a way such that the radius vector between the Sun and the planet sweeps a constant area in a given period of time (nowadays this is commonly known as the law of angular momentum conservation) [5, 6]. He eventually came up with another law relating the axes of the planets' orbits and their orbital periods [5, 7]. These three laws formulated by Kepler became a cornerstone of the Enlightenment era understanding of the cosmic order.

In the late seventeenth century, English natural philosopher Robert Hooke first theorised that the force of gravitational attraction is proportional to the inverse square of the distance [8, 9]. In his famous work *Philosophiæ Naturalis Principia Mathematica*, Isaac Newton built upon the works of Kepler and Hooke by formulating an expression for the gravitational force that was also dependent on the masses of two bodies, and explains Kepler's three laws of planetary motion:

$$F = G\,\frac{M_1 M_2}{R^2}. \tag{1.1}$$

The now famous law formed the basis of his theory of gravitation, which he developed extensively and presented in *Principia* [10]. The constant of proportionality G in this formula was measured only in 1797 after experiments by Henry Cavendish [11].

Newton's theory soon amassed credibility, and gained popularity among the scientific community, since it neatly explained the motion of all the known planets (Mercury, Venus, Earth, Mars, Jupiter, and Saturn) around the Sun, as well as their known satellites around them, and successfully predicted the existence of Neptune, which had not been discovered yet [12]. Although there was a plagiarism dispute between Newton and Hooke regarding the author of the original idea, it is now widely recognised that it was Newton who came up with the idea for explaining the motion of the heavenly bodies in the form of a new theory of gravity.

Even though this theory enjoyed much deserved success, owed greatly to its simplicity and universality, by the end of the nineteenth century certain aspects of the theory led physicists to believe that it was, in fact, incomplete [13]. This conclusion was drawn from theoretical and observational findings. The main theoretical shortcoming of Newton's theory

is the lack of a mediator particle to act as the carrier of the field; this was clear even to Newton, but he could not come up with a resolution [14]. Today, there is a massless, chargeless, theoretical spin-2 particle called the graviton which mediates the force of gravity, however it is impossible to observe gravitons with any current detector [15, 13]. A further issue with Newtonian gravity is that it propagates instantaneously through space and time, which clearly defies the modern understanding of causality [16].

The observations which defied Newton's theory were naturally more convincing than the theoretical concerns at the time of their discovery. One such observation was the precession of the perihelion of planets' orbits, and especially that of Mercury, which was first measured in the nineteenth century [17]. Since no perturbing body could be found to account for the planet's perturbed orbit, it was prudent to conclude that there was a flaw in the theory of gravity.

1.2 Einstein's theory

Between 1907 and 1916, Albert Einstein laid down the foundations of general relativity, a fundamentally novel theory of gravity, which managed to explain the discrepancies that undermined Newton's theory. Einstein's breakthrough was the realisation that gravity is the result of the interaction between matter and space-time [18]. According to this theory of relativity, matter directs the curvature of space-time, and this curvature produces the apparent gravitational field near massive objects [19]. The curved space-time commands the movement of objects: free-falling observers traverse straight lines (geodesics) of the space-time. Thus the gravitational force is rendered fictitious, and is the result of the curvature of space-time [18]. While the gravitational interaction according to Newton is instantaneous, requiring action-at-a-distance to be invoked, in Einstein's theory there is a limit to the speed of propagation of light and signals. This limit is now defined to be $c = 299792458\,\mathrm{ms}^{-1}$ [20]. This relationship between space-time and matter is expressed mathematically through Einstein's field equations, a set of ten simultaneous non-linear differential equations which link the curvature of space-time to the mass and energy distribution [21]:

$$G_{\mu\nu} + \Lambda g_{\mu\nu} = \frac{8\pi G}{c^4} T_{\mu\nu}. \tag{1.2}$$

Here $G_{\mu\nu}$ is the Einstein tensor, a measure of the curvature of space-time, G is the gravitational constant (also appearing as the constant of proportionality in Newton's law of gravity) [22], and $T_{\mu\nu}$ is the stress-energy-momentum tensor that describes the distribution and flux of

energy and momentum in the four dimensions of space-time [13]. The extra term appearing on the left-hand side of the equations was introduced later as a modification of Einstein's original formulation which resulted in an expanding Universe. The commonly accepted view at the time was that the Universe was static, and this cosmological term fixed that conflict [23]. Λ is the cosmological constant, and is measured to have a value of $1.11 \times 10^{-52}\,\mathrm{m}^{-2}$ which is consistent with an accelerating universe [24].

From now on, the system of natural units will be used, where units are measured based on universal physical constants. These constants are defined so that their values are dimensionless and (usually) set to 1. For example, in this case, c is a natural unit of speed. Furthermore, the gravitational constant G is also a natural unit with value 1 in this system. Hence, in further expressions, these constants will be omitted.

The general theory of relativity has proven to be extremely successful, particularly in accounting for the effects which Newton's theory could not explain. The remaining 8% of the precession of Mercury's orbit was accurately accounted for by Einstein's field equations [21], and the angle of light-ray deflection by the Sun was measured during the 1919 solar eclipse and found to be accurately described by relativistic effects (Newtonian gravity predicted only half the value of this angle) [25]. Einstein's theory has since passed numerous further tests which solidified its reputation as the best explanation of the large scale of the Universe that we have to date. General Relativity (GR) has correctly predicted that time flows slower in regions of lower gravitational potential (gravitational redshift), a proposition which was confirmed conclusively by the GPS constellation of satellites [26]. Furthermore, the time delay of light passing near massive bodies, known as the Shapiro delay, was predicted [27] and later confirmed using signals from space probes [28].

Despite its many successes, it was realised around the middle of the twentieth century that GR could not be a complete theory of gravity, since it could not be reconciled with the theory of quantum mechanics which emerged in the preceding decades [29]. Attempts to re-write the theory of relativity in the framework of quantum field theory have yielded little progress so far. Therefore, despite its great success at explaining large-scale gravity, it is believed that GR will be superseded by a more powerful theory, which should encompass both the quantum and cosmic scales [30].

Even though it has been concluded that GR is incomplete, the theory has continued to enjoy unprecedented success, and has been validated by numerous observations and measurements thus far. Perhaps the most interesting, and recent testament to its validity to date comes from the problem of gravitational radiation. It was explained by Einstein in a 1916 article that proposed energy is emitted and carried in the form of gravitational waves

(GWs), which are (periodic) disturbances of space-time originating from certain accelerating systems [31, 32].

1.3 Gravitational waves

In the theory of general relativity, the space-time is represented by a 4-dimensional manifold, $\mathscr{M}$, endowed with a metric $g_{\mu\nu}$ with a mostly-positive signature $(-,+,+,+)$. The metric encodes the structure of the space-time, including its curvature and symmetry.

The Einstein tensor, appearing on the left-hand side of the Einstein equations, is a function of the space-time metric, $G_{\mu\nu} = G_{\mu\nu}(\mathbf{g})$. The Einstein tensor can be expressed in terms of the Ricci tensor $R_{\mu\nu}$ and the Ricci scalar $R = g^{\mu\nu}R_{\mu\nu}$:

$$G_{\mu\nu} = R_{\mu\nu} - \frac{1}{2} R\, g_{\mu\nu}, \tag{1.3}$$

and the Ricci tensor is a contraction of the Riemann tensor: $R_{\mu\nu} = R^{\rho}{}_{\mu\rho\nu}$. The Riemann tensor itself can be expressed as a function of the metric tensor as

$$R^{\mu}{}_{\nu\rho\sigma} = \partial_\rho \Gamma^{\mu}_{\nu\sigma} - \partial_\sigma \Gamma^{\mu}_{\nu\rho} + \Gamma^{\mu}_{\rho\lambda}\Gamma^{\lambda}_{\nu\sigma} - \Gamma^{\mu}_{\sigma\lambda}\Gamma^{\lambda}_{\nu\rho}, \tag{1.4}$$

where the Christoffel symbol $\Gamma^{\mu}_{\nu\rho}$ is defined as

$$\Gamma^{\mu}_{\nu\rho} = \frac{1}{2}\, g^{\mu\sigma}\left(\partial_\nu g_{\sigma\rho} + \partial_\rho g_{\nu\sigma} - \partial_\sigma g_{\nu\rho}\right). \tag{1.5}$$

As pointed out above, the Einstein field equations are non-linear, and therefore, it is usually impossible to find solutions for a generic matter-energy distribution. Gravitational waves are solutions to the linearized Einstein equations, and to understand this statement better I will outline the derivation of the wave equation.

Since the flat Minkowski space-time metric $\eta_{\mu\nu} = \mathrm{diag}(-1,1,1,1)$ is a solution of (1.2), it makes sense to investigate linear-order perturbations to this solution of the form $h_{\mu\nu}$. The new metric of the space-time can be written as

$$g_{\mu\nu} = \eta_{\mu\nu} + h_{\mu\nu} \tag{1.6}$$

This analysis is truncated at first order and therefore indices can be raised and lowered with the background metric $\eta_{\mu\nu}$. The trace of the perturbation is $h = \eta^{\mu\nu}h_{\mu\nu}$. The trace-reversed

metric perturbation is defined for convenience as

$$\bar{h}_{\mu\nu} = h_{\mu\nu} - \frac{1}{2} h \eta_{\mu\nu}. \tag{1.7}$$

The Einstein equations (1.2) can be written in terms of this quantity as

$$-\frac{1}{2}\partial_\rho \partial^\rho \bar{h}_{\mu\nu} + \frac{1}{2}\partial_\mu \partial^\rho \bar{h}_{\rho\nu} + \frac{1}{2}\partial_\nu \partial^\rho \bar{h}_{\mu\rho} - \frac{1}{2}\partial^\rho \partial^\sigma \bar{h}_{\rho\sigma}\,\eta_{\mu\nu} = 8\pi T_{\mu\nu}. \tag{1.8}$$

Since the space-time is physically invariant under a change of coordinates, there is a gauge freedom which allows the following coordinate transformation: $x^\mu \to x'^\mu = x^\mu + \xi^\mu$, where ξ^μ is small arbitrary smooth vector field. Under this transformation the metric perturbations transform as

$$h_{\mu\nu} \to h'_{\mu\nu} = h_{\mu\nu} - \partial_\mu \xi_\nu - \partial_\nu \xi_\mu \tag{1.9a}$$

$$\bar{h}_{\mu\nu} \to \bar{h}'_{\mu\nu} = \bar{h}_{\mu\nu} - \partial_\mu \xi_\nu - \partial_\nu \xi_\mu + \partial_\rho \xi^\rho \eta_{\mu\nu}. \tag{1.9b}$$

Since ξ^μ is arbitrary by definition, it can be freely chosen so that $\partial^\mu \bar{h}_{\mu\nu} = 0$ (this is called the harmonic, or Lorenz, gauge). This renders the linearised Einstein equations in a wave equation form:

$$\partial_\rho \partial^\rho \bar{h}_{\mu\nu} = -16\pi T_{\mu\nu}. \tag{1.10}$$

From the above equation it is obvious that Einstein's equations permit a time-dependent solution even in vacuum ($T_{\mu\nu} = 0$). Newton's theory, in contrast, does not have this property.

There is residual gauge freedom which can be exploited to choose ξ^0 such that $\bar{h}' = 0$ (through eq. (1.9b)). In this sub-gauge $h = 0$ (traceless) and hence $\bar{h}_{\mu\nu} = h_{\mu\nu}$, so the bar notation can be dropped. Furthermore, eq. (1.9b) allows ξ^i to be chosen such that $h_{0i} = 0$. Finally, the harmonic gauge condition $\partial^\mu h_{\mu\nu} = 0$ implies that $\partial^0 h_{00} = 0$ and since only time-dependent solutions are of interest, h_{00} can be set to 0. Therefore, the transverse-traceless gauge can be defined through the following equations

$$h_{0\mu} = 0, \tag{1.11a}$$ $$h^i{}_i = 0, \tag{1.11b}$$ $$\partial^i h_{ij} = 0. \tag{1.11c}$$

The equations can be solved using the ansatz $h_{ij} = H_{ij} \exp\left(\mathrm{i} k_\mu x^\mu\right)$, where H_{ij} is a constant spatial tensor, and the wave vector k_μ is null (according to the Einstein equations). The most general solution involves a linear combination of the two basis tensors (polarization modes)

in this gauge, which for k_μ aligned with the z-axis are given by:

$$H^+ = \begin{pmatrix} 1 & 0 & 0 \\ 0 & -1 & 0 \\ 0 & 0 & 0 \end{pmatrix}, \qquad H^\times = \begin{pmatrix} 0 & 1 & 0 \\ 1 & 0 & 0 \\ 0 & 0 & 0 \end{pmatrix}. \tag{1.12}$$

Gravitational waves are produced by accelerating systems which don't exhibit spherical symmetry. Those include, for example, two bodies orbiting each other, or a rapidly rotating object, such as a neutron star, which is not exactly spherical. In the case of a compact source of linear dimension $\sim R$ which orbits at a speed $v \sim \omega R \ll 1$ the far-field limit $|\mathbf{x}| \gg 1/\omega$ of the gravitational wave perturbation is

$$h_{ij}(t,\mathbf{x}) = \frac{2G}{|\mathbf{x}|}\,\ddot{I}_{ij}(t-|\mathbf{x}|/c), \tag{1.13}$$

where the trace-free quadrupole moment tensor is defined as

$$I^{ij} = \int \mathrm{d}^3x\, T^{00}\left(x^i x^j - \frac{1}{3}\,\delta^{ij}x^k x_k\right). \tag{1.14}$$

The typical frequency of a gravitational wave system is given by $f \sim (M/R^3)^{1/2}$, where M is the mass of the system, and R is its length scale. This results in a broad spectrum, namely in the range 10^{-16} Hz to 10^4 Hz [13]. Various sources of gravitational waves and their (expected) frequencies are shown in Fig. 1.1.

Gravitational waves have proven to be the most elusive feature of Einstein's theory of Relativity. They were first confirmed indirectly in 1974 by Joseph Taylor and Russell Hulse, who observed the first binary pulsar, and over a period of time concluded that the gradual contraction of the time between arrival of the pulses is consistent with gravitational wave emission from the binary system [33]. Hulse and Taylor were awarded the 1993 Nobel prize in Physics for their discovery, which was the first confirmation that gravitational waves exist. Direct detection of these phenomena did not occur for another four decades after their discovery.

Most notably, in the late nineties, the Laser Interferometer Gravitational Wave Observatory (LIGO) was built – a pair of earth-based detectors aimed at detecting gravitational waves directly using the method of interferometry [34, 35]. Eventually, on 14 September 2015, after a planned sensor upgrade to the Advanced LIGO detectors [36, 37], the first ever direct

GW EVENT	TYPE	$m_1/M_\odot$	$m_2/M_\odot$	$M/M_\odot$	DISTANCE/Mpc	REFERENCE
GW150914	BH–BH	36	29	62	410	[38]
GW151226	BH–BH	14.2	7.5	20.8	440	[40]
GW170104	BH–BH	31.2	19.4	48.7	880	[41]
GW170608	BH–BH	12	7	18	340	[42]
GW170814	BH–BH	30.5	25.3	53.2	540	[43]
GW170817	NS–NS	1.81	1.11	2.82	40	[44]

Table 1.1 High-confidence gravitational wave detection events which have been detected so far. Listed are the designation and the type of collision, as well as the masses of the two bodies ($m_1 > m_2$), the mass M after the merger (all in units of solar masses) and the distance from Earth. Note that only the values with highest likelihood have been included, each of these numbers is associated with some varying degree of uncertainty, most prominent in GW170817; consult the reference for each event for details.

observation of a gravitational wave signal was achieved by the teams of the LIGO and Virgo Collaboration (LVC) [38].

The first ever GW event detection involved the merger of two black holes, one with mass $36M_\odot$ and the other with mass $29M_\odot$, and took place 410 Mpc away, roughly 1.4 billion years ago[1]. The resulting black hole from this merger had a mass of $62M_\odot$, which means that approximately 3 solar masses worth of energy (approximately 5.3×10^{47} J) were released in the form of gravitational waves within less than 1 second of coalescence [38]. The discovery was formally announced at a press-conference on 11 February 2016, a century after Einstein first proposed the existence of gravitational waves, and later the 2017 Nobel Prize in Physics was awarded in relation to this breakthrough [39].

Since then, five further detections of gravitational wave events using Advanced LIGO have been announced, four of them involving pairs of black holes, and the fifth one involving a binary with at least one neutron star. The latter constituted the first multi-messenger detection, where the gravitational wave signal was accompanied by an electromagnetic wave signal. All of them are summarised in Table 1.1 alongside some of their properties.

While the current rate of detection is of the order of a few events per year, future upgrades to the LIGO detectors promise increased sensitivity which will increase the number of detected events. The first official observing run (O1) took place between 12 September 2015 and 19 January 2016 [45], and was followed by the O2 observing run, which started on 30 November

[1] At that point of time, the most advanced life forms on Earth were single-cell eukaryotes.

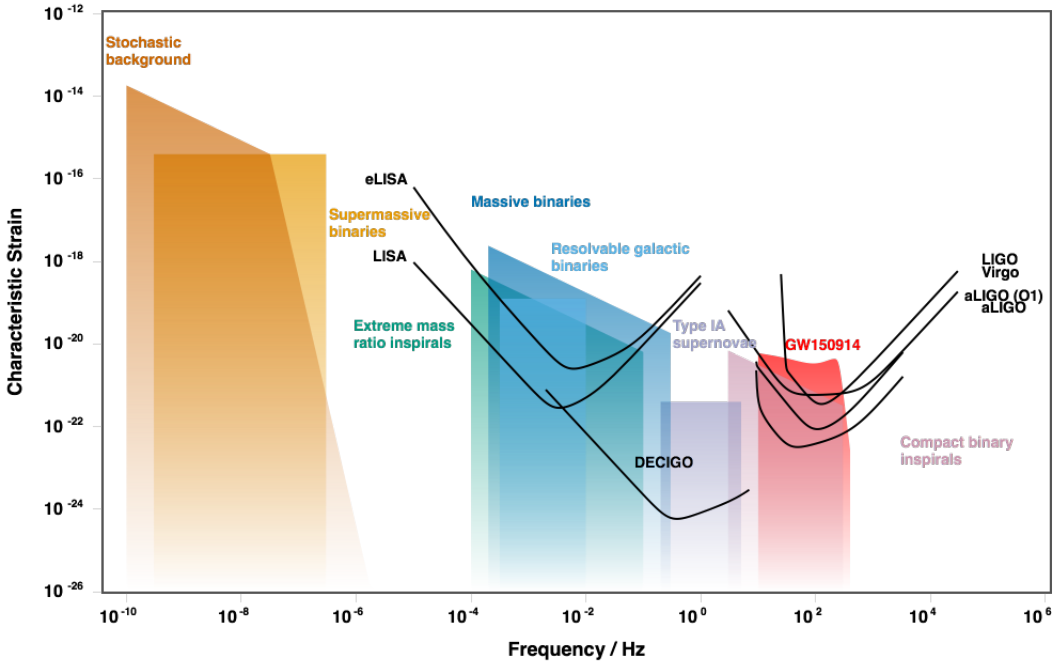

Fig. 1.1 Frequency spectrum of gravitational wave events and sensitivity of detectors [47]. The sensitivity of *Gaia* spans the region between 10^{-8} and 3×10^{-7} Hz.

2016 and finished on 25 August 2017. Following a new round of hardware upgrades, a 9-month observing run, O3, is scheduled to commence in early 2019. This process of incremental improvement in the hardware will continue and the detectors will reach their design sensitivity, currently projected for 2021 [46].

Since 2017, LIGO is, in fact, not operating alone. The Virgo detector, located in Italy and operated by the Virgo Collaboration, was taken on-line after nearly 2 decades of planning, building, and commissioning [48]. Even though it has the same design configuration as the pair of LIGO detectors, the laser cavities of Virgo are 3 km in length (compared to 4 km for LIGO) and the sensitive range achieved in O2 was lower by a factor of 10 [43]. During a joint run Virgo successfully contributed to the detection of GW170814 and GW170817 [43, 44]. A major hardware upgrade is currently underway which promises to increase the sensitivity of Virgo by a factor of 10 (compared to the initial configuration) by 2018 [49].

Additional LIGO-type detectors are currently being developed in several locations around the globe. The Kamioka Gravitational Wave Detector (KAGRA) is under construction in Japan and is expected to enter full-scale operation before 2020 [50–52]. The Indian Initiative in Gravitational-wave Observations (IndIGO) is partnering with LIGO to install a further detector in India, with a proposed start date of exploitation in 2024 [53].

Other future gravitational wave detectors are also planned: the Laser Interferometer Space Antenna (LISA) by the European Space Agency (ESA) is the most important of them, and is projected to launch in 2034 [54]. This project involves a constellation of 3 space-crafts on a Helio-centric orbit, relying on a method of direct detection using laser interferometry [55]. TianQin is another proposed space-borne gravitational wave observatory; construction began in 2016, and the launch is scheduled between 2025 and 2030 [56, 57]. The Deci-Hertz Interferometer Gravitational wave Observatory (DECIGO) is a space-based Japanese project which is still seeking appropriate funding [58]. The Einstein Telescope (ET) is a next-generation ground-based detector which is still in the initial study phase [59]. The sensitivities of some of these detectors, as well as their frequency ranges, are shown in Fig. 1.1.

Much has been written about the events leading up to these detections, and numerous articles have been published analysing the signals which have been detected thus far. I was fortunate enough to start my academic research work shortly before this momentous event in the history of astronomy. While detecting gravitational waves is a significant milestone for the astronomical community, we are currently able to explore only a tiny portion of the entire GW spectrum. Future missions are currently being designed to explore gravitational waves originating from unexplored sources. While these planned efforts are important, they will not bear results for another few decades. If one wants to explore the GW spectrum outside of the sensitivity of LIGO, one needs to look at other missions currently producing data which can be used to search for gravitational wave signals.

Part I

Gravitational waves and astrometry

2

Astrometry and the Gaia mission

This is adapted from the introduction to [60], which was written in collaboration with Christopher Moore and my supervisors.

The first direct detection of gravitational waves (GWs) from a binary black hole was achieved in September 2015 by the LVC collaboration using the ground-based Advanced LIGO detectors [38]. This event, as well as subsequent binary black hole detections [40, 41, 43, 42], and the first multi-messenger observations of a binary neutron star merger [44], have paved the way for the development of a host of new research topics in astronomy, astrophysics and cosmology [61–64]. In particular, gravitational waves afford the possibility to test the theory of general relativity (GR) in regimes which are inaccessible through light-based observations (e.g. strong gravity), and to constrain the deviations from general relativity far better than has previously been possible [65–67].

There are, however, GW tests of GR which are difficult or impossible to perform with current instruments. For example, the geometry of the two LIGO detectors alone hinders accurate determination of the GW polarization; this has been improved by the addition of Virgo which helped constrain the polarization content of GW170814 [43]. However, there may still exist combinations of GW polarizations (the transverse and longitudinal scalar modes) which laser interferometers cannot distinguish [68, 69]. It is well known that pulsar timing arrays (PTAs) provide one method which can distinguish between all 6 possible GW polarizations [70] and can even have an enhanced response to some non-Einsteinian polarisations [71].

The Gaia mission, launched in 2013 by ESA, is carrying out a thorough mapping of more than a billion objects in the Milky Way [72]. As part of this survey, star positions, velocities, and accelerations (among other observables) will be mapped with an unprecedented precision;

this new map of the Milky Way objects will allow for an entirely updated understanding of the dynamics and composition of our Galaxy and of the Local Group [73].

The idea of using high-precision astrometric measurements as an alternative avenue to detecting gravitational wave signals is not new: [74] were the first to examine the physical principles at play, and later [75] applied them to quasar proper motions. More recently [76] published an in-depth analysis of the concept applied to astrometric measurements, [77] evaluated the viability of finding this effect in detector data, and [78] discussed it in direct relation to the *Gaia* mission. The approach has been investigated numerically in the context of *Gaia*, and future Data Releases promise better sensitivity to single GW sources than existing techniques in a certain frequency range [79]. This part of my thesis explores the possibility of using such high-precision astrometric measurements to ascertain the polarization of a stochastic GW background, and hence constrain modified theories of gravity.

Within GR, gravitational waves travel at the speed of light and carry a superposition of two transverse, traceless polarization modes; usually denoted $+$ and $\times$ [80]. Generic metric theories of gravity have up to four additional polarization modes: a purely transverse scalar mode, two vectorial modes with mixed transverse and longitudinal properties, and a purely longitudinal scalar mode [69]. It should be noted that modified theories of gravity must now satisfy the polarization constraints from the LIGO-Virgo observations (e.g. [43]) of compact binary sources in the frequency range $\sim 10^1 - 10^3$ Hz. In general, these polarization modes may travel at speeds different from the speed of light; while the speed of the transverse traceless modes is strongly constrained by the recent electromagnetic and GW multi-messenger observations [67]. Detections of GWs using astrometric methods would allow for additional constraints to be placed on their polarisation and speed. This Chapter considers all six GW polarizations, but the discussion is restricted to waves travelling at the speed of light.

While still not explicitly detected, another possible target for gravitational wave detectors is a stochastic gravitational wave background (SGWB) created by a large number of random, uncorrelated, and individually unresolvable sources. According to the their origin, backgrounds can be classed as astrophysical or cosmological. Astrophysical sources range from supernovae and mergers of compact objects (BH-BH, BH-NS, and NS-NS binaries) to supermassive black hole binaries. Backgrounds of this origin are generally believed to have a power law spectrum and exist at frequencies above $\sim 10^{-12}$ Hz [81]. Cosmological backgrounds, on the other hand, include early-Universe events like reheating or inflation, or even more exotic alternatives like primordial black hole mergers or QCD phase transitions. These generally have more unusual spectra, and are more powerful at lower frequencies than astrophysical backgrounds. Astrophysical backgrounds, specifically SMBH binaries

corresponding to galaxy mergers, are by far the most promising in the context of astrometric and PTA-based methods for detection. The most constraining upper limits on the stochastic GW background at frequencies of several nanohertz come from pulsar timing. The North American Nanohertz Observatory for Gravitational Waves (NANOGrav) [82] and the European Pulsar Timing Array (EPTA) [83] placed 95% Bayesian upper limits on the amplitude of a stochastic gravitational-wave background of 1.5×10^{-4} and 3.0×10^{-15} respectively at a frequency of 1 year^{-1}. Currently the most stringent limit comes from the Parkes Pulsar Timing Array (PPTA) which placed a 95% upper limit on the amplitude of 1.0×10^{-15} at a frequency of 1 year^{-1} [84] whilst the International Pulsar Timing Array (IPTA) [85] has placed a 2σ upper limit of 1.7×10^{-15} at the same frequency.

This part of my dissertation analyses the astrometric response to a gravitational wave and the detector cross-correlation functions (or overlap reduction functions) for an astrophysical background in the context of all possible gravitational wave polarization states. In Section 3.1 the relativistic principles that are responsible for the periodic shift in a star's apparent position on the sky due to a gravitational wave are presented. Similar analyses have been published previously (e.g. [76]), but it is repeated here with a focus on the astrometric response to non-GR polarization states. Chapter 3 summarizes the mathematical formulation of GW polarization tensors. The characteristic astrometric patterns produced by each polarization are then plotted and analyzed in terms of the geometry of the astrometric response function.

Chapter 4 presents the numerical pipeline which can be used to search for GW signals in a *Gaia* data sets, including the algorithm used for compressing the data sets while preserving most of the sensitivity. The expected value of the correlation between the response function of two independent detectors is defined and derived for each of the polarization states in Chapter 5. Their significance and possible applications are also presented, alongside suitable depictions of their geometry. Pulsar timing and astrometry are two techniques which are capable of detecting GWs from similar sources. It is therefore interesting to consider the possibility of combining PTA and astrometric data sets to achieve improved sensitivities. As a first step in this direction, Section 5.2 considers the cross-correlation between the astrometric deflection and the PTA measured redshift for each of the possible GW polarizations.

The astrometric correlations due to a stochastic background of GWs with non-Einsteinian polarizations has not been explored previously. However, the redshift correlations due to such backgrounds have been the object of previous work, in the context of pulsar timing arrays. Notably, [70] sets out a thorough overview of the topic, and [86] calculates all relevant correlations for scalar and vector backgrounds. Throughout this discussion, the astrometric correlations derived will be compared with the existing results for the redshift correlations.

3

Astrometric response of a gravitational wave

Material in this Chapter is the result of my collaboration with Christopher Moore and my supervisors. It has been peer reviewed and published in Physical Review Letters as [79] and Physical Review D as [60]. My work consisted of re-deriving the theory in this Chapter subject to the constraints that are relevant to the analysis in subsequent Chapters.

3.1 Astrometric response of a gravitational wave

Astrometric measurements of any distant objects could, in principle, be used to detect GWs (the term "star" will be used to refer to any such distant object, although the same reasoning applies to any light source). The telescope used for the astrometric measurements will not be at rest (Gaia orbits at the Sun-Earth L2 point, and moves on a Lissajous-type orbit) and it will be necessary to correct for the detector motion; the term "Earth" will be used to refer to the location of an idealized stationary observer, and for simplicity it will be assumed that the necessary corrections in the data have already been made. Fig. 3.1 depicts the relationship between the "star", the gravitational wave source, and the "Earth".

In this chapter the periodic astrometric deflection of a distant "star" as viewed from the "Earth" due to a weak, plane-fronted GW signal is derived. The background space-time is assumed to be flat (the mostly positive metric $\eta_{\mu\nu} = \mathrm{diag}(-,+,+,+)$ is used here) and only leading-order terms in the metric perturbation are retained. We designate coordinates in which the Earth is at the spatial origin, $x_E^\mu(t) = (t,0)$, and the Star is at fixed spatial position, $x_S^\mu(t) = (t,x_S^i)$, with $x_S^i \equiv const$. While the results in this chapter are not new (in particular our derivation is similar to that in [76]) it will be useful to re-derive them here, paying special

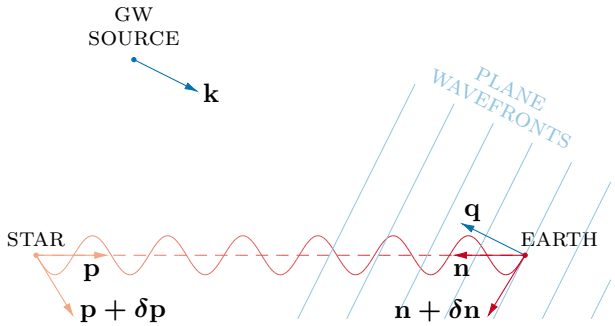

Fig. 3.1 An illustration of the geometric setup under consideration. The star lies on the past light cone of the Earth, and the two are linked by an unperturbed null geodesic with tangent vector p^μ and the apparent position of the star is given by $n_{\hat{\imath}}$. When the metric is perturbed by a GW with wavevector $k^\mu = -q^\mu$, the tangent to the null geodesic is perturbed, $p^\mu + \delta p^\mu$, along with the apparent position of the star, $n_{\hat{\imath}} + \delta n_{\hat{\imath}}$. The apparent position of the GW source is $q_{\hat{\imath}}$. Figure appeared in [60].

attention to the case of non-Einsteinian polarization states. The reader might be interested to consult [87] for a simplified discussion of this effect and a comparison of the interferometric, pulsar timing, and astrometric methods for GW detection.

In the absence of a metric perturbation the star and the Earth are joined by the following one-parameter family of null geodesics in the flat space-time, labeled by t_0,

$$x^\mu_{t_0}(\lambda) = (\Omega\lambda + t_0, -\Omega\lambda n^i). \tag{3.1}$$

Here Ω is the unperturbed frequency of the photons coming from the star, $-n^i$ is a unit three-vector in the direction of its propagation, the affine parameter λ varies from $\lambda_s \equiv -|\mathbf{x}_s|/\Omega$ to 0 between the star and the observer, and the tangent vector $p^\mu \equiv \mathrm{d}x^\mu/\mathrm{d}\lambda = \Omega(1,-n^i)$ (4-momentum) is null.

The observer (source) is equipped with a time independent orthonormal tetrad $\varepsilon^\mu_{\hat{a}}$ ($\sigma^\mu_{\hat{a}}$), satisfying $\eta_{\mu\nu}\varepsilon^\mu_{\hat{a}}\varepsilon^\nu_{\hat{b}} = \eta_{\mu\nu}\sigma^\mu_{\hat{a}}\sigma^\nu_{\hat{b}} = \eta_{\hat{a}\hat{b}}$, where the time-like basis vector is taken to be the 4-velocity, $\varepsilon^\mu_{\hat{0}} = \sigma^\mu_{\hat{0}} = (1,0,0,0)$. The tetrad is parallel-transported along the worldline of the observer (source), who measures the following tetrad components (denoted with a hat) of the 4-momentum,

$$p_{\hat{a}} = \eta_{\mu\nu}p^\mu\varepsilon^\nu_{\hat{a}} = -\Omega\,(1,n_{\hat{\imath}})\,, \text{ where } n_{\hat{\imath}} \equiv \varepsilon^\mu_{\hat{\imath}}n_\mu\,, \tag{3.2}$$

(and similarly for the source). The observed frequency is given by $\Omega_{\rm obs} \equiv -p_{\hat{0}}$ whilst the astrometric position is given by $n_{\hat{\imath}} \equiv p_{\hat{\imath}}/p_{\hat{0}}$.

Now consider perturbing this setup with a monochromatic, plane-fronted GW with angular frequency ω radiated from a distant source in the direction of the vector q^i, extending over a region including the source and the observer (Fig. 3.1). The metric perturbation is given by

$$h_{\mu\nu}\left(t,x^i\right) = \Re\left\{H_{\mu\nu}\exp\left(\mathrm{i}k_\rho x^\rho\right)\right\}, \tag{3.3}$$

where the $H_{\mu\nu}$ are small complex constants satisfying $H_{\mu\nu} = H_{\nu\mu}$, and the GW wavevector is $k^\mu = (\omega, -\omega q^i)$, where q^i is a 3-vector pointing from the Earth to the GW source. Hereafter, the $\Re$ is implicit in all complex expressions. Additionally, diffeomorphism invariance allows a spatial gauge choice to be made for the metric perturbation, $H_{0\mu} = 0$. In GR it is possible to further restrict to the well known "transverse-traceless" gauge; this is not done here as our focus will be on alternative polarizations. The perturbed space-time metric is $g_{\mu\nu} = \eta_{\mu\nu} + h_{\mu\nu}$, and its inverse $g^{\mu\nu} = \eta^{\mu\nu} - h^{\mu\nu}$. The connection coefficients for this metric are

$$\Gamma^\mu_{\nu\rho} = \frac{1}{2}g^{\mu\sigma}\left(\partial_\nu g_{\sigma\rho} + \partial_\rho g_{\nu\sigma} - \partial_\sigma g_{\mu\nu}\right) = \frac{1}{2}\left(\partial_\nu h^\mu{}_\rho + \partial_\rho h_\nu{}^\mu - \partial^\mu h_{\nu\rho}\right) + \mathscr{O}\left(h^2\right), \tag{3.4}$$

and the non-zero components are given explicitly by

$$\begin{aligned} &\Gamma^0_{ij} = \frac{1}{2}\partial_0 h_{ij}\,, \quad \Gamma^i_{0j} = \Gamma^i_{j0} = \frac{1}{2}\partial_0 h_{ij}\,, \\ &\text{and} \quad \Gamma^i_{jk} = \frac{1}{2}\left(\partial_k h_{ij} + \partial_j h_{ik} - \partial_i h_{jk}\right). \end{aligned} \tag{3.5}$$

The worldlines of the Earth ($x^\mu_E(t) = (t,0)$) and star ($x^\mu_s(t) = (t, x^i_s)$) are geodesics in both the unperturbed ($\eta_{\mu\nu}$) and perturbed ($\eta_{\mu\nu}+h_{\mu\nu}$) metrics; in this gauge these worldlines are unaffected by the GW. However, the null geodesics $x^\mu_{t_0}(\lambda)$ and the tetrads $\varepsilon^\mu_{\hat{a}}$ and $\sigma^\mu_{\hat{a}}$ are affected, and so are the tetrad components $p_{\hat{a}}$ defined in eq. (3.2).

Firstly, consider the tetrad along the Earth's worldline; this is perturbed $\varepsilon^\mu_{\hat{a}} \mapsto \varepsilon^\mu_{\hat{a}} + \delta\varepsilon^\mu_{\hat{a}}(t)$ according to the parallel transport equations (the 4-velocity is $\varepsilon^\mu_{\hat{0}}$),

$$\frac{\mathrm{d}}{\mathrm{d}t}\,\delta\varepsilon^\mu_{\hat{a}}(t) = -\Gamma^\mu_{\nu\rho}\,\varepsilon^\nu_{\hat{a}}\,\varepsilon^\rho_{\hat{0}} + \mathscr{O}\left(h^2\right), \tag{3.6}$$

where the symbols $\Gamma^\mu_{\nu\rho}$ are to be understood as being evaluated along the worldline of the Earth, $x^\mu_E(t)$. When integrating eq. (3.6) the constants of integration may be discarded as it is the time-dependent change in astrometric position which we ultimately seek to measure.

Substituting for the connection coefficients from eq. (3.5) and integrating eq. (3.6) along the worldline of the observer shows that the only nonzero components of $\delta\varepsilon^{\mu}_{\hat{a}}(t)$ are

$$\delta\varepsilon^{j}_{\hat{i}}(t) = -\frac{1}{2}H^{j}{}_{\hat{i}}\exp(-\mathrm{i}\omega t_0)\,. \tag{3.7}$$

Note that the time-like component of the tetrad is unaffected. Similar equations hold for the deviation $\delta\sigma^{j}_{\hat{i}}(t)$.

Secondly, consider the null geodesics and their tangents; these are perturbed $x^{\mu}\mapsto x^{\mu}+\delta x^{\mu}(\lambda)$ and $p^{\mu}\mapsto p^{\mu}+\delta p^{\mu}(\lambda)$ according to the geodesic equation,

$$\frac{\mathrm{d}^2}{\mathrm{d}\lambda^2}\,\delta x^{\mu}_{t_0}(\lambda) = \frac{\mathrm{d}}{\mathrm{d}\lambda}\,\delta p^{\mu}_{t_0}(\lambda) = -\Gamma^{\mu}_{\nu\rho}\,p^{\nu}p^{\rho} + \mathscr{O}\big(h^2\big)\,. \tag{3.8}$$

In the above equation the symbols $\Gamma^{\mu}_{\nu\rho}$ are to be understood as being evaluated along the unperturbed trajectory $x^{\mu}_{t_0}(\lambda)$ (corrections to this trajectory enter at order of h^2). Substituting for the connection coefficients from eq. (3.5) and for the metric perturbation from eq. (3.3) gives

$$\frac{\mathrm{d}}{\mathrm{d}\lambda}\,\delta p^{0}_{t_0}(\lambda) = \frac{\mathrm{i}\omega\Omega^2}{2}H_{ij}n^{i}n^{j}f(t_0,\lambda)\,, \tag{3.9a}$$

$$\frac{\mathrm{d}}{\mathrm{d}\lambda}\,\delta p^{i}_{t_0}(\lambda) = \frac{\mathrm{i}\omega\Omega^2}{2}\Big(-2H^{i}{}_{j}n^{j} + \Big(q_jH^{i}{}_{k} + q_kH^{i}{}_{j} - q^{i}H_{jk}\Big)n^{j}n^{k}\Big)f(t_0,\lambda)\,, \tag{3.9b}$$

where $f(t_0,\lambda) = \exp\big(-\mathrm{i}\omega\Omega\lambda\,(1-q^{i}n_i) - \mathrm{i}\omega t_0\big)$. Provided $q^{i}n_i \neq 1$, integrating eq. (3.9a) with respect to λ with the initial condition that the emission frequency in the rest frame of the star is unaffected by the GW ($\Omega_{\mathrm{emit}} \equiv \eta_{\mu\nu}\sigma^{\mu}_{\hat{0}}p^{\nu} = \Omega$, which reduces to $\delta p^{0}_{t_0}(\lambda_s) = 0$ because $\delta\sigma^{\mu}_{\hat{0}} = 0$) gives

$$\delta p^{0}(\lambda) = \frac{-\Omega}{2(1-q^{k}n_k)}H_{ij}n^{i}n^{j}\big(f(t_0,\lambda) - f(t_0,\lambda_{\mathrm{s}})\big)\,. \tag{3.10}$$

Integrating eq. (3.9b) twice with respect to λ gives

$$\delta x^{i}(\lambda) = \frac{-\mathrm{i}}{2\omega(1-q^{l}n_l)^2}\Big(-2H^{i}{}_{j}n^{j} + \big(q_jH^{i}{}_{k} + q_kH^{i}{}_{j} - q^{i}H_{jk}\big)n^{j}n^{k}\Big)f(t_0,\lambda) + \lambda A^{i} + B^{i}\,, \tag{3.11}$$

where A^{i} and B^{i} are constants of integration. The boundary conditions needed to determine A^{i} and B^{i} are:

(a) The family of geodesics $x^\mu_{t_0}(\lambda)+\delta x^\mu_{t_0}(\lambda)$ remain null; at leading order this condition becomes

$$h_{\mu\nu}(\Omega\lambda+t_0,-\Omega\lambda n^i)p^\mu p^\nu+2\eta_{\mu\nu}p^\mu\delta p^\nu_{t_0}(\lambda)=0. \tag{3.12}$$

(b) The geodesics intersect the Earth's worldline, the freedom to reparametrize the geodesics $\lambda\mapsto\lambda+\lambda_0$ may be used to ensure that the intersection occurs at $\lambda=0$, so this condition becomes $\delta x^i_{t_0}(0)=0$.

(c) The geodesics intersect the star's worldline at some value $\lambda_s+\delta\lambda_s$ (where $\delta\lambda_s=\mathscr{O}(h)$), so this condition becomes $x^i_{t_0}(\lambda_s+\delta\lambda_s)+\delta x^i_{t_0}(\lambda_s+\delta\lambda_s)=x^i_s$.

Boundary condition (b) fixes the constants B^i leaving

$$\begin{aligned}\delta x^i(\lambda)=\frac{-\mathrm{i}}{2\omega(1-q^\ell n_\ell)^2}\Big(-2H^i{}_j n^j+\big(q_jH^i{}_k+q_kH^i{}_j-q^iH_{jk}\big)n^jn^k\Big)\times\\ \times\big(f(t_0,\lambda)-f(t_0,0)\big)+\lambda A^i.\end{aligned} \tag{3.13}$$

Next, we decompose $A^i=A^i_\perp+A^i_\parallel$ in parallel and perpendicular directions to n^i. It is sufficient to enforce condition (a) at $\lambda=\lambda_s$ (where it is most straightforward to do so because $\delta p^0_{t_0}(\lambda_s)=0$) as the norm of a tangent is automatically preserved along a geodesic; this gives

$$A^i_\perp=\frac{-\Omega n^i}{2(1-q^\ell n_\ell)}H_{jk}n^jn^kf(t_0,\lambda_s+q_kH^i{}_j). \tag{3.14}$$

Finally, condition (c) is applied to fix $A^i_\parallel$ and $\delta\lambda_s$, although only the former is needed here,

$$\begin{aligned}A^i_\parallel=\frac{\mathrm{i}}{2\lambda_s\omega\left(1-q^\ell n_\ell\right)^2}\Big(2H^i{}_jn^j-\big(q_jH^i{}_k+q_kH^i{}_j-q^iH_{ij}\big)n^jn^k-2n^iH_{jk}n^jn^k\\ +n^iq^mn_mH_{jk}n^jn^k\Big)\big(f(t_0,0)-f(t_0,\lambda_s)\big).\end{aligned} \tag{3.15}$$

As discussed following eq. (3.2), the observed frequency is given by the temporal tetrad component of the photon $\Omega_{\mathrm{obs}}\equiv-p_{\hat0}$,

$$\begin{aligned}\Omega_{\mathrm{obs}}&=\big(\eta_{\mu\nu}+h_{\mu\nu}(t_0,0)\big)\big(p^\mu+\delta p^\mu_{t_0}(0)\big)\big(\varepsilon^\nu_{\hat0}+\delta\varepsilon^\nu_{\hat0}(t_0)\big)\\ &=\Omega\left(1-\frac{H_{ij}n^in^j}{2(1-q^kn_k)}\big(f(t_0,0)-f(t_0,\lambda_s)\big)\right).\end{aligned} \tag{3.16}$$

Therefore, the redshift, defined as $1+z \equiv \Omega/\Omega_{\rm obs}$, where Ω is the emitted frequency, is obtained from eq. (3.16) as

$$z = \frac{n^i n^j}{2(1-q^k n_k)} \left(h_{ij}(\mathrm{E}) - h_{ij}(\mathrm{S})\right). \tag{3.17}$$

The redshift depends anti-symmetrically on the metric perturbations at the "emission" and "absorption" events at the star and the Earth, respectively ($h_{ij}(\mathrm{E}) \equiv H_{ij} f(t_0, 0)$ and $h_{ij}(\mathrm{S}) \equiv H_{ij} f(t_0, \lambda_{\rm s})$). This symmetry arises from the endpoints of the integral along the null geodesic linking the star to the Earth. The redshift varies periodically in time due to the GW. This redshifting, applied to a distant pulsar, causes individual pulses to arrive at the Earth periodically early and late; it is this timing residual which is searched for by PTAs.

As discussed following eq. (3.2), the star's astrometric position is given by $n_{\hat{\imath}} \equiv p_{\hat{\imath}}/p_{\hat{0}}$ where $p_{\hat{0}}$ is the negative of $\Omega_{\rm obs}$ in eq. (3.16) and

$$p_{\hat{\imath}} = \left(\eta_{\mu\nu} + h_{\mu\nu}(t_0, 0)\right)\left(p^\mu + \delta p^\mu_{t_0}(0)\right)\left(\varepsilon^\nu_{\hat{\imath}} + \delta\varepsilon^\nu_{\hat{\imath}}(t_0)\right). \tag{3.18}$$

Combining the previous results gives the observed astrometric deflection of the star due to a plane GW, this is the same result as was found in [76] (their eq. (36)) with minor changes in notation;

$$\begin{aligned}\delta n_{\hat{\imath}} = \Bigg[\Bigg(& \left\{1 + \frac{\mathrm{i}(2-q^r n_r)}{\omega\lambda_s\Omega(1-q^\ell n_\ell)}\left(1 - \exp\left(-\mathrm{i}\omega\Omega\lambda_s(1-q^s n_s)\right)\right)\right\} n_{\hat{\imath}} \\ & - \left\{1 + \frac{\mathrm{i}}{\omega\lambda_s\Omega(1-q^\ell n_\ell)}\left(1 - \exp\left(-\mathrm{i}\omega\Omega\lambda_s(1-q^s n_s)\right)\right)\right\} q_{\hat{\imath}} \Bigg) \frac{H_{jk} n^j n^k}{2(1-q^\ell n_\ell)} \\ & - \left\{\frac{1}{2} + \frac{\mathrm{i}}{\omega\lambda_s\Omega(1-q^\ell n_\ell)}\left(1 - \exp\left(-\mathrm{i}\omega\Omega\lambda_s(1-q^s n_s)\right)\right)\right\} H_{\hat{\imath}j} n^j \Bigg] \exp(-\mathrm{i}\omega t_0)\,.\end{aligned} \tag{3.19}$$

As was found for the redshift, the deflection depends on the metric perturbations at the star and at the Earth; although not symmetrically. This loss of symmetry is because the deflection depends both on an integral along the null geodesic trajectory as per eq. (3.9b), and an integral along the Earth's worldline as per eq. (3.6).

In the PTA analysis of stochastic GW backgrounds it is common to drop the "pulsar term" (which is called the "star term" here). This is possible because in the limit where the GW wavelength is much shorter than the distance to the star, $\omega\lambda_s\Omega \gg 1$, the overlap reduction

function (ORF) tends to the result obtained by simply ignoring the "pulsar term" in eq. (3.17) [88].

In the astrometric case the "star terms" can also sometimes be neglected, albeit for slightly different reasons. Consider eq. (3.19) in the distant source limit $\omega\lambda_s\Omega \gg 1$ (i.e. where the star is many GW wavelengths distant from the observer). At leading order, only the first term in each set of curly brackets remains, and the result becomes

$$\delta n_{\hat{i}} = \frac{1}{2}\left(\frac{n_{\hat{i}} - q_{\hat{i}}}{1 - q^{\ell} n_{\ell}} h_{\hat{j}\hat{k}}(\mathrm{E})\, n^{\hat{j}} n^{\hat{k}} - h_{\hat{i}\hat{j}}(\mathrm{E})\, n^{\hat{j}}\right). \tag{3.20}$$

Notice that in this limit all dependence on $h_{ij}(\mathrm{S})$ has been lost. Also notice that the distant source limit was taken for the astrometric response of a single star, not for the statistical response of a network (quantified via the ORF) as in the PTA case. In eq. (3.20) all contractions have been written using tetrad components; hereafter the hat notation denoting tetrad components will be dropped, and the astrometric deflections in eq. (3.20) will simply be denoted δn_i.

The sensitivity of Gaia to GWs comes largely from the fact that it observes a large number of stars. These stars are generally well separated (by many gravitational wavelengths), therefore the small star terms will be uncorrelated between stars. At small angular separation many stars are at similar distances (star clusters); this needs consideration in any practical application. In contrast, the larger Earth term is correlated between all stars; it is this that Gaia will aim to detect. The independent star terms may be treated as an effective noise source in the experiment. Including all the individual "star terms" would slightly increase the sensitivity of Gaia to the lowest GW frequencies, however this would involve fitting for the distance to every observed star individually.

A problem occurs with the distant source limit of the astrometric deflection when the GW source is collinear with a star (i.e. when $q^i n_i = 1$); the expression in eq. (3.20) will, in general, diverge. In fact, this is usually not a problem, because in GR the GW polarizations are transverse (i.e. $h_{ij}q^j = 0$) which ensures that eq. (3.20) has a smooth limit as $n^i \to q^i$. However, the divergence is a problem when working with alternative polarizations with a longitudinal component (i.e. when $h_{ij}q^j \neq 0$). For the remainder of this work we work with the distant source limit in eq. (3.20) whenever possible, and fall back on the full (non-divergent) expression in eq. (3.19) when the distant source limit approximation breaks down.

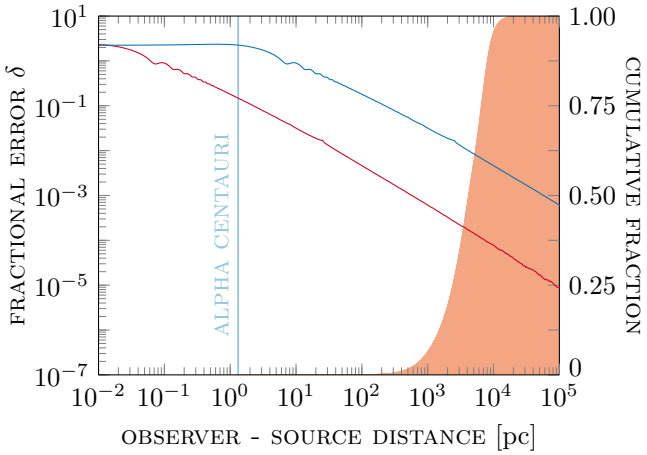

Fig. 3.2 The fractional error, δ (see eq. (3.21)), in the distant source approximation as a function of the distance to the star. The red and blue curves correspond to frequencies of $5\times10^{-7}\,Hz$ and $5\times10^{-9}\,Hz$ respectively; these are the upper and lower frequency limits of Gaia's GW sensitivity [79]. Also shown on the secondary y-axis is the cumulative distribution of distances to objects in the Gaia DR1 catalog (simulated distances to stars taken from the *Gaia Universe Model Snapshot* [89]). The distant-source limit is a good approximation for the majority of stars in the catalog. Figure appeared in [60].

For a transverse GW the distant source limit does not diverge and we may study the fractional error in the distant source approximation. The error is defined as

$$\delta = \frac{|\delta n_i - \delta n_i^{\mathrm{ds}}|}{|\delta n_i|}, \tag{3.21}$$

where δn_i is given by eq. (3.19), and δn_i^{ds} by eq. (3.20). This quantity is plotted in Fig. 3.2 as a function of the distance to the source for two frequencies at the edges of the Gaia's GW bandwidth, $(10^{-8}-3\times10^{-7})\,Hz$ [79]. Also shown in Fig. 3.2 is the cumulative distribution of the distances to stars in the Gaia catalog. Fig. 3.2 shows that even for the longest GW wavelengths of interest to Gaia the error $\delta < 10^{-2}$ for 90% of stars in the Gaia catalog. This justifies the use of the distant source limit eq. (3.20) whenever it is not divergent.

3.2 Gravitational wave polarizations

Whilst GR only allows for two GW polarization modes (the transverse and traceless $+$ and $\times$ modes), alternative theories can include up to 4 additional modes. Besides the two GR modes, there may be a transverse trace scalar mode, two vectorial modes with mixed transverse and

longitudinal components, and a purely longitudinal scalar mode. For a detailed discussion the reader is referred to [69].

In order to define the 6 GW polarization basis tensors we first introduce the orthonormal coordinate basis associated with the spherical polar coordinates (r,θ,ϕ);

$$\hat{e}_i^r = (\sin\theta\cos\phi, \sin\theta\sin\phi, \cos\theta), \tag{3.22a}$$
$$\hat{e}_i^\theta = (\cos\theta\cos\phi, \cos\theta\sin\phi, -\sin\theta), \tag{3.22b}$$
$$\hat{e}_i^\phi = (-\sin\phi, \cos\phi, 0). \tag{3.22c}$$

The symmetric spatial GW polarization tensor, H_{ij}, for a GW traveling in direction $q_i = -\hat{e}_i^r$ can then be decomposed in terms of basis tensors as

$$H_{ij} = A_+\varepsilon_{ij}^+ + A_\times\varepsilon_{ij}^\times + A_S\varepsilon_{ij}^S + A_X\varepsilon_{ij}^X + A_Y\varepsilon_{ij}^Y + A_L\varepsilon_{ij}^L, \tag{3.23}$$

where the 6 GW basis tensors, ε_{ij}^P, are defined as

$$\varepsilon_{ij}^+(q_k) = \hat{e}_i^\theta\hat{e}_j^\theta - \hat{e}_i^\phi\hat{e}_j^\phi, \tag{3.24a}$$
$$\varepsilon_{ij}^\times(q_k) = \hat{e}_i^\theta\hat{e}_j^\phi + \hat{e}_i^\phi\hat{e}_j^\theta, \tag{3.24b}$$
$$\varepsilon_{ij}^S(q_k) = \hat{e}_i^\theta\hat{e}_j^\theta + \hat{e}_i^\phi\hat{e}_j^\phi, \tag{3.24c}$$
$$\varepsilon_{ij}^X(q_k) = \hat{e}_i^\theta\hat{e}_j^r + \hat{e}_i^r\hat{e}_j^\theta, \tag{3.24d}$$
$$\varepsilon_{ij}^Y(q_k) = \hat{e}_i^\phi\hat{e}_j^r + \hat{e}_i^r\hat{e}_j^\phi, \tag{3.24e}$$
$$\varepsilon_{ij}^L(q_k) = \sqrt{2}\,\hat{e}_i^r\hat{e}_j^r. \tag{3.24f}$$

The factor of $\sqrt{2}$ in the definition of $\varepsilon_{ij}^L(q_k)$ is for normalisation convenience and accounts for the fact that this tensor has only a single non-zero component, while all others have exactly 2. In the standard Cartesian coordinate system for $\mathbf{q} = (0,0,1)$ the generalized perturbation tensor takes the form

$$H = \begin{pmatrix} A_+ + A_S & A_\times & A_X \\ A_\times & -A_+ + A_S & A_Y \\ A_X & A_Y & \sqrt{2}A_L \end{pmatrix}. \tag{3.25}$$

Shown in Fig. (3.3) are the distant source limit astrometric deflection patterns for each of the 3 transverse GW polarization states, and in Fig. (3.4) the exact astrometric deflection patterns for the other 3 GW polarization modes with longitudinal components. The results in Fig. (3.3) were calculated using eq. (3.20) for the $+$, $\times$, and S polarization states, in Fig. (3.4) using eq. (3.19) for the X, Y, and L states. Polarization tensors $H_{ij} = A_P\varepsilon_{ij}^P$ with $A_P = 0.1$ (unrealistically large for visualization purposes) were used throughout, and in the latter three cases, all stars were placed 10 gravitational wavelengths away from Earth. If the distant

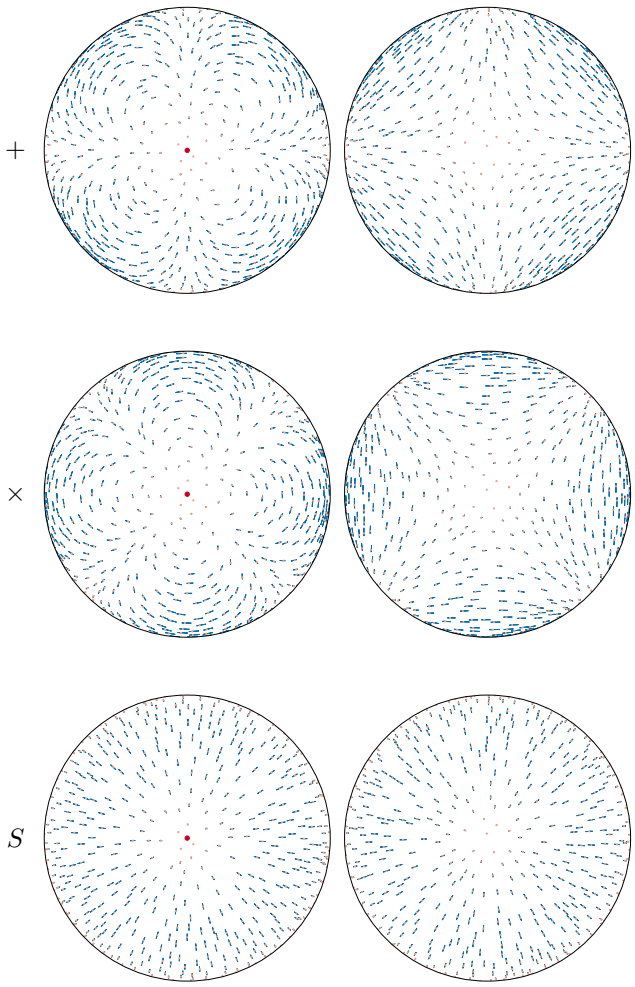

Fig. 3.3 Orthographic projections of the Northern (left) and Southern (right) hemispheres of the three transverse polarization modes. Randomly placed on the sky are 1000 stars. A GW from a source located in the direction of the North pole (indicated by the red dots) is incident on the Earth causing the stars to move periodically at the GW frequency. The blue lines show the traces which each star would leave as it moves on the sky. For clarity, the incident GW has the unphysically large characteristic strain amplitude $A = 0.1$. The $+$ and $\times$ patterns are related to each other by a rotation through $\pi/4$). The astrometric patterns for the two GR states including the star terms are presented additionally in Appendix A. Figure appeared in [60].

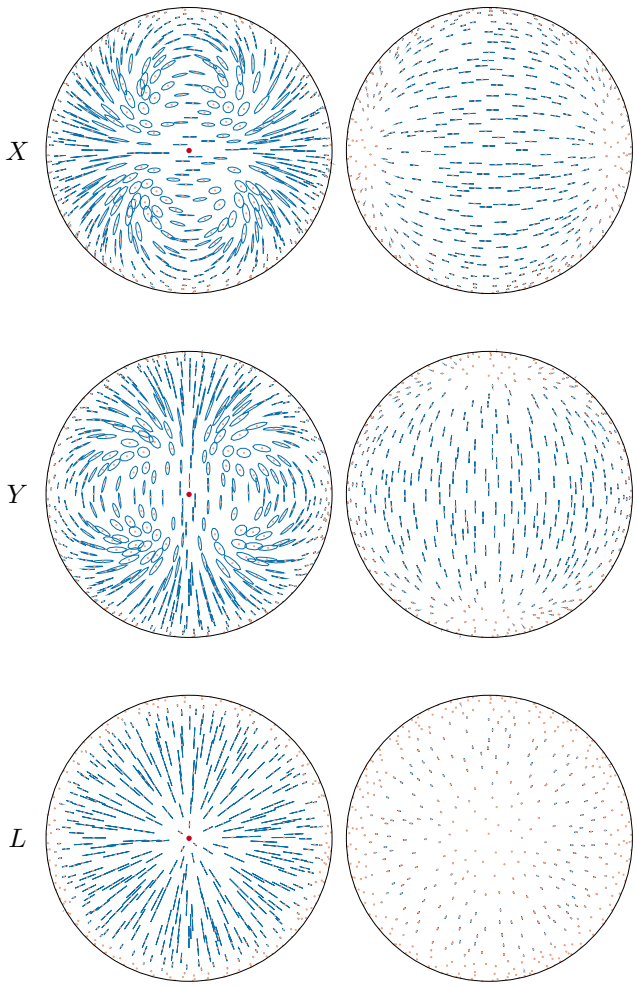

Fig. 3.4 Orthographic projections of the Northern (left) and Southern (right) hemispheres of the three modes with longitudinal components. Randomly placed on the sky are 1000 stars. A GW from a source located in the direction of the North pole (indicated by the red dots) is incident on the Earth causing the stars to move periodically at the GW frequency. The blue lines show the traces which each star would leave as it moves on the sky. For clarity, the incident GW has the unphysically large characteristic strain amplitude $A = 0.1$, and the star terms are included in the calculation of the astrometric deflection in order to avoid it becoming divergent near the North pole. In these three samples, all stars are placed at a distance of 10 gravitational wavelengths from the Earth. In reality, these neat elliptical patterns would appear more chaotic, since the distances to each star are generally different. The X and Y patterns are related by a rotation through $\pi/2$. Figure appeared in [60].

source limit were used for the three longitudinal modes, the plots would incorrectly show a divergence in the astrometric deflection pattern at the North pole due to the factor of $1 - q^{\ell} n_{\ell}$ in the denominator of eq. (3.20).

4

An astrometric search method for gravitational waves

Material in this Chapter is the result of my collaboration with Dr Christopher Moore and my supervisors. This work has been peer reviewed and published in Physical Review Letters as [79]. My original contribution consisted of developing a parallel version of the original pipeline (which is no longer supported), developing the Voronoi grids and the algorithm for assigning stars to the Voronoi cells, and deriving the directional sensitivity pattern of Gaia. This chapter is a summary of the letter [79].

4.1 Data analysis

The previous Chapter calculated the astrometric deflection due to a gravitational wave. It is interesting to consider whether this effect can be detected in practice. In this Chapter I describe a numerical methodology for searching for a monochromatic gravitational wave signal in a *Gaia*-like astrometric dataset. The expected source of such a GW is a (circular) supermassive black hole binary system in its post-Newtonian period of in-spiral, with total mass of the system in the range 10^7–$10^{10}\,M_\odot$. This period of the trajectory is characterized by a weak gravitational field (since the bodies are far apart), which also ensures that the system evolves slow enough and the frequency can be assumed to stay constant.

The metric perturbation for a plane, monochromatic gravitational wave may in GR be written as

$$h_{ij}\left(\overline{\Psi}\right) = \Re\left\{\left(A_+ H_{ij}^{+}(\mathbf{q})\, e^{\mathrm{i}\phi_+} + A_\times H_{ij}^{\times}(\mathbf{q})\, e^{\mathrm{i}\phi_\times}\right) \mathrm{e}^{2\pi \mathrm{i} f t}\right\}, \tag{4.1}$$

where $\overline{\Psi}$ is a 7-dimensional parameter vector which characterizes the gravitational wave completely: two amplitudes $\{A_+, A_\times\}$, two phases $\{\phi_+, \phi_\times\}$, the GW frequency f, and two angles describing the direction $\mathbf{q}$ to the source, and H_{ij}^{+} and $H_{ij}^{\times}$ are the two GW basis tensors from eq. (1.12).

A *Gaia* data set would consist (in principle) of N astrometric measurements (observations) of M stars in the catalogue. For simplicity here the time between observations is assumed to be the same, although this would not be a valid assumption for a real data set, and is not necessary in this context:

$$\mathscr{S} = \{\mathbf{s}_{I,J} | I = 1,2,\ldots,M; J = 1,2,\ldots,N\}\,. \tag{4.2}$$

Each individual measurement $\mathbf{s}_{I,J}$ signifies the position of a star on the sky (at a time $t_{I,J}$), which is a combination of the background star position $\mathbf{n}_I(t_{I,J})$, the instrument noise $\mathbf{r}_{I,J}$, and a possible GW signal $\mathbf{h}$:

$$\mathbf{s}_{I,J} = \mathbf{n}_I(t_{I,J}) + \mathbf{r}_{I,J} + \mathbf{h}\left(\overline{\Psi}, \mathbf{n}_I(t_{I,J}), t_{I,J}\right)\,. \tag{4.3}$$

Each measurement is a point on the sphere (sky), and can be represented in any one of a number of coordinate systems, although for simplicity here it shall be assumed that the right ascension and declination are used.

The background star position also contains the star's proper motion; this is accounted for and corrected by fitting a quadratic function to the set $\{\vec{n}_I(t_{I,J})\}$ and subtracting the trend from the data. This procedure removes the background position, the velocity, and the acceleration from the astrometric data, thus rendering it solely a combination of the instrument noise and a gravitational wave signal, if such is present. The noise in each instrument $\sigma \equiv \sigma_{I,J}$ is assumed to be identical and independent, although this is not necessary for the method to yield results. Thus the expectation of the product of the noise at two stars at two different times is

$$\mathrm{E}\left[\mathbf{r}_{I,J} \cdot \mathbf{r}_{I',J'}\right] = \sigma^2 \delta_{II'} \delta_{JJ'}\,. \tag{4.4}$$

Given the above assumptions about the GW signal and the instrument noise, the likelihood of detecting the signal in the dataset $\mathscr{S}$ may be written down as follows [90]

$$P\left(\mathscr{S}|\overline{\Psi}\right) \propto \exp\left(\sum_{I=1}^{M}\sum_{J=1}^{N} \frac{-\left|\mathbf{s}_{I,J} - \mathbf{h}\left(\overline{\Psi}, \mathbf{n}_I(t_J), t_J\right)\right|^2}{2\sigma^2}\right). \tag{4.5}$$

The posterior probability is, according to Bayes' theorem

$$P\left(\overline{\Psi}|\mathscr{S}\right) = \frac{\Pi\left(\overline{\Psi}\right) P\left(\mathscr{S}|\overline{\Psi}\right)}{\mathscr{Z}_{\text{signal}}}, \tag{4.6}$$

where $\Pi\left(\overline{\Psi}\right)$ is the prior for this type of event. For the purposes of this Chapter, the priors used for the amplitudes $\{A_+, A_\times\}$ are log-uniform, the priors for the phase angles $\{\phi_+, \phi_\times\}$ are uniform and periodic, the prior for the frequency is log-uniform in the range $f \sim \mathscr{U}\left[1/T, N/2T\right]$, and the prior for $\mathbf{q}$ is uniform on the sphere (sky). $\mathscr{Z}_{\text{signal}}$ is the Bayesian signal evidence and is used to normalise the distribution in eq. (4.6):

$$\mathscr{Z}_{\text{signal}} = \int \mathrm{d}\overline{\Psi}\, \Pi\left(\overline{\Psi}\right) P\left(\mathscr{S}|\overline{\Psi}\right). \tag{4.7}$$

The noise evidence $\mathscr{Z}_{\text{noise}}$, on the other hand, is evaluated using eq. (4.5) with $\mathbf{h} = 0$. The Bayes' factor for the detection is defined as $\mathscr{B} \equiv \mathscr{Z}_{\text{signal}}/\mathscr{Z}_{\text{noise}}$ and is a measure of the detection likelihood: signals for which $\mathscr{B} > \mathscr{B}_{\text{threshold}} = 10^{1.5}$ are assumed likely to be detected, although this choice is somewhat arbitrary and depends on the specifics of the problem at hand. In the development of this pipeline, the MULTINEST [91] implementation of nested sampling [92] was used.

Since a final *Gaia* data set is not readily available, for the purposes of testing this pipeline and testing possible future searches, a mock set of data was constructed as follows: $N = 75$ measurements of $M = 10^5$ stars on the sky were generated, spread evenly over a period of $T = 5$ years (the nominal duration of the *Gaia* mission), with appropriate simulated noise [93]. As a first step towards preparations for data analysis, the fitting procedure was carried out, which removed zeroth, first, and second order trends in the data, as described above. Additionally, a gravitational wave signal was injected into the data set: each black hole in the binary has mass $m_1 = m_2 = 5 \times 10^8 M_\odot$, on a circular orbit of radius $R = 1500\,\text{au}$ at a distance of 20 Mpc from the Earth (black hole spin is 0, and the angular momentum of the system is aligned along the line-of-sight). This would yield a circularly polarized gravitational wave with amplitude $A_+ = A_\times = 3 \times 10^{-14}$ and frequency $\omega = 2\pi f = 2 \times 10^{-7}\,\text{Hz}$.

Using the method described above, the signal was recovered with $\mathscr{B} = 10^{4.2} > \mathscr{B}_{\text{threshold}}$. The 1-dimensional marginalised posterior distributions are depicted in Fig. 4.1.

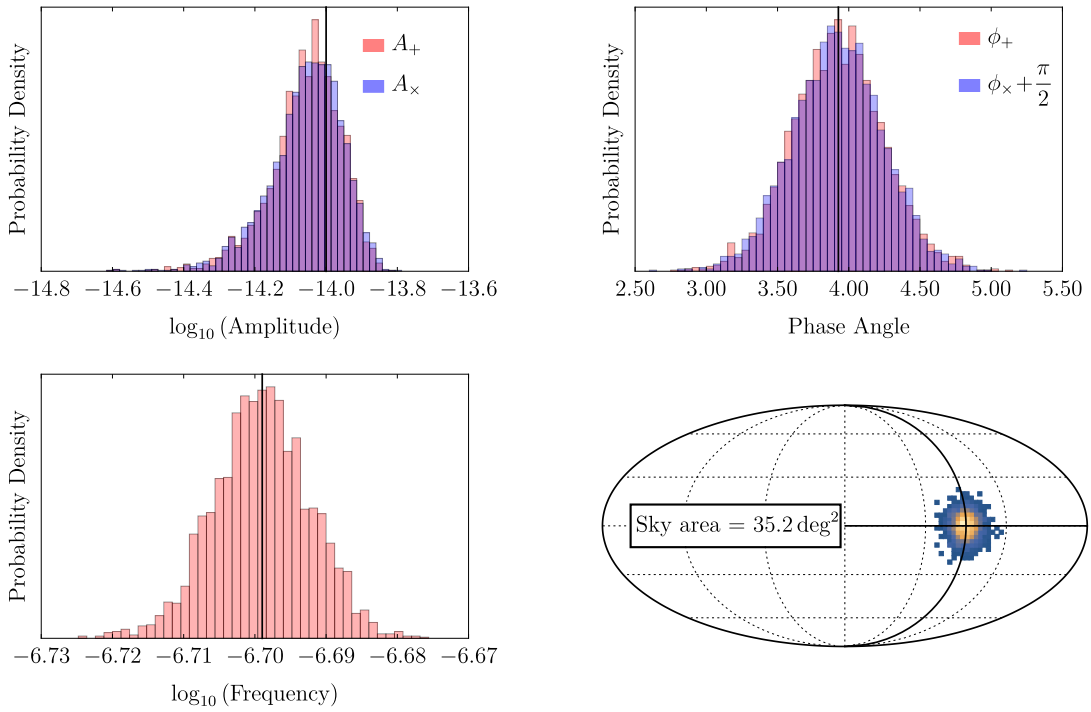

Fig. 4.1 1–dimensional marginalised posteriors on $\overline{\Psi}$ (black lines indicate injected values). The injected GW was circularly polarised (i.e $\phi_+ - \phi_\times = \pi/2$) so the $\phi_\times$ posterior is shifted such that it overlaps with ϕ_+. The Mollweide sky map is shown with the area of the 68% credible region given. Figure appeared in [79].

4.2 Compressing the Gaia dataset

Searches using large number of stars ($M = 10^5$, or the full *Gaia* catalogue of 10^9 stars) are too computationally expensive, and this renders the method described above intractable for practical use. In order to make the method viable and efficiently explore this problem, one needs to develop a near-lossless compression method for the astrometric data. For this purpose, a set of "virtual stars" $\tilde{M}(\ll M)$ are placed on the sky, each virtual star defines a Voronoi cell $\mathscr{V}_{\tilde{I}}, \tilde{I} = 1, 2, \ldots, \tilde{M}$ consisting of all points lying on the sphere which are closer to that virtual star than any other [94]. Each star in the set M is then assigned to one of the virtual stars according to the Voronoi cell in which the star is located. In order to compress the data set, each virtual star is endowed with the averaged astrometric deflections of all the stars in its corresponding Voronoi cell (a tilde here denotes the virtual data set)

$$\tilde{\mathbf{s}}_{\tilde{I},J} = \frac{1}{|\mathscr{V}_{\tilde{I}}|} \sum_{I \in \mathscr{V}_{\tilde{I}}} \mathbf{s}_{I,J}\,, \qquad \frac{1}{\tilde{\sigma}^2_{\tilde{I},J}} = \sum_{I \in \mathscr{V}_{\tilde{I}}} \frac{1}{\sigma^2_{I,J}}\,, \tag{4.8}$$

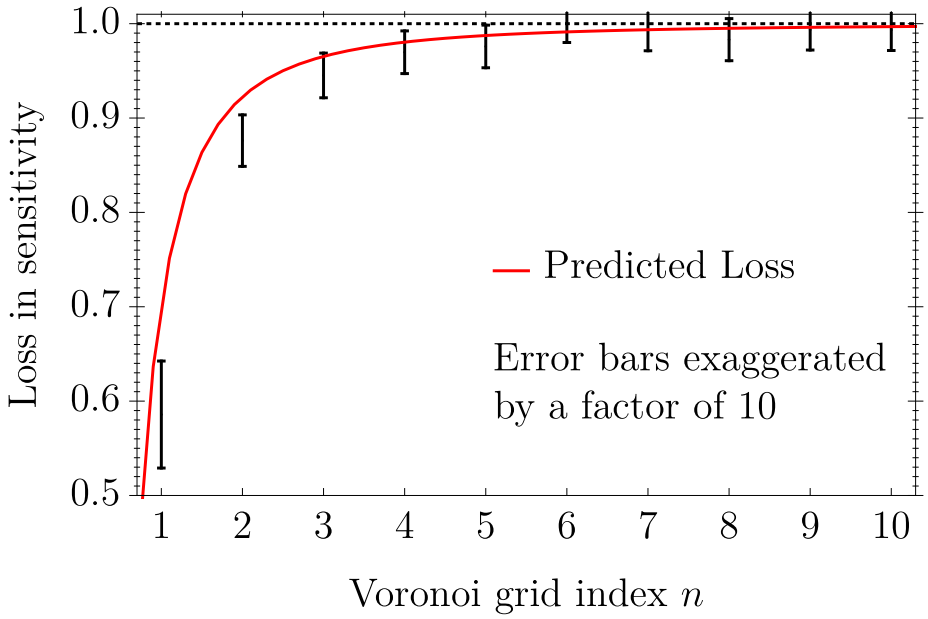

Fig. 4.2 The horizon distance (relative to that for the uncompressed data) is reduced during compression onto Voronoi grid $n = 1, 2, \ldots, 10$. Shown in red is an estimate of the loss obtained by considering the angle between astrometric deflections for stars in the same Voronoi cell. Figure appeared in [79].

where $|\mathscr{V}_{\tilde{I}}|$ is the number of real stars in the Voronoi cell $\mathscr{V}_{\tilde{I}}$. This new "virtual" data set $\tilde{\mathscr{S}} = \{\tilde{\mathbf{s}}_{\tilde{I},J} | \tilde{I} = 1, \ldots, \tilde{M}; J = 1, \ldots, N\}$ is now ready to be analyzed using the numerical method described in the previous Section.

The compression from the "real" to the "virtual" data sets would be completely lossless if two conditions were satisfied: (i) the instrument noise was independent (c.f. eq. (4.4)), and (ii) the astrometric deflections in a given Voronoi cell were perfectly collinear. Condition (i) cannot be expected to hold perfectly, although the data-taking method of *Gaia* works favourably in this case: as the space-craft constantly rotates, separate measurements of the same object will be taken with different parts of the CCD array. Furthermore, correlations for co-located stars vanish for star separations of more than 0.7° [95]. The astrometric deflection is a smooth vector field on the sphere, therefore for sufficiently small Voronoi cells, condition (ii) above would become satisfied.

In this analysis, the Voronoi cells on the surface of the sphere were chosen to be geodesic domes with icosahedron as the base polyhedron. The method for generating sub-divisions of the icosahedron involved dividing the great circle arcs between its vertices into $n = 2, 3, \ldots$ smaller arcs, and the constructing n^2 near-isosceles spherical triangles on each face. The n^{th} Voronoi grid therefore has $\tilde{M} = 20 \times n^2$ virtual stars.

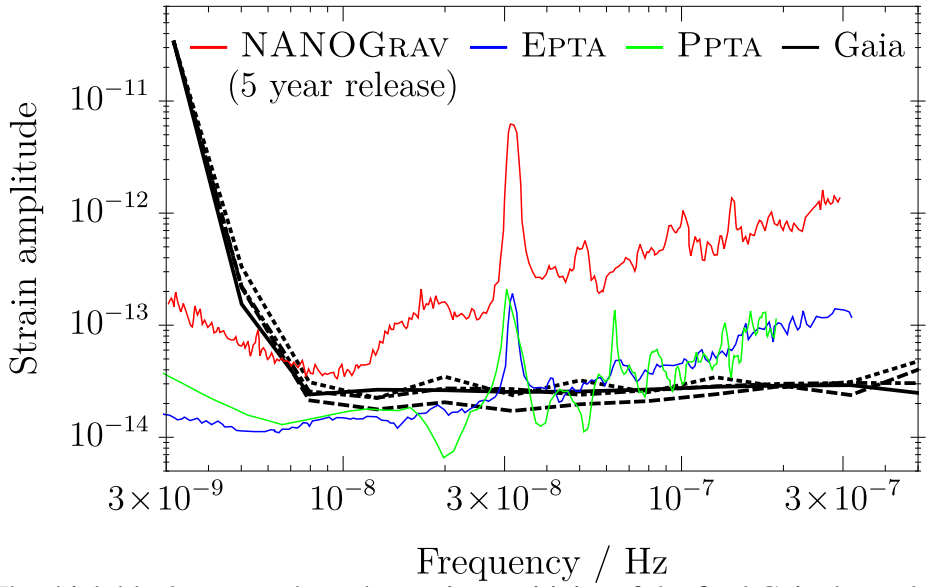

Fig. 4.3 The thick black curves show the strain sensitivity of the final Gaia data release using the different time samplings; T_0 is the solid line, T_1 is the dotted line, T_2 is the dashed line, and T_3 is the dot-dashed line. The four curves are very similar. For comparison the thin coloured lines show the 95% upper limits from the three PTA collaborations: NANOGrav ([96] red), EPTA ([97] blue) and PPTA ([98] green). The curves in this plot show different quantities and are only intended to allow for approximate comparissons; the NANOGrav curve is a Bayesian 95% upper limit, the EPTA and PPTA curves are frequentist 95% upper limits, while the Gaia curves show the amplitude necessary to achieve a (conservative) threshold Bayes' factor. It should be noted that the PTA limits plotted are several years old and constraints improve over time; Gaia's sensitivity will not improve further. However, it is clear that, especially at higher frequencies, Gaia promises to provide a useful complement to the existing limits from pulsar timing. Figure appeared in [79].

In order to establish the loss of sensitivity due to compression, the original data set was analysed after being compressed on each of the grids with $n = 10, 9, \ldots, 1$ separately, and the resulting virtual data sets were each analysed with the method described above. The reason for signal loss (smaller Bayes' factor) for grids with lower n is the fact that astrometric deflections are not parallel in larger Voronoi cells, and therefore the deflections partially cancel each other out when averaged, and is depicted in Fig. 4.2. The reduction in the Bayes' factor due to compression is effectively a reduction of the distance at which an event may be successfully detected. This loss of sensitivity is less than 1% for grids with $n \geq 7$, while the reduction in size for the full data set would be of the order of 10^6.

Now that an efficient method for searching for gravitational waves has been established, the sensitivity of *Gaia* can be explored in detail.

4.3 Gaia's frequency sensitivity

In order to examine the frequency sensitivity of *Gaia*, circularly polarized gws were injected with varying amplitudes and frequencies, and the resulting data sets were compressed onto the $n = 10$ Voronoi grid. For fixed values of the frequency in the range $(10^{-8.5}$–$10^{-6})$Hz several successive injections were performed and recovered in order to establish the minimum amplitude necessary for a successful detection. Additionally, the effect of uniform vs. non-uniform sampling was also explored. The uniform time sampling, T_0, assumes $N = 75$ measurements spread over $T = 5$ years. The more realistic non-uniform time samplings were constructed using the *Gaia* observing schedule applied to three points on the sky which simulate the variability in the *Gaia* sampling function (these are denoted by $T_\alpha, \alpha \in \{1,2,3\}$).

The strain sensitivity of *Gaia* is nearly flat in the region $f \gtrsim 1/T$, unlike PTAs whose sensitivities degrade linearly with the increase of frequency. This effect can be explained by considering how each of these methods work: PTAs rely on measuring the timing residual, i.e. the integral over time of the redshift caused by the passing of the gravitational wave. This integration over time suppresses the sensitivity of PTAs for frequencies $f \gtrsim 1/T$. On the other hand, the astrometric search method relies on quantifying the astrometric deflection which is proportional to the strain of the GW (eq. (3.20)). Eventually, when both methods are applied to data and yield results, they would be able to complement each other in the high frequency region, near $f \gtrsim 10^{-7.5}$ Hz [79].

4.4 Gaia's directional sensitivity

Since the distribution of stars in the Milky Way (and in the *Gaia* catalogue) is not uniform, it is natural to expect that the sensitivity of *Gaia* as a GW detector will vary with the direction of $\mathbf{q}$. Here this directional sensitivity pattern of *Gaia* is investigated.

Let's first consider the astrometric response for a GW source which lies on the positive z-axis ($\mathbf{q} = \{0,0,1\}$) and a single star in the $x-z$ plane ($\mathbf{n} = \{\sin\gamma, 0, \cos\gamma\}$); the astrometric shift as a function of the angle γ is given by (cf. eqs. (4.1) and (3.20))

$$|\delta\vec{n}| = \frac{1}{2}\sqrt{A_+^2 + A_\times^2}\,\sin\gamma\,. \tag{4.9}$$

Evidently, the response is greatest in magnitude for stars which lie in a plane that is orthogonal to the direction of propagation of the GW, and hence the peak sensitivity of *Gaia* is to be

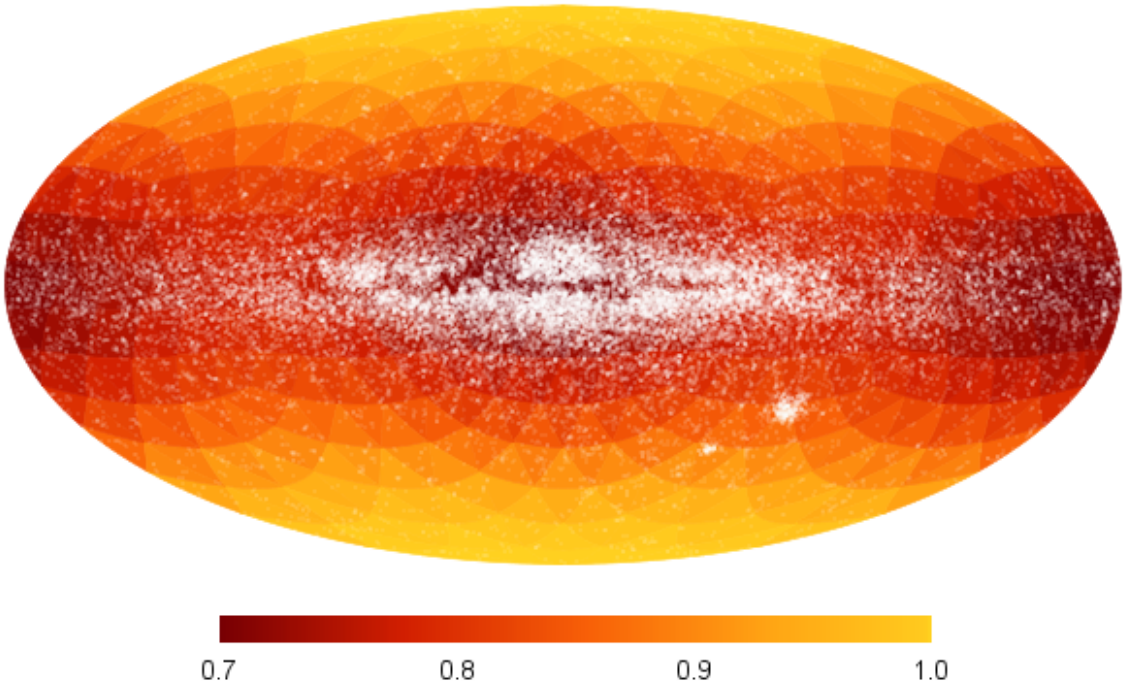

Fig. 4.4 The variation in *Gaia*'s sensitivity over the sky, $F(\theta,\phi)$. A sample of 60,000 stars drawn randomly from the *Gaia* catalogue are shown as white dots. The sensitivity varies by $\sim$30% across the sky with minima at (and antipodal to) the galactic centre, and maxima at the galactic poles. Figure appeared in [79].

expected for signals coming from directions which are orthogonal to regions of high stellar density, i.e. from the two galactic poles.

In order to quantify this conclusion, GW signals were injected in the set of stars from the first *Gaia* data release (https://www.cosmos.esa.int/web/gaia/dr1), and recovered using the routine described above (the sampling was chosen to be uniform over the lifetime of the mission). The process was repeated for 500 locations on the sky (each time the data set was compressed onto the $n = 5$ Voronoi grid in order to expedite the search). The resulting variation in sensitivity (antennae pattern) is plotted in Fig. 4.4.

5

Gravitational Wave Backgrounds with non-Einsteinian Polarizations

Material in this Chapter is the result of my collaboration with Dr Christopher Moore and my supervisors. This work has been peer reviewed and published in Physical Review D as [60]. As the first author of that publication, my contribution included all the theoretical work, namely deriving the correlation functions in each case, and using code developed by Christopher Moore to generate random realisations of the correlated stochastic backgrounds.

5.1 Correlated Astrometric Deflections

In Chapter 3 the astrometric response to a single monochromatic GW was derived. In this Section the astrometric response to a stochastic background of GWs is considered. A stochastic background of GWs generates a stochastic pattern of astrometric deflections over the sky which is highly correlated at large angular scales. The pattern of this correlation depends on the polarization of the GWs which make up the background. The general framework for considering correlated vector fields on the sphere is introduced, and then in Sections 5.1.1 to 5.1.4 below, the correlation for several different combinations of the polarization states discussed in Section 3.2 are explicitly evaluated.

The discussion in this Chapter is restricted to stochastic GW backgrounds which are Gaussian, stationary, isotropic and unpolarized (at this point we do not specify which polarization states comprise the background, just that they are uncorrelated with each other so the background is statistically unpolarized). The astrometric deflection is then a Gaussian random vector field on the sphere, and the statistical properties of this field are described by a correlation matrix. Adopting a convenient decomposition for this correlation matrix allows

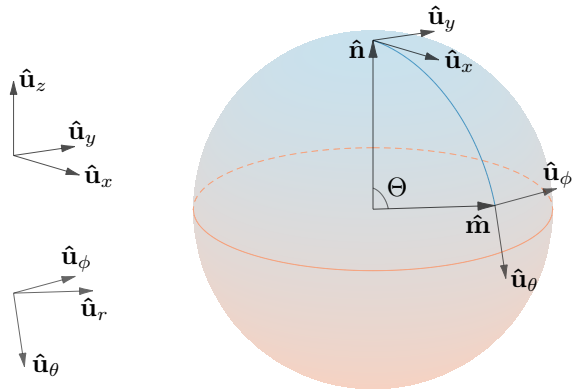

Fig. 5.1 Geometrical setup of the vectors involved in the calculation of the overlap reduction functions. A pair of stars, one of them nominally placed at the North pole, and a second one at angular separation Θ (along the arc $\phi = 0$) are considered. Each of them experiences astrometric response due to a background of gravitational radiation. On the left-hand side of the Figure are shown the Cartesian triad associated with the point $\hat{n}^i$ (top) and the curvilinear triad associated with the point $\hat{m}^i$ (bottom). The astrometric deflection at point $\hat{n}^i$ ($\hat{m}^i$) is a vector in the tangent plane to the sphere, and can be decomposed in terms of just $\hat{\mathbf{e}}_x$ and $\hat{\mathbf{e}}_y$ ($\hat{\mathbf{e}}_\theta$ and $\hat{\mathbf{e}}_\phi$). We are interested in the correlations between these vector components. Figure appeared in [60].

for an intuitive visualization of key features of the correlation over the sphere of the sky. This decomposition will also permit a clear comparison with the analogous calculations in the pulsar timing literature.

Consider the correlation between the astrometric deflections at two different points on the sky. The astrometric response is given by the distant source limit formula, eq. (3.20) (specific examples when this formula is not valid will be considered later in this Section). In this limit, the astrometric deflection depends only on the "Earth term" metric perturbation; this time-dependent metric perturbation can be Fourier decomposed as

$$h_{ij}(t) = \Re\left\{\sum_P \int_0^\infty \mathrm{d}f \int_{S^2} \mathrm{d}\Omega_{\mathbf{q}}\, A_P(\mathbf{q},f)\, e^{-2\pi \mathrm{i} f t}\, \varepsilon^P_{ij}(\mathbf{q})\right\}, \tag{5.1}$$

where $f = \omega/2\pi$ is the linear GW frequency, $A_P(\mathbf{q},f)$ are the (complex) Fourier coefficients, $\mathrm{d}\Omega_{\mathbf{q}}$ is the area element on the sphere, and $\mathbf{q} \equiv q_i$ is the direction from which the GW originates. The label P indicates the GW polarization which, at this stage, may be any of the six states $P \in \{+,\times,S,X,Y,L\}$ described in Section 3.2.

The GW background is assumed to be Gaussian, zero-mean, stationary, isotropic, and unpolarized. The expectation values of the Fourier coefficients in such a background satisfy

$$\left\langle A_P(\mathbf{q},f)A^*_{P'}\left(\mathbf{q}',f'\right)\right\rangle = C(f)\,\delta_{PP'}\,\delta_{S^2}(\mathbf{q},\mathbf{q}')\,\delta(f-f') \tag{5.2a}$$

$$\left\langle A_P(\mathbf{q},f)A_{P'}\left(\mathbf{q}',f'\right)\right\rangle = 0, \tag{5.2b}$$

where angle brackets denote expectation values, and the function $C(f)$ is related to the spectral energy density in the GW background [99].

The astrometric deflection is linear in the metric perturbation, and the response to each Fourier mode may be calculated individually:

$$\delta n_i(\mathbf{n},t) = \Re\left\{\sum_P \int_0^\infty \mathrm{d}f\, e^{-2\pi \mathrm{i} f t}\int_{S^2}\mathrm{d}\Omega_{\mathbf{q}}\, A_P(\mathbf{q},f)\,\Delta_i{}^{jk}(\mathbf{n},\mathbf{q})\,\varepsilon^P_{jk}(\mathbf{q})\right\}, \tag{5.3}$$

where we have defined

$$\Delta_i{}^{jk}(\mathbf{n},\mathbf{q}) = \frac{1}{2}\left(\frac{n_i - q_i}{1-q^\ell n_\ell}\,n^j n^k - \delta_i{}^j n^k\right). \tag{5.4}$$

The linearity of the astrometric deflection with the metric perturbation also ensures that it will be a Gaussian random variable, and that its statistical properties depend only on the two-point correlation. Using eqs. (5.2) and (5.3), it is straightforward to show that the expectation of the product of astrometric responses δn_i and δm_i of two stars, situated at two different points on the sky, n_i and m_i, separates into a factor depending on the measurement times and a factor depending on the locations of the stars on the sky,

$$\left\langle \delta n_i(\mathbf{n},t)\,\delta m_j(\mathbf{m},t')\right\rangle = T(t,t')\,\Gamma_{ij}(\mathbf{n},\mathbf{m})\,. \tag{5.5}$$

Because both $\delta n_i(\mathbf{n},t)$ and $\delta m_j(\mathbf{m},t)$ have zero mean, this expectation is proportional to the correlation between the two quantities. As is well known, the temporal correlation factor is given by the cosine transform of the GW frequency spectrum;

$$T(t,t') = \frac{1}{4}\int_0^\infty \mathrm{d}f\, C(f)\left(e^{2\pi\mathrm{i}f(t-t')} + e^{-2\pi\mathrm{i}f(t-t')}\right). \tag{5.6}$$

The spatial correlation factor is a sum of integrals of products of vectors over the sphere for each mode P (cf. the factor of $\delta_{PP'}$ in eq. (5.2a)):

$$\Gamma_{ij}(\mathbf{n},\mathbf{m}) = \sum_P \Gamma^P_{ij}(\mathbf{n},\mathbf{m})\,, \tag{5.7}$$

where, for each polarization state, it has been defined

$$\Gamma^{P}_{ij}(\mathbf{n},\mathbf{m}) = \int_{S^2} \mathrm{d}\Omega_{\mathbf{q}}\, \delta n^{P}_{i}(\mathbf{n},\mathbf{q})\, \delta m^{P}_{j}(\mathbf{m},\mathbf{q}), \tag{5.8}$$

$$\text{where } \delta n^{P}_{i}(\mathbf{n},\mathbf{q}) = \Delta_{i}^{\ jk}(\mathbf{n},\mathbf{q})\, \varepsilon^{P}_{jk}(\mathbf{q})\,. \tag{5.9}$$

Only the spatial part of the correlation, $\Gamma_{ij}(\mathbf{n},\mathbf{m})$, depends on the polarization content of the GW background. Hereafter, only spatial correlations will be investigated.

Since the background is isotropic, the sky sphere can be rotated into the most convenient orientation. The first star, n_i, is placed at the North Pole, and the second, m_i, in the x-z plane (for anisotropic backgrounds, this transformation is still possible, though in that case the background needs to also be rotated into the new frame; see [86] for details). The stars have coordinates

$$\mathbf{n} = (0,0,1), \tag{5.10a}$$

$$\mathbf{m} = (\sin\Theta, 0, \cos\Theta). \tag{5.10b}$$

The astrometric deflection vectors lie in the tangent plane of the sphere; it is now necessary to introduce a pair of basis vectors at both points on the sphere. The choice of basis is of course arbitrary; however, the following choice will prove to be convenient. For any pair of points n_i and m_i there is a unique (shortest) geodesic on the sphere, γ, linking n_i to m_i; at both n_i and m_i the unit tangent vector to γ and the unit vector pointing to the left of γ form an orthonormal basis. For the values of n_i and m_i in eq. (5.10) the coordinate expressions for these basis vectors are

$$\hat{u}^{x} = (1,0,0), \tag{5.11a}$$

$$\hat{u}^{y} = (0,1,0), \tag{5.11b}$$

$$\hat{u}^{\theta} = (\cos\Theta, 0, -\sin\Theta), \tag{5.12a}$$

$$\hat{u}^{\phi} = (0,1,0), \tag{5.12b}$$

whilst the general definitions for two arbitrary points on the sphere are

$$\hat{u}^{x} = \frac{(\hat{n}\times\hat{m})\times\hat{n}}{\sqrt{1-(\hat{n}\cdot\hat{m})^2}}, \tag{5.13a}$$

$$\hat{u}^{y} = \frac{\hat{n}\times\hat{m}}{\sqrt{1-(\hat{n}\cdot\hat{m})^2}}, \tag{5.13b}$$

$$\hat{u}^{\theta} = \frac{(\hat{n}\times\hat{m})\times\hat{m}}{\sqrt{1-(\hat{n}\cdot\hat{m})^2}}, \tag{5.14a}$$

$$\hat{u}^{\phi} = \frac{\hat{n}\times\hat{m}}{\sqrt{1-(\hat{n}\cdot\hat{m})^2}}. \tag{5.14b}$$

The geometric setup is illustrated in Fig. 5.1.

The astrometric deflections may now be decomposed into this basis;

$$\delta n^{P}_{i}(\mathbf{q}) = \delta n^{P}_{x}(\mathbf{q})\, \hat{u}^{x}_{i} + \delta n^{P}_{y}(\mathbf{q})\, \hat{u}^{y}_{i}\,, \tag{5.15a}$$

$$\delta m^{P}_{i}(\mathbf{q}) = \delta m^{P}_{\theta}(\mathbf{q})\, \hat{u}^{\theta}_{i} + \delta m^{P}_{\phi}(\mathbf{q})\, \hat{u}^{\phi}_{i}\,, \tag{5.15b}$$

where the scalar coefficients are given by

$$\delta n^P_x(\mathbf{q}) = \delta n^P_i(\mathbf{q})\,\hat{u}^i_x, \tag{5.16a}$$

$$\delta n^P_y(\mathbf{q}) = \delta n^P_i(\mathbf{q})\,\hat{u}^i_y, \tag{5.16b}$$

$$\delta m^P_\theta(\mathbf{q}) = \delta m^P_i(\mathbf{q})\,\hat{u}^i_\theta, \tag{5.17a}$$

$$\delta m^P_\phi(\mathbf{q}) = \delta m^P_i(\mathbf{q})\,\hat{u}^i_\phi. \tag{5.17b}$$

Substituting eqs. (5.15) into eq. (5.8) and expanding gives an expression for the spatial correlation function as a sum of scalar integrals over the sphere,

$$\Gamma^P_{ij}(\Theta) = \hat{u}^x_i \hat{u}^\theta_j \int_{S^2} \mathrm{d}\Omega_{\mathbf{q}}\; \delta n^P_x(\mathbf{q})\,\delta m^P_\theta(\mathbf{q}) \tag{5.18a}$$

$$+ \hat{u}^x_i \hat{u}^\phi_j \int_{S^2} \mathrm{d}\Omega_{\mathbf{q}}\; \delta n^P_x(\mathbf{q})\,\delta m^P_\phi(\mathbf{q}) \tag{5.18b}$$

$$+ \hat{u}^y_i \hat{u}^\theta_j \int_{S^2} \mathrm{d}\Omega_{\mathbf{q}}\; \delta n^P_y(\mathbf{q})\,\delta m^P_\theta(\mathbf{q}) \tag{5.18c}$$

$$+ \hat{u}^y_i \hat{u}^\phi_j \int_{S^2} \mathrm{d}\Omega_{\mathbf{q}}\; \delta n^P_y(\mathbf{q})\,\delta m^P_\phi(\mathbf{q})\,. \tag{5.18d}$$

In fact, it can be shown that for any correlated vector field on the sphere which is statistically invariant under both rotations and parity transformations the y-θ and x-ϕ terms (i.e. (5.18b) and (5.18c)) vanish. These terms can also explicitly be shown to vanish for each GW polarization considered individually in Sections 5.1.1 to 5.1.4 below. Therefore, remarkably, the full spatial correlation matrix is always fully specified by just two real-valued functions, and may be written as

$$\Gamma^P_{ij}(\mathbf{n},\mathbf{m}) = \Gamma^P_{x\theta}(\Theta)\,\hat{u}^x_i \hat{u}^\theta_j + \Gamma^P_{y\phi}(\Theta)\,\hat{u}^y_i \hat{u}^\phi_j\,, \tag{5.19}$$

where $\Theta = \arccos(\mathbf{n}\cdot\mathbf{m})$, the unit vectors are defined in terms of n_i and m_i in eqs. (5.13) and (5.14) and the functions $\Gamma^P_{x\theta}(\Theta)$ and $\Gamma^P_{y\phi}(\Theta)$ are defined as the integrals in terms (5.18a) and (5.18d) respectively. This result is the equivalent of eq. (71) in [76].

One advantage of the decomposition of the spatial correlation matrix in eq. (5.19) is that the functions $\Gamma^P_{x\theta}(\Theta)$ and $\Gamma^P_{y\phi}(\Theta)$ have the clear interpretation as the *scalar* correlations of the "parallel" and "perpendicular" components of the astrometric deflection. Here "parallel" means tangent to the geodesic linking the two points, and "perpendicular" means pointing to the left of this curve; see Fig. 5.1.

It is well known that any vector field v_i on the sphere admits a unique Helmholtz decomposition into gradient and curl parts; $v_i = \nabla_i \phi + (\nabla\wedge)_i\,\psi$, where ∇ is the surface gradient on the sphere, $(\nabla\wedge) = \mathbf{r}\wedge\nabla$ is the surface curl, and ϕ and ψ are scalar fields on the sphere. Another advantage of the spatial correlation matrix in eq. (5.19) is that the functions $\Gamma^P_{x\theta}(\Theta)$ and $\Gamma^P_{y\phi}(\Theta)$ govern the statistical properties of the gradient and curl parts respectively. By comparing components, it can be seen that the $\Gamma^P_{x\theta}(\Theta)$ and $\Gamma^P_{y\phi}(\Theta)$ terms in eq. (5.19) are

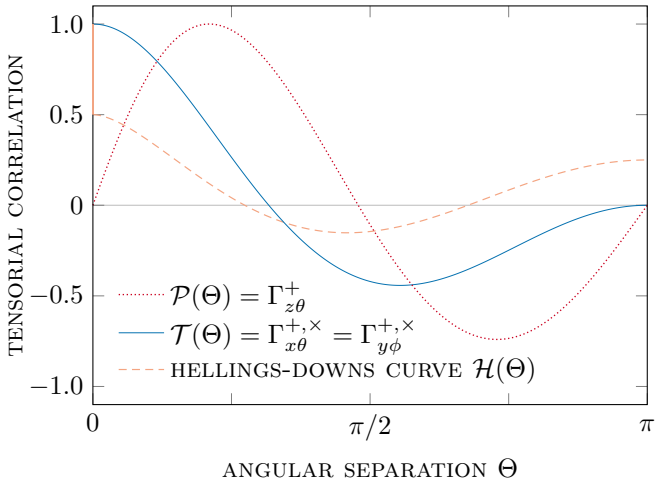

Fig. 5.2 The astrometric and redshift correlations as a function of angular separation on the sky in a background of tensorial, transverse-traceless GWs (i.e. $+$ and $\times$). The well known Hellings–Downs curve, $\mathscr{H}(\Theta)$, determines the redshift correlations and is shown here with the usual normalization $\lim_{\Theta\to 0} H(\Theta) = 1/2$ due to the presence of the pulsar term in eq. (3.17). The astrometric correlations are similarly determined by a single function, $\mathscr{T}(\Theta)$, which is shown with the normalization $\mathscr{T}(0) = 1$ as there is no star term in eq. (3.20). The function $\mathscr{T}(\Theta)$ is the astrometric analog of the Hellings–Downs curve. The function $\mathscr{P}(\Theta)$ is the redshift-astrometry analog of the Hellings–Downs curve and is introduced and discussed in Section 5.2. Figure appeared in [60].

exactly the general divergence and curl kernels Ψ_{div} and Ψ_{curl} defined in [100]. A random vector field described by spatial correlation matrix with $\Gamma_{y\phi} = 0$ will be a pure divergence, and a vector field described by correlation matrix with $\Gamma_{x\theta} = 0$ will be a pure curl.

5.1.1 Tensorial Transverse-Traceless Polarizations

This section considers the astrometric correlations arising in a background of just the two GR polarization modes; i.e. $P \in \{+, \times\}$. This calculation was considered previously in [76], here this result is reproduced within the framework outlined in the previous section.

In Appendix B it is shown how to evaluate the integrals $\Gamma^{+}_{x\theta}$, $\Gamma^{+}_{y\phi}$, $\Gamma^{\times}_{x\theta}$, and $\Gamma^{\times}_{y\phi}$ defined in eq. (5.8). Following eq. (5.7), the spatial correlation matrix in a background with multiple polarizations is the sum of the individual spatial correlations, so $\Gamma^{+,\times}_{x\theta}(\Theta) = \Gamma^{+}_{x\theta}(\Theta) + \Gamma^{\times}_{x\theta}(\Theta)$, and similarly for $\Gamma^{+,\times}_{y\phi}(\Theta)$. Remarkably, these two functions turn out to be equal in this

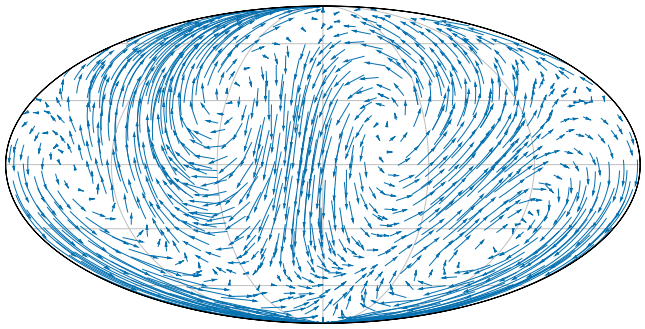

Fig. 5.3 A random realization of the astrometric deflection field for a background of tensorial $+$ and $\times$ waves. The position of each star is recorded twice, separated by a time Δt. These two position are shown here (in Mollweide projection) at the foot and head respectively of each arrow. The length of each arrow is proportional to the total power in the GW background at frequencies $f < 1/\Delta t$. The length of the arrows has been greatly scaled up here for clarity. Figure appeared in [60].

particular case,

$$\mathscr{T}(\Theta) = \Gamma^{+,\times}_{x\theta}(\Theta) = \Gamma^{+,\times}_{y\phi}(\Theta) = \frac{2\pi}{3} - \frac{14\pi}{3}\sin^2(\Theta/2) - 8\pi\frac{\sin^4(\Theta/2)}{1-\sin^2(\Theta/2)}\ln(\sin(\Theta/2))\,. \tag{5.20}$$

Throughout this section all correlation functions are written in terms of $\sin(\Theta/2)$. Therefore, the correlated astrometric deflection field generated by a Gaussian, stationary, isotropic, unpolarized GW background in GR is fully specified by a single real-valued function of the angular separation on the sphere, $\mathscr{T}(\Theta)$.

This function ought to be compared to the corresponding result for Pulsar Timing. The spatial correlation between the redshift at two different points on the sky is given by the well-known Hellings-and-Downs curve [101],

$$\mathscr{H}(\Theta) = \frac{1}{2}(1+\beta) - \frac{1}{4}\sin^2(\Theta/2) + 3\sin^2(\Theta/2)\ln(\sin(\Theta/2))\,, \tag{5.21}$$

where $\beta = 1$ for co-located pulsars and is zero otherwise. The standard PTA normalization is $\lim_{\Theta\to 0}\mathscr{H}(\Theta) = 1/2$; the β in eq. (5.21) comes from the expectation of the pulsar terms in eq. (3.17) which is non-zero only for the autocorrelation. In the astrometric case there are no star terms (see eq. (3.20)), so in the case of a total time correlation ($T(t,t') = 1$), the normalization $\mathscr{T}(0) = 1$ can be chosen. Regardless, it is the "shape" of these curves that is of most interest here.

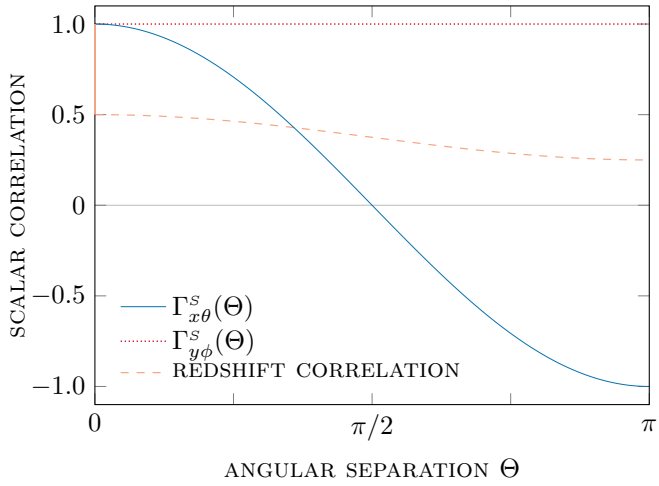

Fig. 5.4 The astrometric and redshift correlations as a function of angular separation on the sky in a background of scalar, "breathing" GWs (i.e. S). The functions which determine the astrometric correlations ($\Gamma^s_{x\theta}(\Theta)$ and $\Gamma^s_{y\phi}(\Theta)$, see eq. (5.22)) are normalized so that their maximum is unity. The PTA result for the correlated redshift in eq. (5.23) is plotted, normalized to $1/2$ at $\Theta = 0$. Figure appeared in [60].

The well known Hellings–Downs curve governs the spatial correlation of the redshift on the sky. Similarly, the function $\mathscr{T}(\Theta)$ governs the spatial correlation of the astrometric deflection on the sky. The function $\mathscr{T}(\Theta)$ can therefore be considered as the astrometric analog of the Hellings–Downs curve. Both $\mathscr{T}(\Theta)$ and $\mathscr{H}(\Theta)$ are shown in Fig. 5.2.

In order to gain a better understanding of what this vector field correlation over the sky means it is useful to draw a realization of this random process and to plot the result. The results are shown in Fig. 5.3, and an overview of the procedure used to produce the data in this plot can be found in Appendix C.

5.1.2 Scalar "Breathing" Polarization

The astrometric correlations arising in a background of transverse scalar GWs (i.e. $P \in \{S\}$) is considered here. Appendix D shows how to evaluate the integrals $\Gamma^s_{x\theta}$ and $\Gamma^s_{y\phi}$ defined in eq. (5.8); here only the results of these integrals are presented.

$$\Gamma^s_{x\theta}(\Theta) = \frac{\pi}{3}\cos\Theta \equiv \frac{\pi}{3} - \frac{2\pi}{3}\sin^2(\Theta/2)\,, \tag{5.22a}$$

$$\Gamma^s_{y\phi}(\Theta) = \frac{\pi}{3}. \tag{5.22b}$$

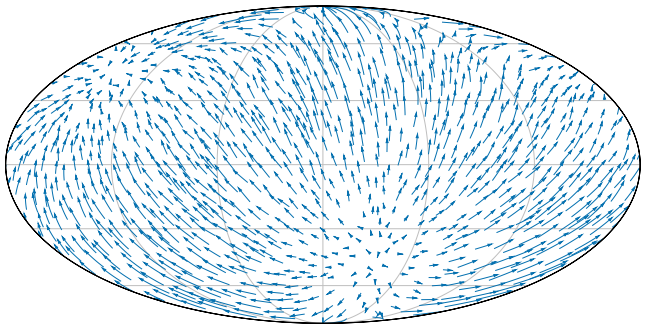

Fig. 5.5 A random realization of the astrometric deflection field for a background of scalar "breathing" S waves. This was produced in the same way as Fig. 5.3. It is clear from the plot that the astrometric deflection vector field has a random dipole-like structure on the sphere; the origin of this behavior is the fact that $\Gamma^{S}_{y\phi}(\Theta) \equiv$ constant, and the astrometric deflection at any two points on the sky are perfectly correlated. Figure appeared in [60].

Again, this should be compared to the PTA result for the redshift correlation in a stochastic background of "breathing" GWs. This was derived by [70] as

$$\mathrm{corr}(\Theta) = \frac{1}{2}(1+\beta) + \frac{1}{2} - \frac{1}{4}\sin^2(\Theta/2)\,, \tag{5.23}$$

the variable β is defined just after eq. (5.21). All three of these functions are plotted in Fig. 5.4.

The most surprising aspect of astrometric correlation is the result for $\Gamma^{s}_{y\phi}(\Theta)$; the "perpendicular" components of the astrometric deflection at any two points on the sky are always *perfectly* correlated. This is an extremely strong constraint which any allowed realizations of the vector field must obey. The interpretation of this becomes clearer when a random realization of the correlation is drawn; this is shown in Fig. 5.5.

The random realizations of the astrometric deflections plotted in Figs. 5.3 and 5.5 are qualitatively different. The transverse traceless polarisations of GR produce a distinctive curl-like pattern at large angular scales, whereas the transverse-trace (or scalar) mode generates a dipole-like structure on the sky. The polarization content of the stochastic GW background determines the spatial correlations among the astrometric deflections. If *Gaia*, or some other future astrometry mission, is able to measure the stochastic pattern of astrometric deflections due to a background of GWs, the measured correlations will encode details of the polarization content of the background and thereby enable a test of GR.

5.1.3 Vectorial Polarizations

After analysing the tensorial modes and the scalar “breathing" mode, it is interesting to consider the astrometric correlations arising in a background of just the two vectorial polarization modes; i.e. $P \in \{X, Y\}$. These calculations have an additional complication over those in the preceding sections as the vectorial polarizations have a longitudinal component which introduces a singularity into the “Earth term”-only redshift and astrometric responses (see eqs. (3.17) and (3.20)). In the case of the redshift correlation, as was found in [70], this means the correlation curve diverges at $\Theta = 0$;

$$\Gamma_z^{X,Y}(\Theta) = -\frac{28\pi}{3} + \frac{32\pi}{3}\sin^2(\Theta/2) - 8\pi\ln(\sin(\Theta/2))\,. \tag{5.24}$$

This result is plotted in Fig. 5.6. The divergence at the origin is a result of the use of the “Earth term”-only redshift response. If the “star term” is included the result becomes finite, and the correlation depends on the distance to the star. When including the star term the integration must be performed numerically; the results of this numerical integration are also shown in Fig. 5.6 for two pulsars at distances of 100 and 200 gravitational wavelengths respectively.

In contrast, the divergence in the astrometric response is of a logarithmic nature (i.e., of the type $\int \mathrm{d}x\, f(x)/x$), and is regularized by the integral over the sky. This means that the resulting correlation curve is non-divergent, even though the two individual astrometric responses do diverge. Appendix E discusses how to evaluate the integrals $\Gamma_{x\theta}^{X}$, $\Gamma_{y\phi}^{X}$, $\Gamma_{x\theta}^{Y}$, and $\Gamma_{y\phi}^{Y}$ analytically. Following eq. (5.7), the spatial correlation matrix in a background with multiple polarizations is the sum of the individual spatial correlations: $\Gamma_{x\theta}^{X,Y}(\Theta) = \Gamma_{x\theta}^{X}(\Theta) + \Gamma_{x\theta}^{Y}(\Theta)$, and similarly for $\Gamma_{y\phi}^{X,Y}(\Theta)$. Again, these two functions turn out to be equal:

$$\Gamma_{x\theta}^{X,Y}(\Theta) = \Gamma_{y\phi}^{X,Y}(\Theta) = \frac{4\pi}{3} + \frac{8\pi}{3}\sin^2(\Theta/2) + 8\pi\,\frac{\sin^2(\Theta/2)}{1-\sin^2(\Theta/2)}\ln(\sin(\Theta/2))\,. \tag{5.25}$$

This vectorial astrometric correlation function is also plotted in Fig. 5.6.

5.1.4 Scalar “Longitudinal” Polarization

The scalar longitudinal mode, on the other hand, is more interesting, as in this case the “Earth term”-only astrometric correlation curves do diverge at $\Theta = 0$. These functions are given by (see Appendix F for details of the evaluation of the relevant integrals, and Fig. 5.7 for plots

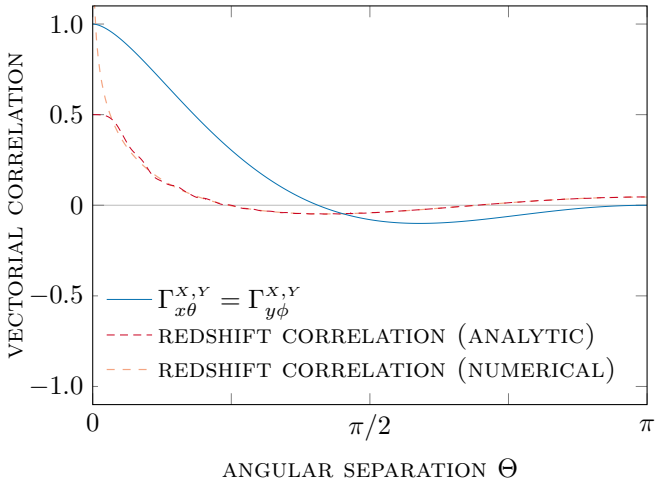

Fig. 5.6 The astrometric and redshift correlations as a function of angular separation on the sky in a background of vectorial GWs (i.e. $P \in \{X,Y\}$). The function which determines the astrometric correlation ($\Gamma^{X,Y}_{x\theta}(\Theta) = \Gamma^{X,Y}_{y\phi}(\Theta)$, see eq. (5.25)) is normalized so that its maximum is unity. The numerical redshift result (for pulsars at distances $(100\lambda_{\rm GW}, 200\lambda_{\rm GW})$) for the correlated redshift is plotted (normalized to $1/2$ at $\Theta = 0$) along with the divergent result from eq. (5.24). Figure appeared in [60].

of the two functions)

$$\Gamma^{L}_{x\theta}(\Theta) = -\frac{10\pi}{3} + \frac{8\pi}{3}\sin^2(\Theta/2) - 2\pi\frac{\ln(\sin(\Theta/2))}{1-\sin^2(\Theta/2)}, \tag{5.26a}$$

$$\Gamma^{L}_{y\phi}(\Theta) = -\frac{4\pi}{3} - 2\pi\frac{\ln(\sin(\Theta/2))}{1-\sin^2(\Theta/2)}. \tag{5.26b}$$

Similarly to vectorial redshift correlation, the divergence is a result of using the "Earth term"-only astrometric response in eq. (3.20). If instead, the full astrometric response in eq. (3.19) is used the correlation is finite, although the integrals need to be evaluated numerically in this case (see Appendix F.1 for details). When using the full astrometric response, the correlation curves depend on the distance to the stars; two such curves are shown in Fig. 5.7 for stars at distances of 100 and 200 gravitational wavelengths.

One conclusion which can be drawn from the curves in Fig. 5.7 is that that for a longitudinally-polarized GW background there are only strong astrometric correlations between stars at small angular separations. This is in marked contrast to the GR case of a tensorial $\{+,\times\}$ background, where correlations of order unity persist at all angular scales.

In order to better understand the behaviour at $\Theta = 0$, it is useful to consider the full (non-divergent) correlation including the distances to the stars at the point $\Theta = 0$. At this point the full integral can be evaluated analytically, giving a correlation which is a function

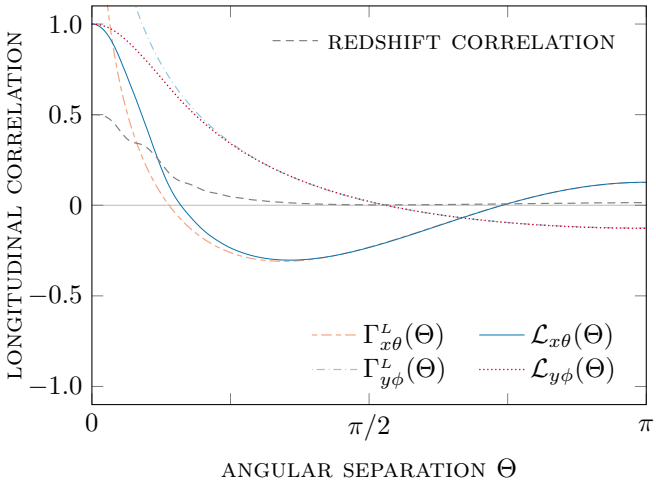

Fig. 5.7 The astrometric and redshift correlations as a function of angular separation on the sky in a background of scalar longitudinal GWs (i.e. *L*). The numerical curves which determine the astrometric correlation ($\mathscr{L}_{x\theta}(\Theta)$ and $\mathscr{L}_{y\phi}(\Theta)$, see Appendix F.1) are normalized so that their maximum is unity; the two analytical divergent curves $\Gamma^L_{x\theta}(\Theta)$ and $\Gamma^L_{y\phi}(\Theta)$ (see eq. (5.26)) are also plotted. The numerical redshift result for the correlated redshift is plotted, normalized to $1/2$ at $\Theta = 0$. Figure appeared in [60].

of just the distances d_n and d_m to the two stars. This function quantifies the cross-correlation of the deflections of two stars which appear at the same point on the sky, but are separated in distance by many gravitational wavelengths. A plot of this function is given in Fig. 5.8 and an explicit expression for it is given in Appendix F.2.

5.2 Redshift-Astrometry correlations

As discussed above, a stochastic background of GWs can, in principle, be detected by both pulsar timing or astrometric measurements. However, improved sensitivities can be obtained by combining these two techniques. In addition to the straightforward increase in signal to noise that comes with the increased amount of data, there is an additional benefit that comes from now being able to search for GWs in the cross-correlation between the two data sets. It is this redshift-astrometric correlation which is considered here.

As described above, an isotropic, unpolarized background of GWs causes a correlated redshift pattern on the sky. The correlation at two points on the sky is described by a single real-valued function of the angular separation ($\mathscr{H}(\Theta)$, see eq. (5.21) and Fig. 5.2) known as the Hellings–Downs curve [101]. This result is a very robust prediction within GR; it depends only on the existence of the two polarizations predicted by the theory and the homogeneity

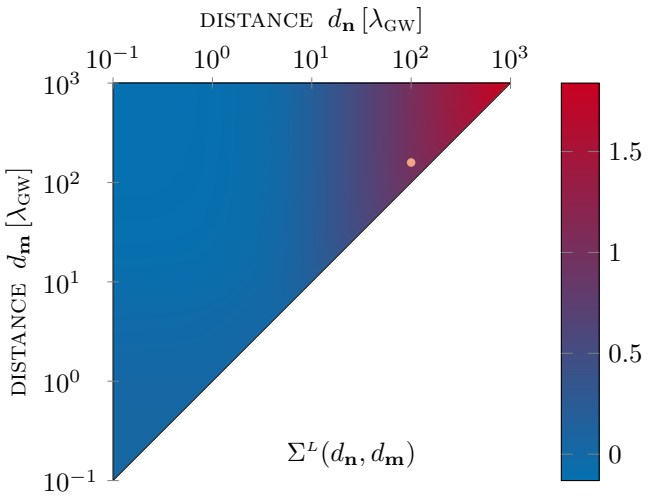

Fig. 5.8 Surface plot of the astrometric longitudinal correlation at $\Theta = 0$, given by $\Sigma^{L}(d_{\mathbf{n}}, d_{\mathbf{m}})$ for $d_{\mathbf{m}} \geq d_{\mathbf{n}}$ (see eq. (F.8) in Appendix F.2 for the precise expression. The two distances are expressed in terms of gravitational wavelengths. A dot marks the point $(d_{\mathbf{n}}, d_{\mathbf{m}}) = (100, 200)$, which is used for computing the numerical integral in Fig. 5.7. Figure appeared in [60].

and isotropy of the universe on scales comparable to the distance to the GW sources. It does not depend on the dynamics of the individual sources generating the background. Detection of a Hellings–Downs correlated redshift pattern via pulsar timing would be clear evidence for a stochastic GW background.

Similarly, a background of GWs causes a correlated astrometric deflection pattern on the sky. This correlation pattern is also fully specified by a single real-valued function of the angular separation ($\mathscr{T}(\Theta)$, see eq. (5.20) and Fig. 5.2) which was first derived in [76], although not in the current form. This is the astrometric analog of the Hellings–Downs curve; it is a similarly robust prediction of GR and detection of this pattern via astrometric measurements would provide similarly clear evidence for a stochastic GW background.

Additionally, there is a correlation between the redshift and astrometric deflection. The redshift of a pulsar in direction $\mathbf{n}$ is correlated with the astrometric deflection of a star in direction $\mathbf{m}$, $\delta m_i = \delta m_\theta\, \hat{u}_i^\theta + \delta m_\phi\, \hat{u}_i^\phi$, via

$$\begin{aligned}\big\langle z(\mathbf{n})\, \delta m_i(\mathbf{m})\big\rangle &\propto \int \mathrm{d}\Omega_{\mathbf{q}}\, z(\mathbf{n})\, \delta m_i(\mathbf{m}) \\ &\propto \int \mathrm{d}\Omega_{\mathbf{q}}\, z(\mathbf{n}) \big(\delta m_\theta\, \hat{u}_i^\theta + \delta m_\phi\, \hat{u}_i^\phi\big) \\ &\propto \Gamma_{z\theta}(\Theta)\, \hat{u}_i^\theta + \Gamma_{z\phi}(\Theta)\, \hat{u}_i^\phi\,, \end{aligned} \tag{5.27}$$

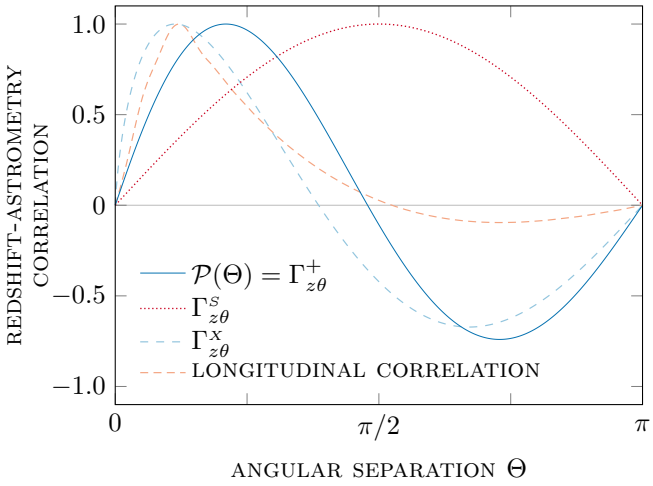

Fig. 5.9 The redshift-astrometric correlations as a function of angular separation on the sky, given by eqs. (5.28), (5.30), and (5.31) for different polarizations. The numerical result for the scalar longitudinal correlation is plotted too (see Appendix F.1). All functions are normalized so that their maximum is unity. Figure appeared in [60].

where $\Theta = \arccos(\mathbf{n}\cdot\mathbf{m})$. General considerations again show that $\Gamma_{z\phi}$ always vanishes. For a GW background of $+$ and $\times$ waves the remaining function evaluates to

$$\mathscr{P}(\Theta) = \Gamma^{+}_{z\theta}(\Theta) = \frac{8\pi}{3}\sin(\Theta/2)\cos(\Theta/2) + 8\pi\frac{\sin^3(\Theta/2)}{\cos(\Theta/2)}\ln(\sin(\Theta/2))\,. \tag{5.28}$$

The basis vectors $\hat{u}^{\theta}_i$ and $\hat{u}^{\phi}_i$ are defined in Section 5.1 and illustrated in Fig. 5.1. From eq. (5.27) it follows that the redshift of a pulsar is correlated with the "parallel component" of the astrometric deflection of a star, and is uncorrelated with the "perpendicular component" (see Fig. 5.1 for an illustration of the geometric setup).

Furthermore, the correlation between a pulsar and the response from a $\times$-polarized GW vanishes,

$$\Gamma^{\times}_{z\theta}(\Theta) = \Gamma^{\times}_{z\phi}(\Theta) = 0; \tag{5.29}$$

therefore the entire correlation between the redshift of a pulsar and the astrometric deflection of a star for $P \in \{+,\times\}$ is governed by $\mathscr{P}(\Theta)$ in eq. (5.28). This is shown, together with the other curves relevant to GR, in Fig. 5.2, and with the other redshift-astrometry curves in Fig. 5.9.

PTA-astrometry correlations like the one in eq. (5.28) can be found for the other polarization states, too. In particular, the curves can be derived explicitly in the case of scalar

"breathing" and vectorial modes:

$$\Gamma^{s}_{z\theta}(\Theta) = -\frac{20\pi}{3}\sin(\Theta/2)\cos(\Theta/2) - 8\pi\frac{\sin(\Theta/2)}{\cos(\Theta/2)}\ln(\sin(\Theta/2))\,, \tag{5.30}$$

$$\Gamma^{x}_{z\theta}(\Theta) = \frac{2\pi}{3}\sin(\Theta/2)\cos(\Theta/2)\,, \tag{5.31}$$

while the correlations $\Gamma^{s}_{z\phi}$, $\Gamma^{x}_{z\phi}$, $\Gamma^{y}_{z\theta}$ and $\Gamma^{y}_{z\phi}$ all vanish. The scalar longitudinal mode curve cannot be derived explicitly using this method, and has therefore been computed numerically (again, only the $x-\theta$ correlation is non-zero). Plots of all 4 curves can be found in Fig. 5.9.

Again, the redshift-astrometric correlation pattern is fully described by a single real-valued function of the angular separation, $\mathscr{P}(\Theta)$. This is the redshift-astrometric analog of the Hellings–Downs curve, and is a similarly robust prediction within GR. The three functions $\mathscr{H}(\Theta)$, $\mathscr{T}(\Theta)$ and $\mathscr{P}(\Theta)$ provide a starting point for searching for a stochastic GW background using a combination of pulsar timing and astrometric data; $\mathscr{H}(\Theta)$ describes the spatial correlations of the redshift over the sky, $\mathscr{T}(\Theta)$ describes the astrometric correlations, and $\mathscr{P}(\Theta)$ describes the cross-correlation between the redshifts and astrometric deflections.

Part II

Resonances in EMRIs

6

Resonances in EMRIs

This chapter is adapted from the introduction to [1], which was authored by me in collaboration with Jonathan Gair.

Systems which are expected to produce gravitational waves are those that are accelerating and exhibit asymmetry in their configuration: for instance a binary [102], a supernova [103], or a spinning star with a pronounced bulge. Among the range of binary celestial systems, we focus on the case of a compact object (of several solar masses, usually a stellar-mass black hole, or a neutron star) gradually spiralling towards a supermassive black hole (typically between 10^5 and 10^{12} solar masses, although the ones of interest to us are between 10^5 and $10^7\ M_\odot$, since these generate gravitational waves at frequencies in the range of sensitivity of LISA [54, 104]). Since the mass m of the compact object is in the range of $10^0 - 10^2 M_\odot$, the ratio of the masses is typically $\varepsilon = m/M \sim 10^{-6}$ to 10^{-4}. Termed extreme-mass-ratio inspirals (EMRIs), these binaries are expected to radiate gravitational waves with frequency in the range 10^{-4} Hz to 10^{-2} Hz. This fact places them in a position to be likely candidates for detection by the LISA mission. EMRIs reside near the centres of galaxies (where supermassive black holes are situated [105]) and clusters of stars and stellar remnants are available for capture by the black hole. Plenty of scientific effort has been invested into modelling the evolution of EMRIs [106–109], computing their waveforms [110], predicting the rates and timescales of inspiral [111, 112], and estimating the parameters of the orbit [106, 113]. Applications of gravitational wave observations of EMRIs to inference on astrophysical populations [114], cosmology [115] and fundamental physics [116] have also been explored in detail.

The mass of the compact object in an EMRI is typically at least 4 orders of magnitude smaller than the mass of the supermassive black hole. This allows us to treat the presence of the compact body in the background space-time of the central object as a perturbation.

According to the uniqueness theorem for black holes, they can be uniquely characterised by three parameters - mass, spin and charge. Since electromagnetic repulsion is much stronger than gravitational attraction (about 40 orders of magnitude), we can assume that astrophysical black holes have negligible net charge. Hence, we consider the Kerr metric, where black holes are described only by their mass and spin. The Kerr space-time is well-known, with a complete set of integrals of motion, and the geodesics can be characterised by three constants ([117] and Appendix H). For a point mass, the trajectory would be that of a geodesic around the black hole, but while the point-mass notion is convenient mathematically, it does not apply in the context of the current problem. Therefore, we need to address the finite size and mass of the compact object. The deviation from geodesic motion can be quantified by allowing for the gravitational self-force on the compact object, [118, 119], also known as the gravitational radiation reaction force, since it is responsible for the gravitational radiation emission from the object. There is a radiative component of the self-force that leads to evolution of the orbital frequencies, as well as a conservative component that changes the instantaneous values of the orbital frequencies. The trajectory can be modelled as a sequence of geodesics, each one with lower energy than the previous one, and therefore (on average) closer to the central object. This method is called the osculating element approach [120–122]. Individual orbits are well approximated as geodesics, however the defining parameters of these geodesics are continuously changing, and this is what shapes the inspiral orbit. This effect will be visible over a large number of orbits – typically over a timescale of $\mathscr{O}\left(\varepsilon^{-1}\right)$.

As the test body progresses along its in-spiral, at certain points two of the three frequencies of motion will become rational multiples of each other, putting the system into resonance [123]. While in general the behaviour of the inspiral is well-studied and modelled [124], during resonance the system exhibits unusual behaviour, accompanied by changes in the orbital parameters [123]. The evolution of EMRIs during resonances, and their effect on gravitational wave emission is currently an interesting topic in gravitational wave astronomy [125].

There are two approaches in the literature that treat the behaviour of extreme-mass-ratio inspirals on resonance. On one hand is the instantaneous value treatment by [114], with manifestations in both frequency and phase formalisms, and on the other is the approach by [123], which separates the timescales associated with the in-spiral into small and large timescale. We will describe both methods here, but focus on extending the former approach to higher order, as we anticipate the predictions of the latter to be consistent with the phase formalism in the former. Developing these formalisms is important for understanding the problem of resonances in EMRIs, which in turn bears significance for accurate waveform

modelling of these events. High-quality waveforms are important for tackling the data analysis challenges which future GW observatories (e.g. LISA) will present.

6.1 The Gravitational Self-force

The geodesic principle of General Relativity dictates that free point particles, traverse time-like geodesics of the space-time. Unfortunately, while treating bodies in General Relativity as point masses is mathematically convenient, in reality this approach is far from accurate, and introduces immense difficulties to the problem we are considering. As the size R of a body is scaled down to 0, its mass M should decrease accordingly, scaling to 0 at the same time as the size of the body [126], otherwise a black hole solution would form before the point-limit of the body is reached. We can account for the finite size and mass of the body if we consider the effect of these on the deviation from geodesic motion. At leading order, we ignore the presence of the space-time generated by the compact object in the background space-time, and in this idealised system, the test body follows a time-like geodesic, whose shape can be accurately computed (see Appendix I and Figure I.1 for details). The next order accounts for the non-infinitesimal size and mass of the object, and this causes a deviation from the geodesic motion described above. We quantify this phenomenon by introducing the gravitational self-force, responsible for the inward spiral of the compact object [118, 123]. This force is at the same time responsible for dissipating the energy made available by the inspiral motion in the form of gravitational radiation.

A proper treatment of the gravitational self-force is not the objective of this work. The reader may wish to consult [127], as well as the more concise review [128]. Further recommended reading is [118] and [129], or the more mathematical approach described in [126].

In the context of this work, it is worth knowing that since the self-force is the perturbation in the mass parameter to the geodesic, its leading order dependence on the mass of the test body is linear. Further, the self-force will depend on the shape of the orbit, which for the Kerr space-time is specified by three constants of the motion, for example the energy $\mathscr{E}$, the 3$^{\text{rd}}$ component of the angular momentum $\mathscr{L}_z$, and Carter's constant, $\mathscr{Q}$. Furthermore, the individual components of this self-force will depend on the position of the test body along the orbit, specified, for example, by the action-angle coordinates q_α, where the index $\alpha \in \{t, r, \theta, \phi\}$ (this implies there are 4 separate action-angle coordinates, with 4 corresponding components of the self-force. In fact, only 3 of these force components are independent, as can be verified by differentiating the condition $g_{\alpha\beta}u^\alpha u^\beta = 1$ with respect

to the proper time τ to obtain $u^\alpha a_\alpha = 0$ [121]). With this in mind, we can assume that the linear order gravitational self-force can be written in the form [128, 130]

$$a_\alpha = \frac{\mathrm{d}^2 x_\alpha}{\mathrm{d}\tau^2} = \varepsilon F_\alpha(\mathbf{q}, \mathbf{J}), \tag{6.1}$$

where $\varepsilon = m/M$ is the ratio of the compact object mass to the mass of the supermassive black hole, and the vector $\mathbf{J}$ contains the three constants of motion defining the shape of the orbit. The values of $\mathbf{q}$ and $\mathbf{J}$ in general depend on the way the orbit evolved before the moment at which they are computed. Thus, it can be regarded that the instantaneous self-force is in fact given by an integral over the past history of the orbit.

6.2 Orbital resonances

We already reasoned why the gravitational self-force depends on the shape of the orbit, i.e. the values of the three constants of motion in the Kerr metric. These quantities can be mapped to the three fundamental frequencies of orbital motion $\{\omega_r, \omega_\theta, \omega_\phi\}$ [131]. Therefore, instead of eq. (6.1), we can write the expression for the self-force as $\varepsilon \mathbf{F}(\mathbf{q}, \boldsymbol{\omega})$. The fundamental frequencies are another valid way to label orbits of the Kerr space-time, and can be used in lieu of the geodesic constants of motion. It should be noted that the reverse substitution, from $\boldsymbol{\omega}$ to $\mathbf{J}$ is not always possible, on the account of the isofrequency pairs exhibited by the proper time frequencies [132]. For the discussion in this Chapter, we can assume local invertibility, however it should be noted that this is not universal.

The three fundamental frequencies evolve independently according to their equations of motion. However, at certain points along the trajectory, two of the frequencies will become commensurate, and the system will temporarily exhibit a qualitatively different behaviour, a resonance, with a reduced number of degrees of freedom. Since the Kerr metric (Appendix G and Figure G.1) does not depend explicitly on the azimuthal angle ϕ, the corresponding fundamental frequency ω_ϕ is not relevant for any resonant motion. While the azimuthal frequency is trivial, the radial and the polar frequencies will have independently varying values along the in-spiral. Resonance occurs when these two frequencies become commensurate with each other, or, in more formal terms, when their ratio is a rational number [133]:

$$\frac{\omega_r}{\omega_\theta} = \frac{n_\theta}{n_r}, \quad \{n_r, n_\theta\} \subset \mathbb{Z}. \tag{6.2}$$

During resonance, the apparent effect of the self-force on the orbit is modified, in particular there is a fractional change of order $\mathscr{O}\left(\varepsilon^0\right)$ to the dynamics of the in-spiral – the evolution rate of parameters and the in-spiral rate [123]. A typical EMRI passes through several resonance points before the two objects merge. Obviously, this complicates the numerical analysis of the in-spiral, since one has to develop a formalism to account for the occurrence of resonances, and to quantify the effects these have on the orbital dynamics [123].

In this part of my dissertation, I will first describe the two approaches to resonance modelling that have appeared in the literature, which were suggested by [134] and [130]. I will then describe what the differences in the model assumptions are, explain why there is a preferred case of physical relevance to resonances in EMRIs, and argue that full knowledge of the self-force is required to robustly identify the most relevant model. I will then extend the results of [130] to obtain complete results describing the transition through resonance in that model, at leading order in the mass-ratio.

7

Instantaneous frequency approach

This literature review appeared in [1], which was authored by me in collaboration with Jonathan Gair.

This method is described in detail in [130], although here we will give an outline of the approach to aid further discussions. As explained above, individual orbits of the compact object around the black hole can be thought of as tri-periodic geodesics with fundamental frequencies $\{\omega_r, \omega_\theta, \omega_\phi\}$. This encourages us to employ the "osculating element" formalism, where the in-spiral is modelled as a sequence of geodesics, with the constants of motion continuously evolving as the orbit approaches the black hole, and furthermore, the effect of the compact body on the trajectory can be treated as a perturbation [120]. Since these constants of the motion do not change on a given geodesic, at leading order, and only evolve (continuously) as the object spirals into the supermassive black hole, we can argue that, to leading order, this effect is driven by the self-force on the object. Hence, we can write the evolution equation for $J_\mu = (\mathscr{E}, \mathscr{L}_z, \mathscr{Q})$ as follows:

$$\frac{\mathrm{d}J_\mu}{\mathrm{d}\tau} = \varepsilon\, \mathscr{F}_\mu(\mathbf{q}, \mathbf{J}, \mathbf{F}) + \mathscr{O}\left(\varepsilon^2\right), \tag{7.1}$$

where $\mathscr{F}_\mu$ is a function of the coordinates, the generalised coordinates, and the self-force, which describes the rate of change of orbital parameters as the object moves along the inspiral. We argued that the self-force is itself a function of the coordinates and the fundamental frequencies (see Section 6.2), hence we can write $\mathscr{F}_\mu = \mathscr{F}_\mu(\mathbf{q}, \boldsymbol{\omega})$. Similarly, the action-angle coordinates of the system evolve proportionally to the fundamental frequencies, with a correction owing to the self-force:

$$\frac{\mathrm{d}q_\mu}{\mathrm{d}\tau} = \omega_\mu + \varepsilon\, \mathscr{H}_\mu(\mathbf{q}, \boldsymbol{\omega}) + \mathscr{O}\left(\varepsilon^2\right). \tag{7.2}$$

We will not concern ourselves with the precise form of the functions $\mathscr{F}_\mu$ and $\mathscr{H}_\mu$, but rather will point out that they can be expanded in tri-harmonic Fourier series as discussed above, which is valid without any loss of generality. ω_μ is the instantaneous value of the frequency at this moment along the trajectory. This is calculated according to eq. (7.1), and the value is continuously updated to reflect the motion of the body along its inspiral and the effect of the self-force. Without the self-force, the frequencies will, of course, remain constant, since the trajectory would be that of a geodesic around the black hole, unaffected by gravitational wave emission.

Before carrying out the Fourier mode expansion, we recall that a geodesic in Kerr space-time is uniquely specified by three constants. Instead of the orbital parameters $\mathscr{E}$, $\mathscr{L}_z$, and $\mathscr{Q}$, we could use the set of fundamental frequencies – the radial frequency, ω_r, the polar frequency, ω_θ, and the azimuthal frequency, ω_ϕ, to specify the geodesics, as these are constant along a given geodesic. Since these can be mapped to the aforementioned integrals of the motion [131], we can use these maps to argue that the fundamental frequencies evolve along the trajectory according to a differential equation of the same form as eq. (7.1):

$$\frac{\mathrm{d}\omega_\mu}{\mathrm{d}\tau} = \varepsilon \mathscr{G}_\mu(\mathbf{q}, \boldsymbol{\omega}) + \mathscr{O}\left(\varepsilon^2\right). \tag{7.3}$$

The two orbital frequencies relevant to the occurrence of resonances are the radial and the polar (lateral) frequencies. As noted previously, the third frequency ω_ϕ, that of azimuthal motion, does not play a role in the occurrence of resonances due to the axisymmetric nature of the Kerr space-time. We use this property to write a bi-periodic expansion for the function of the self-force in Fourier modes of the two frequencies $\{\omega_r, \omega_\theta\}$:

$$\frac{\mathrm{d}\omega_\mu}{\mathrm{d}\tau} = \varepsilon \sum_{l,m} \left(A_{lm} \cos\Big[\left(l\omega_r + m\omega_\theta\right)\tau\Big] + B_{lm} \sin\Big[\left(l\omega_r + m\omega_\theta\right)\tau\Big] \right) + \mathscr{O}\left(\varepsilon^2\right). \tag{7.4}$$

We can regard this equation as an adiabatic evolution equation – at leading order the terms on the right-hand side are constant in time since they are taken along the same geodesic, while the differential on the left-hand side expresses their evolution along the trajectory of the compact object towards the black hole. Of course, the quantities on the right-hand side are instantaneous, and their values are constantly updated through the evolution equations. The sum is over the non-negative integers l and m. The coefficients of the expansion depend smoothly on the constant parameters of the geodesic. Therefore, we can expand the coefficients in orders of the mass ratio, and neglect all terms sub-leading in ε.

Alternatively, instead of using the $\{\omega_\mu\}$ as the basis for the Fourier expansion, we could rewrite the evolution equation in terms of the phase angle variables $\{\phi_\mu\}$. Phase variables are related to the fundamental frequencies through $\dot{\phi}_\mu = \omega_\mu$, and since on a geodesic the frequencies remain constant, $\phi_\mu = \omega_\mu \tau$. Changing variables from frequencies to phase angles in eq. (7.4), we arrive at a second-order differential equation:

$$\frac{\mathrm{d}^2\phi_\mu}{\mathrm{d}\tau^2} = \varepsilon \sum_{l,m} \Big(C_{lm} \cos\left(l\phi_r + m\phi_\theta\right) + D_{lm} \sin\left(l\phi_r + m\phi_\theta\right) \Big) + \mathscr{O}\left(\varepsilon^2\right) \tag{7.5}$$

Geodesic resonances occur when the two frequencies become commensurate, or, more precisely, when their ratio is a rational number (eq. (6.2)). Therefore, near resonance the term $(l_0\,\omega_r - m_0\,\omega_\theta)$ will approach 0 (for some l_0 and m_0 and their integer multiples), and the sum will contain both slowly-oscillating resonance terms, and rapidly oscillating off-resonance terms. Let us now restructure eq. (7.4) to change variables to $\bar{\omega} = l_0\,\omega_r - m_0\,\omega_\theta$, which is small near a resonance. Now the arguments of the oscillating modes on the right-hand side can be written as a linear combination of $\bar{\omega}$ and $\{\omega_\mu\}$ (we can use either of them, but choose ω_r for definitiveness):

$$\frac{\mathrm{d}\bar{\omega}}{\mathrm{d}\tau} = \varepsilon \sum_{l,m} \left(A_{lm} \cos\Big[\left(l\bar{\omega} + m\omega_r\right)\tau\Big] + B_{lm} \sin\Big[\left(l\bar{\omega} + m\omega_r\right)\tau\Big] \right) + \mathscr{O}\left(\varepsilon^2\right). \tag{7.6}$$

Similarly, we can rewrite the phase equation in terms of $\bar{\phi}$ and ϕ_r, where $\bar{\phi} = l_0\,\phi_r + m_0\,\phi_\theta$ vanishes on resonance:

$$\frac{\mathrm{d}^2\bar{\phi}}{\mathrm{d}\tau^2} = \varepsilon \sum_{l,m} \Big(C_{lm} \cos\left(l\bar{\phi} + m\phi_r\right) + D_{lm} \sin\left(l\bar{\phi} + m\phi_r\right) \Big) + \mathscr{O}\left(\varepsilon^2\right). \tag{7.7}$$

Let us change variables to absorb the factor of the mass ratio appearing on the right-hand sides, namely:

$$\hat{\omega} = \frac{\bar{\omega}}{\sqrt{\varepsilon}}, \quad \hat{x} = \sqrt{\varepsilon}\,\tau \quad \text{in eq. (7.6)}$$

and

$$\hat{\phi} = \bar{\phi}, \quad \hat{\phi}_r = \sqrt{\varepsilon}\,\phi_r, \quad \hat{x} = \sqrt{\varepsilon}\,\tau \quad \text{in eq. (7.7).}$$

Using this substitution, eqs. (7.6) and (7.7) become

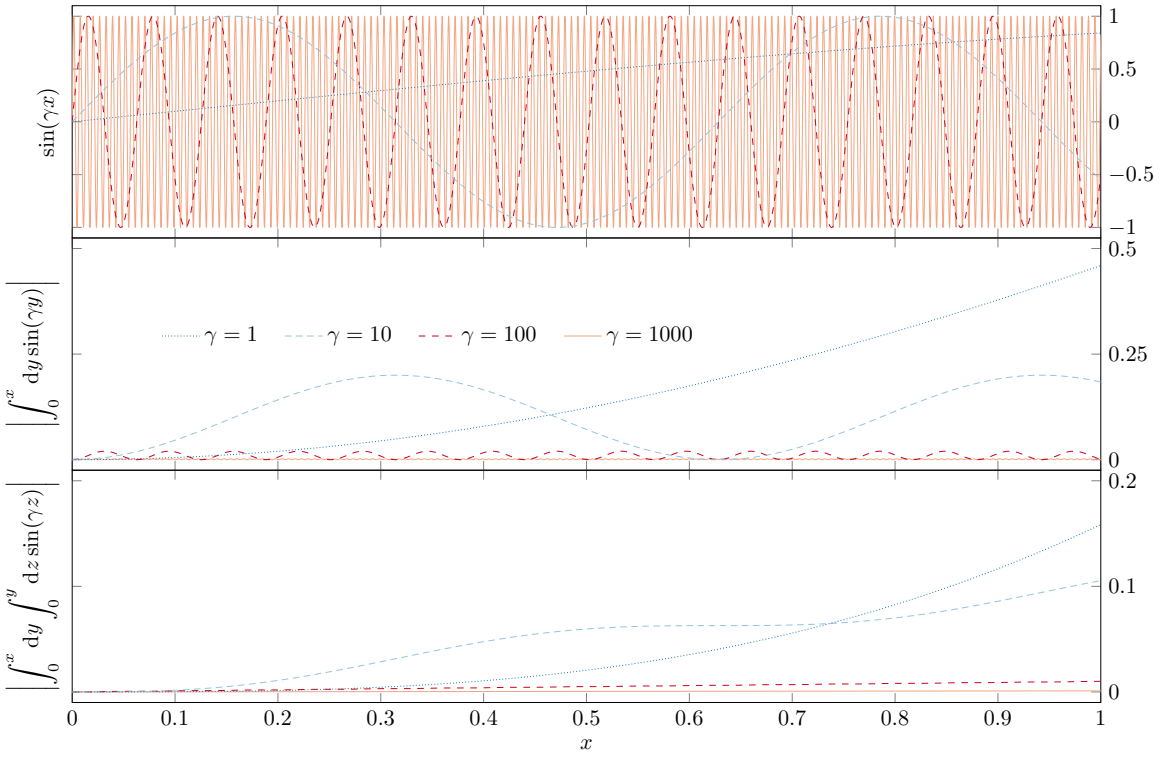

Fig. 7.1 *Upper panel:* the oscillating function $\sin(\gamma x)$, for $\gamma = 1, 10, 100$ and 1000. It is evident that as γ increases, the function oscillates more rapidly, crossing the horizontal axis more times per unit interval. *Middle panel:* the integral of the functions in the upper panel, of the form $|(1/\gamma)(1-\cos(\gamma x))|$, for the same values of γ. *Lower panel:* the double integral of the functions in the upper panel. As we can see, both graphically and analytically, as γ increases, the maxima of the integrals become smaller, and their amplitude decreases as $1/\gamma$. This allows us to neglect terms with $\gamma \gtrsim 10^3$ when compared to terms where $\gamma \sim 1$. Figure appeared in [1].

$$\frac{\mathrm{d}\hat{\omega}}{\mathrm{d}\hat{x}} = \sum_{l,m}\left(A_{lm}\cos\left(l\hat{x}\hat{\omega} + \frac{m\omega_r\hat{x}}{\sqrt{\varepsilon}}\right) + B_{lm}\sin\left(l\hat{x}\hat{\omega} + \frac{m\omega_r\hat{x}}{\sqrt{\varepsilon}}\right)\right) + \mathscr{O}(\varepsilon)\,, \tag{7.8}$$

$$\frac{\mathrm{d}^2\hat{\phi}}{\mathrm{d}\hat{x}^2} = \sum_{l,m}\left(C_{lm}\cos\left(l\hat{\phi} + \frac{m\hat{\phi}_r}{\sqrt{\varepsilon}}\right) + D_{lm}\sin\left(l\hat{\phi} + \frac{m\hat{\phi}_r}{\sqrt{\varepsilon}}\right)\right) + \mathscr{O}(\varepsilon)\,. \tag{7.9}$$

For any non-zero value of the index m, corrections to the frequency or phase equations are of the form $\cos(\gamma x+\delta)$, which oscillate rapidly owing to the $\gamma \sim \varepsilon^{-1/2} \sim 10^3$ factor both on resonance and away from it (and therefore will average out to zero over the timescales under consideration — this is illustrated in Figure 7.1). Hence, the correction to the first order solution of the phase equation is of the form $(1/\gamma^2)\cos(\gamma x+\delta)$ and that of the frequency equation is $(1/\gamma)\sin(\gamma x+\delta)$. These are terms of order ε and $\varepsilon^{1/2}$, respectively. Hence, we can perform an expansion to establish that they are corrections of higher order in the mass ratio and hence can be ignored at the same level as the other higher order in mass ratio terms that we have omitted. We can therefore consider only terms with $m = 0$, and relabel the remaining modes by n, obtaining

$$\frac{\mathrm{d}\hat{\omega}}{\mathrm{d}\hat{x}} = \sum_{n}\Big(A_n\cos\left(n\hat{x}\hat{\omega}\right) + B_n\sin\left(n\hat{x}\hat{\omega}\right)\Big) + \mathscr{O}(\varepsilon) \tag{7.10}$$

$$\frac{\mathrm{d}^2\hat{\phi}}{\mathrm{d}\hat{x}^2} = \sum_{n}\Big(C_n\cos\big(n\hat{\phi}\big) + D_n\sin\big(n\hat{\phi}\big)\Big) + \mathscr{O}(\varepsilon)\,. \tag{7.11}$$

We combine the two oscillating modes together, and this introduces a phase to the oscillating term. This could sometimes be set to 0 by suitable choice of initial coordinates, however it is not always possible, since the resonance phase depends on the prior evolution of the binary system. To preserve generality of the problem, we will include it in our equations. The presence of phase does not complicate the method of solution, only brings in additional terms, as we will demonstrate later in Section 9. Hence

$$\frac{\mathrm{d}\hat{\omega}}{\mathrm{d}\hat{x}} = \sum_{n}\mathscr{A}_n\cos\left(n\hat{x}\hat{\omega} - \delta\chi_n\right) + \mathscr{O}(\varepsilon) \tag{7.12}$$

$$\frac{\mathrm{d}^2\hat{\phi}}{\mathrm{d}\hat{x}^2} = \sum_{n}\mathscr{B}_n\cos\big(n\hat{\phi} - \delta\psi_n\big) + \mathscr{O}(\varepsilon)\,, \tag{7.13}$$

where

$$\begin{aligned} \mathscr{A}_n &= \sqrt{A_n^2 + B_n^2}, \quad \mathscr{B}_n = \sqrt{C_n^2 + D_n^2}, \\ \delta\chi_n &= \arctan\left(\frac{B_n}{A_n}\right) \quad \text{and} \quad \delta\psi_n = \arctan\left(\frac{D_n}{C_n}\right). \end{aligned} \tag{7.14}$$

Finally, we split the first term from the sum, $n = 0$, which is constant (with respect to time or phase, respectively):

$$\frac{\mathrm{d}\hat{\omega}}{\mathrm{d}\hat{x}} = \mathscr{A}_0 \cos(\delta\chi_0) + \sum_{n>0} \mathscr{A}_n \cos(n\hat{x}\hat{\omega} - \delta\chi_n) + \mathscr{O}(\varepsilon) \tag{7.15}$$

$$\frac{\mathrm{d}^2\hat{\phi}}{\mathrm{d}\hat{x}^2} = \mathscr{B}_0 \cos(\delta\psi_0) + \sum_{n>0} \mathscr{B}_n \cos\left(n\hat{\phi} - \delta\psi_n\right) + \mathscr{O}(\varepsilon) \tag{7.16}$$

and make a suitable, final change of variables:

$$\begin{aligned} \omega &= \left(\mathscr{A}_0 \cos(\delta\chi_0)\right)^{-1/2} \hat{\omega} \\ x_\omega &= \left(\mathscr{A}_0 \cos(\delta\chi_0)\right)^{1/2} \hat{x} \end{aligned} \qquad \text{in eq. (7.15)}$$

and

$$\begin{aligned} x_\phi &= \left(\mathscr{B}_0 \cos(\delta\psi_0)\right)^{1/2} \hat{x} \\ \phi &= \hat{\phi} \end{aligned} \qquad \text{in eq. (7.16)}$$

to bring the equations to their most simplified form:

$$\omega' = 1 + \sum_n \kappa_n \cos\left(n x_\omega\, \omega - \delta\chi_n\right) \tag{7.17a}$$

$$\phi'' = 1 + \sum_n \lambda_n \cos\left(n\phi - \delta\psi_n\right) \tag{7.17b}$$

where $\kappa_n = (\mathscr{A}_n/\mathscr{A}_0)\sec(\delta\chi_0)$ and $\lambda_n = (\mathscr{B}_n/\mathscr{B}_0)\sec(\delta\psi_0)$ are in principle known constants, dependent on the orbital parameters at resonance, prime denotes a derivative with respect to the rescaled time x and the quantities $\{\delta\chi_i\}$ and $\{\delta\phi_j\}$ are constants. The sums over n run from 1 to ∞, however we will later consider finite number of modes on the right-hand side. In order to achieve convergence when solving these equations, we need to make the assumption that the series $\{\kappa_n\}$ and $\{\lambda_n\}$ follow a power law of the form $n^{-\alpha}$, with $\alpha \gtrsim 2$, this is discussed in detail in Section 9.1. In this Chapter, we are attempting to find solutions to eqs. (7.17a) and (7.17b) in increasing order of complexity. It is worth noting that while one

of them is a first-order equation, the other is of second order. They derive from equivalent representations of the geodesics, however the first and second order equations are no longer equivalent, because they make different assumptions about the expansion of the self-force.

Before proposing the respective solutions, we will focus on presenting an alternative approach to describing the behaviour of an EMRI near resonance.

8

Two-timescale approach

This literature review appeared in [1], which was authored by me in collaboration with Jonathan Gair.

An alternative approach to describing the transition of EMRIs through resonances was first suggested by [134], and is often called the "two-timescale method" since it differentiates between processes which occur on short (orbital) timescales, and those happening on long (orbit evolution) timescales. A good overview is offered by [135].

Here we will present this method as described by [136], while it is also advisable that the reader consults [137], and the original article by [134]. Again, we consider the motion of a compact object spiralling towards a supermassive black hole, and describe the evolution in terms of the perturbative parameter, the mass ratio ε. At leading order, we recover the geodesic equations of motion, as before. At next order, we need to introduce corrections due to the self-force acting on the compact object, in analogy with eq. (7.1) in the instantaneous frequency approach:

$$\frac{\mathrm{d}J_\mu}{\mathrm{d}\tau} = \varepsilon\, \mathscr{I}_\mu(\mathbf{q}, \mathbf{F}) + \mathscr{O}\left(\varepsilon^2\right) \tag{8.1}$$

While the equations in [137] are presented in terms of the Mino time λ [138], we can map λ to the proper time τ through a function involving the coordinates of the compact object. We can absorb this dependence into the functions $\mathscr{I}_\mu$ on right-hand side of eq. (8.1) and work in terms of the proper time. As before, we can exchange the integrals of the motion $\mathbf{J}$ in favour of the fundamental frequencies $\boldsymbol{\omega}$, since mappings between these exist [131], albeit not invertable over the entire domain. Further we can implicitly write the self-force as a

function of the coordinates and their corresponding frequencies (cf. eq. (7.3)) to obtain:

$$\frac{\mathrm{d}\omega_\mu}{\mathrm{d}\tau} = \varepsilon\, \mathscr{J}_\mu(\mathbf{q},\mathbf{J}) + \mathscr{O}\left(\varepsilon^2\right) \tag{8.2}$$

Similarly, the action-angle variables evolve as per eq. (7.2):

$$\frac{\mathrm{d}q_\mu}{\mathrm{d}\tau} = \omega_\mu\left(\mathbf{J}\right) + \varepsilon\, \mathscr{K}_\mu(\mathbf{q},\mathbf{J}) + \mathscr{O}\left(\varepsilon^2\right). \tag{8.3}$$

We construct the resonant frequency $\bar{\nu} = l_0\,\omega_r - m_0\,\omega_\theta$, and the corresponding action-angle variable combination $\bar{q} = l_0\,q_r - m_0\,q_\theta$. $\bar{\nu}$ is the analogous variable to $\bar{\omega}$ in Section 7, but we use a different notation here to differentiate between the two methods. Again, we ignore the third fundamental frequency ω_ϕ, since the motion is axisymmetric. Let $\bar{J}$ denote the action conjugate to $\bar{q}$, which can be mapped to $\bar{\nu}$. Further, let us rescale the proper time to write $x_\nu = \sqrt{\varepsilon}\,\tau$. We now expand the frequency and coordinate variables in powers of ε:

$$\bar{\nu}\left(x_\nu,\varepsilon\right) = \bar{\nu}_0 + \varepsilon^{1/2}\,\bar{\nu}_1(x_\nu) + \mathscr{O}\left(\varepsilon^2\right) \tag{8.4a}$$

$$\bar{q}\left(x_\nu,\varepsilon\right) = \bar{q}_0(x_\nu) + \varepsilon^{1/2}\,\bar{q}_1(x_\nu) + \mathscr{O}\left(\varepsilon^2\right). \tag{8.4b}$$

Plugging these power laws into the (averaged) evolution equations (8.2) and (8.3) yields the resonance equations:

$$\frac{\mathrm{d}\bar{\nu}_1}{\mathrm{d}x_\nu} = \bar{\mathscr{J}}\left(\bar{q},\bar{J}\right) + \mathscr{O}(\varepsilon) \tag{8.5a}$$

$$\frac{\mathrm{d}\bar{q}_0}{\mathrm{d}x_\nu} = \bar{\nu}_1(x_\nu) + \mathscr{O}(\varepsilon). \tag{8.5b}$$

This relays the leading terms in the expansions (8.4). Further members of the series $\{\bar{\nu}_n\}$ and $\{\bar{q}_n\}$ can be found iteratively by substituting the results from eqs. (8.5) back into the resonance evolution equations.

In [123], eq. (8.4a) was further simplified by expanding $\bar{\nu}_1$ as a series in $\sqrt{\varepsilon}\,x_\nu$. The leading term is then $\nu_1(x_\nu - x_0)$ for a constant ν_1. Proceeding with the two timescale expansion then yields a result accurate to first order in the resonant modification, $\{\lambda_n\}$, which agrees with the result obtained from the asymptotic Fourier series approach in [130]. Corrections at higher order in λ_n, but leading order in mass ratio, cannot be found in this way, since the assumption of a linearly evolving frequency is only valid close to the resonance point. The two-timescale approach can be extended to higher order by using a less restrictive ansatz for $\bar{\nu}_1$, which is given implicitly by eqs (23) and (25) in [136]. Explicit solutions to higher order in the resonant modification at leading order in mass ratio have not been computed in the two-timescale approach. However, we anticipate that these will agree with

the phase version of the asymptotic Fourier series approach. The purpose of this work is to extend previous calculations to higher order in resonant modification and to include multiple modes in the resonance. To do this we will use the asymptotic Fourier series approach and this will be the focus for the remainder of this part of my dissertation.

9

Solutions of the resonance equations

This chapter is adapted from [1], which was authored by me in collaboration with Jonathan Gair. My contribution consisted of deriving the solutions to these equations and testing their validity numerically.

We are now in a position to solve the instantaneous frequency approach equations that we derived earlier in Section 7. Evolution of the action-angle coordinates according to the instantaneous frequency of the system yields the 2 non-linear differential eqs. (7.17a) and (7.17b), both of them describing the problem from different perspectives. Due to the constant additive term on their right-hand sides, these equations cannot be solved exactly, and therefore we need to come up with an alternative approach. In this Section we propose solutions to these equations in an increasing order of complexity. Solutions for the single-mode versions of eqs. (7.17) are provided in [130], we will start by re-deriving those to depict how the order-by-order solution algorithm works. Following this, we relax the assumptions which have been considered in [130] in order to build up solutions to the generalised source equations.

9.1 Regime and domain of the variables

Before attempting to solve the resonance equations, we need to specify their domains and any special limits we are taking. The time parameters $x_{\{\omega,\phi,\nu\}}$ range from $-\infty$ to $+\infty$, however we are interested in the vicinity of $x = 0$ as this is when resonance occurs, hence where we have specified the initial conditions. In this notation, $-\infty$ corresponds to times long before resonance, and $+\infty$ to times when the resonance has had an effect on the orbit. Therefore, in solving these equations, we will consider definite integrals of the form $\int_0^x \mathrm{d}\bar{x}$, where x can take large positive or negative values. Since the equations are not coupled, and each rescaled

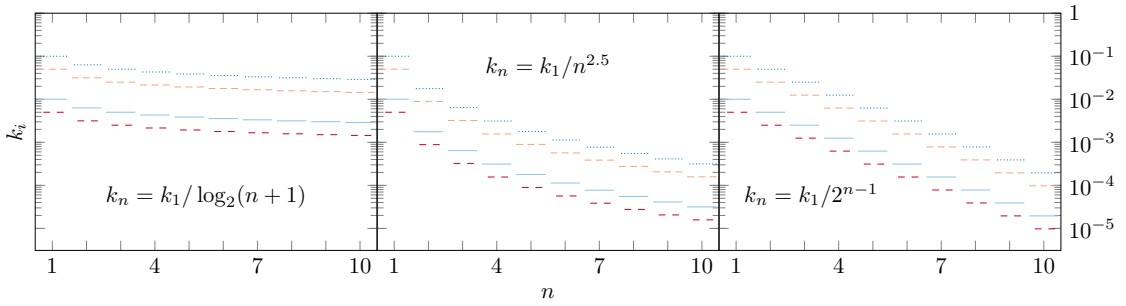

Fig. 9.1 Visualisation of several types of series for the mode parameters $k_i = \{\kappa_i, \lambda_i\}$. For each of them, we take 4 different values of the initial parameter: $k_1 = 0.1$ (·····), $k_2 = 0.05$ (– – –), $k_3 = 0.01$ (——), and $k_4 = 0.005$ (– –). *Left panel:* Logarithmic progression with base 2, $k_n = k_1/\log_2(n+1)$, which is too slow to satisfy our conditions for convergence. *Centre panel:* Power law $k_n = k_1/n^{\alpha}$, with $\alpha = 2.5$, as suggested by [108] (the lower bound is $\alpha \gtrsim 2$). *Right panel:* Exponential series $k_n = k_1/2^{n-1}$. It is expected that in reality, this progression will start as a power law (centre panel) and will gradually evolve into an exponential series for large values of n (right panel). This data is represented numerically in Table 9.1. Figure appeared in [1].

time variable appears in the differential equation for its corresponding quantity, we will drop the subscripts on x, and will keep track of them by the subject of the equation we are solving.

More attention needs to be devoted to the fractional resonance modifications, κ_i and λ_j, which are themselves functions of the orbital parameters. As discussed in [130], if these modifications are of order unity, there can be a qualitative difference in the on-resonance behaviour, with the possibility of sustained resonances. These were explored in more detail in [136]. A complete study of the size of on-resonance flux modifications has not yet been carried out. Some insight on the likely size of these corrections can be obtained by studying solutions to the Teukolsky equation, which provide a decomposition of the off-resonance energy flux into different Fourier modes. Such results can be found in [108]. Section I C of that paper indicates that the size of the terms in this decomposition initially follows a power law of the form $\sim n^{-\alpha}$ before eventually falling off exponentially (see Figure 9.1 for an illustration different rates of fall off). From Fig. 3 of that paper it appears that $\alpha \gtrsim 2$ for all n, but as a lower limit in our calculations we will use the value of $\alpha = 5/2$. [108] also indicate that the size of the first term in the series is less than unity, and in fact of order $\kappa_1 \sim \lambda_1 \sim 0.1$. This implies that the resonance is likely to be "weak", but the Teukolsky results do not directly give the size of the on-resonance flux change. The size of the resonance effect was assessed more carefully in [139], who computed the flux change for a number of different resonances for a few systems and found that the resonant flux change was only $\sim 1\%$ in all cases. This also suggests that κ_1 and λ_1 are small, typically ~ 0.01. Based on

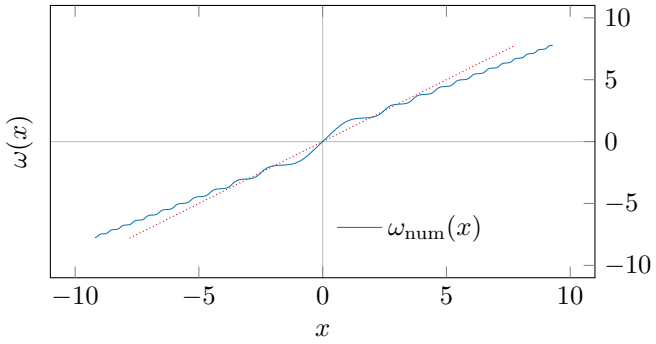

Fig. 9.2 Numerical solution of the equation $\omega' = 1 + \kappa\cos(x\omega)$, with $\kappa = 0.9$, an exaggerated value is used to demonstrate the notable features of the solution, namely the slope and the decaying oscillations. The initial condition $\omega(0)$ depends on the initial phase of the resonance, and has been set to 1 here. The line $\omega(x) = 1 + x$ is plotted (in red dots) for reference. Figure appeared in [1].

this evidence it seems unlikely that strong resonances will occur in practice and so in this case we focus on the weak resonance case with $\kappa_1 \ll 1$, which will allow us to perform an expansion in κ_1. However, we should note that [139] did not thoroughly explore the resonance parameter space and so it is still possible that there are regions of parameter space where strong sustained resonances may exist. If this is possible, it would be very interesting, as discussed in detail in [136].

Regarding the other relevant parameters, the mass-ratio ε is typically in the range $\sim 10^{-6} - \sim 10^{-3}$. The quantity $\varepsilon^{1/2}$ is therefore $\mathscr{O}\left(10^{-3} - 10^{-1.5}\right)$. The phases on resonance, $\delta\chi_i$ and $\delta\psi_j$, are constants in the range $[0, 2\pi)$, which depend only on the coefficients of the Fourier series in eqs. (7.4) and (7.5), and the index n.

9.2 Frequency resonance equation

Consider the generalised frequency resonance equation:

$$\omega' = 1 + \sum_n \kappa_n \cos\left(n x_\omega\, \omega - \delta\chi_n\right), \tag{7.17a}$$

where prime denotes differentiation with respect to the rescaled time parameter x_ω. Before attempting to solve this equation in the general case, we consider only the single oscillatory mode ($n = 1$, besides the $n = 0$ mode) on the right-hand side, neglect the phase $\delta\chi_1$, and as agreed, drop the subscript on x. The resulting problem is not much simpler to solve, however

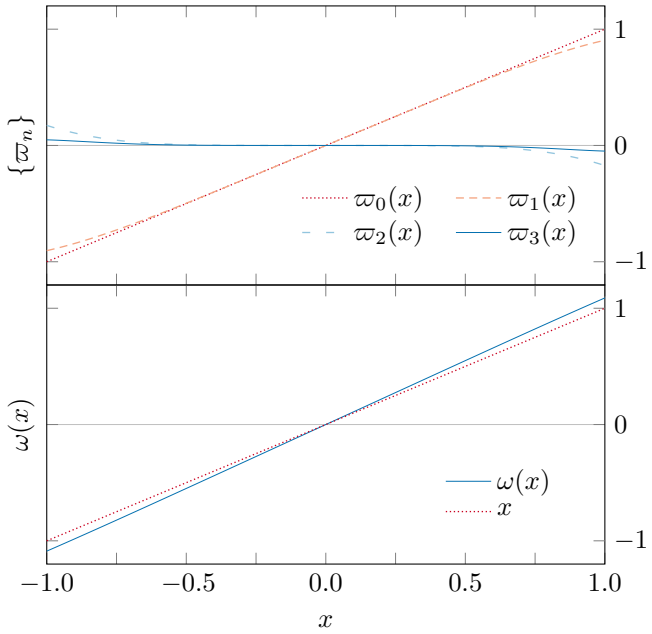

Fig. 9.3 Analytical solution to the frequency equation for $|x| < 1$. *Top panel:* The solutions at each order from 0 to 3 inclusive, plotted as a function of x. *Bottom panel:* The combined solution at third order, eq. (9.12). Figure appeared in [1].

it will provide useful insight about the method:

$$\omega'(x) = 1 + \kappa \cos(x\omega), \tag{9.1}$$

where $\kappa \equiv \kappa_1$. Inspired by the numerical solution of eq. (9.1), shown in Fig. (9.2), we split the solution in two parts: the first for the region where the oscillations are still growing, and the second where the oscillations gradually decay. After we establish appropriate solutions to eq. (9.1) in each of these regions, we will come up with a way to match them on the boundary region.

Let us initially look for a solution in the $\kappa|x| \ll 1$ region. That is, find an expansion of the frequency ω as a function of x in the region immediately around $x = 0$, in powers of the fractional resonance modification κ:

$$\omega(x) = \sum_{n=0}^{\infty} \kappa^n \varpi_n(x). \tag{9.2}$$

We remind ourselves that the parameter $\kappa \ll 1$, as per the previous Section. In order to find explicit forms of the functions $\{\varpi_n\}$, we substitute the expansion (9.2) in eq. (9.1) and proceed to match terms on both sides. The results we now derive are plotted in Figure 9.3.

At lowest order, we disregard all terms of $\mathscr{O}(\kappa)$ and higher:

$$\varpi_0'(x) = 1 \quad \Leftrightarrow \quad \varpi_0(x) = x, \tag{9.3}$$

where it is important to note that the integration has been carried out between 0 and x. Further terms in the series (9.2) will be reduced by one or more factors of $\kappa \ll 1$, hence we can treat them as a perturbation to $\varpi_0(x)$:

$$\sum_{n=1}^{\infty} \kappa^n \varpi_n(x) = \kappa \cos\left[x^2 + \sum_{n=1}^{\infty} \kappa^n x\, \varpi_n(x)\right]. \tag{9.4}$$

At the next higher order we find the equation for $\varpi_1(x)$:

$$\kappa \varpi_1'(x) + \mathscr{O}\left(\kappa^2\right) = \kappa \cos\left(x^2\right) + \mathscr{O}\left(\kappa^2\right). \tag{9.5}$$

integrating the right-hand side yields the solution:

$$\varpi_1(x) = \int_0^x \mathrm{d}y \cos\left(y^2\right) = \frac{\sqrt{2\pi}}{2} C\left(\frac{\sqrt{2}x}{\sqrt{\pi}}\right), \tag{9.6}$$

where $C(\bullet)$ is the Fresnel cosine integral (see Appendix J and Figure J.1 for details). At $\mathscr{O}\left(\kappa^2\right)$, we find:

$$\varpi_2'(x) = -\frac{\sqrt{\pi}}{\sqrt{2}} x \sin\left(x^2\right) C\left(\frac{\sqrt{2}x}{\sqrt{\pi}}\right). \tag{9.7}$$

Solving this differential equation (which also involves a simple integration by parts) provides the solution:

$$\varpi_2(x) = \frac{\sqrt{2\pi}}{4} \cos\left(x^2\right) C\left(\frac{\sqrt{2}x}{\sqrt{\pi}}\right) - \frac{\sqrt{\pi}}{8} C\left(\frac{\sqrt{4}x}{\sqrt{\pi}}\right) - \frac{x}{4}.$$

It is obvious that with increasing order the functional form of $\varpi_n(x)$ become more and more involved. It will become apparent later on why we do not need solutions at $\mathscr{O}\left(\kappa^4\right)$ and beyond. However, at third order, we find the following differential equation for the functional $\varpi_3(x)$.

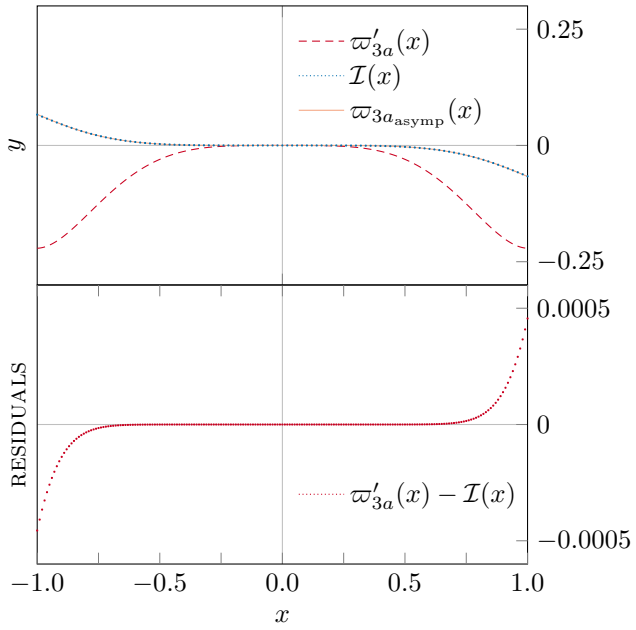

Fig. 9.4 Approximate integral of $\varpi'_{3a}(x)$ near the origin. *Top panel:* The integrand, the numerical integral, and the approximation. *Bottom panel:* Residuals between the approximation and the numerical solution, showing the validity of eq. (9.10). Figure appeared in [1].

$$\varpi'_3(x) = -\frac{\pi}{4} x^2 \cos\left(x^2\right) C^2\left(\frac{\sqrt{2}x}{\sqrt{\pi}}\right) - x \sin\left(x^2\right) \varpi_2(x).$$

We divide ϖ_3 into two parts, $\varpi_3(x) = \varpi_{3a}(x) + \varpi_{3b}(x)$, defined via the two differential equations:

$$\varpi'_{3a}(x) = -\frac{\pi}{4} x^2 \cos\left(x^2\right) C^2\left(\frac{\sqrt{2}x}{\sqrt{\pi}}\right) \tag{9.8a}$$

$$\varpi'_{3b}(x) = -x \sin\left(x^2\right) \varpi_2(x). \tag{9.8b}$$

Unfortunately, the term $\varpi_{3a}(x)$ above is the only integral in our analysis which cannot be performed analytically. However, we can proceed by expanding the Fresnel term on the right hand side for small x and integrating the resulting terms. We then define $\varpi_{3a_{\text{approx}}}(x)$ to be the terms arising from this integration, given analytically by eq. (9.10). This has the property $\varpi'_{3a}(x) - \varpi'_{3a_{\text{approx}}}(x) \sim \mathscr{O}\left(x^9\right)$ and hence $\varpi_{3a}(x) - \varpi_{3a_{\text{approx}}}(x) \sim \mathscr{O}\left(x^{10}\right)$. Finally, we need

to verify that this is a valid approximation; we can do this by tabulating the function

$$\mathscr{I}(x) = \int_0^x \mathrm{d}y\, \varpi'_{3a}(y) \tag{9.9}$$

for values of x between -1 and 1, and comparing this with our (approximate) analytical result for the integral, eq. (9.10). The integrand, both functions, and the residuals of the approximation are shown in Fig. 9.4.

The term in eq. (9.8b) can be integrated analytically, and the result is given by expression (9.11). Gathering the above results together, we can write down an approximate solution to the Frequency equation, which is given in eq. (9.12). We note that this is valid for $\kappa|x| \ll 1$ up to $\mathscr{O}\left(\kappa^2\right)$, while the result for $\varpi_3(x)$ is only valid when $|x| \ll 1$. Later on, as the need arises, we will find a solution for $\varpi_3(x)$ which is valid in other regimes.

$$\begin{aligned}\varpi_{3a_{\text{approx}}}(x) = \frac{33\sqrt{2\pi}}{64} C\left(\frac{\sqrt{2}x}{\sqrt{\pi}}\right) - \frac{33}{32} x\cos\left(x^2\right) - \frac{11}{16} x^3 \sin\left(x^2\right) \\ + \frac{7}{40} x^5 \cos\left(x^2\right) + \frac{1}{20} x^7 \sin\left(x^2\right)\end{aligned} \tag{9.10}$$

$$\begin{aligned}\varpi_{3b}(x) = \frac{\sqrt{\pi}}{16}\left(\frac{\sqrt{2}}{2}\cos\left(2x^2\right) C\left(\frac{\sqrt{2}x}{\sqrt{\pi}}\right) - \cos\left(x^2\right) C\left(\frac{\sqrt{4}x}{\sqrt{\pi}}\right)\right) \\ + \frac{\sqrt{\pi}}{32}\left(\frac{\sqrt{6}}{6} C\left(\frac{\sqrt{6}x}{\sqrt{\pi}}\right) + \frac{5\sqrt{2}}{2} C\left(\frac{\sqrt{2}x}{\sqrt{\pi}}\right)\right) - \frac{1}{8} x\cos\left(x^2\right)\end{aligned} \tag{9.11}$$

$$\begin{aligned}\omega(x) = x + \kappa\frac{\sqrt{2\pi}}{2} C\left(\frac{\sqrt{2}x}{\sqrt{\pi}}\right) + \kappa^2\left(\frac{\sqrt{2\pi}}{4}\cos\left(x^2\right) C\left(\frac{\sqrt{2}x}{\sqrt{\pi}}\right) - \frac{\sqrt{\pi}}{8} C\left(\frac{\sqrt{4}x}{\sqrt{\pi}}\right) - \frac{x}{4}\right) \\ + \kappa^3\, \varpi_3(x) + \mathscr{O}\left(\kappa^4\right)\end{aligned} \tag{9.12}$$

Before we continue with our analysis, let us consider the asymptotic value of this solution in the limit of it's validity, i.e. for $1 \ll |x| \ll \kappa^{-1}$. The non-oscillating part of solution (9.12) can be written as

$$\omega(x) \sim x + f(\kappa). \tag{9.13}$$

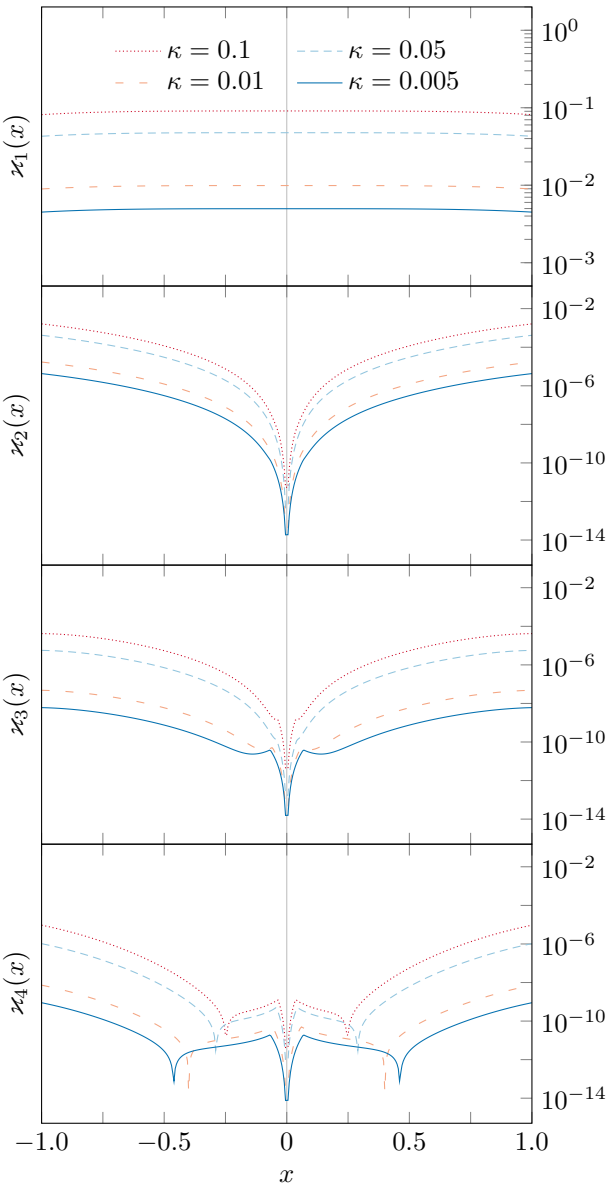

Fig. 9.5 Graphical demonstration of the validity of solution (9.12). It is evident that the residuals scale with the value of the resonance modification κ, and for each order n of the solution, the remainder is of order $\mathscr{O}\left(\kappa^{n+1}\right)$. Figure appeared in [1].

We see that any constant term in the solution for $\omega(x)$ is at least $\mathscr{O}(\kappa)$, rather than $\mathscr{O}\left(\kappa^0\right)$. To confirm the validity of solution (9.12) we compute the quantities

$$\varkappa_{n+1} = \left| \frac{\omega_{\text{num}} - \omega^{(n)}(x)}{\omega_{\text{num}}} \right|, \tag{9.14}$$

where $\omega^{(n)}(x)$ is eq. (9.12) restricted only to order n (e.g. $\omega^{(1)}(x) = \varpi_0(x) + \kappa\varpi_1(x)$). If our solution is correct, then we would find that the fractional error, computed by the above formula is $\mathscr{O}\left(\kappa^{n+1}\right)$. This scaling is evident in the plot of these functions, shown in Figure 9.5.

Let us now seek a solution in the region of decaying oscillations, $|x| \gg 1$. At lowest order, the solution is

$$\omega_0(x) = x. \tag{9.15}$$

At higher order, we attempt an ansatz, composed of a constant, a linear term, and a decaying oscillating term. We allow for three undetermined constants, a_1, b_1 and c_1, as suggested by [130]:

$$\omega_1(x) = a_1 + (1+b_1)x + \frac{c_1}{x}\sin\left[a_1 x + (1+b_1)x^2\right] \tag{9.16}$$

where the subscript "1" on the slope correction term indicates that it pertains to the solution $\omega_1(x)$, as this will change for higher-order solutions. When we substitute this ansatz into the model eq. (9.1):

$$\omega_1'(x) \sim 1 + \kappa\cos\left(x\omega_1\right), \tag{9.17}$$

we ignore $\mathscr{O}\left(x^{-1}\right)$ terms and beyond, and use our knowledge of the behaviour of each separate term to reason about the values of the undetermined constants in eq. (9.18) below. Using standard trigonometric identities, we can expand the second term on the right-hand side, as shown explicitly in eq. (9.19) below.

$$\begin{aligned} 1 + b_1 + 2(1+b_1)c_1\cos\left[ax + (1+b_1)x^2\right] + \mathscr{O}\left(x^{-1}\right) \sim \\ \sim 1 + \kappa\cos\left[ax + (1+b_1)x^2 + c_1\sin\left[x + (1+b_1)x^2\right]\right] \end{aligned} \tag{9.18}$$

$$\begin{aligned} b_1 + 2(1+b_1)\, c_1 \cos\Big[ax + (1+b_1)x^2\Big] + \mathscr{O}\big(x^{-1}\big) \sim \\ \sim \kappa \cos\Big[ax + (1+b_1)x^2\Big] \cos\Big[c_1 \sin\Big[ax + (1+b_1)x^2\Big]\Big] \\ - \kappa \sin\Big[ax + (1+b_1)x^2\Big] \sin\Big[c_1 \sin\Big[ax + (1+b_1)x^2\Big]\Big] \end{aligned} \tag{9.19}$$

At this point we introduce a shorthand notation for the oscillating terms. Please refer to Appendix K (and the plots in Figure K.1) for details.

$$S_n(x) \equiv \sin\Big[n\Big(ax + (1+b)x^2\Big)\Big] \tag{9.20a}$$

$$C_n(x) \equiv \cos\Big[n\Big(ax + (1+b)x^2\Big)\Big] \tag{9.20b}$$

Using these, we cast our last equation (9.19) in the form:

$$b_1 + 2(1+b_1)\, c_1 C_1(x) + \mathscr{O}\big(x^{-1}\big) \sim \kappa C_1(x) \cos\big[c_1 S_1(x)\big] - \kappa S_1(x) \sin\big[c_1 S_1(x)\big] \tag{9.21}$$

Comparing terms on both sides of eq. (9.21), we notice that in order for this identity to hold, it is necessary that $c_1 \sim \mathscr{O}(\kappa)$. We remind ourselves of the assumption that $\kappa \ll 1$ which justifies the small angle approximation we used above. Since the range of the sine function is between -1 and 1, and $c_1 \sim \mathscr{O}(\kappa) \ll 1$, we can safely assume that $c_1 \sin\big[ax + (1+b)x^2\big] \ll 1$ for all x and expand both trigonometric terms in eq. (9.21):

$$b_1 + 2(1+b_1)\, c_1 C_1(x) \sim \kappa C_1(x) - \kappa c_1 S_1^2(x) \tag{9.22}$$

As we only retain the leading order terms in these expansions, we must disregard any $\mathscr{O}\big(\kappa^3\big)$ or higher terms in our further calculations. Since we exclude them at this stage, such terms can no longer appear in the final solution for $\omega_1(x)$. We match the coefficients of the two $\mathscr{O}(\kappa)$ terms on either side of the relation (9.22): $2(1+b)\, c_1 \sim \kappa$. Therefore:

$$c_1 \sim \frac{\kappa}{2(1+b_1)}. \tag{9.23}$$

By using the double-angle trigonometric identities on the remaining term on the right-hand side of (9.22), we find

$$b_1 \sim -\frac{\kappa c_1}{2}\big(1 - C_2(x)\big) \sim -\frac{\kappa c_1}{2}. \tag{9.24}$$

Combining this with result (9.23), we establish that $b_1 \sim \mathscr{O}\left(\kappa^2\right)$, i.e., 0 to linear order. This result follows solely from the linear independence of the $\{C_n\}$ terms. While they are not orthogonal (this can be easily verified by analytical integration), they are linearly independent, and therefore the coefficients on both sides need to match for eq. (9.24) to hold true. Similarly, we obtain the revised result $c_1 \sim \kappa/2 + \mathscr{O}\left(\kappa^3\right)$. The additive constant $a \equiv \omega(0)$ can be determined by comparing the limit $|x| \gg 1$ of solution (9.12) to the ansatz (9.16) in the regime $\kappa|x| \ll 1$:

$$x \pm \kappa \frac{\sqrt{2\pi}}{4} + \kappa \frac{1}{2} \frac{\sin\left(x^2\right)}{x} + \mathscr{O}\left(x^{-2}\right) \sim a + x + \kappa \frac{1}{2} \frac{\sin\left(x^2\right)}{x} + \mathscr{O}\left(\kappa^3\right) \tag{9.25}$$

where on each side there are terms which we have ignored in the respective analysis. We find that $a = \pm\left(\sqrt{2\pi}/4\right)\kappa$ to linear order, and we can write down the leading-order solution (9.26) to the frequency equation (for a single oscillatory mode and no initial phase). Note that here, and for the rest of this work, whenever the symbols $^{\pm}/_{\mp}$ are used, the upper sign is valid for $x \geq 0$, and the lower for $x \leq 0$. The function in question is thus defined piecewise, but we will use this notation throughout for brevity.

$$\omega_1(x) = \pm \frac{\sqrt{2\pi}}{4} \kappa + x + \kappa \frac{1}{2} \frac{1}{x} \sin\left(x^2\right) \tag{9.26}$$

Once we have established the suitability of this ansatz, we propose a further trial solution by adding an extra term to eq. (9.16). It accounts for the terms in eq. (9.24) we ignored when considering only first-order corrections:

$$\frac{c_2}{x} \sin\left[2\left(ax + (1+b)x^2\right)\right]. \tag{9.27}$$

The full ansatz can now be written as:

$$\omega_2(x) = a + (1+b_2)x + \frac{c_1}{x} S_1(x) + \frac{c_2}{x} S_2(x). \tag{9.28}$$

We substitute this into the source equation (9.1) and carry out a similar procedure to establish the new values of the constants, as detailed below. On the left-hand side, we ignore terms of $\mathscr{O}\left(x^{-1}\right)$ in the derivative:

$$\omega_2' \sim 1 + b_2 + 2(1+b_2)c_1 C_1 + 4(1+b_2)c_2 C_2, \tag{9.29}$$

while on the right-hand side, we need to unpack the argument of the cosine function. Previously we established that $c_1 \sim \mathscr{O}(\kappa)$, and since we expect that the new terms originating from $\omega_2(x)$ will match the remaining term in eq. (9.24), we expect $c_2 \sim \mathscr{O}\left(\kappa^2\right)$. This justifies the further use of the small-angle approximation for the latter two terms. We point out that we need to ignore non-constant terms of $\mathscr{O}\left(\kappa^3\right)$ in this expansion, as they will not be matched by a suitable term in the ansatz.

$$\begin{aligned} 1+\kappa\cos\left[ax+(1+b_2)x^2+c_1S_1+c_2S_2\right] &\sim 1+\kappa C_1-\kappa c_1 S_1^2-\kappa c_2 S_1 S_2 \\ &= 1-\frac{\kappa c_1}{2}+\kappa C_1(x)-\frac{\kappa c_1}{2}C_2(x)+\mathscr{O}\left(\kappa^3\right) \end{aligned} \tag{9.30}$$

Matching the coefficients of terms in eqs. (9.29) and (9.30), we obtain the coupled equations:

$$b_2 \sim -\frac{\kappa c_1}{2},\ 2(1+b_2)c_1 \sim \kappa,\ 4(1+b_2)c_2 \sim \frac{\kappa c_1}{2}. \tag{9.31}$$

These imply that $c_1 \sim \kappa/2+\mathscr{O}\left(\kappa^3\right)$ and $b_2 \sim -\kappa^2/4+\mathscr{O}\left(\kappa^4\right)$. The last equation above determines the value of the newly introduced constant c_2:

$$c_2 \sim \frac{\kappa c_1}{8(1+b_2)} \sim \frac{\kappa^2}{16(1+b_2)} \sim \frac{\kappa^2}{16}+\mathscr{O}\left(\kappa^4\right). \tag{9.32}$$

To find the constant a at second order, we need to match this solution to the $\mathscr{O}\left(\kappa^2\right)$ part of solution (9.12) in the buffer zone where both solutions are valid, as per eq. (9.33). Expanding (9.12) for $x \gg 1$ and the above ansatz for $\kappa|x| \ll 1$ (both to order $\mathscr{O}\left(x^{-1}\right)$ inclusive), we find that all functional term match on both sides. The constant term is the value of a at second order, $\left(\mp\sqrt{\pi}/16\right)\kappa^2$. Combining these results together, we establish the improved solution $\omega_2(x)$, given by eq. (9.34).

$$\begin{aligned} &\frac{\sqrt{2\pi}}{4}\cos\left(x^2\right)C\left(\frac{\sqrt{2}x}{\sqrt{\pi}}\right)-\frac{\sqrt{\pi}}{8}C\left(\frac{\sqrt{4}x}{\sqrt{\pi}}\right)-\frac{1}{4}x\Bigg|_{x\gg 1} \\ &\qquad = a-\frac{1}{4}x+\frac{\sqrt{2\pi}}{8}\cos\left(x^2\right)+\frac{1}{16}\frac{\sin\left(2x^2\right)}{x^2}+\mathscr{O}\left(x^{-2}\right) \end{aligned} \tag{9.33}$$

$$\begin{aligned}\omega_2(x) = \pm\frac{\sqrt{2\pi}}{4}\kappa \mp \frac{\sqrt{\pi}}{16}\kappa^2 + \left(1-\frac{\kappa^2}{4}\right)x \\ + \kappa\frac{1}{2}\frac{1}{x}\sin\left[\left(\pm\frac{\sqrt{2\pi}}{4}\kappa\right)x + x^2\right] + \kappa^2\frac{1}{16}\frac{1}{x}\sin\left(2x^2\right)\end{aligned} \tag{9.34}$$

At the next order, the task of finding appropriate terms becomes more complicated, since we need to balance the terms in eq. (9.10). At this order there is a logarithmic trend, as well as an oscillatory part, hence we propose the following ansatz which reflects the nature of the solution:

$$\omega_3(x) = a + (1+b_3)x + c_1\frac{S_1(x)}{x} + c_2\frac{S_2(x)}{x} + c_3\frac{S_3(x)}{x} + d_1\frac{S_1(x)}{x^2} + d_2\frac{S_2(x)}{x^2} + l\ln|x|. \tag{9.35}$$

The details of calculating the expressions for these constants are burdensome, hence we have left them in Appendix L.1. The important message here is that we have still managed to find a set of terms which satisfy the governing equation (9.1), without conflicting the previous solutions (i.e. without producing new terms at $\mathscr{O}\left(\kappa, x^{-1}\right)$).

To determine the new value of the constant a, we again need to turn to our solution near the origin. In particular, here we need an expansion of $\varpi_3(x)$ for large x. However, we used a small-x approximation to obtain $\varpi_{3a_{\text{asymp}}}(x)$ earlier, which is not valid in the buffer zone where both solutions (9.12) and (9.35) are valid. We need to go back to the original problem (9.8a), and instead of expanding in the small-x regime, we expand for $|x| \gg 1$ (which is valid when $\kappa|x| \ll 1$). To do this, we expand the Fresnel term on the right hand side of eq. (9.8a) for large $|x|$, truncate the series at $\mathscr{O}\left(x^{-5}\right)$ and then compute the integral of this series, the function $\varpi_{3a_{\text{asymp}}}$ given in eq. (9.38). This procedure ensures that $\varpi_{3a}(x) - \varpi_{3a_{\text{asymp}}}(x) \sim \alpha + \mathscr{O}\left(x^{-4}\right)$. The constant α is the asymptotic value of $\varpi_{3a}(x) - \varpi_{3a_{\text{asymp}}}(x)$, which may be found by integrating $\varpi_{3a}(x) - \varpi_{3a_{\text{asymp}}}(x)$ from 0 to infinity

$$\alpha = \int_0^{x_c} \mathrm{d}y\, \varpi'_{3a}(y) - \varpi_{3a_{\text{asymp}}}(x_c) + \int_{x_c}^{\infty} \mathrm{d}y\, \left(\varpi'_{3a}(y) - \varpi'_{3a_{\text{asymp}}}(y)\right). \tag{9.36}$$

The quantity x_c is arbitrary, but by choosing a value $x_c \sim 1/k_1 \sim 10$ we may bound the value of the second integral by 10^{-5}. Numerical evaluation of the terms on the first line of eq. (9.36) then give $\alpha = \mp 0.00991$. We deduce that, asymptotically, we may write $\varpi_3(x) = \alpha + \varpi_{3a_{\text{asymp}}}(x) + \varpi_{3b}(x)$, with higher-order corrections which scale as x^{-4}.

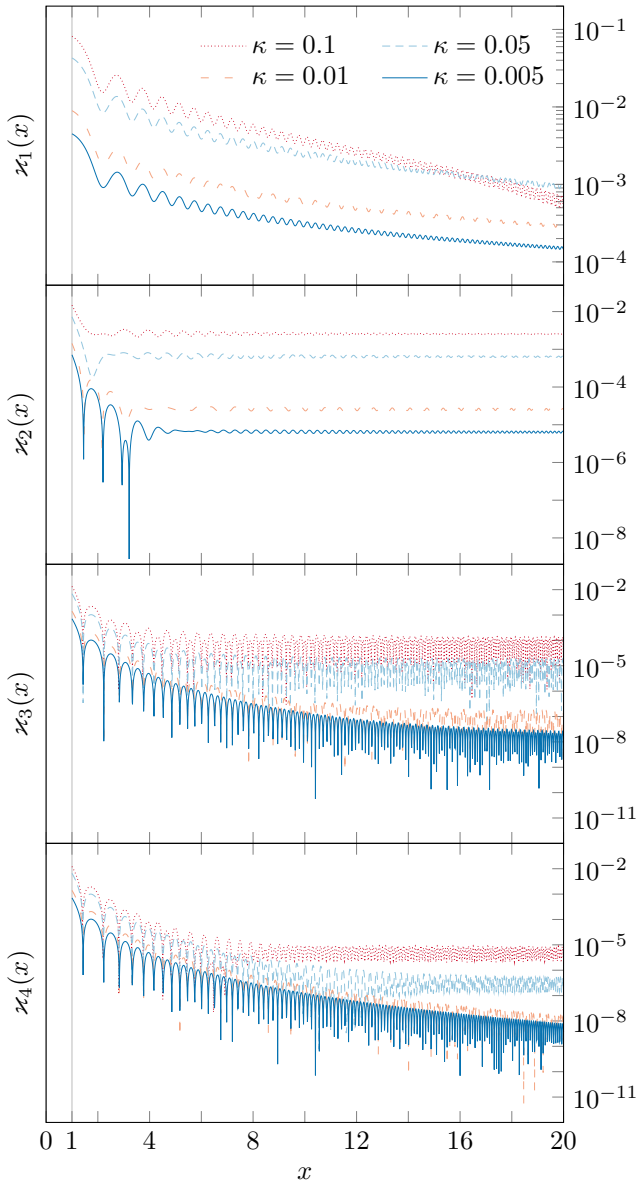

Fig. 9.6 Graphical demonstration of the validity of solutions (9.15) – (9.40). The fractional errors scale with the value of the resonance modification κ. At each order n of the solution, the remainder is of order $\mathscr{O}\left(\kappa^{n+1}\right)$, as expected. Figure appeared in [1].

Combining these resulting terms with the ones coming from eq. (9.11), we arrive at the left-hand side of eq. (9.39). The right-hand side of eq. (9.39) is comprised of the terms in an expansion of the ansatz (9.35) for small $\kappa|x|$.

The terms match nicely as we would expect, apart from the coefficients of $\sin\left(x^2\right)/x$ and $\cos\left(x^2\right)/x$. The reason for this is that to determine these terms accurately we need to extend the asymptotic solution to the next order in $1/x$. At that order we get a term of the form $C_1(x)/x^3$ in the solution, and it is straightforward to deduce that, at leading order, the coefficient in front of this term is $-\kappa/4$. This additional term contributes terms at order κ^3 on the right hand side of eq. (9.39) and those terms are $\pi\cos\left(x^2\right)/(64x)$ and $-\sin\left(x^2\right)/(16x)$, which are exactly what is needed to match the terms from the $\kappa|x| \ll 1$ solution on the left hand side of eq. (9.39).

We can now read off the third-order piece of the coefficient a from eq. (9.39)

$$a_3 = \left(\alpha \pm \frac{\sqrt{2\pi}}{32} \pm \frac{\sqrt{6\pi}}{192} \pm \frac{\sqrt{2}\,\pi^{3/2}}{128}\right)\kappa^3 \approx \pm 0.15255\,\kappa^3 \tag{9.37}$$

The third-order solution $\omega_3(x)$ is given in eq. (9.40). This is the most accurate solution to the single-mode, zero-phase frequency equation that we will present. The lack of necessity for higher order iterations will be explained when discussing the multi-mode frequency equation.

Once we have obtained these solutions, it is worthwhile to investigate their properties visually. To confirm their validity, Figure 9.6 demonstrates that these solutions are correct at their respective order by computing the quantities $\varkappa_n(x)$ defined in eq. (9.14), and showing graphically that they have the expected magnitudes. Please note we have shown only the region $x > 0$, with the region $x < 0$ being a mirror image of this one.

Figure 9.7 shows how the intercept a, the slope $(1-b)$, and the coefficients of the oscillating modes $\{c_n\}$ and $\{d_n\}$ vary with the parameter κ.

$$\begin{aligned}\varpi_{3a_{\text{asymp}}}(x) = {} & \pm\frac{\sqrt{2\pi}}{32}\ln|x| - \frac{\sqrt{2\pi}}{64}C\left(\frac{\sqrt{2}x}{\sqrt{\pi}}\right) + \frac{\sqrt{2}\,\pi^{3/2}}{64}S\left(\frac{\sqrt{2}x}{\sqrt{\pi}}\right) + \frac{\sqrt{6\pi}}{192}C\left(\frac{\sqrt{6}x}{\sqrt{\pi}}\right) \\ & - \frac{\pi}{32}x\sin\left(x^2\right) \pm \frac{\sqrt{2\pi}}{64}\cos\left(2x^2\right) \pm \frac{\sqrt{2\pi}}{128}\frac{\sin\left(2x^2\right)}{x^2} - \frac{1}{64}\frac{\cos\left(x^2\right)}{x^3} \\ & - \frac{1}{192}\frac{\cos\left(3x^2\right)}{x^3} \mp \frac{\sqrt{2\pi}}{64}\frac{\cos\left(2x^2\right)}{x^4} - \frac{3}{256}\frac{\sin\left(x^2\right)}{x^5} - \frac{3}{256}\frac{\sin\left(3x^2\right)}{x^5}\end{aligned} \tag{9.38}$$

	$k_n = k_1/\log_2(n+1)$				$k_n = k_1/n^{2.5}$				$k_n = k_1/2^{n-1}$			
n	0.1	0.05	0.01	0.005	0.1	0.05	0.01	0.005	0.1	0.05	0.01	0.005
2	6.31^{-2}	3.15^{-2}	6.31^{-3}	3.15^{-3}	$\underline{1.77^{-2}}$	8.84^{-3}	1.77^{-3}	8.84^{-4}	5.00^{-2}	2.50^{-2}	5.00^{-3}	2.50^{-3}
3	5.00^{-2}	2.50^{-2}	5.00^{-3}	2.50^{-3}	$\overline{6.42^{-3}}$	$\underline{3.21^{-3}}$	6.42^{-4}	3.21^{-4}	2.50^{-2}	1.25^{-2}	2.50^{-3}	1.25^{-3}
4	4.31^{-2}	2.15^{-2}	4.31^{-3}	2.15^{-3}	3.13^{-3}	$\overline{1.56^{-3}}$	3.13^{-4}	1.56^{-4}	$\underline{1.25^{-2}}$	6.25^{-3}	1.25^{-3}	6.25^{-4}
5	3.87^{-2}	1.93^{-2}	3.87^{-3}	1.93^{-3}	1.79^{-3}	8.94^{-4}	1.79^{-4}	8.94^{-5}	$\overline{6.25^{-3}}$	$\underline{3.13^{-3}}$	6.25^{-4}	3.13^{-4}
6	3.56^{-2}	1.78^{-2}	3.56^{-3}	1.78^{-3}	$\underline{1.13^{-3}}$	5.67^{-4}	$\underline{1.13^{-4}}$	5.67^{-5}	3.13^{-3}	$\overline{1.56^{-3}}$	3.13^{-4}	1.56^{-4}
7	3.33^{-2}	1.67^{-2}	3.33^{-3}	1.67^{-3}	$\overline{7.71^{-4}}$	3.86^{-4}	$\overline{7.71^{-5}}$	3.86^{-5}	$\underline{1.56^{-3}}$	7.81^{-4}	$\underline{1.56^{-4}}$	7.81^{-5}
8	3.15^{-2}	1.58^{-2}	3.15^{-3}	1.58^{-3}	5.52^{-4}	2.76^{-4}	5.52^{-5}	$\underline{2.76^{-5}}$	$\overline{7.81^{-4}}$	3.91^{-4}	$\overline{7.81^{-5}}$	$\underline{3.91^{-5}}$
9	3.01^{-2}	1.51^{-2}	3.01^{-3}	1.51^{-3}	4.12^{-4}	2.06^{-4}	4.12^{-5}	$\overline{2.06^{-5}}$	3.91^{-4}	$\underline{1.95^{-4}}$	3.91^{-5}	$\overline{1.95^{-5}}$
10	2.89^{-2}	1.45^{-2}	2.89^{-3}	1.45^{-3}	3.16^{-4}	1.58^{-4}	3.16^{-5}	1.58^{-5}	1.95^{-4}	$\overline{9.77^{-5}}$	1.95^{-5}	9.77^{-6}

Table 9.1 The first 10 terms of the series $\{k_n\}$ for the three different series of interest, for each of our 4 chosen numerical values: $0.1, 0.05, 0.01$, and 0.005. These were plotted in Figure 9.1. It should be noted that the numbers in this table are given using the scientific notation $\overline{a.bc}^{\,d} \equiv \overline{a.bc} \times 10^d$. The horizontal lines in the data represent numerical boundaries: numbers below the first line in a column are smaller than k_i^2, and numbers below the second line are smaller than k_i^3. Table appeared in [1].

$$
\begin{aligned}
&\alpha \pm \frac{\sqrt{2\pi}}{32} \pm \frac{\sqrt{6\pi}}{192} \pm \frac{\sqrt{2}\,\pi^{3/2}}{128} \pm \frac{\sqrt{2\pi}}{32}\ln|x| - \frac{\pi}{32}x\sin\left(x^2\right) - \frac{1}{8}x\cos\left(x^2\right) \\
&\qquad \mp \frac{\sqrt{\pi}}{32}\cos\left(x^2\right) \pm \frac{\sqrt{2\pi}}{32}\cos\left(2x^2\right) + \frac{1}{32}\frac{\sin\left(x^2\right)}{x} + \frac{1}{96}\frac{\sin\left(3x^2\right)}{x} - \frac{\pi}{64}\frac{\cos\left(x^2\right)}{x} \\
&= a_3 \mp \frac{\pi}{32}x\sin\left(x^2\right) \mp \frac{\sqrt{\pi}}{32}\cos\left(x^2\right) - \frac{1}{8}x\cos\left(x^2\right) \pm \frac{\sqrt{2\pi}}{32}\cos\left(2x^2\right) \\
&\qquad + \frac{3}{32}\frac{\sin\left(x^2\right)}{x} + \frac{1}{96}\frac{\sin\left(3x^2\right)}{x} - \frac{\pi}{32}\frac{\cos\left(x^2\right)}{x} \pm \frac{\sqrt{2\pi}}{32}\ln|x|
\end{aligned}
\tag{9.39}
$$

$$
\begin{aligned}
\omega_3(x) = \pm &\left(\frac{\sqrt{2\pi}}{4}\kappa - \frac{\sqrt{\pi}}{16}\kappa^2 + 0.15255\,\kappa^3\right) + \left(1 - \frac{\kappa^2}{4}\right)x \\
&+ \kappa\frac{1}{2}\frac{1}{x}\sin\left[\left(\pm\frac{\sqrt{2\pi}}{4}\kappa \mp \frac{\sqrt{\pi}}{16}\kappa^2\right)x + \left(1 - \frac{\kappa^2}{4}\right)x^2\right] \\
&+ \kappa^2\frac{1}{16}\frac{1}{x}\sin\left[2\left(\left(\pm\frac{\sqrt{2\pi}}{4}\kappa\right)x + x^2\right)\right] + \kappa^3\frac{1}{x}\left(\frac{3}{32}\sin\left(x^2\right) + \frac{1}{96}\sin\left(3x^2\right)\right) \\
&\mp \kappa^2\frac{\sqrt{2\pi}}{16}\frac{1}{x^2}\sin\left[\left(\pm\frac{\sqrt{2\pi}}{4}\kappa\right)x + x^2\right] \\
&\pm \kappa^3\left(\frac{\sqrt{\pi}}{64}\frac{1}{x^2}\sin\left(x^2\right) - \frac{\sqrt{2\pi}}{64}\frac{1}{x^2}\sin\left(2x^2\right) + \frac{\sqrt{2\pi}}{32}\ln|x|\right)
\end{aligned}
\tag{9.40}
$$

The solution can be made more accurate, by adding terms at higher orders, of the form $c_n S_n(x)/x$ and $d_j S_n(x)/x^2$ to the ansatz (9.28). Below we see the general case of having m oscillatory terms in the trial solution $\omega_m(x)$, where m could be either a finite number or infinity:

$$\omega_m(x) = a + (1+b)\,x + \sum_{j=1}^{m} \left(c_j \frac{S_j(x)}{x} + d_j \frac{S_j(x)}{x^2} \right). \tag{9.41}$$

We shall discuss later (after we solve the multimode version of the phase equation) why there is no practical need for solutions beyond third order. If we seek to find lower-order corrections in $\mathcal{O}(x^{-p})$, we add terms of the form:

$$\sim \frac{1}{x^p} \sum_{j=1}^{m} \left(c_j^{(p)} S_j(x) + d_j^{(p)} C_j(x) \right). \tag{9.42}$$

However, instead of following through with this procedure, we look at extensions of eq. (9.1) to find the general solution of eq. (7.17a). Initially, we allow for multiple oscillation modes, each with a different amplitude (parameter κ_i), and following this, we include a non-vanishing phase in our calculations.

In the following we will use bold quantities, e.g., $\boldsymbol{\omega}(x)$, to indicate values of the coefficients in the multiple mode case. We note that these are not vectors, but the scalars that appear in the multiple mode solution. To solve for the evolution of the frequency resonances,

$$\boldsymbol{\omega}'(x) = 1 + \sum_n \kappa_n \cos\left(n x_\omega \boldsymbol{\omega}\right) \tag{9.43}$$

we can again look at the problem from two scales: small and large $|x|$. Near the origin, we can write down a series expansion similar to eq. (9.2):

$$\boldsymbol{\omega}(x) = \sum_{m=0}^{\infty} \sum_{n=0}^{\infty} \kappa_n^m \boldsymbol{\varpi}_{m,n}(x). \tag{9.44}$$

Similarly to before, we can derive solutions for $n = 0, 1$:

$$\boldsymbol{\varpi}_{0,n}(x) = x \tag{9.45a}$$

$$\boldsymbol{\varpi}_{1,n}(x) = \frac{\sqrt{\pi}}{\sqrt{2n}} C\left(\frac{\sqrt{2n}\,x}{\sqrt{\pi}} \right) \tag{9.45b}$$

Further solutions are not going to be pursued, as higher orders of κ_n (for small n) would be of the same size as κ_n for some larger n. Hence, $\boldsymbol{\omega}(x)$ near the origin can be most completely written down as

$$\boldsymbol{\omega}(x) = x + \sum_n \kappa_n \frac{\sqrt{\pi}}{\sqrt{2n}} C\left(\frac{\sqrt{2n}\,x}{\sqrt{\pi}}\right) \tag{9.46}$$

For $|x| \gg 1$, we propose an extended ansatz of the form:

$$\boldsymbol{\omega}_1(x) = \boldsymbol{a} + (1+\boldsymbol{b}_1)\,x + \sum_n \boldsymbol{c}_n \frac{S_n(x)}{x} \tag{9.47}$$

with derivative

$$\boldsymbol{\omega}_1' = 1 + \boldsymbol{b}_1 + \sum_n 2n(1+\boldsymbol{b})\,\boldsymbol{c}_n C_n(x) + \mathscr{O}\left(x^{-1}\right). \tag{9.48}$$

We substitute this into the governing eq. (9.43) and proceed to match the relevant coefficients on both sides of this relation. It is important to explain here that the leading order dependence of each coefficient $\boldsymbol{c}_n$ will be the same as if considering its corresponding mode on its own (see Appendix L.2 for derivation), with higher-order corrections due to cross-terms emerging from the cosine term (see Appendix L.3), and therefore $\boldsymbol{c}_n \sim \mathscr{O}(\kappa_n/n) \sim \mathscr{O}\left(\kappa_1/n^{\alpha+1}\right)$. Thus, each coefficient $\boldsymbol{c}_n$ is smaller than the previous one in the series, and we can expand the trigonometric terms on the right-hand side, to obtain the form (9.49). Evidently, to be able to match the constant term $\boldsymbol{b}$ on the left-hand side, we need to find a constant term on the right-hand side too. Such a constant could only arise from the second term on the right-hand side, in the case $n = m$, and yields eq. (9.50). The remaining terms must combine to form an expression for $\boldsymbol{c}_n$, and we match them using the linear independency of the functions $\{C_n(x)\}$, yielding eq. (9.51). On the right-hand side of this equation, we omitted a pre-factor of $(1+\boldsymbol{b})^{-1} \sim 1 + \mathscr{O}\left(\kappa_1^2\right)$, since we know that $\boldsymbol{b} \sim \mathscr{O}\left(\kappa_1^2\right)$.

$$\boldsymbol{b} + 2(1+\boldsymbol{b}) \sum_n n\,\boldsymbol{c}_n C_n(x) \sim \sum_n \kappa_n C_n(x) - \frac{1}{2}\sum_{n,m} n\,\kappa_n\,\boldsymbol{c}_m C_{n-m}(x) + \frac{1}{2}\sum_{n,m} n\,\kappa_n\,\boldsymbol{c}_m C_{n+m}(x) \tag{9.49}$$

$$\boldsymbol{b} \sim -\frac{1}{2}\sum_n n\,\kappa_n\,\boldsymbol{c}_n \tag{9.50}$$

$$\boldsymbol{c}_n \sim \frac{\kappa_n}{2n} - \frac{1}{4n}\sum_{m,p} m\,\kappa_m\,\boldsymbol{c}_p\,\delta_{|m-p|,n} + \frac{1}{4n}\sum_{m,p} m\,\kappa_m\,\boldsymbol{c}_p\,\delta_{(m+p),n} \tag{9.51}$$

We now proceed to demonstrate that the second and third terms in the relation (9.51) are sub-leading compared to the first term, and therefore can be ignored in the final expression. To do this, we remind ourselves of our assumption that $\kappa_n \sim \kappa_1/n^\alpha$, with $\alpha \gtrsim 2$ and substitute this into our expression for $\boldsymbol{c}_n$. From the first term we can see that $\boldsymbol{c}_n \sim \mathscr{O}(\kappa_n/n)$. Using this, the formula for $\boldsymbol{c}_n$ can be written down solely in terms of κ_1. After applying the action of the Krönecker delta operators, the second and third terms of eq. (9.51) become

$$\Xi_n(\kappa_1) = -\frac{\kappa_1^2}{8n}\sum_{p=1}^{\infty}\frac{1}{(n+p)^{\alpha-1}\,p^{\alpha+1}}\,\delta_{|m-p|,n} \tag{9.52}$$

and

$$\Upsilon_n(\kappa_1) = \frac{\kappa_1^2}{8n}\sum_{m=1}^{n-1}\frac{1}{m^{\alpha-1}(n-m)^{\alpha+1}}\,\delta_{(m+p),n}. \tag{9.53}$$

We need to inspect and bound each of these terms, in order to show they are sub-leading compared to the first term in eq. (9.51), $\kappa_1/n^{\alpha+1}$. In eq. (9.52), we split off the $p=1$ term from the sum, and bound the remaining terms from above by an integral over the index p:

$$\sum_{p=1}^{\infty}\frac{1}{(n+p)^{\alpha-1}\,p^{\alpha+1}} < \frac{1}{(n+1)^{\alpha-1}} + \int_1^{\infty}\frac{\mathrm{d}p}{(n+p)^{\alpha-1}\,p^{\alpha+1}} \tag{9.54}$$

We re-scale by writing $p = n\tilde{p}$, and the integral becomes:

$$\frac{1}{n^{2\alpha-1}}\int_{1/n}^{\infty}\frac{\mathrm{d}\tilde{p}}{(1+\tilde{p})^{\alpha-1}\,\tilde{p}^{\alpha+1}}. \tag{9.55}$$

We split the integration region in two intervals: from $(1/n)$ to 1, and from 1 to ∞. The first of the resulting integrals can be bounded as follows

$$\int_{1/n}^{\infty}\frac{\mathrm{d}\tilde{p}}{(1+\tilde{p})^{\alpha-1}\,\tilde{p}^{\alpha+1}} < \int_{1/n}^{\infty}\frac{\mathrm{d}\tilde{p}}{\tilde{p}^{\alpha+1}} = \frac{n^\alpha - 1}{\alpha}, \tag{9.56}$$

while the second one can be solved and the solution expressed in terms of the hypergeometric function ${}_2F_1$, independently of the integration variable $\tilde{p}$. We find that the term $\Xi_n(\kappa_1)$ is bounded above by (ξ_i are constants):

$$\Xi_n(\kappa_1) < -\frac{\kappa_1^2}{8n}\left(\frac{1}{(n+1)^{\alpha-1}} + \frac{\xi_1}{n^{2\alpha-1}} + \frac{\xi_2}{n^{\alpha-1}}\right) \sim \frac{\kappa_1^2}{n^\alpha}. \tag{9.57}$$

Considering the term in eq. (9.53), we can find a bound using a similar argument, albeit the reasoning is slightly longer, as the sum has definite bounds on both ends, and the integrand is not monotonic for the interval of integration. We strip off the first and last terms of the sum: $(n-1)^{-\alpha+1}$ and $(n+1)^{-\alpha-1}$, respectively. The remainder can be bound from above by an integral, and a suitable substitution can be applied to obtain:

$$\frac{1}{n^{2\alpha-1}} \int_{1/n}^{1-1/n} \frac{\mathrm{d}\tilde{p}}{(1-\tilde{p})^{\alpha-1}\,\tilde{p}^{\alpha+1}}. \tag{9.58}$$

We proceed to split the integral for some $n > 1$, say 2:

$$\int_{1/n}^{1/2} \frac{\mathrm{d}\tilde{p}}{(1-\tilde{p})^{\alpha-1}\,\tilde{p}^{\alpha+1}} + \int_{1/2}^{1-1/n} \frac{\mathrm{d}\tilde{p}}{(1-\tilde{p})^{\alpha-1}\,\tilde{p}^{\alpha+1}} \tag{9.59}$$

Each of the two integrals can be bounded as follows:

$$\int_{1/n}^{1/2} \frac{\mathrm{d}\tilde{p}}{(1-\tilde{p})^{\alpha-1}\,\tilde{p}^{\alpha+1}} < \frac{1}{(1-1/2)^{\alpha-1}} \int_{1/n}^{1/2} \frac{\mathrm{d}\tilde{p}}{\tilde{p}^{\alpha+1}} \tag{9.60a}$$

$$\int_{1/2}^{1-1/n} \frac{\mathrm{d}\tilde{p}}{(1-\tilde{p})^{\alpha-1}\,\tilde{p}^{\alpha+1}} < \frac{1}{(1/2)^{\alpha+1}} \int_{1/2}^{1-1/n} \frac{\mathrm{d}\tilde{p}}{(1-\tilde{p})^{\alpha-1}}. \tag{9.60b}$$

Evaluating these and putting everything back together, we conclude that a bound on the term (9.53) is given by

$$\begin{aligned} \Upsilon_n(\kappa_1) &= \frac{\kappa_1^2}{8n} \sum_{m=1}^{n-1} \frac{1}{m^{\alpha-1}(n-m)^{\alpha+1}} \\ &< \frac{\kappa_1^2}{8n} \left(\frac{1}{(n-1)^{\alpha-1}} + \frac{1}{(n+1)^{\alpha+1}} + \frac{\upsilon_1}{n^{\alpha-1}} + \frac{\upsilon_2}{n^{\alpha+1}} + \frac{\upsilon_3}{n^{2\alpha-1}} \right) \sim \frac{\kappa_1^2}{n^\alpha} \end{aligned} \tag{9.61}$$

where υ_i are constants. We have found that the latter two terms in eq. (9.51) are of the order of κ_1^2/n^α. We still need to determine how this compares to the magnitude of the first term in this result, namely $\kappa_1/n^{\alpha+1}$:

$$\frac{\kappa_1}{n^{\alpha+1}} \gtrsim \frac{\kappa_1^2}{n^\alpha} \quad \Leftrightarrow \quad n \lesssim \kappa_1^{-1}. \tag{9.62}$$

We can therefore say that for values of n smaller than κ_1^{-1} the second and third terms are much smaller than the first and can therefore be ignored. For values of n above this limit all terms are of comparable magnitude. However, this $\bar{n}$ can be related to the order of the

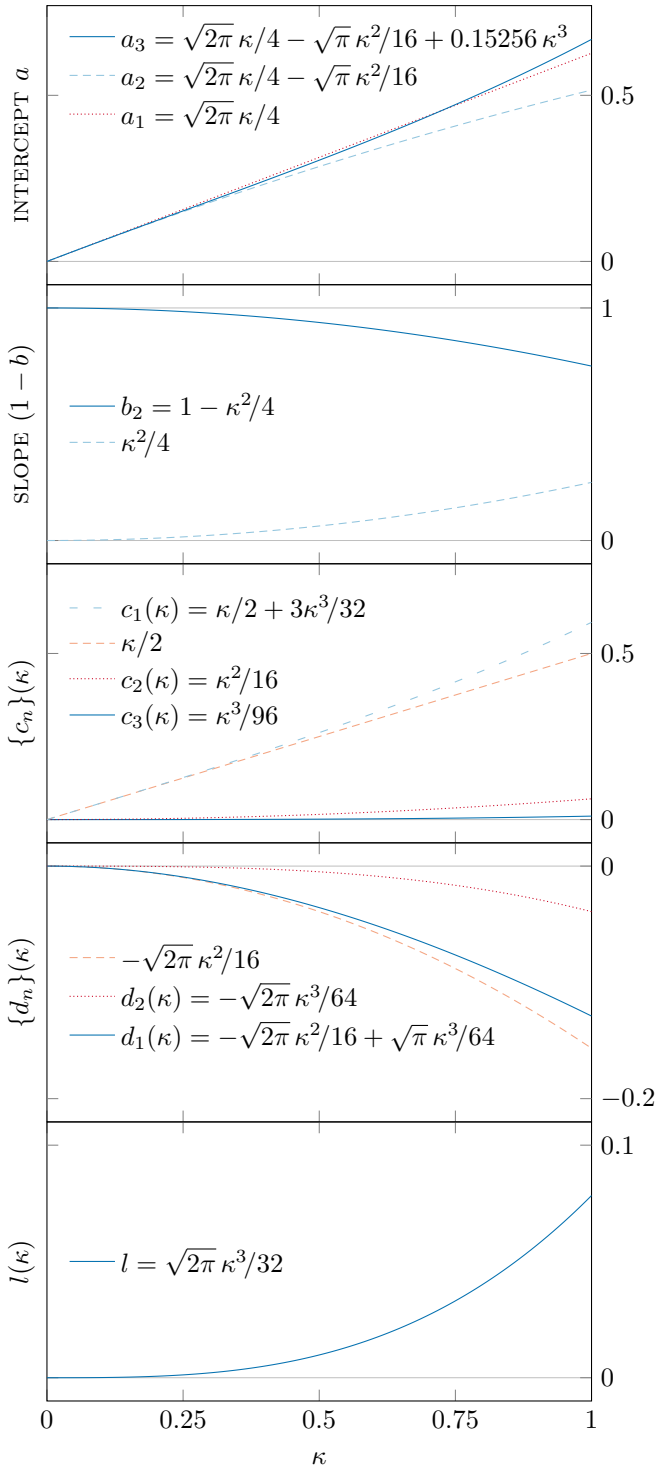

Fig. 9.7 Features and coefficients of solutions (9.26) – (9.40) as functions of the mode parameter κ. Figure appeared in [1].

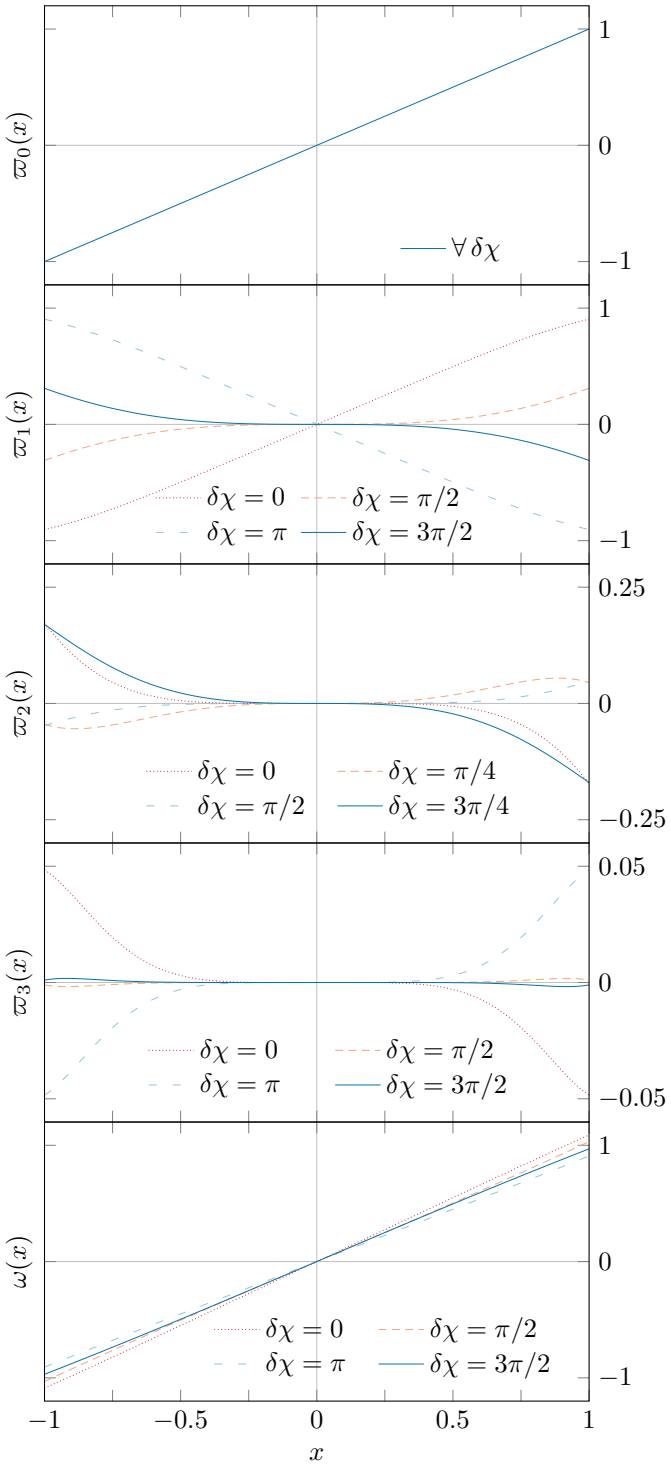

Fig. 9.8 Variation of the components of the solution to the frequency resonance equation for different values of the phase angle. The bottom panel uses $\kappa = 0.1$. Figure appeared in [1].

parameters $\{\kappa_i\}$:

$$\kappa_{\bar{n}} = \frac{\kappa_1}{n^\alpha} \sim \kappa_1^{1+\alpha} < \kappa_1^3. \tag{9.63}$$

and so ignoring these higher terms leads to an error smaller than κ_1^3. Therefore, we have discovered that we are free to ignore the terms discussed above, and in general ignore the interference between the magnitude of κ_1 and the large values of the index n, as long as we do not concern ourselves with corrections beyond third order. We may write:

$$\boldsymbol{c}_1^{(n)} \sim \frac{\kappa_n}{2n}. \tag{9.64}$$

As before, the constant $\boldsymbol{a}$ in eq. (9.47) can be determined if we compare our multimode ansatz to solution (9.46) in the buffer zone where both solutions are valid. This means expanding (9.46) for large x, and comparing with eq. (9.47) (see eq. (9.67). This suggests that the value of $\boldsymbol{a}$ is:

$$\boldsymbol{a} = \pm \sum_n \kappa_n \frac{\sqrt{\pi}}{2\sqrt{2n}} \tag{9.65}$$

Our final solution with this ansatz is given by eq. (9.68).

To test the validity of this solution, we devise a test similar to eq. (9.14), but include the presence of multiple modes in the definition of the quantifier:

$$\boldsymbol{\varkappa}_2(m,x) = \left| \frac{\boldsymbol{\omega}_{\text{num}} - \boldsymbol{\omega}^{(1)}(x)}{\boldsymbol{\omega}_{\text{num}}} \right|_m. \tag{9.66}$$

Here, $\boldsymbol{\omega}(x)$ is given by eq. (9.68), $\boldsymbol{\omega}_{\text{num}}$ is the respective numerical solution, and the subscript m signifies that all equations and solutions have been limited to the first m terms only. In Figures 9.10 and L.1 we demonstrate graphically the validity of our solution for $m = \{2,5,10,20\}$ and in the intervals $|x| \leq 1$ and $1 \leq x \leq 20$, respectively.

We could try to extend this approach further, by naively including $S_{2n}(x)$ terms in the ansatz. These terms, however, are redundant, as for n ranging from 1 to $+\infty$, the set $\{2n\}$ is a subset of $\{n\}$, and therefore the latter terms in the sum can be absorbed into the former one. Thus, eq. (9.47) is the only ansatz we can use for the equation with an infinite number of modes. Finding higher-order solutions is also complicated by the fact that taking powers of the infinite sum introduces an increasing number of cross-terms.

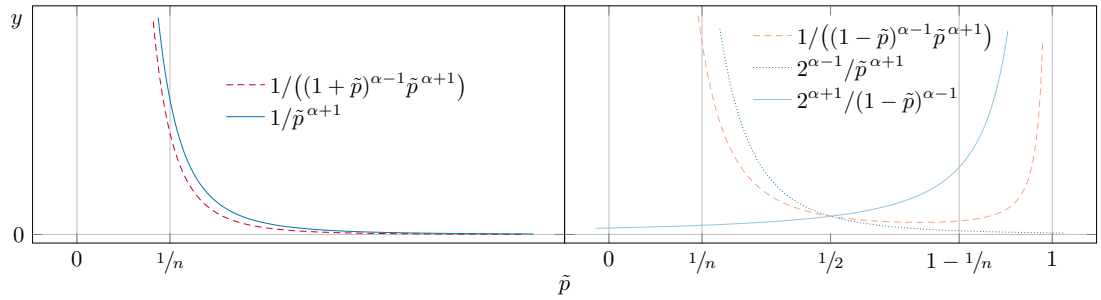

Fig. 9.9 Visual representation of the integral bounds we use in the discussion of the multi-mode frequency equation. *Left panel:* Graph of inequality (9.56). *Right panel:* Graph of inequalities (9.60a) and (9.60b). Note that these plots show only the integrands, while the integrals we discuss are given by the area between these curves and the $\tilde{p}-$axis. Figure appeared in [1].

$$x+\sum_n \kappa_n \frac{\sqrt{\pi}}{\sqrt{2n}}\left(\pm\frac{1}{2}+\frac{\sin\left(nx^2\right)}{\sqrt{2\pi n}x}\right)+\mathscr{O}\left(x^{-2}\right)\sim \boldsymbol{a}+x+\sum_n \frac{\kappa_n}{2n}\frac{1}{x}\sin\left(nx^2\right) \tag{9.67}$$

$$\boldsymbol{\omega}_1(x)=\pm\sum_n \kappa_n \frac{\sqrt{\pi}}{2\sqrt{2n}}+x+\sum_n \kappa_n \frac{1}{2n}\frac{1}{x}\sin\left(nx^2\right) \tag{9.68}$$

Instead, we return to the single-mode version of the frequency equation and include a non-zero phase $\delta\chi$:

$$\omega'(x)=1+\kappa\cos\left(x\omega-\delta\chi\right). \tag{9.69}$$

To find the solution for small $|x|$, we can expand the cosine term on the right-hand side of the equation, and proceed in an analogous way to the zero-phase case:

$$\omega'(x)=1+\kappa\cos\left(\delta\chi\right)\cos\left(x\omega\right)+\kappa\sin\left(\delta\chi\right)\sin\left(x\omega\right). \tag{9.70}$$

The zeroth-order solution is $\varpi_0(x)=x$, while higher-order solutions will differ from our previous results. The first-order function can be found from

$$\varpi_1'(x)=\cos(\delta\chi)\cos\left(x^2\right)+\sin(\delta\chi)\sin\left(x^2\right). \tag{9.71}$$

After integrating, we arrive at the following result:

$$\varpi_1(x) = \frac{\sqrt{\pi}}{\sqrt{2}}\left(\cos(\delta\chi)\,C\left(\frac{\sqrt{2}x}{\sqrt{\pi}}\right) + \sin(\delta\chi)\,S\left(\frac{\sqrt{2}x}{\sqrt{\pi}}\right)\right). \tag{9.72}$$

The next-order function obeys the differential equation

$$\varpi_2'(x) = -x\sin\left(x^2 - \delta\chi\right)\varpi_1(x), \tag{9.73}$$

and its solution is given in eq. (9.84). The third-order function, $\varpi_3(x)$ deserves a little more attention, as was the case for the zero-phase equation. Part of the derivative is again not integrable analytically, but could be approximated for the cases $|x| \ll 1$ and $|x| \gg 1$, so we split the solution in two parts, given in eqs. (9.74) and (9.75).

$$\varpi_{3a}(x) = -\frac{\pi}{4}\int_0^x \mathrm{d}y\, y^2\cos\left(y^2 - \delta\chi\right)\left(\cos^2(\delta\chi)\,C^2\left(\frac{\sqrt{2}y}{\sqrt{\pi}}\right) + \sin^2(\delta\chi)\,S^2\left(\frac{\sqrt{2}y}{\sqrt{\pi}}\right)\right) \tag{9.74}$$

and

$$\begin{aligned}\varpi_{3b}(x) = &-\frac{\sqrt{\pi}}{4\sqrt{2}}\int_0^x \mathrm{d}y\, y\sin\left(2y^2 - 2\delta\chi\right)\left(\cos(\delta\chi)\,C\left(\frac{\sqrt{2}y}{\sqrt{\pi}}\right) + \sin(\delta\chi)\,S\left(\frac{\sqrt{2}y}{\sqrt{\pi}}\right)\right)\\ &+\frac{\sqrt{\pi}}{8}\int_0^x \mathrm{d}y\, y\sin\left(y^2 - \delta\chi\right)\left(\cos(2\delta\chi)\,C\left(\frac{\sqrt{4}y}{\sqrt{\pi}}\right) + \sin(2\delta\chi)\,S\left(\frac{\sqrt{4}y}{\sqrt{\pi}}\right)\right)\\ &+\frac{1}{4}\int_0^x \mathrm{d}y\, y^2\sin\left(y^2 - \delta\chi\right)\end{aligned} \tag{9.75}$$

To find a solution for $\varpi_{3a}(x)$, we proceed in an analogous way to the $\delta\chi = 0$ case, and take the appropriate limits of interest of the Fresnel function. For $|x| \ll 1$, the expansion is a polynomial, finding an analytical approximation is straightforward, and the result is given by eq. (9.85). Hence the third-order solution near the origin is

$$\varpi_3(x) = \varpi_{3a_{\text{approx}}}(x) + \varpi_{3b}(x). \tag{9.76}$$

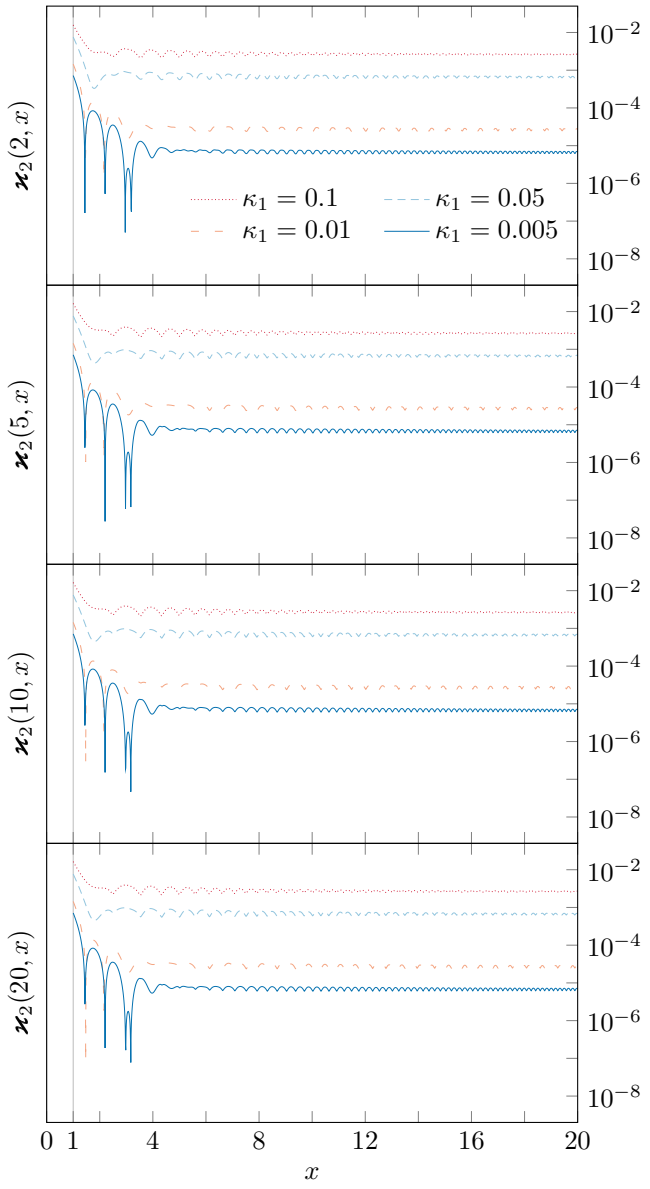

Fig. 9.10 Graphical demonstration of the validity of solution (9.68) for different number of modes. Here the coefficients $\{\kappa_n\}$ follow the power law $\kappa_1/n^{2.5}$. The fractional errors scale with the value of the primary resonance modification κ_1. Figure appeared in [1].

We also calculate the asymptotic expression for $\varpi_{3a}(x)$, by expanding the Fresnel function for $|x| \gg 1$, the solution is given by eq. (9.86). The additive constant accounting for the value of the integral at the origin is

$$\begin{aligned}\alpha = &\mp 0.00991\cos^3(\delta\chi) \pm 0.08018\cos^2(\delta\chi)\sin(\delta\chi) \\ &\mp 0.00185\cos(\delta\chi)\sin^2(\delta\chi) \pm 0.03110\sin^3(\delta\chi)\end{aligned} \tag{9.77}$$

The asymptotic expression for $\varpi_3(x)$ can be written as

$$\varpi_3(x) = \alpha + \varpi_{3a_{\text{asymp}}}(x) + \varpi_{3b}(x). \tag{9.78}$$

The validity of these solutions can be demonstrated in an analogous way to the zero-phase case, by computing:

$$\varkappa_{n+1} = \left| \frac{\omega_{\text{num}} - \omega^{(n)}(x)}{\omega_{\text{num}}} \right|, \tag{9.79}$$

where $\omega^{(n)}(x)$ is the solution to eq. (9.69) for $|x| \ll 1$, and ω_{num} is the respective numerical solution. Plots of these functions for $n = 0, \ldots, 3$ are given in Figure 9.12. No further calculations are needed to find the constants $\{b_i, c_1, c_2, c_3, d_1, d_2, l\}$, since we can use modified ansätze which include a phase term in their oscillating factors:

$$\mathscr{S}_n(x) \equiv \sin\left[n\Big(ax + (1+b)x^2 - \delta\chi\Big)\right] \tag{9.80a}$$

$$\mathscr{C}_n(x) \equiv \cos\left[n\Big(ax + (1+b)x^2 - \delta\chi\Big)\right]. \tag{9.80b}$$

To establish the constants $\{a_i\}$, we match the ansatz against the new (asymptotic) solution:

$$\omega(x) = \varpi_0(x) + \kappa\varpi_1(x) + \kappa^2\varpi_2(x) + \kappa^3\varpi_3(x), \tag{9.81}$$

where the last term is the combination of terms (9.78) and α is given by eq. (9.77). The three separate orders of the constant a as a function of the phase difference $\delta\chi$ are:

$$a_1 = \pm\frac{\sqrt{2\pi}}{4}\big(\cos(\delta\chi) + \sin(\delta\chi)\big) \tag{9.82a}$$

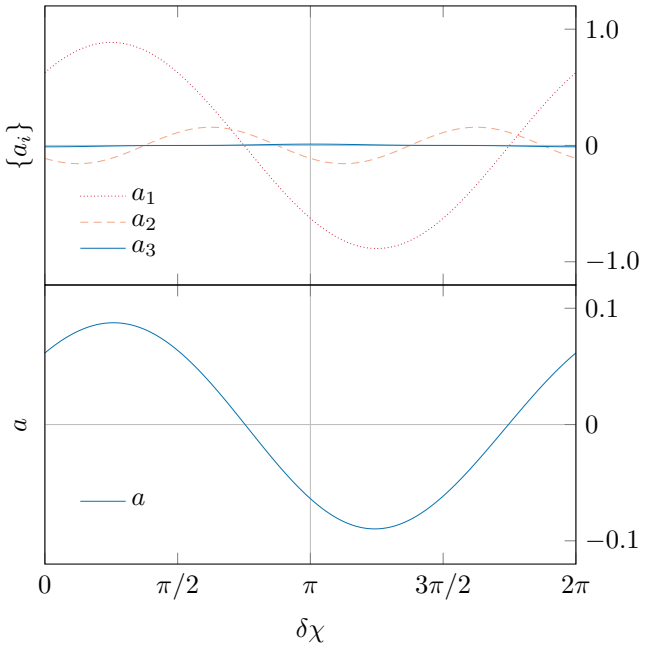

Fig. 9.11 Plot of the components of the constant a, and plot of the combined constant for $\kappa = 0.1$ as functions of $\delta\chi$. Figure appeared in [1].

$$a_2 = \mp\frac{\sqrt{\pi}}{16}\big(\cos(2\delta\chi)+\sin(2\delta\chi)\big) \tag{9.82b}$$

$$\begin{aligned} a_3 = {} & \mp 0.00991\cos^3(\delta\chi) \pm 0.08018\cos^2(\delta\chi)\sin(\delta\chi) \mp 0.00185\cos(\delta\chi)\sin^2(\delta\chi) \\ & \pm 0.03110\sin^3(\delta\chi) \pm \frac{\sqrt{2\pi}}{256}\big(\cos(3\delta\chi)-\sin(3\delta\chi)+7\cos(\delta\chi)+7\sin(\delta\chi)\big) \\ & \pm \frac{\sqrt{6\pi}}{768}\big(3\cos(3\delta\chi)+3\sin(3\delta\chi)+\cos(\delta\chi)-\sin(\delta\chi)\big) \\ & \pm \frac{\sqrt{2}\,\pi^{3/2}}{128}\big(\cos(\delta\chi)-\sin(\delta\chi)\big) \end{aligned} \tag{9.82c}$$

The constant a itself is given by

$$a = a_1\kappa + a_2\kappa^2 + a_3\kappa^3 \tag{9.83}$$

Plots of these functions are given in Figure 9.11.

$$\begin{aligned}\varpi_2(x) = \frac{\sqrt{\pi}}{2\sqrt{2}}\cos\left(x^2-\delta\chi\right)\left(\cos(\delta\chi)C\left(\frac{\sqrt{2}x}{\sqrt{\pi}}\right)+\sin(\delta\chi)S\left(\frac{\sqrt{2}x}{\sqrt{\pi}}\right)\right)\\ -\frac{\sqrt{\pi}}{8}\left(\cos(2\delta\chi)C\left(\frac{\sqrt{4}x}{\sqrt{\pi}}\right)+\sin(2\delta\chi)S\left(\frac{\sqrt{4}x}{\sqrt{\pi}}\right)\right)-\frac{x}{4}\end{aligned} \tag{9.84}$$

$$\begin{aligned}&\varpi_{3a_{\text{approx}}}(x) =\\ &=\left(33\cos^2(\delta\chi)-\frac{35}{3}\sin^2(\delta\chi)\right)\left[\frac{\sqrt{2\pi}}{64}\left(\cos(\delta\chi)C\left(\frac{\sqrt{2}x}{\sqrt{\pi}}\right)+\sin(\delta\chi)S\left(\frac{\sqrt{2}x}{\sqrt{\pi}}\right)\right)\right.\\ &\qquad\left.-\frac{1}{32}x\cos\left(x^2-\delta\chi\right)-\frac{1}{48}x^3\sin\left(x^2-\delta\chi\right)\right]\\ &\quad+\left(\frac{1}{5}\cos^2(\delta\chi)-\frac{1}{9}\sin^2(\delta\chi)\right)\left[\frac{7}{8}x^5\cos\left(x^2-\delta\chi\right)+\frac{1}{4}x^7\sin\left(x^2-\delta\chi\right)\right]\end{aligned} \tag{9.85}$$

$$\begin{aligned}\varpi_{3a_{\text{asymp}}}(x) &= \pm\frac{\sqrt{2\pi}}{32}\left(\cos^3(\delta\chi)+\sin^3(\delta\chi)\right)\ln|x|\\ &\mp\frac{\sqrt{2\pi}}{64}\sin(2\delta\chi)\left(\cos(\delta\chi)-\sin(\delta\chi)\right)\left(x^2+\frac{3}{4x^2}\right)\\ &-\frac{\sqrt{2\pi}}{64}\left(\cos^3(\delta\chi)C\left(\frac{\sqrt{2}x}{\sqrt{\pi}}\right)+\sin^3(\delta\chi)S\left(\frac{\sqrt{2}x}{\sqrt{\pi}}\right)\right)\\ &-\frac{3\sqrt{2\pi}}{128}\sin(2\delta\chi)\left(\cos(\delta\chi)S\left(\frac{\sqrt{2}x}{\sqrt{\pi}}\right)+\sin(\delta\chi)C\left(\frac{\sqrt{2}x}{\sqrt{\pi}}\right)\right)\\ &+\frac{\sqrt{2}\pi^{3/2}}{64}\left(\cos(\delta\chi)S\left(\frac{\sqrt{2}x}{\sqrt{\pi}}\right)-\sin(\delta\chi)C\left(\frac{\sqrt{2}x}{\sqrt{\pi}}\right)\right)\\ &+\frac{\sqrt{6\pi}}{192}\cos(2\delta\chi)\left(\cos(\delta\chi)C\left(\frac{\sqrt{6}x}{\sqrt{\pi}}\right)+\sin(\delta\chi)S\left(\frac{\sqrt{6}x}{\sqrt{\pi}}\right)\right)\\ &-\frac{\pi}{32}x\sin\left(x^2-\delta\chi\right)\\ &\pm\frac{\sqrt{2\pi}}{64}\left(1-\frac{1}{x^4}\right)\left(\cos^2(\delta\chi)\cos\left(2x^2-\delta\chi\right)+\sin^2(\delta\chi)\sin\left(2x^2-\delta\chi\right)\right)\end{aligned}$$

$$\pm\frac{\sqrt{2\pi}}{128}\frac{1}{x^2}\left(\cos^2(\delta\chi)\sin\left(2x^2-\delta\chi\right)-\sin^2(\delta\chi)\cos\left(2x^2-\delta\chi\right)\right)$$
$$-\frac{1}{64}\frac{1}{x^3}\cos(2\delta\chi)\left(\cos\left(x^2+\delta\chi\right)+\frac{1}{3}\cos\left(3x^2-\delta\chi\right)\right)$$
$$-\frac{5}{128}\sin(2\delta\chi)\frac{\cos\left(x^2+\delta\chi\right)}{x^5}-\frac{3}{256}\frac{1}{x^5}\cos(2\delta\chi)\left(\sin\left(3x^2-\delta\chi\right)+\sin\left(x^2+\delta\chi\right)\right) \tag{9.86}$$

$$\varpi_{3b}(x)=\frac{\sqrt{2\pi}}{32}\cos\left[2(x^2-\delta\chi)\right]\left(\cos(\delta\chi)C\left(\frac{\sqrt{2}x}{\sqrt{\pi}}\right)+\sin(\delta\chi)S\left(\frac{\sqrt{2}x}{\sqrt{\pi}}\right)\right)$$
$$-\frac{\sqrt{\pi}}{16}\cos\left(x^2-\delta\chi\right)\left(\cos(2\delta\chi)C\left(\frac{\sqrt{4}x}{\sqrt{\pi}}\right)+\sin(2\delta\chi)S\left(\frac{\sqrt{4}x}{\sqrt{\pi}}\right)\right)$$
$$+\frac{\sqrt{6\pi}}{192}\left(\cos(3\delta\chi)C\left(\frac{\sqrt{6}x}{\sqrt{\pi}}\right)+\sin(3\delta\chi)S\left(\frac{\sqrt{6}x}{\sqrt{\pi}}\right)\right)$$
$$+\frac{5\sqrt{2\pi}}{64}\left(\cos(\delta\chi)C\left(\frac{\sqrt{2}x}{\sqrt{\pi}}\right)+\sin(\delta\chi)S\left(\frac{\sqrt{2}x}{\sqrt{\pi}}\right)\right)-\frac{1}{8}x\cos\left(x^2-\delta\chi\right) \tag{9.87}$$

$$\omega_3(x)=$$
$$=\left(a_1\kappa+a_2\kappa^2+a_3\kappa^3\right)+\left(1-\frac{\kappa^2}{4}\right)x+\kappa\frac{1}{2}\frac{1}{x}\sin\left[\left(a_1\kappa+a_2\kappa^2\right)x+\left(1-\frac{\kappa^2}{4}\right)x^2-\delta\chi\right]$$
$$+\kappa^2\frac{1}{16}\frac{1}{x}\sin\left[2\left(a_1\kappa x+x^2-\delta\chi\right)\right]+\kappa^3\frac{1}{x}\left(\frac{3}{32}\sin\left(x^2-\delta\chi\right)+\frac{1}{96}\sin\left[3\left(x^2-\delta\chi\right)\right]\right)$$
$$\mp\kappa^2\frac{\sqrt{2\pi}}{16}\frac{1}{x^2}\sin\left(a_1\kappa x+x^2-\delta\chi\right)$$
$$\pm\kappa^3\left(\frac{\sqrt{\pi}}{64}\frac{1}{x^2}\sin\left(x^2-\delta\chi\right)-\frac{\sqrt{2\pi}}{64}\frac{1}{x^2}\sin\left[2\left(x^2-\delta\chi\right)\right]+\frac{\sqrt{2\pi}}{32}\ln|x|\right). \tag{9.88}$$

A more rigorous derivation of this result is presented in Appendix L.4. This paves the way for finding a solution to the general equation with an infinite number of modes.

Before we proceed with this, we check graphically the validity of solution (9.88). Figure 9.12 depicts the fractional errors $\varkappa_4(x)$ for the usual values of κ, and for 4 different values of the initial phase offset.

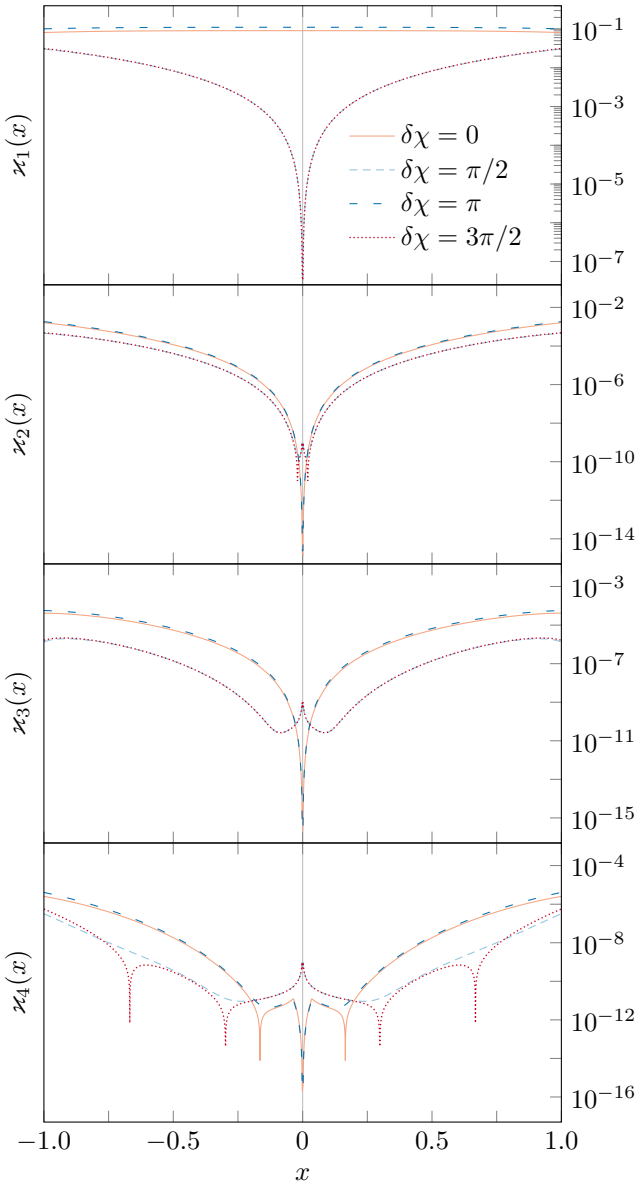

Fig. 9.12 Graphical demonstration of the validity of solutions $\varpi_0(x) = x$, (9.72), (9.84), and (9.76). In each plot we have used $\kappa = 0.1$. It is evident that the fractional errors scale with the value of the resonance modification κ, and for each order n of the solution, the remainder is of order $\mathscr{O}\left(\kappa^{n+1}\right)$. Figure appeared in [1].

Finally, we consider the multi-mode frequency equation with a non-vanishing initial phase:

$$\boldsymbol{\omega}'(x) = 1 + \sum_n \kappa_n \cos(n x_\omega \, \boldsymbol{\omega} - \delta\chi_n)\,, \tag{7.17a}$$

where the array of constants $\{\delta\chi_n\}$ is known and can in principle be computed from the constants of motion through eq. (7.14). Before proceeding, we elect to write the equation out in the following more revealing way

$$\boldsymbol{\omega}'(x) = 1 + \sum_n \kappa_n \cos(\delta\chi_n)\cos(n x_\omega \, \boldsymbol{\omega}) + \kappa_n \sin(\delta\chi_n)\sin(n x_\omega \, \boldsymbol{\omega})\,. \tag{9.89}$$

For small $|x|$, we find consecutively:

$$\boldsymbol{\varpi}_0(x) = x \tag{9.90}$$

and

$$\boldsymbol{\varpi}_{1,n}(x) = \frac{\sqrt{\pi}}{\sqrt{2n}} \left(\cos(\delta\chi_n)\, C\left(\frac{\sqrt{2n}\,x}{\sqrt{\pi}}\right) + \sin(\delta\chi_n)\, S\left(\frac{\sqrt{2n}\,x}{\sqrt{\pi}}\right)\right) \tag{9.91}$$

As before, higher-order solutions are not necessary, so we can write the solution for $|x| \ll 1$ as

$$\boldsymbol{\omega}_1(x) = \boldsymbol{\varpi}_0(x) + \sum_n \kappa^n \boldsymbol{\varpi}_{1,n}(x). \tag{9.92}$$

Next we choose an elaborate ansatz of the form:

$$\boldsymbol{\omega}_1(x) = \boldsymbol{a} + (1 + \boldsymbol{b})\, x + \sum_n \boldsymbol{c}_n \frac{\mathscr{S}_n(x)}{x} \tag{9.93}$$

where we note that we neglect terms of $\mathscr{O}\left(x^{-2}\right)$, which correspond to oscillations which die out quickly with $|x|$. The derivative of this ansatz is given by

$$\boldsymbol{\omega}_1'(x) = 1 + \boldsymbol{b} + 2\,(1 + \boldsymbol{b}) \sum_n n\, \boldsymbol{c}_n \mathscr{C}_n(x). \tag{9.94}$$

This needs to match the right-hand side of eq. (7.17a). We perform analysis similar to our earlier discussion on the zero-phase multi-mode version to find the solution (9.97). Note that

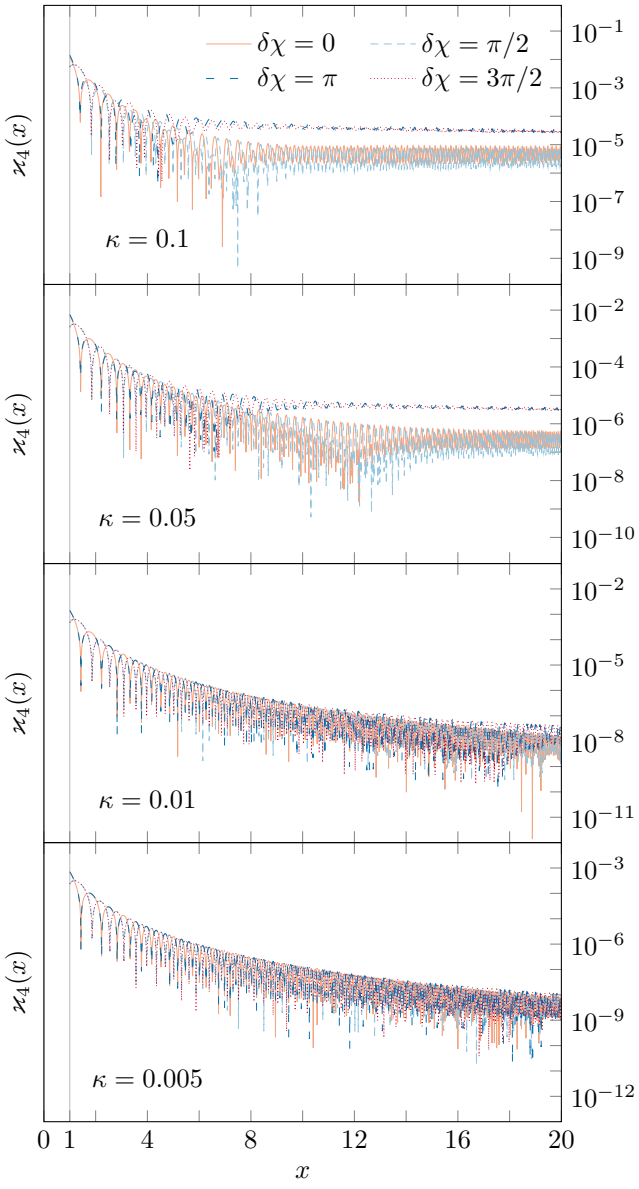

Fig. 9.13 Graphical demonstration of the validity of solution (9.88) for characteristic values of κ and for sample values of $\delta\chi$. Figure appeared in [1].

the slope correction is still zero at leading order, and we discover that the constants $\{\delta\chi_n\}$ only appear in the argument of the oscillation modes. The constant $\boldsymbol{a}$ is found by comparing the above ansatz with the $|x| \gg 1$ limit of solution (9.92).

$$\boldsymbol{a} = \pm\sum_n \kappa_n \frac{\sqrt{\pi}}{2\sqrt{2n}} \big(\cos(\delta\chi_n) + \sin(\delta\chi_n)\big) \tag{9.95}$$

Validating these solutions can be done in the same manner as earlier, by computing the quantities analogous to eq. (9.14) and eq. (9.66), but this time incorporating the phase variable into the checks. These are depicted in Figures 9.14 and L.2. For these figures, we have assumed that the phases $\{\delta\chi_n\}$ cycle the set $\{0, \pi/2, \pi, 3\pi/2\}$,

$$\delta\chi_n = \big(\delta\chi_1 + (n-1)\,\pi/2\big) \mod 2\pi \tag{9.96}$$

As before, it is very challenging to correctly determine higher-order solutions in terms of the parameters $\{\kappa_n\}$ as higher order corrections include contributions from cross-terms between modes, which significantly complicate the analysis. Instead, we will focus on the more interesting phase resonance equation, where this problem is avoided, and higher-order solutions can still be found in the multi-mode case.

$$\boldsymbol{\omega}_1(x) = \pm\sum_n \kappa_n \frac{\sqrt{\pi}}{2\sqrt{2n}} \big(\cos(\delta\chi_n) + \sin(\delta\chi_n)\big) + x + \sum_n \kappa_n \frac{1}{2n}\frac{1}{x}\sin\big(nx^2 - \delta\chi_n\big). \tag{9.97}$$

This concludes our discussion of the frequency resonance equation. We have produced a series of solutions with increasing generality, and have provided graphical evidence of their validity. We note that some results have been intentionally left to the Appendix, since they are simple extensions of less general cases presented within this Section. We can now turn our attention to the phase resonance equation and its solutions before summarising our findings in the Conclusion.

9.3 Phase resonance equation

The phase-resonance equation is derived in Section 7 and makes use of the action-angle variables $\{q_\mu\}$, instead of the fundamental frequencies $\{\omega_\mu\}$ to write down the Fourier modes of the self-force function. In the case of a multitude of modes in this expansion, as

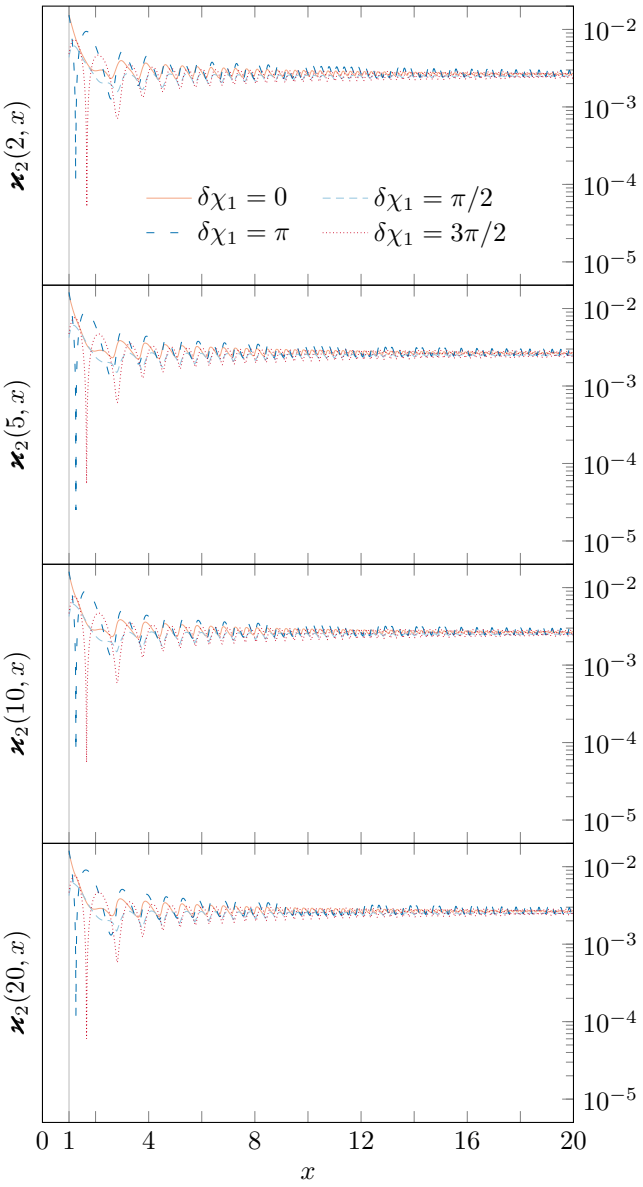

Fig. 9.14 Graphical demonstration of the validity of solution (9.97) for different number of terms on the right-hand side and for values of $\{\delta\chi_n\}$ given by eq. (9.96). In all panels we have used $\kappa_1 = 0.1$ with consecutive values given by $\kappa_n = \kappa_1/n^{2.5}$. Figure appeared in [1].

well as a non-vanishing initial phase offset, the equation takes the form

$$\phi''(x) = 1 + \sum_{n>0} \lambda_n \cos(n\phi - \delta\psi_n)\,. \tag{7.17b}$$

Similarly to our approach to the frequency resonance equation, we examine the case in which we ignore all higher-order modes beyond the first one ($n = 1$), and assume a zero initial phase, so eq. (7.17b) simplifies to

$$\phi''(x) = 1 + \lambda \cos\big(\phi(x)\big). \tag{9.98}$$

The equation is again non-linear due to the additive constant, and an analytic solution cannot be provided in the general case. Instead we employ an iterative approach to establish a series of solutions in increasing order of the mode parameter $\lambda \equiv \lambda_1 \ll 1$. At first, we ignore the term involving λ, and seek a solution to the equation:

$$\phi_0''(x) = 1 + \mathscr{O}(\lambda)\,, \tag{9.99}$$

which straightforwardly yields the zeroth-order solution to the phase resonance equation in the current regime

$$\phi_0(x) = \frac{x^2}{2}. \tag{9.100}$$

Further solutions are obtained by substituting the current solution on the right-hand side of the source equation (9.98), while on the left-hand side we include this solution plus the next-order correction. In the general case, we would need to solve the equation (for $n \geq 1$)

$$\phi_n''(x) = 1 + \lambda \cos(\phi_{n-1}(x))\,, \tag{9.101}$$

where $\phi_n(x)$ is the complete n^{th}-order solution. We apply this iterative technique to find the first-order correction: we use the function $\phi_0(x)$ as the source for the next order solution $\phi_1(x) = \phi_0(x) + \phi_{(1)}(x)$. That means we write $\phi_0(x)$ as the argument on the right-hand side, while on the left-hand side we solve for $\phi_1(x)$, a combination of the zeroth-order $\phi_0(x)$ and the first-order correction $\phi_{(1)}(x)$. Throughout our current discussion, we shall use $\phi_n(x)$ to denote the complete solution to order n, while $\phi_{(n)}(x)$ would denote the n^{th}-order correction

to $\phi_0(x)$, i.e. $\phi_n(x) = \phi_0(x) + \phi_{(n)}(x)$. Using this, we write:

$$\phi_1''(x) = \left(\phi_0 + \phi_{(1)}\right)'' = 1 + \phi_{(1)}'' = 1 + \lambda\cos(\phi_0)\,. \tag{9.102}$$

From this, we find a differential equation for $\phi_{(1)}(x)$:

$$\phi_{(1)}''(x) = \lambda\cos\left(\frac{x^2}{2}\right). \tag{9.103}$$

The details of finding this solution are described in Appendix M.1, here we only quote the final result:

$$\phi_{(1)}(x) = \lambda\left[\sqrt{\pi}\,x C\left(\frac{x}{\sqrt{\pi}}\right) - \sin\left(\frac{x^2}{2}\right)\right]. \tag{9.104}$$

Combining this with $\phi_0(x)$, we find the complete first-order-in-λ solution to eq. (9.98), given by (9.105). It is worth explaining that the solution has been rearranged into a form which is more useful for our discussion later on. More specifically, we have grouped together terms which oscillate around the value $\phi(x) = 0$ – both $(C(\bullet) \mp 1/2)$ and $\sin(\bullet)$ are such functions (see Appendix J for details about the former). Moreover, we have collected the terms proportional to x^2 and x into a single quadratic term (by completing the square, which inevitably introduces a further constant, however it is of second order in the mode parameter λ, and not relevant here). Hence the solution is comprised of a modified (shifted along the x-axis) quadratic term and a term ρ_1 which oscillates around $\phi = 0$, and whose frequency of oscillations increases with the value of x.

A number of results in this section contain the symbols "$\pm$" and "$\mp$". Similarly to the discussion of the solutions of the frequency resonance equation, these do not signify two alternative equations, but rather that the lower signs are valid for $x \leq 0$, while the upper signs hold for $x \geq 0$, both part of the same solution.

$$\begin{aligned}\phi_1(x) &= \frac{\pi}{2}\left(\frac{x}{\sqrt{\pi}} \pm \frac{1}{2}\lambda\right)^2 + \lambda\left[\pi\left(\frac{x}{\sqrt{\pi}}\right)\left(C\left(\frac{x}{\sqrt{\pi}}\right) \mp \frac{1}{2}\right) - \sin\left[\frac{\pi}{2}\left(\frac{x}{\sqrt{\pi}}\right)^2\right]\right] \\ &\equiv \frac{\pi}{2}\left(\frac{x}{\sqrt{\pi}} \pm \frac{1}{2}\lambda\right)^2 + \lambda\,\rho_1\left(\frac{x}{\sqrt{\pi}}\right).\end{aligned} \tag{9.105}$$

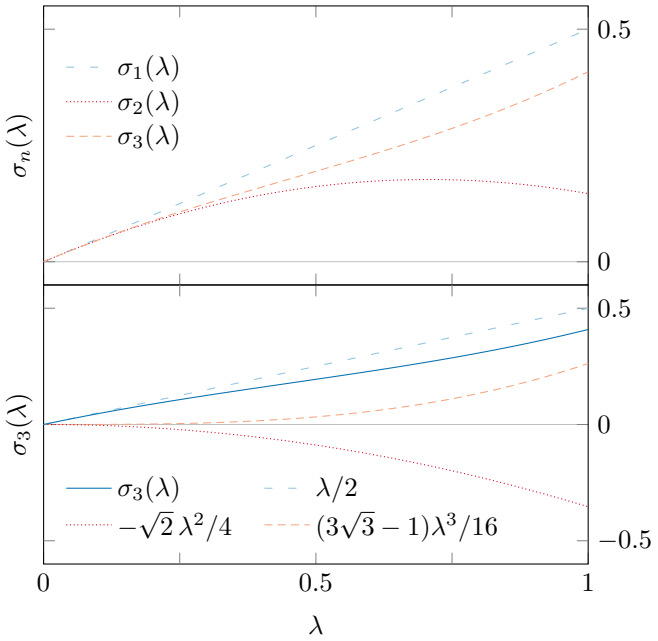

Fig. 9.15 Evolution of the slope of the phase resonance solutions. The domain of the plot shows all possible values for the mode parameter: $0 \leq \lambda \leq 1$. *Upper panel:* the evolution of the slope for all three solutions which have been calculated explicitly in the text. *Lower panel:* the individual components which make up the slope function $\sigma_3(\lambda)$. Figure appeared in [1].

It is important to note that for large values of x, the oscillating terms become small, and the approximate slope of $\phi_1(x)$ is given by $\sqrt{\pi}\,\lambda/2$. We will see later how this slope evolves when we add higher-order-in-λ terms, but for now let us denote $\sigma_1(\lambda) = \lambda/2$, which is the shift in the position of the leading parabolic term.

Applying the same iterative approach, we use the combined function $\phi_1(x)$ as the source for the second-order asymptotic solution $\phi_2(x) = \phi_0(x) + \phi_{(2)}(x)$, where the second-order correction $\phi_{(2)}(x)$ is comprised both of first- and second- order terms. This notation is convenient since $\phi_0''(x) = 1$ cancels with the constant term on the right-hand side, and upon integrating twice, we obtain an expression for $\phi_{(2)}(x)$, the complete solution to second order in λ, only without the zeroth-order quadratic term. On the right-hand side, we substitute the complete first-order solution, $\phi_1(x) = \phi_0(x) + \phi_{(1)}(x)$,

$$\phi_{(2)}''(x) = \lambda \cos\big(\phi_0 + \phi_{(1)}\big)\,. \tag{9.106}$$

In fact, from eqs. (9.103) and (9.106) we can infer the general form of this differential equation (for $n > 1$):

$$\begin{aligned}\phi''_{(n)}(x) &= (\phi_n - \phi_0)''(x) = \\ &= \lambda \cos(\phi_{n-1}) = \lambda \cos\big(\phi_0 + \phi_{(n-1)}\big)\,.\end{aligned} \tag{9.107}$$

The details involved in solving eq. (9.106) are presented in Appendix M.1, together with the full-form solution. Here, we omit these details, and simply quote the final combined result $\phi_2(x) = \phi_0(x) + \phi_{(2)}(x)$ in the form of a modified quadratic term, plus two terms, both of them $\mathscr{O}\big(\lambda^2\big)$ that oscillate and remain small for all x.

$$\phi_2(x) = \frac{\pi}{2}\left(\frac{x}{\sqrt{\pi}} \pm \left[\frac{1}{2}\lambda - \frac{\sqrt{2}}{4}\lambda^2\right]\right)^2 + \lambda\,\rho_1\!\left(\frac{x}{\sqrt{\pi}} \pm \sigma_1(\lambda)\right) + \lambda^2\rho_2\!\left(\frac{x}{\sqrt{\pi}}\right). \tag{9.108}$$

We note some interesting features of this solution. Most notably, the shift in the quadratic x term has changed from $\sigma_1(\lambda) = \lambda/2$ to $\sigma_2(\lambda) = \lambda/2 - \sqrt{2}\,\lambda^2/4$ (and the slope for large $|x|$ has changed from $\sqrt{\pi}\,\sigma_1(\lambda)$ to $\sqrt{\pi}\,\sigma_2(\lambda)$. The term which is proportional to λ has the same functional form as the corresponding term in solution (9.105), however we see that in (9.108) each instance of $x/\sqrt{\pi}$ has been modified by exactly $\pm\sigma_1(\lambda)$. We also have a new class of terms, all of which also oscillate around the x-axis, and they are proportional to λ^2. We will investigate the numerical performance of these solutions after we explore the next-order solution.

The solutions presented in [130] do not continue further than this order. Since our goal is to solve the multi-mode equation (7.17b), as a form of sanity check, we would like to present the solution to third order in the single-mode parameter λ, i.e. the solution to the following generating equation:

$$\phi_3''(x) = 1 + \lambda\cos\big(\phi_2(x)\big) \tag{9.109}$$

The solution follows via the same technique as the previous two, and again it is not practical to present the details of the derivation here. Instead, the reader is invited to consult Appendix M.1 for the technicalities of the calculation as well as the full solution without abbreviations. With every successive iteration we obtain new terms, and we have grouped them together in a similar fashion to before. Here we have terms which are proportional to λ^3, as well as modified terms, originating from the lower-order solutions. The result (9.110) is the complete solution to third order, for a single mode with amplitude λ, with vanishing

initial phase $\delta\psi = 0$.

$$\begin{aligned}\phi_3(x) = \frac{\pi}{2}\left(\frac{x}{\sqrt{\pi}} \pm \left[\frac{1}{2}\lambda - \frac{\sqrt{2}}{4}\lambda^2 + \frac{3\sqrt{3}-1}{16}\lambda^3\right]\right)^2 + \lambda\,\rho_1\left(\frac{x}{\sqrt{\pi}} \pm \sigma_2(\lambda)\right) \\ + \lambda^2\rho_2\left(\frac{x}{\sqrt{\pi}} \pm \sigma_1(\lambda)\right) + \lambda^3\rho_3\left(\frac{x}{\sqrt{\pi}}\right)\end{aligned} \tag{9.110}$$

In (9.110), the x-shift of the quadratic term is now

$$\sigma_3(\lambda) = \frac{1}{2}\lambda - \frac{\sqrt{2}}{4}\lambda^2 + \frac{3\sqrt{3}-1}{16}\lambda^3, \tag{9.111}$$

and consequently, the slope of the graph for large x is given by $\sqrt{\pi}\,\sigma_3(\lambda)$. In fact [130] numerically computed the change in the slope of the phase solution at λ^3 order:

$$\phi_3'(x) \sim \frac{\sqrt{\pi}}{2}\lambda - \frac{\sqrt{\pi}}{2\sqrt{2}}\lambda^2 + 0.4648\,\lambda^3 + \mathscr{O}\left(\lambda^4\right). \tag{9.112}$$

As a form of consistency check, we can directly compare this with the (analytically derived) factor multiplying the λ^3 term in the coefficient of x in eq. (9.110) and confirm that both numerical values agree:

$$\sqrt{\pi} \times \frac{3\sqrt{3}-1}{16}\lambda^3 \approx 0.4648\,\lambda^3. \tag{9.113}$$

Moreover, we can notice a parallel between the terms proportional to λ in each of (9.105) — (9.110): all three brackets have the same dependence on x, meaning that for $\lambda = 0$, they would be equal. However, in each of them, each instance of $x/\sqrt{\pi}$ is modified by a different function of the mode parameter λ. Compared to (9.105), each $x/\sqrt{\pi}$ in (9.108) is shifted by $\pm\sigma_1(\lambda)$, and in (9.110), it is shifted by $\pm\sigma_2(\lambda)$. Similar evolution can be noticed in the terms proportional to λ^2 in (9.108) and (9.110). In the latter, each instance of a term involving x is shifted by $\sigma_1(\lambda)$ compared to the former. While it is hard to predict what terms at higher order would look like, because the x-dependence cannot be inferred from the first three solutions, we can nevertheless expect that at fourth order, the term proportional to λ^3 would look similar to its counterpart in (9.110), with each $x/\sqrt{\pi}$ term modified by $\pm\sigma_1(\lambda)$, and so on. It is evident that the functions $\sigma_n(\lambda)$ play an important role in the phase resonance solutions, and at least in the evolution of the slope of the graph for large $|x|$. In Figure 9.15, we plot these functions and present what they look like for different values of λ.

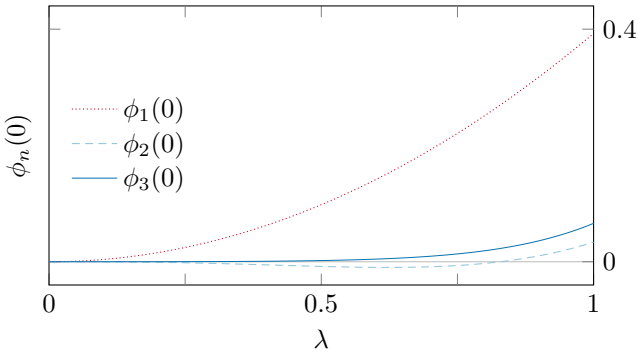

Fig. 9.16 Plot of the functions $\phi_{\{1,2,3\}}(0)$ as functions of λ. Figure appeared in [1].

Let us investigate the properties of solutions (9.100) — (9.110): each of them contains a quadratic term of the form $\pi/2\,(x/\sqrt{\pi}\pm\sigma_i)^2$. Since the magnitudes of the rest of the terms in each solution scale with λ^n, the functions look similar when plotted together, as can be seen in Figure M.3. It is hard to distinguish them in this plot, unless we zoom in closely on a region. For example, if we focus on the region around $x=0$ we see that while $\phi_0(x)=x^2/2$ goes through the origin, the rest of the solutions deviate slightly from zero. This is due to the fact that a perturbative solution of order n is only approximate, and is correct up to a remainder of $\mathscr{O}\left(\lambda^{n+1}\right)$. Indeed, if we consider each solution $\phi_{\{1,2,3\}}(x)$ for $x=0$:

$$\begin{aligned}
\phi_1(0) &= \frac{\pi}{8}\lambda^2,\\
\phi_2(0) &= \pi\left(\frac{1-\sqrt{2}}{8}\lambda^3+\frac{1}{16}\lambda^4\right),\\
\phi_3(0) &= \pi\left(\frac{3\sqrt{3}-4\sqrt{2}+1}{32}\lambda^4-\frac{3\sqrt{6}-4-\sqrt{2}}{64}\lambda^5+\frac{28-6\sqrt{3}}{512}\lambda^6\right)
\end{aligned}$$

we find that they are indeed of the expected order in each case (see Figure 9.16 for a plot of these functions). These expressions have further higher order corrections coming from sub-leading order terms in the expansion of Fresnel cosine integrals (see eq. (J.4b) in Appendix J). Since these solutions are hard to examine graphically, we need to employ other techniques to compare the accuracy of the solutions. Specifically, we compare them with a purely numerical solution of the phase equation.

A simple plot like the lower one in Fig. M.3 shows that our highest-order solution, eq. (9.110), does indeed compare well — within $\mathscr{O}\left(\lambda^4\right)$ — to a purely numerical solution [140]. We need to quantify the comparison between this numerical solution and our analytical solutions as the mode parameter λ varies.

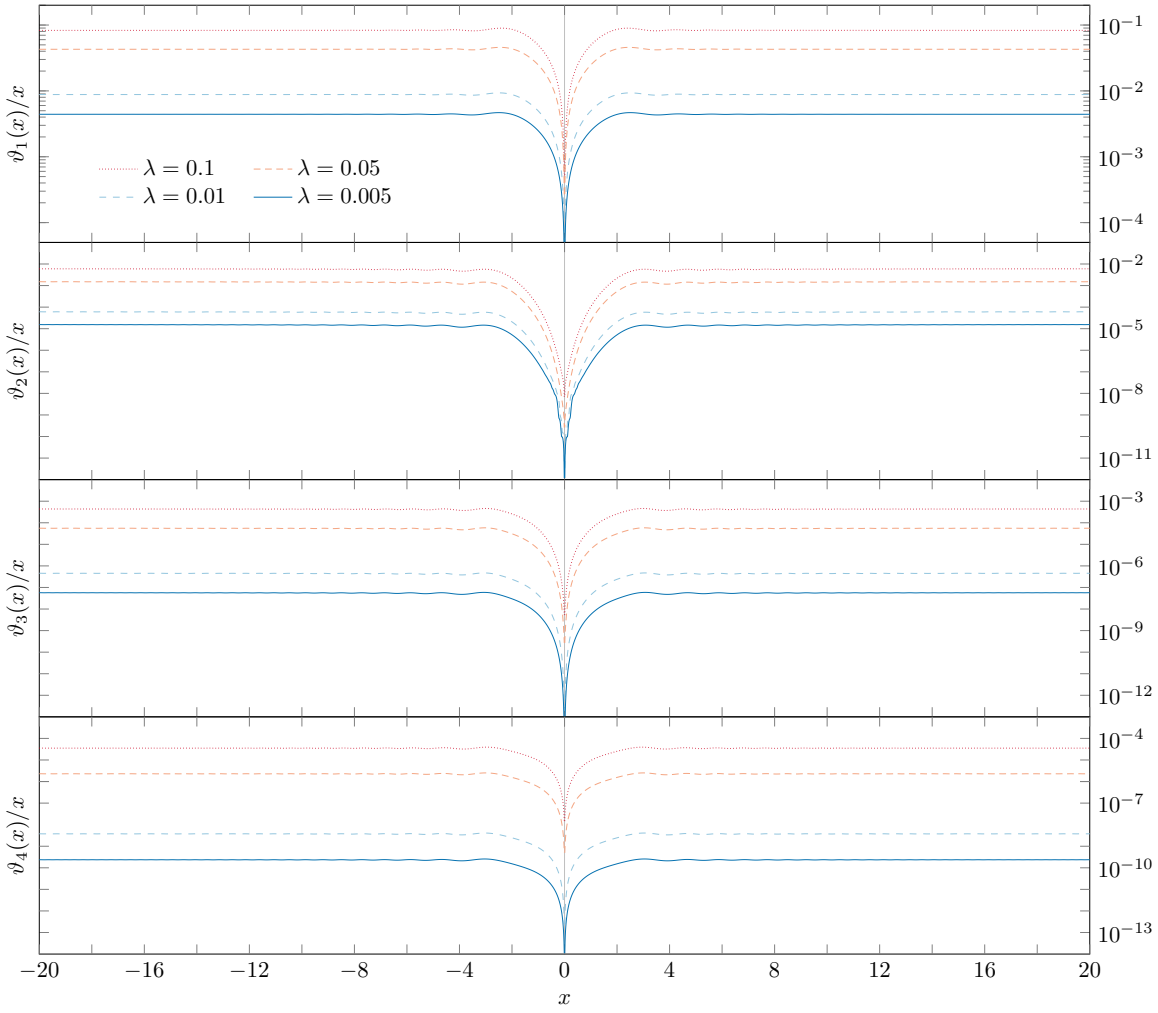

Fig. 9.17 Graphical demonstration of the validity of the phase resonance solution for 4 different values of the parameter λ. The remainders $\{\vartheta_n(x)\}$ are normalised by x in order to remove the linear trend. It is evident that the remainders scale with the value of the resonance modification λ, and for each order n of the solution, the remainder is of order $\mathscr{O}\left(\lambda^{n+1}\right)$. Figure appeared in [1].

It is important to demonstrate that each of the corrections $\phi_{(n)}(x)$ appropriately captures all of the behaviour of the solution up to order $\mathscr{O}(\lambda^n)$, i.e., that the difference between the full numerical solution $\phi_{\text{num}}(x)$ and the correction is of order $\mathscr{O}\left(\lambda^{n+1}\right)$ at most. To do this, we employ a technique that allows us to solve numerically for that difference (instead of naively subtracting each analytical solution from the numerical map, which results in worse numerical solutions). Consider eq. (9.98) which is our initial source equation:

$$\phi''(x) = 1 + \lambda \cos\big(\phi(x)\big). \tag{9.98}$$

As per our recipe, we would substitute the highest-known-order solution $\phi_n(x)$ on the right-hand side, and solve the equation for the next-order solution $\phi_{n+1}(x)$. In reality, the solution we are looking for appears on either side of the equation, and furthermore the functions $\phi(x)$ also contain the orders beyond n which we have so far been ignoring in eqs. (9.101) and (9.107):

$$\phi(x) = \phi_0(x) + \phi_{(n)}(x) + \vartheta_{n+1}(x). \tag{9.114}$$

Here, $\phi_0(x) = x^2/2$ and $\phi_{(n)}(x)$ is the correction to ϕ_0. $\vartheta_{n+1}(x)$ is the remainder of the complete solution which is not included into $\phi_n(x)$. We can easily find a generic equation satisfied by the functions $\vartheta_{n+1}(x)$ by using expression (9.114) in eq. (9.98) and making use of eq. (9.98). In general, $\vartheta_{n+1}(x)$ satisfies the differential equation

$$\vartheta''_{n+1}(x) = \lambda \cos(\phi_n + \vartheta_{n+1}(x)) - \phi''_{(n)}(x). \tag{9.115}$$

For $n = 0$ we can find directly from the source equation

$$\vartheta''_1(x) = \lambda \cos(\phi_0(x) + \vartheta_1(x)). \tag{9.116}$$

By solving for $\vartheta_{n+1}(x)$ and confirming that the result is $\mathscr{O}\left(\lambda^{n+1}\right) \forall x$ we verify that $\phi_n(x)$ capture the complete $\mathscr{O}(\lambda^n)$ behaviour. The plots for $\vartheta_n(x)/x$ (to remove the expected linear-in-x general trend) are shown in Figure 9.17, where we have performed the computation for 4 distinct values of λ: $0.1, 0.05, 0.01$, and 0.005.

The corrections $\phi_{(n)}(x)$ themselves are plotted (for $\lambda^{(1)} = 0.1$) in Figure M.4, found in the Appendix. Similarly, plots of the oscillating functions $\rho_1(x)$, $\rho_2(x)$, and $\rho_3(x)$ can be found in Figures M.5, M.6, and M.7, respectively, with other relevant discussions in Appendix M.2.

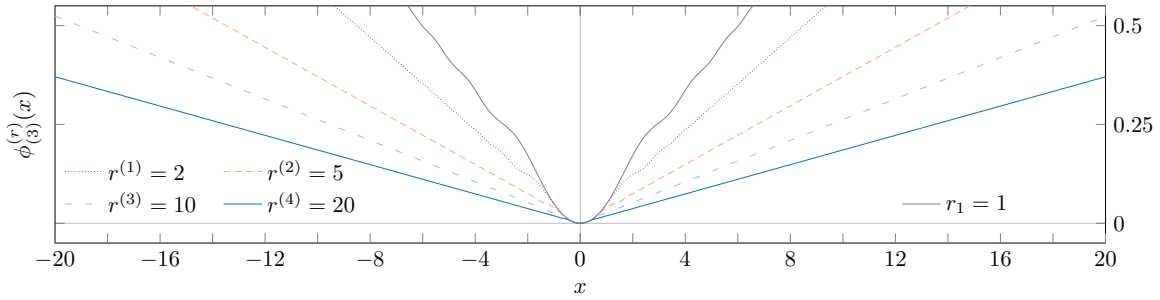

Fig. 9.18 The third-order correction to the phase resonance equation for different values of the mode number r. These solutions all have mode parameters $\lambda_r = 0.1$, so the graph only reflects the effect which the number of the mode has on the solution. Figure appeared in [1].

Before moving on to the case of multiple modes, it is intriguing to look into several other toy models. So far we have only looked at the resonance equation with a single mode $n = 1$. We now consider the same equation, but with the sole mode $n = r$ on the right-hand side. The leading-order solution is still (9.100).

$$\left(\phi^{(r)}(x)\right)'' = 1 + \lambda_r \cos(r\phi)\,. \tag{9.117}$$

The explicit solution of the above equation is redundant, since it can be obtained from eq. (9.98) by setting

$$\phi \;\mapsto\; \phi^{(r)} = r\phi, \tag{9.118a}$$

$$x \;\mapsto\; \sqrt{r}x. \tag{9.118b}$$

and therefore its corrections could be obtained from eqs. (9.105) – (9.110) by applying these transformations. The explicit form of the solutions is presented in Appendix M.3. In Figure 9.18 we show these solutions (at third order, i.e. complete) for different values of the mode number r. The modified σ-terms are presented in Figure M.8, while the numerical validation of these solutions can be found in Figure M.9.

Another toy model which deserves attention is the case of two distinct modes on the right-hand side:

$$\left(\phi^{(r,s)}(x)\right)'' = 1 + \lambda_r \cos(r\phi) + \lambda_s \cos(s\phi)\,. \tag{9.119}$$

The leading-order solution is unchanged, while the higher-order corrections are presented in Appendix M.4. We note that at first order, the correction is just the sum of the corrections due to each of the separate oscillating modes on the right-hand side. This, however, is not the

case at higher order, where cross-terms appear. It is important to note that these cross-terms are not sub-leading to the other quadratic terms in the solution. This is in contrast to the frequency-resonance equation, where these cross-terms were sub-leading in this respect (see Appendix L.3). In Figure M.10 we can examine the σ-terms associated with this equation, while the validity of the solutions is presented in Figure M.11.

Our objective in this and subsequent Chapters is to extend this approach beyond the scope which has been developed thus far. So far we have explored the solution to third order in the mode parameter. However, we are still limited to the case of a single mode, and we are assuming that the initial phase is $\phi(0) = 0$. We now relax the first of these restrictions and allow for an infinite number of oscillating modes, each with a distinct parameter λ_i. This is achieved through allowing for multiple modes in the Fourier expansion, thus lifting the assumption that the contribution derives primarily from the first Fourier mode.

We derived the phase resonance equation in Section 7. In the regime of an unrestricted number of oscillating modes, still assuming that the initial phase is 0, the form of the phase resonance equation is given by ($\boldsymbol{\phi}(x)$ denotes a solution to the multimode equation)

$$\boldsymbol{\phi}''(x) = 1 + \sum_n \lambda_n \cos(n\boldsymbol{\phi}) \tag{9.120}$$

Similar to the previous equation under consideration, this is a second order non-linear differential equation, and therefore finding an exact solution is not possible, and a perturbative solution quickly grows to become heavily involved. For brevity, here we only present the final solutions, while details about the solutions and relevant discussion are collected in Appendix M. At zero'th order in the mode parameters $\{\lambda_n\}$, we ignore any oscillating terms on the right-hand side, and the resulting differential equation is identical to that in the single-mode case, eq. (9.99); the solution is obtained by integrating twice:

$$\boldsymbol{\phi}_0'' = 1 \quad \Leftrightarrow \quad \boldsymbol{\phi}_0(x) = \frac{x^2}{2} \tag{9.121}$$

Building onto this result, we construct the equivalent to eq. (9.101), which in the multi-mode case is now given by

$$\boldsymbol{\phi}_{m+1}''(x) = 1 + \sum_n \lambda_n \cos\left(n\,\boldsymbol{\phi}_m(x)\right). \tag{9.122}$$

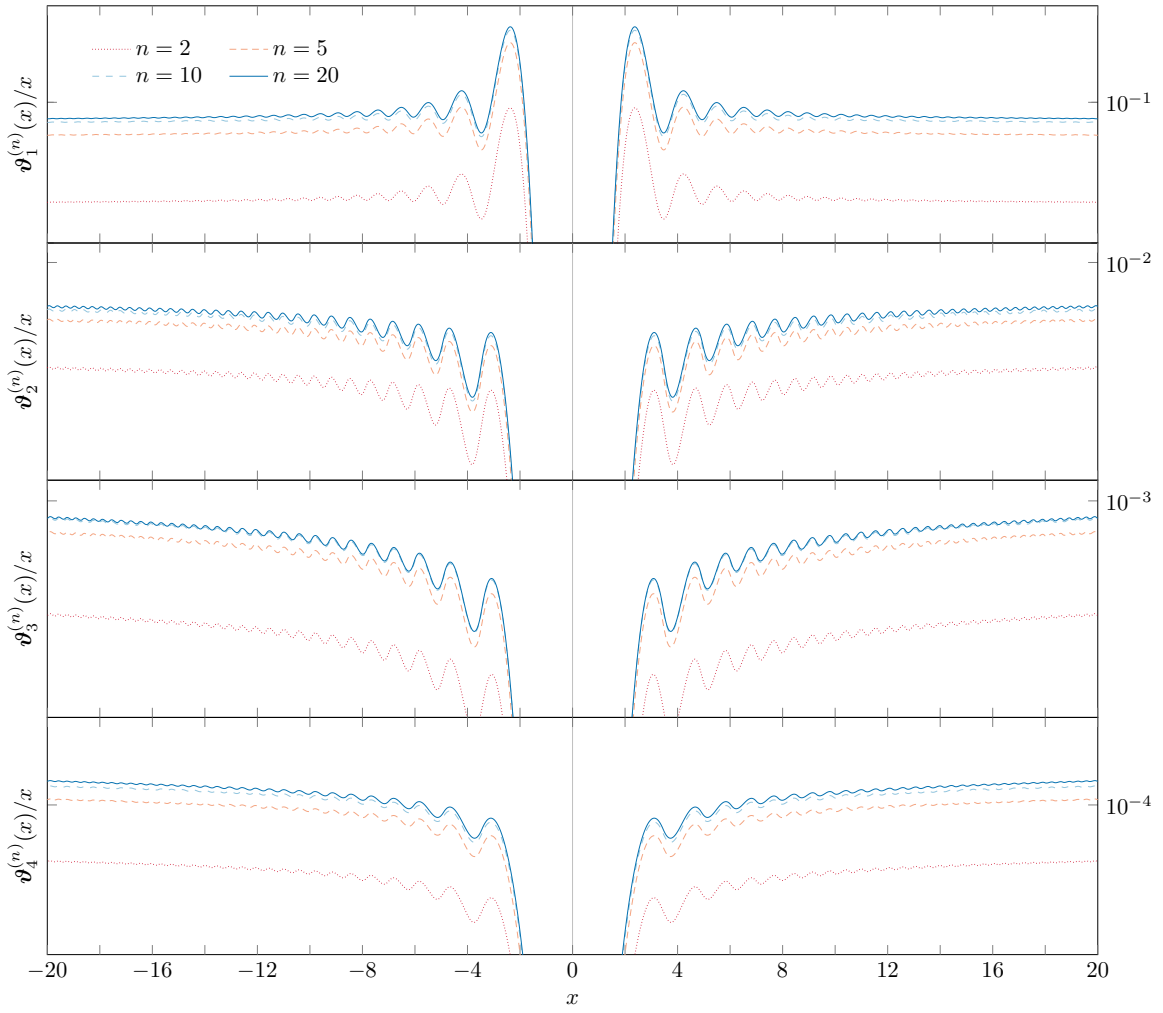

Fig. 9.19 Graphical demonstration of the validity of solutions (9.121), (9.124), (M.53), and (M.55). All these solutions are for $\lambda_1 = 0.1$, but include numbers of modes. The λ parameters follow the law $\lambda_n = \lambda_1/n^{2.5}$. Figure appeared in [1].

We will solve this consecutively for $m = 0, 1$ and 2, and we will obtain the respective solutions to the phase resonance equation for the multi-mode case. At first instance, we use $\boldsymbol{\phi}_0(x) = x^2/2$ as the argument of the trigonometric function on the right-hand side, and investigate the solution to this equation to first order in $\{\lambda_n\}$, which will yield the first-order correction $\boldsymbol{\phi}_{(1)}(x)$:

$$\boldsymbol{\phi}''_{(1)}(x) = \sum_n \lambda_n \cos\left(n\boldsymbol{\phi}_0\right) \tag{9.123}$$

The details of finding the first-order correction can be found in Appendix M.5. Combining $\boldsymbol{\phi}_{(1)}(x)$ with (9.121), we establish the complete first-order solution.

$$\boldsymbol{\phi}_1(x) = \frac{\pi}{2}\left(\frac{x}{\sqrt{\pi}} \pm \frac{1}{2}\sum_n \frac{\lambda_n}{\sqrt{n}}\right)^2 + \sum_n \frac{\lambda_n}{n}\boldsymbol{\rho}_1^n\left(\frac{x}{\sqrt{\pi}}\right). \tag{9.124}$$

Here $\boldsymbol{\rho}_1^n(x)$ is an oscillating term proportional to $|\lambda|$, equivalent to $\rho_1(x)$, and given explicitly in the Appendix. Compared to (9.121), eq. (9.124) has a modified quadratic term and a part which oscillates around 0 for all x.

We apply the same technique to find the second-order solution, namely $\boldsymbol{\phi}_{(2)}(x)$, which contains terms that are quadratic in the parameters $\{\lambda_n\}$. Similarly to previous iterations, we use the current highest-order solution $\boldsymbol{\phi}_1(x)$ to establish a differential equation for $\boldsymbol{\phi}_{(2)}(x)$. The differential equation we want to solve is given by

$$\boldsymbol{\phi}''_{(2)}(x) = \sum_n \lambda_n \cos\left(n\,\boldsymbol{\phi}_1(x)\right) \tag{9.125}$$

We should remark again that the solution of this equation would yield $\boldsymbol{\phi}_{(2)}(x)$, the second-order correction to the quadratic solution. It will contain terms which are first-order in the mode parameters, as well as other terms which are of second order. This is an artefact of the method we use for asymptotically establishing higher-order corrections to our source equation. In practice, we need to solve the equation

$$\boldsymbol{\phi}''_{(2)}(x) = \sum_n \lambda_n \cos\left(n\left(\boldsymbol{\phi}_0(x) + \boldsymbol{\phi}_{(1)}(x)\right)\right) \tag{9.126}$$

Then, by adding the zero'th order part $\boldsymbol{\phi}_0(x)$ to the solution of eq. (9.126) we will obtain the complete solution to second order in $\{\lambda_n\}$. Solving this equation is rather involved, therefore it is better to leave the practicalities of obtaining the solution to Appendix M.5. Here we only

present the final solution:

$$\begin{aligned}\boldsymbol{\phi}_2(x) = \frac{\pi}{2}\Bigg(\frac{x}{\sqrt{\pi}} \pm \Bigg[\frac{1}{2}\sum_n \frac{\lambda_n}{\sqrt{n}} + \sum_{n,m}\frac{1}{8}\left(|n-m|^{3/2} - (n+m)^{3/2}\right)\frac{\lambda_n}{n}\frac{\lambda_m}{m}\Bigg]\Bigg)^2 \\ + \sum_n \frac{\lambda_n}{n}\boldsymbol{\rho}_1^n\left(\frac{x}{\sqrt{\pi}} \pm \boldsymbol{\sigma}_1\right) + \sum_{n,m}\frac{\lambda_n}{\sqrt{n}}\frac{\lambda_m}{\sqrt{m}}\boldsymbol{\rho}_2^{nm}\left(\frac{x}{\sqrt{\pi}}\right)\end{aligned} \tag{9.127}$$

While the solution to second order is already quite involved, we continued our calculations and derived the solution to third order, so we can draw a comparison with the single-mode result eq. (9.110). The generating equation involves the new correction $\boldsymbol{\phi}_{(3)}(x)$ on the left-hand side, and the current solution, $\boldsymbol{\phi}_2(x)$ as the argument on the right-hand side:

$$\boldsymbol{\phi}''_{(3)}(x) = \sum_n \lambda_n \cos\left(n\,\boldsymbol{\phi}_2(x)\right). \tag{9.128}$$

The solution is rather long, and hence we have placed it, together with explanations, in Appendix M.5. The correction at third order is given by eq. (M.55).

After having derived these solutions, it is important to verify their validity numerically, using the same method as in the single-mode case. The results from this verification are presented in Figure 9.19, where we have shown that the equation is valid for several different values of the total number of modes. To depict the effect a larger number of modes has on the solution, we have used the same initial value of the resonant flux modification λ.

So far we have solved the single- and multi-mode equations up to third order in the parameters $\{\lambda_n\}$. It is important to carefully consider these solutions we have obtained thus far, and evaluate the need for further iterations. Let us investigate the governing equation

$$\boldsymbol{\phi}''(x) = 1 + \sum_n \lambda_n \cos\left(n\boldsymbol{\phi}\right) \tag{9.120}$$

and consider those terms for which the small-angle approximation for the trigonometric functions breaks down:

$$\cos\left[n\left(\frac{x^2}{2} + \boldsymbol{\phi}_{(i)}(x)\right)\right],\ \boldsymbol{\phi}_{(i)} = \sum_m \frac{\lambda_m}{m}(\bullet) + \dots. \tag{9.129}$$

This occurs when $n\,\lambda_1 \sim 1$. Therefore, we need to impose a restriction on the upper bound of n:

$$\bar{n}\,\lambda_1 \ll 1 \quad \Leftrightarrow \quad \bar{n} \ll \lambda_1^{-1}. \tag{9.130}$$

Although the cross-term corrections here are of the same magnitude as the single-mode solutions, the bound is comparable to that in the frequency equation (cf. eq. (9.62)). We invoke the coefficient scaling law which we discussed in Section 9.1 to link this to values of λ_1:

$$\lambda_{\bar{n}} = \frac{\lambda_1}{\bar{n}^\alpha} \sim \lambda_1^{1+\alpha} < \lambda_1^3 \tag{9.131}$$

for the suggested values of $2 < \alpha < 3$ [108]. We can therefore argue that beyond that order, we would not be able to distinguish our solutions, valid in the regime where the small-angle approximation can be applied, from effects which arise from the violation of this assumption. For this reason, higher-order corrections cannot be easily calculated without restricting the total number of modes n. Finally, proceeding beyond third order is pointless since for the range of values we are investigating, $\lambda^3 \sim \varepsilon^{1/2} \sim \mathscr{O}\big(10^{-3}\big)$, hence in calculating further corrections we need to account for terms arising from higher-order mass-ratio corrections. In this dissertation, I only investigate solutions up to third order inclusive, and disregard higher-order corrections.

We now return to the original differential equation (7.17b), and again consider a single mode, however this time we allow for a non-vanishing initial phase $\delta\psi \neq 0$

$$\varphi''(x) = 1 + \lambda \cos\big(\varphi(x) - \delta\psi\big). \tag{9.132}$$

The zero'th-order solution, when we ignore the term proportional to λ on the right-hand side, is again given by $\varphi_0(x) = x^2/2$. To establish first- and higher-order corrections, we proceed according to the same procedure as before, solving equations of the form:

$$\varphi''_{(n+1)}(x) = \lambda \cos\big(\varphi_n(x) - \delta\psi\big). \tag{9.133}$$

Using this, we find the first-order solution below.

$$\varphi_1(x) = \frac{\pi}{2}\left(\frac{x}{\sqrt{\pi}} \pm \frac{1}{2}\big(\cos(\delta\psi) + \sin(\delta\psi)\big)\lambda\right)^2 + \lambda\,\rho_1\left(\frac{x}{\sqrt{\pi}}\right) \tag{9.134}$$

We notice that the new slope $\varsigma_1(\lambda)$ involves the constant $\delta\psi$, and that the oscillating term ρ_1 has a different form, now involving a Fresnel sine term too. They reduce to their zero-phase counterparts for $\delta\psi = 0$. Following our established algorithm, we can easily derive the second- and third-order corrections to $\varphi_0(x)$. Details of these derivations are left to

Appendix M.5, here we only present the final results.

$$\varphi_2(x) = \frac{\pi}{2}\left(\frac{x}{\sqrt{\pi}} \pm \left[\frac{1}{2}\big(\cos(\delta\psi)+\sin(\delta\psi)\big)\lambda \right.\right.$$
$$\left.\left. - \left(\frac{\sqrt{2}}{4}\big(\cos(2\delta\psi)+\sin(2\delta\psi)\big) - \frac{1}{2}\sin(\delta\psi)\big(\cos(\delta\psi)-\sin(\delta\psi)\big)\right)\lambda^2\right]\right)^2$$
$$+\lambda\,\rho_1\left(\frac{x}{\sqrt{\pi}} \pm \varsigma_1(\lambda)\right) + \lambda^2\rho_2\left(\frac{x}{\sqrt{\pi}}\right) \tag{9.135}$$

$$\varphi_3(x) = \frac{\pi}{2}\left(\frac{x}{\sqrt{\pi}} \pm \left[\frac{1}{2}\big(\cos(\delta\psi)+\sin(\delta\psi)\big)\lambda \right.\right.$$
$$- \left(\frac{\sqrt{2}}{4}\big(\cos(2\delta\psi)+\sin(2\delta\psi)\big) - \frac{1}{2}\sin(\delta\psi)\big(\cos(\delta\psi)-\sin(\delta\psi)\big)\right)\lambda^2$$
$$+ \left(\frac{3\sqrt{3}}{16}\big(\cos(3\delta\psi)+\sin(3\delta\psi)\big) - \frac{\sqrt{2}}{2}\sin(\delta\psi)\big(\cos(2\delta\psi)-\sin(2\delta\psi)\big)\right.$$
$$\left.\left.\left. - \frac{3}{16}\big(\cos(\delta\psi)+\sin(\delta\psi)\big) + \frac{1}{8}\cos(2\delta\psi)\big(\cos(\delta\psi)+\sin(\delta\psi)\big)\right)\lambda^3\right]\right)^2$$
$$+\lambda\,\rho_1\left(\frac{x}{\sqrt{\pi}} \pm \varsigma_2(\lambda)\right) + \lambda^2\rho_2\left(\frac{x}{\sqrt{\pi}} \pm \varsigma_1(\lambda)\right) + \lambda^3\rho_3\left(\frac{x}{\sqrt{\pi}}\right) \tag{9.136}$$

It is important to investigate how the slope of these solutions evolves with $\delta\psi$. At each order we encounter a different function of the initial phase. Figure 9.20 shows how these functions behave over the range of $\delta\psi$. Furthermore, we need to verify that these solutions are valid for different values of the initial phase. We computed the quantities $\vartheta_n(x)$ for different values of the initial phase (keeping λ constant) using the same method as before, and show the results in Figure 9.21.

Finally, we approach the phase resonance equation in the most general regime: including an infinite number of modes each with a different non-zero phase:

$$\boldsymbol{\varphi}''(x) = 1 + \sum_{n>1} \lambda_n \cos\big(n\boldsymbol{\varphi}(x) - \delta\psi_n\big). \tag{7.17b}$$

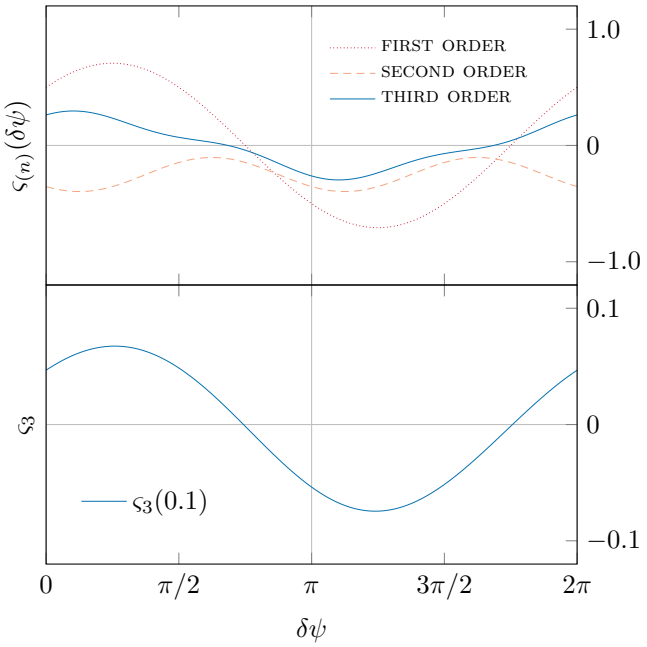

Fig. 9.20 *Upper panel:* plots of the functions (of $\delta\psi$) proportional to λ, λ^2 and λ^3 in the slope of solution (9.136). *Lower panel:* plot of the slope $\varsigma_3(\lambda)$ as a function of $\delta\psi$ for $\lambda = 0.1$. Figure appeared in [1].

The details of the solution are too lengthy to be presented in enough detail here and can be found in Appendix M.7: the first-order correction is given by eq. (M.61) and the second-order correction by eq. (M.62). Upon closer examination these bear the same features of our previously establishes solutions. Finally, we have established the third-order solution to this equation, $\boldsymbol{\varphi}_3(x)$. It is important to note that solution (9.137) is the most general solution to the phase resonance equation that we could find. It allows for multiple modes and a non-vanishing initial phase, and treats perturbations up to and including third order. The third-order slope function $\boldsymbol{\varsigma}_3$ is given by eq. (M.63) in Appendix M.7. Furthermore, each of the three corrections are given by eqs. (M.64), (M.65), and (M.66).

$$\begin{aligned}\boldsymbol{\varphi}_3(x) = \frac{\pi}{2}\left(\frac{x}{\sqrt{\pi}} \pm \boldsymbol{\varsigma}_3\right)^2 + \sum_n \frac{\lambda_n}{n}\boldsymbol{\rho}_1^n\left(\frac{x}{\sqrt{\pi}} \pm \boldsymbol{\varsigma}_2\right) + \sum_{n,m}\frac{\lambda_n}{\sqrt{n}}\frac{\lambda_m}{\sqrt{m}}\boldsymbol{\rho}_2^{nm}\left(\frac{x}{\sqrt{\pi}} \pm \boldsymbol{\varsigma}_1\right) \\ + \sum_{n,m,p}\lambda_n\frac{\lambda_m}{\sqrt{m}}\frac{\lambda_p}{\sqrt{p}}\boldsymbol{\rho}_3^{nmp}\left(\frac{x}{\sqrt{\pi}}\right)\end{aligned} \tag{9.137}$$

This is the final and most important result. While it is not easily usable in theoretical calculations, it could find applications in modelling resonances in new kludge waveforms, as this is not a feature currently implemented. We have provided a solution to the highest

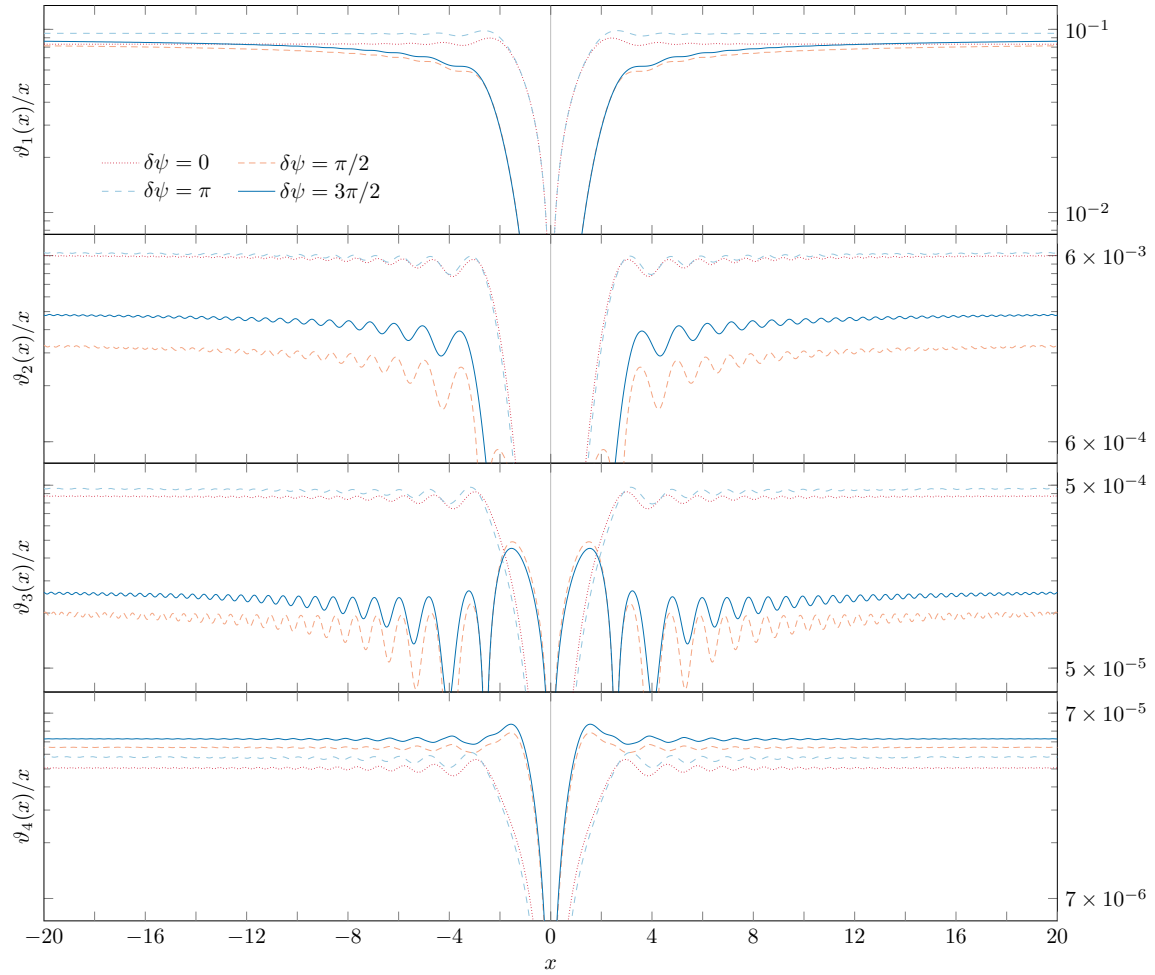

Fig. 9.21 Graphical demonstration of the validity of the solutions to the phase resonance equation with a single mode and a non-zero initial phase, eq. (9.132). All these solutions involve the same $\lambda = 0.1$, but have different initial phases $\delta\psi$. Figure appeared in [1].

possible order of perturbation, which is important for meaningful numerical simulations. Furthermore, we have also provided solutions to simplified versions of this problem, which could be employed in various theoretical calculations regarding EMRIs.

Part III

Conclusions

10

Retrospect

This Chapter combines parts of the conclusions to references [79], [60], and [1], all of which were either written by me, or with my direct contribution.

I was extremely fortunate to start my academic career on the brink of the new era of gravitational wave astronomy. I shared in the excitement of the announcement on 11 February 2016 with my fellow students, colleagues, and supervisors. This moment marked the beginning of a whole new direction in astronomical research with a broad scope for future developments and explorations. Over the course of the past three years I started work on a number of exciting projects, and the results from two of them have been described in detail in this dissertation. In this chapter I summarise the progress which has been made so far, and in the following chapter I present the scope for future developments.

Part I of my dissertation explored how gravitational waves cause the apparent position of distant objects on the sky to oscillate with a characteristic pattern (see Fig. 3.3 and eq. (3.20)). In Chapter 3 the change in the apparent position of a star, or astrometric response, caused by an arbitrarily polarized gravitational wave has been considered and calculated. This astrometric response depends, in general, on both the metric perturbation at the photon emission and absorption events at the star and Earth, respectively. However, if the star is located many gravitational wavelengths away from the Earth, and if the GW polarization is transverse (i.e., $+$, $\times$, or S), then the star term can be neglected and the astrometric deflection depends only on the metric perturbation near Earth.

The *Gaia* mission will produce a large number of ultra-accurate astrometric measurements which could be utilised to search for low frequency GWs using the aforementioned effect. Chapter 4 presented recent efforts to develop a data analysis pipeline to search for GWs in *Gaia*-like data sets, which could recover the parameters of the gravitational wave signal with high degree of certainty. A large astrometric data set may be compressed with little loss

in sensitivity; which makes efficient and computationally cheap searches for GW signals possible. Using a large number of injections into a mock dataset, the frequency and directional sensitivities of *Gaia* were established (see Figs. 4.3 and 4.4). These tell us that *Gaia* may help detect gravitational waves from supermassive black hole binaries of total mass $10^8 - 10^{10} M_\odot$ during their post-Newtonian inspiral period, with frequencies of $10^{-9} - 10^{-7}$ Hz.

Chapter 5 considered the correlated astrometric signal due to a stationary and isotropic GW background. If the background is unpolarized, the correlation separates into a sum of an integral over the sphere of the sky for each polarization state. These integrals we evaluated for each of the 6 possible GW polarization states; although in one case the integration could be performed only numerically. A new decomposition for the astrometric correlation matrix was introduced. This decomposition has a clear geometric interpretation and enables a nice comparison to be drawn with existing results for the redshift correlations from the pulsar timing literature. In the special case of a tensorially polarized GW background, the astrometric correlation is governed by a single function which can be thought of the astrometric analogue of the Hellings-Downs curve.

Additionally, the cross-correlation between the redshift and astrometric signals was also derived for all six GW polarizations. This may form the basis for a joint pulsar timing and astrometric search for the low-frequency stochastic gravitational wave background.

Part II of my thesis investigated the problem of resonances in the in-spirals of extreme mass-ratio binaries. In Chapters 7 and 8 the assumptions and conditions which form the basis of two different methods for analysis of resonances in EMRIs are presented. The two-timescale approach, described in [136] presumes that the functional dependence of the orbital characteristics can be expanded in power series of the mass-ratio and time from resonance. The instantaneous frequency model, as per [130], relies on the instant values of the on-resonance frequencies as a basis for asymptotic analysis, and this is a more complicated function of the (rescaled) time.

After describing the basic approach, Chapter 9 described in detail the solution to the frequency and phase resonance equations derived in the course of describing the instantaneous frequency approach. Some of these solutions were previously published in [130]. The difference between the frequency and phase resonances lies in the assumption about the phasing of the self-force. It is more natural that the phase will be determined by the instantaneous orbital phase (as in the phase treatment) than the orbital phase at some fiducial $\tau = 0$ (as in the frequency investigation). Fully-detailed self-force calculations would be needed to make an informed choice between the two, but it is likely that the phase approach is physically relevant for the resonance problem. The frequency resonance solutions exhibits

interesting effects, in particular the "memory" effect on the slope of the graph, which would be interesting if it really occurred in any physical situation. Here I extended these results, by including higher-order terms and a generalised form of the solutions. I have derived solutions for the case of multiple oscillating modes, given by eq. (9.68). Working further, I relaxed the assumption of a vanishing initial phase, and have presented the single-mode solution in eq. (9.88). Finally, combining these results I presented the complete frequency solution, eq. (9.97).

As mentioned in the text, the phase resonance equation is probably more relevant physically, as it describes the evolution of the phase coordinates near resonance, and its solutions can be related to the two-timescale method results. It is also interesting from a mathematical view point, since it is a second-order non-linear differential equation which can be approached using asymptotic methods. I extended the previously established sequence of results by deriving the third-order solution for the case of a single oscillating mode, eq. (9.110). I presented an order-by-order solution to the phase resonance equation with an arbitrary (possibly infinite) number of modes, eqs. (9.124), (9.127), and (M.55). I have also derived the solution in the most general case, allowing for an arbitrary (and possibly infinite) number of modes, each with an individual initial phase. This solution was given in eq. (9.137). In the case that there is only a single mode, this calculation agrees with the result given in [130], to leading order in the parameter λ, which is equivalent to the order of $G_1(\mathbf{J})$ in the two-timescale analysis.

Both the instantaneous frequency approach and the two-timescale analysis are valid treatments of the EMRI problem — though their foundational assumptions appear different, they both have the same computational complexity and arrive at equivalent conclusions. Previous work on the two-timescale method has only been presented to the lowest order in the mass ratio ε and the resonance flux change parameters $\{\kappa, \lambda\}$. As has been discovered, in certain scenarios higher-order corrections in the latter can be more important than those to the former, hence it is vital to investigate the form of these corrections. This is what the current progress accomplishes.

11

Future work

This Chapter combines parts of the conclusions to references [79], [60], and [1], all of which were either written by me, or with my direct contribution.

The research which I described in this dissertation can be extended and taken forward in many interesting directions. I already have plans for future work that will further build onto these ideas and will present opportunities for even more exciting research. In this Chapter I outline some prospects for the immediate future.

There is a long list of sub-projects which could be undertaken in order to better understand the features of the astrometric search method for gravitational waves. One idea which I intend to research and write about is the effect of gravitational waves with non-luminal speeds. Sub-luminal gravitational waves could be related to a graviton with a non-zero mass, and initial considerations show that they have the effect of changing the overall shape of the overlap reduction functions. The changes to the value of the correlation at a given angle are commensurate with the fractional difference between the speed of light and the speed of the gravitational wave.

Another possible direction for further development of this project would be to map the frequency and directional sensitivity of Gaia with respect to alternative (non-Einsteinian) polarization states. Currently the sensitivity due to GR modes has been tested (Chapter 4), however further work is needed to examine the problem in the context of the 4 further polarization modes described in Chapter 3. This would be achievable by modifying and reconfiguring the code developed by Christopher Moore and me, and the research will be carried out in the near future.

Yet another possible avenue for further work is to expand the analysis to non-isotropic GW backgrounds. Currently the 2-point correlation functions are computed only in the context of isotropic backgrounds, however an interesting theoretical consideration is the possibility of

non-isotropic backgrounds and their treatment in this context. Finally, as time progresses, and future *Gaia* Data Releases become available, it would become possible to carry out all these analyses with real-world data.

Further work on solving the phase-resonance equation would see these solutions utilised in numerical waveform models. These could involve implementing a computationally cheap approximate (kludge) model of EMRI waveforms which include resonance effects [106, 110]. At the moment such models lack the necessary features to predict the change in frequency or phase during resonance, which is precisely what the results in [1] offer. Therefore, this should be pursued in a future publication.

References

[1] Deyan P Mihaylov and Jonathan R. Gair. Transition of EMRIs through resonance: corrections to higher order in the on-resonance flux modification. *J. Math. Phys.*, 58(11):112501, 2017.

[2] E. Grant. *The Foundations of Modern Science in the Middle Ages: Their Religious, Institutional and Intellectual Contexts*. Cambridge Studies in the History of Science. Cambridge University Press, 1996.

[3] O. Pedersen. *Early Physics and Astronomy: A Historical Introduction*. Cambridge University Press, 1993.

[4] A. Armitage. *Copernicus, the founder of modern astronomy*. Dorset Press, 1990.

[5] R. Small. *An Account of the Astronomical Discoveries of Kepler: Including an Historical Review of the Systems which Had Successively Prevailed Before His Time*. J. Mawman, 1804.

[6] J. Kepler and W.H. Donahue. *Astronomia Nova*. Green Lion Press, 2015.

[7] J. Kepler, E.J. Aiton, A.M. Duncan, J.V. Field, and American Philosophical Society. *The Harmony of the World*. Number v. 209 in American Philosophical Society: Memoirs of the American Philosophical Society. American Philosophical Society, 1997.

[8] E.T. Drake and R. Hooke. *Restless Genius: Robert Hooke and His Earthly Thoughts*. Oxford University Press, 1996.

[9] R. Hooke. *The Posthumous Works of Robert Hooke, ... Containing His Cutlerian Lectures, and Other Discourses, Read at the Meetings of the Illustrious Royal Society. ... Illustrated with Sculptures. To These Discourses is Prefixt the Author's Life, ... Publish'd by Richard Waller*. Sam. Smith and Benj. Walford, 1705.

[10] I. Newton. *Philosophiae naturalis principia mathematica*. J. Societatis Regiae ac Typis J. Streater, 1687.

[11] Gerald James Holton, Stephen G. Brush, and James Evans. *Physics, the Human Adventure: From Copernicus to Einstein and Beyond*, volume 54. Rutgers University Press, 10 2001.

[12] A. Sachs. Babylonian observational astronomy. *Philosophical Transactions of the Royal Society of London A: Mathematical, Physical and Engineering Sciences*, 276(1257):43–50, 1974.

[13] C.W. Misner, K.S. Thorne, J.A. Wheeler, and D.I. Kaiser. *Gravitation*. Princeton University Press, 2017.

[14] Carlo Rovelli. Notes for a brief history of quantum gravity. In *Recent developments in theoretical and experimental general relativity, gravitation and relativistic field theories. Proceedings, 9th Marcel Grossmann Meeting, MG'9, Rome, Italy, July 2-8, 2000. Pts. A-C*, pages 742–768, 2000.

[15] D. Blohintsev. *Selected works*. LitRes, 2017.

[16] John Henry. Gravity and de gravitatione: the development of newton's ideas on action at a distance. *Studies in History and Philosophy of Science Part A*, 42(1):11 – 27, 2011.

[17] M. Born and H.L. Brose. *Einstein's Theory of Relativity*. Methuen & Company Limited, 1924.

[18] A. Einstein. *Relativity: The Special and General Theory*. Read Books, 2009.

[19] A.I. Miller. *Albert Einstein's special theory of relativity: emergence (1905) and early interpretation, 1905-1911*. 1905 AND EARLY INTERPRETATION. Addison-Wesley Pub. Co., 1981.

[20] Speed of light. https://physics.nist.gov/cgi-bin/cuu/Value?c%7Csearch_for=speed+of+light. Accessed: 2018-08-22.

[21] A. Einstein. Die Grundlage der allgemeinen Relativitätstheorie. *Annalen der Physik*, 354:769–822, 1916.

[22] Ø. Grøn and S. Hervik. *Einstein's General Theory of Relativity: With Modern Applications in Cosmology*. Springer New York, 2007.

[23] B.S. Ryden. *Introduction to Cosmology*. Addison-Wesley, 2003.

[24] John D. Barrow and Douglas J. Shaw. The Value of the Cosmological Constant. *Gen. Rel. Grav.*, 43:2555–2560, 2011. [Int. J. Mod. Phys.D20,2875(2011)].

[25] F. W. Dyson, A. S. Eddington, and C. Davidson. A Determination of the Deflection of Light by the Sun's Gravitational Field, from Observations Made at the Total Eclipse of May 29, 1919. *Philosophical Transactions of the Royal Society of London Series A*, 220:291–333, 1920.

[26] N. Ashby. Relativity in the Global Positioning System. *Living Reviews in Relativity*, 6:1, January 2003.

[27] I. I. Shapiro. Fourth Test of General Relativity. *Physical Review Letters*, 13:789–791, December 1964.

[28] S. M. Kopeikin, A. G. Polnarev, G. Schäfer, and I. Y. Vlasov. Gravimagnetic effect of the barycentric motion of the Sun and determination of the post-Newtonian parameter γ in the Cassini experiment. *Physics Letters A*, 367:276–280, July 2007.

[29] L. Randall. *Warped Passages: Unraveling the Mysteries of the Universe's Hidden Dimensions*. HarperCollins, 2005.

[30] R.P. Feynman, F.B. Morinigo, W.G. Wagner, and B. Hatfield. *Feynman Lectures on Gravitation*. Advanced book program. Addison-Wesley, 1995.

[31] A. Einstein. Näherungsweise Integration der Feldgleichungen der Gravitation. *Sitzungsberichte der Königlich Preußischen Akademie der Wissenschaften (Berlin), Seite 688-696.*, 1916.

[32] A. Einstein. Über Gravitationswellen. *Sitzungsberichte der Königlich Preußischen Akademie der Wissenschaften (Berlin), Seite 154-167.*, 1918.

[33] J. M. Weisberg, J. H. Taylor, and L. A. Fowler. Gravitational waves from an orbiting pulsar. *Scientific American*, 245:74–82, October 1981.

[34] B. P. Abbott et al. LIGO: The Laser interferometer gravitational-wave observatory. *Rept. Prog. Phys.*, 72:076901, 2009.

[35] Matthew Pitkin, Stuart Reid, Sheila Rowan, and Jim Hough. Gravitational Wave Detection by Interferometry (Ground and Space). *Living Rev. Rel.*, 14:5, 2011.

[36] J. Aasi et al. Advanced LIGO. *Class. Quant. Grav.*, 32:074001, 2015.

[37] J. Aasi et al. Characterization of the LIGO detectors during their sixth science run. *Class. Quant. Grav.*, 32(11):115012, 2015.

[38] B. P. Abbott et al. Observation of Gravitational Waves from a Binary Black Hole Merger. *Phys. Rev. Lett.*, 116(6):061102, 2016.

[39] 2017 nobel prize in physics. https://www.nobelprize.org/prizes/physics/2017/press-release/. Accessed: 2018-08-27.

[40] B. P. Abbott et al. GW151226: Observation of Gravitational Waves from a 22-Solar-Mass Binary Black Hole Coalescence. *Phys. Rev. Lett.*, 116(24):241103, 2016.

[41] Benjamin P. Abbott et al. GW170104: Observation of a 50-Solar-Mass Binary Black Hole Coalescence at Redshift 0.2. *Phys. Rev. Lett.*, 118(22):221101, 2017.

[42] B. P. Abbott et al. GW170608: Observation of a 19-solar-mass Binary Black Hole Coalescence. *Astrophys. J.*, 851(2):L35, 2017.

[43] B. P. Abbott et al. GW170814: A Three-Detector Observation of Gravitational Waves from a Binary Black Hole Coalescence. *Phys. Rev. Lett.*, 119(14):141101, 2017.

[44] B. P. Abbott, R. Abbott, T. D. Abbott, F. Acernese, K. Ackley, C. Adams, T. Adams, P. Addesso, R. X. Adhikari, V. B. Adya, and et al. GW170817: Observation of Gravitational Waves from a Binary Neutron Star Inspiral. *Physical Review Letters*, 119(16):161101, October 2017.

[45] Ligo o1 observing run. https://losc.ligo.org/O1/. Accessed: 2018-08-22.

[46] Benjamin P. Abbott et al. Prospects for Observing and Localizing Gravitational-Wave Transients with Advanced LIGO, Advanced Virgo and KAGRA. *Living Rev. Rel.*, 21:3, 2018. [Living Rev. Rel.19,1(2016)].

[47] Gw plotter. http://gwplotter.com/. Accessed: 2018-08-22.

[48] T. Accadia, F. Acernese, M. Alshourbagy, P. Amico, F. Antonucci, S. Aoudia, N. Arnaud, C. Arnault, K. G. Arun, P. Astone, and et al. Virgo: a laser interferometer to detect gravitational waves. *Journal of Instrumentation*, 7:3012, March 2012.

[49] F. Acernese, M. Agathos, K. Agatsuma, D. Aisa, N. Allemandou, A. Allocca, J. Amarni, P. Astone, G. Balestri, G. Ballardin, and et al. Advanced Virgo: a second-generation interferometric gravitational wave detector. *Classical and Quantum Gravity*, 32(2):024001, January 2015.

[50] K. Kuroda and LCGT Collaboration. Status of LCGT. *Classical and Quantum Gravity*, 27(8):084004, April 2010.

[51] Yoichi Aso, Yuta Michimura, Kentaro Somiya, Masaki Ando, Osamu Miyakawa, Takanori Sekiguchi, Daisuke Tatsumi, and Hiroaki Yamamoto. Interferometer design of the KAGRA gravitational wave detector. *Phys. Rev.*, D88(4):043007, 2013.

[52] T. Akutsu et al. The status of KAGRA underground cryogenic gravitational wave telescope. In *15th International Conference on Topics in Astroparticle and Underground Physics (TAUP 2017) Sudbury, Ontario, Canada, July 24-28, 2017*, 2017.

[53] C. S. Unnikrishnan. IndIGO and LIGO-India: Scope and plans for gravitational wave research and precision metrology in India. *Int. J. Mod. Phys.*, D22:1341010, 2013.

[54] P. Amaro-Seoane, S. Aoudia, S. Babak, P. Binétruy, E. Berti, A. Bohé, C. Caprini, M. Colpi, N. J. Cornish, K. Danzmann, J.-F. Dufaux, J. Gair, O. Jennrich, P. Jetzer, A. Klein, R. N. Lang, A. Lobo, T. Littenberg, S. T. McWilliams, G. Nelemans, A. Petiteau, E. K. Porter, B. F. Schutz, A. Sesana, R. Stebbins, T. Sumner, M. Vallisneri, S. Vitale, M. Volonteri, and H. Ward. Low-frequency gravitational-wave science with eLISA/NGO. *Classical and Quantum Gravity*, 29(12):124016, June 2012.

[55] Pau Amaro-Seoane et al. eLISA/NGO: Astrophysics and cosmology in the gravitational-wave millihertz regime. *GW Notes*, 6:4–110, 2013.

[56] J. Luo, L.-S. Chen, H.-Z. Duan, Y.-G. Gong, S. Hu, J. Ji, Q. Liu, J. Mei, V. Milyukov, M. Sazhin, C.-G. Shao, V. T. Toth, H.-B. Tu, Y. Wang, Y. Wang, H.-C. Yeh, M.-S. Zhan, Y. Zhang, V. Zharov, and Z.-B. Zhou. TianQin: a space-borne gravitational wave detector. *Classical and Quantum Gravity*, 33(3):035010, February 2016.

[57] J. Mei, C. Shao, and Y. Wang. Fundamentals of the TianQin mission. In J.-P. Hsu and et al., editors, *Gravitation, Astrophysics, and Cosmology*, pages 360–361, 2016.

[58] Seiji Kawamura et al. The Japanese space gravitational wave antenna: DECIGO. *Class. Quant. Grav.*, 28:094011, 2011.

[59] S. Hild, S. Chelkowski, and A. Freise. Pushing towards the ET sensitivity using 'conventional' technology. *ArXiv e-prints*, October 2008.

[60] Deyan P. Mihaylov, Christopher J. Moore, Jonathan R. Gair, Anthony Lasenby, and Gerard Gilmore. Astrometric Effects of Gravitational Wave Backgrounds with non-Einsteinian Polarizations. *Phys. Rev.*, D97(12):124058, 2018.

[61] David Blair et al. Gravitational wave astronomy: the current status. *Sci. China Phys. Mech. Astron.*, 58:120402, 2015.

[62] Scott A. Hughes, Szabolcs Marka, Peter L. Bender, and Craig J. Hogan. New physics and astronomy with the new gravitational wave observatories. *eConf*, C010630:P402, 2001.

[63] B. P. Abbott et al. Astrophysical Implications of the Binary Black-Hole Merger GW150914. *Astrophys. J.*, 818(2):L22, 2016.

[64] B. P. Abbott et al. A gravitational-wave standard siren measurement of the Hubble constant. *Nature*, 551(7678):85–88, 2017.

[65] B. P. Abbott, R. Abbott, T. D. Abbott, M. R. Abernathy, F. Acernese, et al. Tests of General Relativity with GW150914. *Phys. Rev. Lett.*, 116(22):221101, June 2016.

[66] B. P. Abbott, R. Abbott, T. D. Abbott, M. R. Abernathy, F. Acernese, et al. Binary Black Hole Mergers in the First Advanced LIGO Observing Run. *Phys. Rev. X*, 6(4):041015, October 2016.

[67] B. P. Abbott, R. Abbott, T. D. Abbott, F. Acernese, K. Ackley, et al. Gravitational Waves and Gamma-Rays from a Binary Neutron Star Merger: GW170817 and GRB 170817A. *Astrophys. J. Lett.*, 848:L13, October 2017.

[68] S. Hou, Y. Gong, and Y. Liu. Polarizations of Gravitational Waves in Horndeski Theory. *ArXiv e-prints*, April 2017.

[69] Clifford M. Will. The Confrontation between General Relativity and Experiment. *Living Rev. Rel.*, 17:4, 2014.

[70] K. J. Lee, F. A. Jenet, and Richard H. Price. Pulsar timing as a probe of non-einsteinian polarizations of gravitational waves. *Astrophys. J.*, 685(2):1304, 2008.

[71] Neil J. Cornish, Logan O'Beirne, Stephen R. Taylor, and Nicolás Yunes. Constraining alternative theories of gravity using pulsar timing arrays. *Phys. Rev. Lett.*, 120(18):181101, 2018.

[72] Gaia Collaboration, T. Prusti, J. H. J. de Bruijne, A. G. A. Brown, A. Vallenari, C. Babusiaux, et al. The Gaia mission. *Astron. Astrophys.*, 595:A1, November 2016.

[73] G. F. Gilmore, M. A. Perryman, L. Lindegren, F. Favata, E. Hoeg, et al. GAIA: origin and evolution of the Milky Way. In R. D. Reasenberg, editor, *Astronomical Interferometry*, volume 3350 of *Proc. SPIE*, pages 541–550, July 1998.

[74] V. B. Braginsky, N. S. Kardashev, A. G. Polnarev, and I. D. Novikov. Propagation of electromagnetic radiation in a random field of gravitational waves and space radio interferometry. *Nuovo Cimento B*, 105:1141–1158, October 1990.

[75] Carl R. Gwinn, T. Marshall Eubanks, Ted Pyne, Mark Birkinshaw, and Demetrios N. Matsakis. Quasar proper motions and low frequency gravitational waves. *Astrophys. J.*, 485:87–91, 1997.

[76] Laura G. Book and Eanna E. Flanagan. Astrometric Effects of a Stochastic Gravitational Wave Background. *Phys. Rev.*, D83:024024, 2011.

[77] F. Mignard and S. Klioner. Analysis of astrometric catalogues with vector spherical harmonics. *Astron. Astrophys.*, 547:A59, November 2012.

[78] Sergei A. Klioner. Gaia-like astrometry and gravitational waves. *Class. Quantum Grav.*, 35(4):045005, 2018.

[79] Christopher J. Moore, Deyan Mihaylov, Anthony Lasenby, and Gerard Gilmore. Astrometric Search Method for Individually Resolvable Gravitational Wave Sources with Gaia. *Phys. Rev. Lett.*, 119(26):261102, 2017.

[80] É. É. Flanagan and S. A. Hughes. The basics of gravitational wave theory. *New J. Phys.*, 7:204, September 2005.

[81] Delphine Perrodin and Alberto Sesana. Radio pulsars: testing gravity and detecting gravitational waves. In *Physics and Astrophysics of Neutron Stars*. Springer, 2017.

[82] Z. Arzoumanian, A. Brazier, S. Burke-Spolaor, S. J. Chamberlin, S. Chatterjee, et al. The NANOGrav Nine-year Data Set: Limits on the Isotropic Stochastic Gravitational Wave Background. *Astrophys. J.*, 821:13, April 2016.

[83] L. Lentati, S. R. Taylor, C. M. F. Mingarelli, A. Sesana, S. A. Sanidas, et al. European Pulsar Timing Array limits on an isotropic stochastic gravitational-wave background. *Mon. Notices Royal Astron. Soc.*, 453:2576–2598, November 2015.

[84] R. M. Shannon et al. Gravitational waves from binary supermassive black holes missing in pulsar observations. *Science*, 349(6255):1522–1525, 2015.

[85] J. P. W. Verbiest, L. Lentati, G. Hobbs, R. van Haasteren, P. B. Demorest, et al. The International Pulsar Timing Array: First data release. *Mon. Notices Royal Astron. Soc.*, 458:1267–1288, May 2016.

[86] Jonathan R. Gair, Joseph D. Romano, and Stephen R. Taylor. Mapping gravitational-wave backgrounds of arbitrary polarisation using pulsar timing arrays. *Phys. Rev. D*, 92(10):102003, 2015.

[87] Bernard F. Schutz. Astrometric and timing effects of gravitational waves. *IAU Symp.*, 261:234–239, 2010.

[88] Lee Samuel Finn, Shane L. Larson, and Joseph D. Romano. Detecting a stochastic gravitational-wave background: The overlap reduction function. *Phys. Rev. D*, 79:062003, Mar 2009.

[89] A. C. Robin, X. Luri, C. Reylé, Y. Isasi, E. Grux, et al. Gaia Universe model snapshot. A statistical analysis of the expected contents of the Gaia catalogue. *Astron. Astrophys.*, 543:A100, July 2012.

[90] Roberto Trotta. Bayes in the sky: Bayesian inference and model selection in cosmology. *Contemp. Phys.*, 49:71–104, 2008.

[91] F. Feroz and M. P. Hobson. Multimodal nested sampling: an efficient and robust alternative to Markov Chain Monte Carlo methods for astronomical data analyses. *Mon. Notices Royal Astron. Soc*, 384:449–463, February 2008.

[92] John Skilling. Nested sampling. *AIP Conference Proceedings*, 735(1):395–405, 2004.

[93] F. Mignard and S. A. Klioner. Gaia: Relativistic modelling and testing. In S. A. Klioner, P. K. Seidelmann, and M. H. Soffel, editors, *Relativity in Fundamental Astronomy: Dynamics, Reference Frames, and Data Analysis*, volume 261 of *IAU Symposium*, pages 306–314, January 2010.

[94] J.R. Sack and J. Urrutia. *Handbook of Computational Geometry*. Elsevier Science, 1999.

[95] B. Holl, L. Lindegren, and D. Hobbs. Error characterization of the Gaia astrometric solution. II. Validating the covariance expansion model. *Astron. Astrophys.*, 543:A15, July 2012.

[96] Z. Arzoumanian, A. Brazier, S. Burke-Spolaor, S. J. Chamberlin, S. Chatterjee, J. M. Cordes, P. B. Demorest, X. Deng, T. Dolch, J. A. Ellis, R. D. Ferdman, N. Garver-Daniels, F. Jenet, G. Jones, V. M. Kaspi, M. Koop, M. T. Lam, T. J. W. Lazio, A. N. Lommen, D. R. Lorimer, J. Luo, R. S. Lynch, D. R. Madison, M. A. McLaughlin, S. T. McWilliams, D. J. Nice, N. Palliyaguru, T. T. Pennucci, S. M. Ransom, A. Sesana, X. Siemens, I. H. Stairs, D. R. Stinebring, K. Stovall, J. Swiggum, M. Vallisneri, R. van Haasteren, Y. Wang, , W. W. Zhu, and NANOGrav Collaboration. Gravitational waves from individual supermassive black hole binaries in circular orbits: Limits from the north american nanohertz observatory for gravitational waves. *The Astrophysical Journal*, 794(2):141, 2014.

[97] S. Babak, A. Petiteau, A. Sesana, P. Brem, P. A. Rosado, S. R. Taylor, A. Lassus, J. W. T. Hessels, C. G. Bassa, M. Burgay, R. N. Caballero, D. J. Champion, I. Cognard, G. Desvignes, J. R. Gair, L. Guillemot, G. H. Janssen, R. Karuppusamy, M. Kramer, P. Lazarus, K. J. Lee, L. Lentati, K. Liu, C. M. F. Mingarelli, S. Osłowski, D. Perrodin, A. Possenti, M. B. Purver, S. Sanidas, R. Smits, B. Stappers, G. Theureau, C. Tiburzi, R. van Haasteren, A. Vecchio, and J. P. W. Verbiest. European Pulsar Timing Array limits on continuous gravitational waves from individual supermassive black hole binaries. *Mon. Notices Royal Astron. Soc*, 455:1665–1679, January 2016.

[98] X.-J. Zhu, G. Hobbs, L. Wen, W. A. Coles, J.-B. Wang, R. M. Shannon, R. N. Manchester, M. Bailes, N. D. R. Bhat, S. Burke-Spolaor, S. Dai, M. J. Keith, M. Kerr, Y. Levin, D. R. Madison, S. Osłowski, V. Ravi, L. Toomey, and W. van Straten. An all-sky search for continuous gravitational waves in the Parkes Pulsar Timing Array data set. *Mon. Notices Royal Astron. Soc*, 444:3709–3720, November 2014.

[99] E. E. Flanagan. Sensitivity of the Laser Interferometer Gravitational Wave Observatory to a stochastic background, and its dependence on the detector orientations. *Phys. Rev. D*, 48:2389–2407, September 1993.

[100] E. J. Fuselier and G. B. Wright. Stability and error estimates for vector field interpolation and decomposition on the sphere with {RBF}s. *J. Num. Anal.*, 47:3213–3239, 2009.

[101] R. W. Hellings and G. S. Downs. Upper limits on the isotropic gravitational radiation background from pulsar timing analysis. *Astrophys. J. Lett.*, 265:L39–L42, February 1983.

[102] J. Aasi, B. P. Abbott, R. Abbott, T. Abbott, M. R. Abernathy, T. Accadia, F. Acernese, K. Ackley, C. Adams, T. Adams, and et al. First all-sky search for continuous gravitational waves from unknown sources in binary systems. *Phys. Rev. D*, 90(6):062010, September 2014.

[103] S. E. Gossan, P. Sutton, A. Stuver, M. Zanolin, K. Gill, and C. D. Ott. Observing Gravitational Waves from Core-Collapse Supernovae in the Advanced Detector Era. *Phys. Rev.*, D93(4):042002, 2016.

[104] Stanislav Babak, Jonathan R. Gair, and Robert H. Cole. Extreme mass ratio inspirals: perspectives for their detection. *Fund. Theor. Phys.*, 179:783–812, 2015.

[105] J. Kormendy and D. Richstone. Inward Bound—The Search For Supermassive Black Holes In Galactic Nuclei. *Annu. Rev. Astron. Astrophys.*, 33:581, 1995.

[106] L. Barack and C. Cutler. LISA capture sources: Approximate waveforms, signal-to-noise ratios, and parameter estimation accuracy. *Phys. Rev. D*, 69(8):082005, April 2004.

[107] J. R. Gair and K. Glampedakis. Improved approximate inspirals of test bodies into Kerr black holes. *Phys. Rev. D*, 73(6):064037, March 2006.

[108] S. Drasco and S. A. Hughes. Gravitational wave snapshots of generic extreme mass ratio inspirals. *Phys. Rev. D*, 73(2):024027, January 2006.

[109] A. J. K. Chua and J. R. Gair. Improved analytic extreme-mass-ratio inspiral model for scoping out eLISA data analysis. *Classical and Quantum Gravity*, 32(23):232002, December 2015.

[110] S. Babak, H. Fang, J. R. Gair, K. Glampedakis, and S. A. Hughes. "Kludge" gravitational waveforms for a test-body orbiting a Kerr black hole. *Phys. Rev. D*, 75(2):024005, January 2007.

[111] K. Glampedakis, S. A. Hughes, and D. Kennefick. Approximating the inspiral of test bodies into Kerr black holes. *Phys. Rev. D*, 66(6):064005, September 2002.

[112] C. Hopman. Extreme mass ratio inspiral rates: dependence on the massive black hole mass. *Classical and Quantum Gravity*, 26(9):094028, May 2009.

[113] K. G. Arun, S. Babak, E. Berti, N. Cornish, C. Cutler, J. Gair, S. A. Hughes, B. R. Iyer, R. N. Lang, I. Mandel, E. K. Porter, B. S. Sathyaprakash, S. Sinha, A. M. Sintes, M. Trias, C. Van Den Broeck, and M. Volonteri. Massive black-hole binary inspirals: results from the LISA parameter estimation taskforce. *Classical and Quantum Gravity*, 26(9):094027, May 2009.

[114] J. R. Gair, C. Tang, and M. Volonteri. LISA extreme-mass-ratio inspiral events as probes of the black hole mass function. *Phys. Rev. D*, 81(10):104014, May 2010.

[115] C. L. MacLeod and C. J. Hogan. Precision of Hubble constant derived using black hole binary absolute distances and statistical redshift information. *Phys. Rev. D*, 77(4):043512, February 2008.

[116] J. R. Gair, M. Vallisneri, S. L. Larson, and J. G. Baker. Testing General Relativity with Low-Frequency, Space-Based Gravitational-Wave Detectors. *Living Reviews in Relativity*, 16:7, September 2013.

[117] B. Carter. Global Structure of the Kerr Family of Gravitational Fields. *Physical Review*, 174:1559–1571, October 1968.

[118] T. Nakamura and M. Sasaki. Gravitational radiation induced by a particle falling along the z-axis into a kerr black hole. *Physics Letters A*, 89(4):185 – 189, 1982.

[119] B. Wardell, I. Vega, J. Thornburg, and P. Diener. Generic effective source for scalar self-force calculations. *Phys. Rev. D*, 85(10):104044, May 2012.

[120] A. Pound and E. Poisson. Osculating orbits in Schwarzschild spacetime, with an application to extreme mass-ratio inspirals. *Phys. Rev. D*, 77(4):044013, February 2008.

[121] J. R. Gair, É. É. Flanagan, S. Drasco, T. Hinderer, and S. Babak. Forced motion near black holes. *Phys. Rev. D*, 83(4):044037, February 2011.

[122] C. F. Sopuerta and N. Yunes. Approximate Waveforms for Extreme-Mass-Ratio Inspirals: The Chimera Scheme. *Journal of Physics Conference Series*, 363(1):012021, June 2012.

[123] Éanna É. Flanagan and Tanja Hinderer. Transient resonances in the inspirals of point particles into black holes. *Phys. Rev. Lett.*, 109:071102, Aug 2012.

[124] L. Barack. TOPICAL REVIEW: Gravitational self-force in extreme mass-ratio inspirals. *Classical and Quantum Gravity*, 26(21):213001, November 2009.

[125] Christopher P. L. Berry, Robert H. Cole, Priscilla Cañizares, and Jonathan R. Gair. Importance of transient resonances in extreme-mass-ratio inspirals. *Phys. Rev. D*, 94(12):124042, 2016.

[126] S. E. Gralla and R. M. Wald. A rigorous derivation of gravitational self-force. *Classical and Quantum Gravity*, 25(20):205009, October 2008.

[127] E. Poisson, A. Pound, and I. Vega. The Motion of Point Particles in Curved Spacetime. *Living Reviews in Relativity*, 14:7, September 2011.

[128] Eric Poisson. Constructing the self-force. *Fundam. Theor. Phys.*, 162:309–325, 2011. [,309(2009)].

[129] Robert M. Wald. Introduction to Gravitational Self-Force. *Fundam. Theor. Phys.*, 162:253–262, 2011. [,253(2009)].

[130] J. Gair, N. Yunes, and C. M. Bender. Resonances in extreme mass-ratio inspirals: Asymptotic and hyperasymptotic analysis. *Journal of Mathematical Physics*, 53(3):032503, March 2012.

[131] W. Schmidt. Celestial mechanics in Kerr spacetime. *Classical and Quantum Gravity*, 19:2743–2764, May 2002.

[132] N. Warburton, L. Barack, and N. Sago. Isofrequency pairing of geodesic orbits in Kerr geometry. *Phys. Rev. D*, 87(8):084012, April 2013.

[133] U. Ruangsri and S. A. Hughes. Census of transient orbital resonances encountered during binary inspiral. *Phys. Rev. D*, 89(8):084036, April 2014.

[134] T. Hinderer and É. É. Flanagan. Two-timescale analysis of extreme mass ratio inspirals in Kerr spacetime: Orbital motion. *Phys. Rev. D*, 78(6):064028, September 2008.

[135] J. Kevorkian. Perturbation techniques for oscillatory systems with slowly varying coefficients. *SIAM Review*, 29(3):391–461, 1987.

[136] M. van de Meent. Conditions for sustained orbital resonances in extreme mass ratio inspirals. *Phys. Rev. D*, 89(8):084033, April 2014.

[137] Christopher P. L. Berry. *Exploring Gravity*. Ph.d. dissertation, University of Cambridge, August 2013.

[138] Y. Mino. Perturbative approach to an orbital evolution around a supermassive black hole. *Phys. Rev. D*, 67(8):084027, April 2003.

[139] Éanna E. Flanagan, Scott A. Hughes, and Uchupol Ruangsri. Resonantly enhanced and diminished strong-field gravitational-wave fluxes. *Phys. Rev. D*, 89(8):084028, 2014.

[140] Wolfram Research, Inc. Mathematica 10.4.

[141] J. Gair, J. D. Romano, S. Taylor, and C. M. F. Mingarelli. Mapping gravitational-wave backgrounds using methods from CMB analysis: Application to pulsar timing arrays. *Phys. Rev. D*, 90(8):082001, October 2014.

[142] R. H. Boyer and R. W. Lindquist. Maximal Analytic Extension of the Kerr Metric. In *Black Holes: Selected Reprints*, page 61. the American Association of Physics Teachers, December 1982.

[143] Matt Visser. The Kerr spacetime: A Brief introduction. In *Kerr Fest: Black Holes in Astrophysics, General Relativity and Quantum Gravity Christchurch, New Zealand, August 26-28, 2004*, 2007.

Appendix A

Additional Astrometric Deflection Patterns

In Figs. 3.3 and 3.4 of Section 3.2 the astrometric deflection patterns were plotted for all 6 GW polarization states; for the three transverse modes ($+$, $\times$, and S) in Fig. 3.3 the distant source limit formula (3.20) was used, whilst for the three modes with longitudinal components (X, Y, and L) in Fig. 3.4 the full formula (including the star terms) eq. (3.19) was used. In this Appendix the effect of including the star terms on the deflection patterns for the two transverse GR modes ($+$ and $\times$) is illustrated. In Fig. A.1 the new astrometric deflection patterns are plotted; these plots were produced in the same way as the two top rows of Fig. 3.3 except eq. (3.19) was used in place of eq. (3.20) (all stars are placed 10 gravitational wavelengths away from the Earth). The extra terms in the full expression for the astrometric deflection introduce an additional oscillatory deflection pattern which is out of phase with the Earth term pattern plotted in Fig. 3.3, this causes each star to trace out a small ellipse on the sky. If the stars are further away from the Earth then the phase difference between the two oscillations changes and the amplitude of the additional oscillation is reduced (the ellipses appear rotated and their eccentricity is increased); in the limit of infinite distance the patterns in Fig. 3.3 are recovered. In these figures the ellipses are aligned in a regular pattern on the sky because the stars are all the same distance from the Earth. If all the distances were different, the ellipses would all be misaligned and the extra motion from the full formula in eq. (3.19) would appear to be a random noise superposed on the regular Earth term pattern plotted in Fig. 3.3.

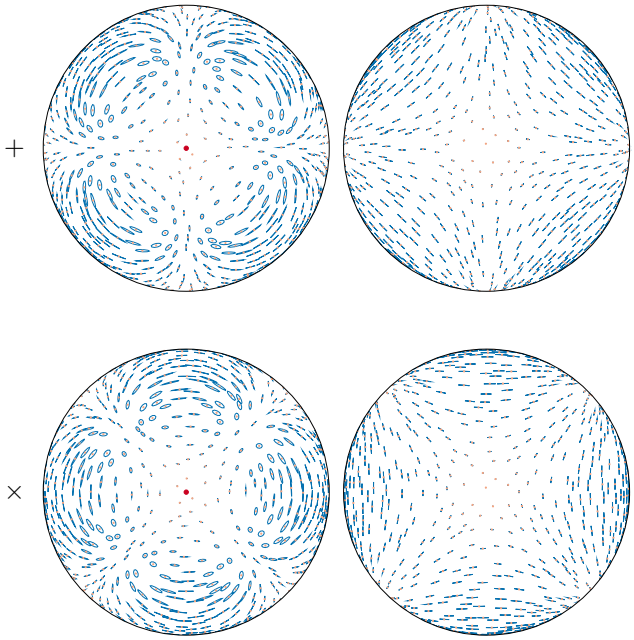

Fig. A.1 Orthographic projections of the Northern (left) and Southern (right) hemispheres. On the sky are chosen 1000 stars. A GW from a source located at the North pole (indicated by the red dots) is incident on the Earth causing the stars to move periodically at the GW frequency, according to eq. (3.19). All stars are placed at a distance of 10 gravitational wavelengths from the Earth; in reality, these neat elliptical patterns would appear more chaotic, since the distances to each star are generally different. The blue lines show the resulting movement tracks. The incident GW has the unphysically large characteristic strain amplitude $A = 0.1$. Figure appeared in [60].

Appendix B

The Tensorial Astrometric Integrals

In Sections 5.1.1 to 5.1.4 the details of the evaluations of the spatial correlation integrals for the different polarization modes were omitted for brevity; the details are presented in this Appendix B, and in Appendices D, E, and F.

In the main text the astrometric response at each of the two star positions was resolved in the tangent plane along a pair of basis vectors. It was then shown how the spatial correlation matrix can be written in terms of just two scalar integrals over the sky; one involving the x and θ components, and one involving the y and ϕ components. In this Appendix these two integrals will be evaluated, first for the $+$ mode and then for the $\times$ mode.

Firstly, the x-θ term for the $+$ polarized GW state is considered; the correlation integral is defined in eq. (5.18a) as

$$\Gamma^{+}_{x\theta}(\Theta) = \int_{S^2} \mathrm{d}\Omega_{\mathbf{q}}\, \delta n^{+}_{x}(\mathbf{q})\, \delta m^{+}_{\theta}(\mathbf{q}) = \int_0^{2\pi} \mathrm{d}\phi \int_0^{\pi} \mathrm{d}\theta\, \sin\theta\, \delta n^{+}_{x}(\theta,\phi)\, \delta m^{+}_{\theta}(\theta,\phi)\,, \tag{B.1}$$

where the vector $\mathbf{q} = (\sin\theta\cos\phi, \sin\theta\sin\phi, \cos\theta)$ is the direction on the sky from which the GW originates. The components of the astrometric deflections, $\delta n^{+}_{x}(\theta,\phi)$ and $\delta m^{+}_{\theta}(\theta,\phi)$, may be evaluated from the definitions in eqs. (5.16a) and (5.17a), using the formula for the astrometric deflection in eq. (3.20), the expression for the GW basis tensor in eq. (3.24a), and the expressions for the basis vectors tangent to the sphere in eqs. (5.11a) and (5.12a):

$$\delta n^{+}_{x}(\theta,\phi) = -\frac{1}{2}\sin\theta\cos\phi\,, \tag{B.2a}$$

$$\begin{aligned}\delta m^{+}_{\theta}(\theta,\phi) = \frac{1}{1-\cos\Theta\cos\theta-\sin\Theta\sin\theta\cos\phi}\Bigg(&\frac{3}{16}\sin\Theta\left(1-\cos(2\theta)\right)\\ &+\frac{1}{4}\left(\cos(2\Theta)\sin(2\theta)-2\cos\Theta\sin\theta\right)\cos\phi\\ &+\frac{1}{16}\left(8\sin\Theta\cos\theta-3\sin(2\Theta)-\sin(2\Theta)\cos(2\theta)\right)\cos(2\phi)\Bigg)\,.\end{aligned} \tag{B.2b}$$

The azimuthal integral over ϕ in eq. (B.1) may be evaluated using the result derived in Appendix B.1 (previously published by [141] with a sign error). Using this result the double integral in eq. (B.1) becomes the single integral

$$\begin{aligned}\Gamma^{+}_{x\theta}(\Theta) = &-2\pi\int_0^{\Theta}\mathrm{d}\theta\left(\cos^4(\theta/2)+\cos^2(\theta/2)-1\right)\frac{\sin^3(\theta/2)}{\cos(\theta/2)}\\ &+2\pi\int_{\Theta}^{\pi}\mathrm{d}\theta\left(\sin^4(\theta/2)+\sin^2(\theta/2)-1\right)\frac{\cos^3(\theta/2)}{\sin(\theta/2)}\\ &+2\pi\cos^2(\Theta/2)\int_0^{\Theta}\mathrm{d}\theta\left(2\cos^4(\theta/2)+1\right)\frac{\sin^3(\theta/2)}{\cos(\theta/2)}\\ &-2\pi\sin^2(\Theta/2)\int_{\Theta}^{\pi}\mathrm{d}\theta\left(2\sin^4(\theta/2)+1\right)\frac{\cos^3(\theta/2)}{\sin(\theta/2)}\\ &-\frac{2\pi}{\sin^2(\Theta/2)}\int_0^{\Theta}\mathrm{d}\theta\,\frac{\sin^5(\theta/2)}{\cos(\theta/2)}+\frac{2\pi}{\cos^2(\Theta/2)}\int_{\Theta}^{\pi}\mathrm{d}\theta\,\frac{\cos^5(\theta/2)}{\sin(\theta/2)}\,.\end{aligned} \tag{B.3}$$

This integral may now be evaluated using standard techniques to give

$$\begin{aligned}\Gamma^{+}_{x\theta}(\Theta) = \frac{7\pi}{3}-\frac{14\pi}{3}\sin^2(\Theta/2)-4\pi\frac{\sin^4(\Theta/2)}{1-\sin^2(\Theta/2)}\ln(\sin(\Theta/2))\\ +4\pi\frac{\cos^4(\Theta/2)}{1-\cos^2(\Theta/2)}\ln(\cos(\Theta/2))\,.\end{aligned} \tag{B.4}$$

Secondly, the y-ϕ component term for the $+$ polarised GW state is considered; the relevant correlation integral was defined in eq. (5.18d) as

$$\Gamma^{+}_{y\phi}(\Theta) = \int_0^{2\pi}\mathrm{d}\phi\int_0^{\pi}\mathrm{d}\theta\,\sin\theta\,\delta n^{+}_{y}(\theta,\phi)\,\delta m^{+}_{\phi}(\theta,\phi)\,. \tag{B.5}$$

The components of the astrometric deflections may be evaluated from the definitions in eqs. (5.16b) and (5.17b), using the formula for the astrometric deflection in eq. (3.20), the expression for the GW basis tensor in eq. (3.24a), and the expressions for the basis vectors in

eqs. (5.11b) and (5.12b):

$$\delta n_y^+(\theta,\phi) = -\frac{1}{2}\sin\theta\sin\phi\,, \tag{B.6a}$$

$$\delta m_\phi^+(\theta,\phi) = \frac{1}{1-\cos\Theta\cos\theta-\sin\Theta\sin\theta\cos\phi}\left(\frac{1}{2}\left(\cos\Theta\sin\theta\cos\theta-\sin(2\Theta)\sin\theta\right)\sin\phi \right.$$
$$\left. +\frac{1}{8}\left(2\sin(2\Theta)\cos\theta-3\sin\Theta-\sin\Theta\cos(2\theta)\right)\sin(2\phi)\right). \tag{B.6b}$$

The integral for $\Gamma^+_{y\phi}(\Theta)$ in eq. (B.5) may be evaluated in the same way as that for $\Gamma^+_{x\theta}(\Theta)$ above to give

$$\Gamma^+_{y\phi}(\Theta) = -\frac{5\pi}{3} - 4\pi\frac{\sin^4(\Theta/2)}{1-\sin^2(\Theta/2)}\ln(\sin(\Theta/2)) - 4\pi\frac{\cos^4(\Theta/2)}{1-\cos^2(\Theta/2)}\ln(\cos(\Theta/2))\,. \tag{B.7}$$

Thirdly, the two analogous integrals for the $\times$ GR polarization state are considered; these correlation integrals are defined in eqs. (5.18a) and (5.18d):

$$\Gamma^\times_{x\theta}(\Theta) = \int_0^\pi \mathrm{d}\theta \int_0^{2\pi}\mathrm{d}\phi\ \sin\theta\ \delta n_x^\times(\theta,\phi)\,\delta m_\theta^\times(\theta,\phi), \tag{B.8a}$$

$$\Gamma^\times_{y\phi}(\Theta) = \int_0^\pi \mathrm{d}\theta \int_0^{2\pi}\mathrm{d}\phi\ \sin\theta\ \delta n_y^\times(\theta,\phi)\,\delta m_\phi^\times(\theta,\phi). \tag{B.8b}$$

The components of the astrometric deflection may be evaluated from the definitions in eqs. (5.16a), (5.17a), (5.16b), and (5.17b), using the formula for the astrometric deflection in eq. (3.20), the expression for the GW basis tensor in eq. (3.24b), and the expressions for the basis vectors in eqs. (5.11a), (5.12a), (5.11b), and (5.12b). Due to the symmtetry between the $+$ and $\times$ modes, these components are closely related to those found above for the $+$ components:

$$\delta n_x^\times(\theta,\phi) = \delta n_y^+(\theta,\phi)\,, \tag{B.9a}$$
$$\delta n_y^\times(\theta,\phi) = -\,\delta n_x^+(\theta,\phi)\,, \tag{B.9b}$$
$$\delta m_\theta^\times(\theta,\phi) = \delta m_\phi^+(\theta,\phi)\,, \tag{B.9c}$$
$$\delta m_\phi^\times(\theta,\phi) = -\,\delta m_\theta^+(\theta,\phi)\,. \tag{B.9d}$$

The two integrals for $\Gamma^\times_{x\theta}(\Theta)$ and $\Gamma^\times_{y\phi}(\Theta)$ in eqs. (B.8a) and (B.8b) may be evaluated in the same way as those for $\Gamma^+_{x\theta}(\Theta)$ and $\Gamma^+_{y\phi}(\Theta)$ above to give

$$\Gamma^{\times}_{x\theta}(\Theta) = \Gamma^{+}_{y\phi}(\Theta)\,, \qquad \text{(B.10a)} \qquad \Gamma^{\times}_{y\phi}(\Theta) = \Gamma^{+}_{x\theta}(\Theta)\,. \qquad \text{(B.10b)}$$

As was described in the main text, for an unpolarised background containing equal power of both $+$ and $\times$ polarization states we may define the combined spatial correlation functions $\Gamma^{+,\times}_{x\theta}(\Theta) = \Gamma^{+}_{x\theta}(\Theta) + \Gamma^{\times}_{x\theta}(\Theta)$ and $\Gamma^{+,\times}_{y\phi}(\Theta) = \Gamma^{+}_{y\phi}(\Theta) + \Gamma^{\times}_{y\phi}(\Theta)$. These new functions may be evaluated by taking the sums of the expression in eqs. (B.4), (B.7), (B.10a), and (B.10b) to give the result which appeared in the main text,

$$\Gamma^{+,\times}_{x\theta}(\Theta) = \Gamma^{+,\times}_{y\phi}(\Theta) = \frac{2\pi}{3} - \frac{14\pi}{3}\sin^2(\Theta/2) - 8\pi\,\frac{\sin^4(\Theta/2)}{1-\sin^2(\Theta/2)}\ln(\sin(\Theta/2))\,. \quad \text{(B.11)}$$

The three functions $\Gamma^{+}_{x\theta}(\Theta) = \Gamma^{\times}_{y\phi}(\Theta)$, $\Gamma^{+}_{y\phi}(\Theta) = \Gamma^{\times}_{x\theta}(\Theta)$, and $\Gamma^{+,\times}_{x\theta}(\Theta) = \Gamma^{+,\times}_{y\phi}(\Theta)$, are plotted in Fig. B.1.

B.1 Azimuthal Integral

The following integral appears in most of the spatial correlation integrals;

$$\begin{aligned} I_n(\theta,\Theta) &= \int_0^{2\pi} \mathrm{d}\phi\, \frac{\cos(n\phi)}{1-\cos\Theta\cos\theta-\sin\Theta\sin\theta\cos\phi} \\ &= \Re\left\{\int_0^{2\pi} \mathrm{d}\phi\, \frac{e^{in\phi}}{1-\cos\Theta\cos\theta-\sin\Theta\sin\theta\cos\phi}\right\}. \end{aligned} \qquad \text{(B.12)}$$

The integral is tidied up by denoting the new variables

$$\mathfrak{a}(\theta,\Theta) = 1-\cos\Theta\cos\theta\,, \qquad \text{(B.13a)} \qquad \mathfrak{b}(\theta,\Theta) = -\frac{\sin\Theta\sin\theta}{1-\cos\Theta\cos\theta}\,. \qquad \text{(B.13b)}$$

If $z = e^{\mathrm{i}\phi}$, then $\mathrm{d}\phi = \mathrm{d}z/(\mathrm{i}z)$ and from $\bar{z} = 1/z = \cos\phi - \mathrm{i}\sin\phi$, it can be found that $\cos\phi = {}^1\!/_2\left(z+z^{-1}\right)$ and finally $I_n(\theta,\Theta)$ is expressed as a complex integral over the circle $\gamma = \{|z| = -1/\mathfrak{b}\}$

$$I_n(\theta,\Theta) = \Re\left\{\frac{2}{\mathrm{i}\mathfrak{a}}\oint_\gamma \mathrm{d}z\,\frac{z^{|n|}}{\mathfrak{b}z^2+2z+\mathfrak{b}}\right\}. \qquad \text{(B.14)}$$

The modulus sign is needed since the cosine function is even. The integrand has 2 distinct poles, each at $z_\pm = \left(-1\pm\sqrt{1-\mathfrak{b}^2}\right)/\mathfrak{b}$. The positions of those poles are determined by the range of the function $\mathfrak{b}(\theta,\Theta)$. Both θ and Θ range from 0 to π; the substitution $x = \cos\theta$

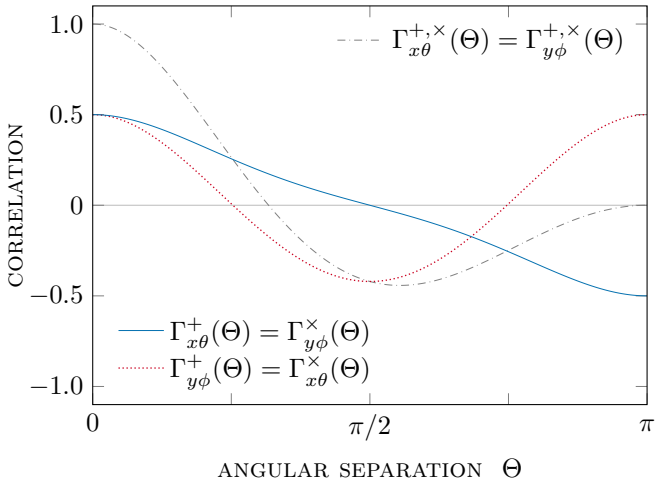

Fig. B.1 Plot of the tensorial correlation functions in eq. (B.11), normalized so that their absolute maximum is unity. Also shown are the functions for each of the two GR modes, given by eqs. (B.4), (B.7), (B.10a), and (B.10b), rescaled by the same normalization constant. Figure appeared in [60].

and $y = \cos\Theta$ leads to

$$\mathfrak{b}(x,y) = -\frac{\sqrt{1-x^2}\sqrt{1-y^2}}{1-xy}. \tag{B.15}$$

By investigating the derivatives of $\mathfrak{b}(x,y)$, it can be established that the function ranges between -1 and 0, which corresponds to $z_- \in [-1/\mathfrak{b}, +\infty)$ and $z_+ \in (0, -1/\mathfrak{b}]$. The value of the contour integral is determined by the residue of the root which lies inside the contour γ;

$$2\pi\mathrm{i}\,\mathrm{Res}_{z=z_+}\left\{\frac{z^n}{\mathfrak{b}z^2+2z+\mathfrak{b}}\right\} = \pi\mathrm{i}\,\frac{z_+^n}{\mathfrak{b}z_++1}. \tag{B.16}$$

Plugging this back into eq. (B.14) yields a result for I_n.

$$I_n(\theta,\Theta) = \frac{2\pi}{\mathfrak{a}\sqrt{1-\mathfrak{b}^2}}\left(\frac{-1+\sqrt{1-\mathfrak{b}^2}}{\mathfrak{b}}\right)^{|n|} \tag{B.17a}$$

$$= \frac{2\pi}{|\cos\theta-\cos\Theta|}\left(\frac{1-\cos\Theta\cos\theta+|\cos\theta-\cos\Theta|}{\sin\Theta\sin\theta}\right)^{|n|} \tag{B.17b}$$

$$= \begin{cases} \dfrac{2\pi}{\cos\theta-\cos\Theta}\left(\dfrac{(1+\cos\Theta)(1-\cos\theta)}{(1-\cos\Theta)(1+\cos\theta)}\right)^{|n|/2}, & 0 \le \theta \le \Theta, \\ \dfrac{2\pi}{\cos\Theta-\cos\theta}\left(\dfrac{(1-\cos\Theta)(1+\cos\theta)}{(1+\cos\Theta)(1-\cos\theta)}\right)^{|n|/2}, & \Theta < \theta \le \pi. \end{cases} \tag{B.17c}$$

Appendix C

Random Realisations of the Astrometric Deflections on the Sky

The Figs. 5.3 and 5.5 show one possible realization of the GW background for the GR and transverse scalar polarizations respectively. In this appendix the method for producing such realizations is described.

Pick N distinct arbitrary points (or "stars") on the sky. The Cartesian coordinates of the i^{th} star are $\mathbf{n}_i = (x_i, y_i, z_i)$ and satisfy $x_i^2 + y_i^2 + z_i^2 = 1$. Consider the following vector of length $3N$ formed from the Cartesian coordinates,

$$\mathbf{x} = (x_1, y_1, z_1, x_2, y_2, z_2, \ldots, x_N, y_N, z_N). \tag{C.1}$$

The quantity one needs to find to find is the change in these coordinates, $\boldsymbol{\delta}\mathbf{x}$. Formally, this is distributed as a zero mean Gaussian random variable,

$$\boldsymbol{\delta}\mathbf{x} \sim \mathscr{N}(\mathbf{0}, \mathbf{C}), \tag{C.2}$$

with the $3N \times 3N$ correlation matrix formed block-by-block from the 3×3 spatial matrices defined in eq. 5.7;

$$\mathbf{C} = \left(\begin{array}{c|c|c|c} \boldsymbol{\Gamma}(\mathbf{n}_1, \mathbf{n}_1) & \boldsymbol{\Gamma}(\mathbf{n}_1, \mathbf{n}_2) & \ldots & \boldsymbol{\Gamma}(\mathbf{n}_1, \mathbf{n}_N) \\ \hline \boldsymbol{\Gamma}(\mathbf{n}_2, \mathbf{n}_1) & \boldsymbol{\Gamma}(\mathbf{n}_2, \mathbf{n}_2) & \ldots & \boldsymbol{\Gamma}(\mathbf{n}_2, \mathbf{n}_N) \\ \hline \vdots & \vdots & \ddots & \vdots \\ \hline \boldsymbol{\Gamma}(\mathbf{n}_N, \mathbf{n}_1) & \boldsymbol{\Gamma}(\mathbf{n}_N, \mathbf{n}_2) & \ldots & \boldsymbol{\Gamma}(\mathbf{n}_N, \mathbf{n}_N) \end{array}\right). \tag{C.3}$$

This is only valid formally, because the matrix $\mathbf{C}$ is not positive definite; in fact, it has N zero eigenvalues. The origin of this behavior is that the 3 Cartesian coordinates are being used to describe an intrinsically 2-dimensional process on the sphere. This can be rectified by instead considering the changes in the polar coordinates of each star;

$$\begin{pmatrix} \delta\theta_i \\ \delta\phi_i \end{pmatrix} = \mathbf{P}_i \cdot \begin{pmatrix} \delta x_i \\ \delta y_i \\ \delta z_i \end{pmatrix}, \quad \text{where} \quad \mathbf{P}_i = \begin{pmatrix} 0 & 0 & -\dfrac{1}{\sqrt{1-z_i^2}} \\ -\dfrac{y_i}{x_i^2+y_i^2} & \dfrac{x_i}{x_i^2+y_i^2} & 0 \end{pmatrix}. \tag{C.4}$$

$$\Rightarrow \quad \boldsymbol{\delta\theta} \equiv (\delta\theta_1, \delta\phi_1, \delta\theta_2, \delta\phi_2, \ldots, \delta\theta_N, \delta\phi_N) = \boldsymbol{\Pi} \cdot \boldsymbol{\delta}\mathbf{x} \quad \text{where} \quad \boldsymbol{\Pi} = \left(\begin{array}{c|c|c|c} \mathbf{P}_1 & \mathbf{0} & \ldots & \mathbf{0} \\ \hline \mathbf{0} & \mathbf{P}_2 & \ldots & \mathbf{0} \\ \hline \vdots & \vdots & \ddots & \vdots \\ \hline \mathbf{0} & \mathbf{0} & \ldots & \mathbf{P}_N \end{array}\right). \tag{C.5}$$

The matrix $\boldsymbol{\Pi}$ has shape $2N \times 3N$. The vector $\boldsymbol{\delta\theta}$ is also distributed as a Gaussian random variable, $\boldsymbol{\delta\theta} \sim \mathcal{N}(\mathbf{0}, \mathbf{C}')$, where the new covariance matrix $\mathbf{C}' = \boldsymbol{\Pi} \cdot \mathbf{C} \cdot \boldsymbol{\Pi}^{\mathrm{T}}$ is strictly positive definite. The parameter A is some overall amplitude chosen in Figs. 5.3 and 5.5 to be $A = 0.01$. A random realization of $\boldsymbol{\delta\theta}$ may now be obtained without an obstacle, and the vector $\boldsymbol{\delta}\mathbf{x}$ can be obtained by simple geometry.

The plots in Figs. 5.3 and 5.5 were produced using $N = 1000$ stars placed regularly on the sky, and show the original star positions, $\mathbf{x}$, and the new positions, $\mathbf{x} + \boldsymbol{\delta}\mathbf{x}$, joined by a smooth curves using the Mollweide projection.

Appendix D

The Transverse Scalar "Breathing" Mode Astrometric Integrals

In this appendix the evaluation of spatial correlation integrals for the transverse scalar GW polarization state, S, is briefly described. The integration is very similar to those for the $+$ and $\times$ states described in Appendix B. The relevant correlation integrals were defined in eqs. (5.18a) and (5.18d) as

$$\Gamma^S_{x\theta}(\Theta) = \int_{S^2} \mathrm{d}\Omega_{\mathbf{q}}\, \delta n^S_x(\mathbf{q})\, \delta m^S_\theta(\mathbf{q}) = \int_0^{2\pi} \mathrm{d}\phi \int_0^{\pi} \mathrm{d}\theta\, \sin\theta\, \delta n^S_x(\theta,\phi)\, \delta m^S_\theta(\theta,\phi)\,, \tag{D.1a}$$

$$\Gamma^S_{y\phi}(\Theta) = \int_{S^2} \mathrm{d}\Omega_{\mathbf{q}}\, \delta n^S_y(\mathbf{q})\, \delta m^S_\phi(\mathbf{q}) = \int_0^{2\pi} \mathrm{d}\phi \int_0^{\pi} \mathrm{d}\theta\, \sin\theta\, \delta n^S_y(\theta,\phi)\, \delta m^S_\phi(\theta,\phi)\,, \tag{D.1b}$$

where the vector $\mathbf{q} = (\sin\theta\cos\phi, \sin\theta\sin\phi, \cos\theta)$ is the direction on the sky from which the GW originates. The components of the astrometric deflections may be evaluated from the definitions in eqs. (5.16a), (5.17a), (5.16b), and (5.17b), using the formula for the astrometric deflection in eq. (3.20), the expression for the GW basis tensor in eq. (3.24c), and the expressions for the basis vectors tangent to the sphere in eqs. (5.11a), (5.12a), (5.11b), and (5.12b):

$$\delta n^S_x(\theta,\phi) = -\frac{1}{2}\sin\theta\cos\phi, \tag{D.2a}$$

$$\delta n^S_y(\theta,\phi) = \delta m^S_\phi(\theta,\phi) = -\frac{1}{2}\sin\theta\sin\phi, \tag{D.2b}$$

$$\delta m^S_\theta(\theta,\phi) = \frac{1}{2}\sin\Theta\cos\theta - \frac{1}{2}\cos\Theta\sin\theta\cos\phi. \tag{D.2c}$$

The azimuthal and polar integrals for $\Gamma^s_{x\theta}(\Theta)$ and $\Gamma^s_{y\phi}(\Theta)$ in eqs. (D.1a) and (D.1b) may be evaluated in the same way as those for $\Gamma^{+,\times}_{x\theta}(\Theta)$ and $\Gamma^{+,\times}_{y\phi}(\Theta)$ in Appendix B to give the results in eqs. (5.22a) and (5.22b) of the main text:

$$\Gamma^s_{x\theta}(\Theta) = \frac{\pi}{3}\cos\Theta \equiv \frac{\pi}{3} - \frac{2\pi}{3}\sin^2(\Theta/2)\,, \tag{5.22a}$$

$$\Gamma^s_{y\phi}(\Theta) = \frac{\pi}{3}. \tag{5.22b}$$

Appendix E

The Vectorial Astrometric Integrals

In this Appendix the evaluation of spatial correlation integrals for the vectorial GW polarization states, X and Y, is briefly described. The derivation is very similar to those for the $+$ and $\times$ states described in Appendix B. What is interesting in this case is that even though the standalone astrometric response in both vectorial polarizations is divergent at the origin (in Fig. 3.4 the "star terms" were added to remove this divergence), the correlation functions are perfectly regular and finite for all relevant values of Θ.

Firstly, the X mode is considered; the relevant correlation integrals were defined in eqs. (5.18a) and (5.18d) as

$$\Gamma^X_{x\theta}(\Theta) = \int_{S^2} \mathrm{d}\Omega_{\mathbf{q}}\, \delta n^X_x(\mathbf{q})\, \delta m^X_\theta(\mathbf{q}) = \int_0^{2\pi} \mathrm{d}\phi \int_0^{\pi} \mathrm{d}\theta\, \sin\theta\, \delta n^X_x(\theta,\phi)\, \delta m^X_\theta(\theta,\phi)\,, \tag{E.1a}$$

$$\Gamma^X_{y\phi}(\Theta) = \int_{S^2} \mathrm{d}\Omega_{\mathbf{q}}\, \delta n^X_y(\mathbf{q})\, \delta m^X_\phi(\mathbf{q}) = \int_0^{2\pi} \mathrm{d}\phi \int_0^{\pi} \mathrm{d}\theta\, \sin\theta\, \delta n^X_y(\theta,\phi)\, \delta m^X_\phi(\theta,\phi)\,, \tag{E.1b}$$

where the vector $\mathbf{q} = (\sin\theta\cos\phi, \sin\theta\sin\phi, \cos\theta)$ is the direction on the sky from which the GW originates. The components of the astrometric deflections may be evaluated from the definitions in eqs. (5.16a), (5.17a), (5.16b), and (5.17b), using the formula for the astrometric deflection in eq. (3.20), the expression for the GW basis tensor in eq. (3.24d), and the expressions for the basis vectors tangent to the sphere in eqs. (5.11a), (5.12a), (5.11b), and (5.12b):

$$\delta n^X_x(\theta,\phi) = \frac{1}{2}(1+2\cos\theta)\cos\phi\,, \tag{E.2a}$$

$$\delta n^X_y(\theta,\phi) = \frac{1}{2}(1+2\cos\theta)\sin\phi\,, \tag{E.2b}$$

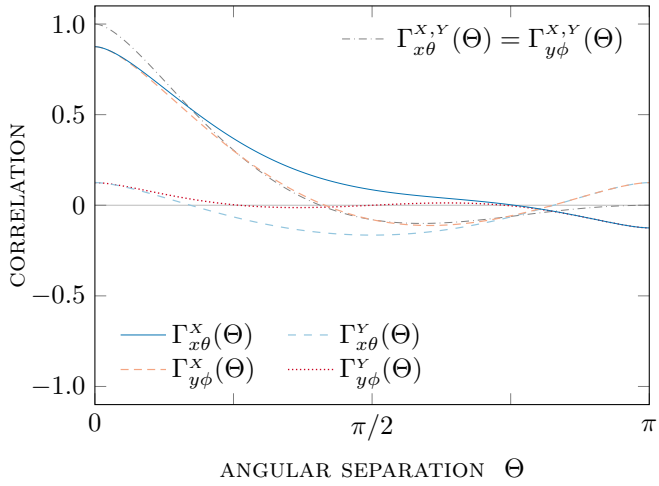

Fig. E.1 Plot of the vectorial correlation functions in eq. (5.25), normalized so that their absolute maximum is unity. Also shown are the functions for each of the two GR modes, given by eqs. (E.3a), (E.3b), (E.6a), and (E.6b), rescaled by the same normalization constant. Figure appeared in [60].

$$\delta m^{X}_{\theta}(\theta,\phi) = \frac{1}{1-\cos\Theta\cos\theta-\sin\Theta\sin\theta\cos\phi}\left(\frac{1}{8}\left(2\sin\Theta\sin\theta-3\sin(2\Theta)\sin(2\theta)\right)\right.$$
$$\left.+\frac{1}{2}\left(\cos\Theta\cos\theta-\cos(2\Theta)\cos(2\theta)\right)\cos\phi+\frac{1}{4}\left(\sin\Theta\,\sin\theta-\sin(2\Theta)\sin(2\theta)\right)\cos(2\phi)\right), \tag{E.2c}$$

$$\delta m^{X}_{\phi}(\theta,\phi) = \frac{1}{1-\cos\Theta\cos\theta-\sin\Theta\sin\theta\cos\phi}\left(\frac{1}{2}\cos\Theta\left(\cos\theta-\cos(2\theta)\right)\sin\phi\right.$$
$$\left.+\frac{1}{4}\left(\sin(2\Theta)\sin\theta-\sin\Theta\sin(2\theta)\right)\sin(2\phi)\right). \tag{E.2d}$$

The equations for $\delta m^{X}_{\theta}(\theta,\phi)$ and $\delta m^{X}_{\phi}(\theta,\phi)$ diverge when $\Theta = 0$. Nevertheless, the azimuthal and polar integrals for $\Gamma^{X}_{y\phi}(\Theta)$ and $\Gamma^{X}_{y\phi}(\Theta)$ in eqs. (E.1a) and (E.1b) may be evaluated in the same way as those for $\Gamma^{+,\times}_{x\theta}(\Theta)$ and $\Gamma^{+,\times}_{y\phi}(\Theta)$ in Appendix B to give two results that are regular for all values of Θ:

$$\Gamma^{X}_{x\theta}(\Theta) = \frac{\pi}{6}+\frac{2\pi}{3}\sin^2(\Theta/2)+6\pi\frac{\sin^2(\Theta/2)}{1-\sin^2(\Theta/2)}\ln(\sin(\Theta/2))$$
$$-2\pi\frac{\cos^2(\Theta/2)}{1-\cos^2(\Theta/2)}\ln(\cos(\Theta/2)), \tag{E.3a}$$

$$\Gamma^{X}_{y\phi}(\Theta) = \frac{13\pi}{6} + \pi\sin^2(\Theta/2) + 6\pi\,\frac{\sin^2(\Theta/2)}{1-\sin^2(\Theta/2)}\,\ln(\sin(\Theta/2)) + 2\pi\,\frac{\cos^2(\Theta/2)}{1-\cos^2(\Theta/2)}\,\ln(\cos(\Theta/2))\,. \tag{E.3b}$$

Secondly, the Y mode is considered; the relevant correlation integrals were defined in eqs. (5.18a) and (5.18d) as

$$\Gamma^{Y}_{x\theta}(\Theta) = \int_0^{2\pi}\mathrm{d}\phi\int_0^{\pi}\mathrm{d}\theta\,\sin\theta\,\delta n^{Y}_{x}(\theta,\phi)\,\delta m^{X}_{\theta}(\theta,\phi)\,, \tag{E.4a}$$

$$\Gamma^{Y}_{y\phi}(\Theta) = \int_0^{2\pi}\mathrm{d}\phi\int_0^{\pi}\mathrm{d}\theta\,\sin\theta\,\delta n^{Y}_{y}(\theta,\phi)\,\delta m^{X}_{\phi}(\theta,\phi)\,. \tag{E.4b}$$

The components of the astrometric deflections may be evaluated from the definitions in eqs. (5.16a), (5.17a), (5.16b), and (5.17b), using the formula for the astrometric deflection in eq. (3.20), the expression for the GW basis tensor in eq. (3.24e), and the expressions for the basis vectors tangent to the sphere in eqs. (5.11a), (5.12a), (5.11b), and (5.12b):

$$\delta n^{Y}_{x}(\theta,\phi) = \frac{1}{2}\cos\theta\sin\phi\,, \tag{E.5a}$$

$$\delta n^{Y}_{y}(\theta,\phi) = -\frac{1}{2}\cos\theta\cos\phi\,, \tag{E.5b}$$

$$\delta m^{Y}_{\theta}(\theta,\phi) = \frac{1}{1-\cos\Theta\cos\theta-\sin\Theta\sin\theta\cos\phi}\left(\frac{1}{2}\left(\cos(2\Theta)-\cos\Theta\cos\theta\right)\cos\theta\sin\phi + \frac{1}{4}\sin\Theta\left(2\cos\Theta-\cos\theta\right)\sin\theta\sin(2\phi)\right), \tag{E.5c}$$

$$\delta m^{Y}_{\phi}(\theta,\phi) = \frac{1}{1-\cos\Theta\cos\theta-\sin\Theta\sin\theta\cos\phi}\left(\frac{3}{16}\sin(2\Theta)\sin(2\theta) + \frac{1}{4}\left(1-2\cos\Theta\cos\theta+\cos(2\Theta)\cos(2\theta)\right)\cos\phi + \frac{1}{16}\left(\sin(2\Theta)\sin(2\theta)-8\sin\Theta\sin\theta\right)\cos(2\phi)\right). \tag{E.5d}$$

The integrals for $\Gamma^{Y}_{y\phi}(\Theta)$ and $\Gamma^{Y}_{y\phi}(\Theta)$ in eqs. (E.4a) and (E.4b) may be evaluated in the same way as the integrals in Appendix B:

$$\Gamma^{Y}_{x\theta}(\Theta) = \frac{7\pi}{6} + 2\pi\,\frac{\sin^2(\Theta/2)}{1-\sin^2(\Theta/2)}\,\ln(\sin(\Theta/2)) + 2\pi\,\frac{\cos^2(\Theta/2)}{1-\cos^2(\Theta/2)}\,\ln(\cos(\Theta/2))\,, \tag{E.6a}$$

$$\Gamma^{Y}_{y\phi}(\Theta) = -\frac{5\pi}{6} + \frac{5\pi}{3}\sin^2(\Theta/2) + 2\pi\frac{\sin^2(\Theta/2)}{1-\sin^2(\Theta/2)}\ln(\sin(\Theta/2)) \\ - 2\pi\frac{\cos^2(\Theta/2)}{1-\cos^2(\Theta/2)}\ln(\cos(\Theta/2))\,. \tag{E.6b}$$

As was described in the main text, for a unpolarised background containing equal power of both X and Y polarization states we may define the combined spatial correlation functions $\Gamma^{X,Y}_{x\theta}(\Theta) = \Gamma_{x\theta}(\Theta)^{X} + \Gamma^{Y}_{x\theta}(\Theta)$ and $\Gamma_{y\phi}(\Theta)^{X,Y} = \Gamma_{y\phi}(\Theta)^{X} + \Gamma^{Y}_{y\phi}(\Theta)$. These new functions may be evaluated by taking the sums of the expressions in eqs. (E.3a), (E.3b), (E.6a), and (E.6b) to give the results which appeared in eq. (5.25) of the main text,

$$\Gamma^{X,Y}_{x\theta}(\Theta) = \Gamma^{X,Y}_{y\phi}(\Theta) = \frac{4\pi}{3} + \frac{8\pi}{3}\sin^2(\Theta/2) + 8\pi\frac{\sin^2(\Theta/2)}{1-\sin^2(\Theta/2)}\ln(\sin(\Theta/2))\,. \tag{5.25}$$

The functions $\Gamma^{X}_{x\theta}(\Theta)$, $\Gamma^{X}_{y\phi}(\Theta)$, $\Gamma^{Y}_{y\phi}(\Theta)$, $\Gamma^{Y}_{x\theta}(\Theta)$, and $\Gamma^{X,Y}_{x\theta}(\Theta) = \Gamma^{X,Y}_{y\phi}(\Theta)$, are plotted in Fig. E.1.

Appendix F

The Scalar Longitudinal Astrometric Integrals

In this Appendix the evaluation of spatial correlation integrals for the longitudinal scalar GW polarization state, L, will be discussed. Using the method established in the previous Appendices will yield divergent curves. These result are still useful, and reasons for the anomaly are discussed in Section 5.1.4. A more careful calculation which removes the divergence is presented in Appendix F.1. The integration is very similar to those for the $+$ and $\times$ states described in Appendix B. The relevant correlation integrals were defined in eqs. (5.18a) and (5.18d) as

$$\Gamma^{L}_{x\theta}(\Theta) = \int_{S^2} \mathrm{d}\Omega_{\mathbf{q}}\, \delta n^{L}_{x}(\mathbf{q})\, \delta m^{L}_{\theta}(\mathbf{q}) = \int_0^{2\pi} \mathrm{d}\phi \int_0^{\pi} \mathrm{d}\theta\, \sin\theta\, \delta n^{L}_{x}(\theta,\phi)\, \delta m^{L}_{\theta}(\theta,\phi)\,, \tag{F.1a}$$

$$\Gamma^{L}_{y\phi}(\Theta) = \int_{S^2} \mathrm{d}\Omega_{\mathbf{q}}\, \delta n^{L}_{y}(\mathbf{q})\, \delta m^{L}_{\phi}(\mathbf{q}) = \int_0^{2\pi} \mathrm{d}\phi \int_0^{\pi} \mathrm{d}\theta\, \sin\theta\, \delta n^{L}_{y}(\theta,\phi)\, \delta m^{L}_{\phi}(\theta,\phi)\,. \tag{F.1b}$$

where the vector $\mathbf{q} = (\sin\theta\cos\phi, \sin\theta\sin\phi, \cos\theta)$ is the direction on the sky from which the GW originates. The components of the astrometric deflections may be evaluated from the definitions in eqs. (5.16a), (5.17a), (5.16b), and (5.17b), using the formula for the astrometric deflection in eq. (3.20), the expression for the GW basis tensor in eq. (3.24f), and the expressions for the basis vectors tangent to the sphere in eqs. (5.11a), (5.12a), (5.11b), and (5.12b):

$$\delta n^{L}_{x} = -\frac{1}{\sqrt{2}}\,\frac{\sin\theta\cos\theta\cos\phi}{1-\cos\theta}, \tag{F.2a}$$

$$\delta n^{L}_{y} = -\frac{1}{\sqrt{2}}\,\frac{\sin\theta\cos\theta\sin\phi}{1-\cos\theta}, \tag{F.2b}$$

$$\delta m^L_\theta = \frac{1}{\sqrt{2}\,(1-\cos\Theta\cos\theta-\sin\Theta\sin\theta\cos\phi)}\left(\frac{1}{8}\sin(2\Theta)\,(1+3\cos(2\theta))\right.$$
$$\left.+\frac{1}{4}\cos(2\Theta)\sin(2\theta)\,\cos\phi+\frac{1}{8}\sin(2\Theta)\,(\cos(2\theta)-1)\cos(2\phi)\right), \tag{F.2c}$$

$$\delta m^L_\phi = \frac{1}{\sqrt{2}\,(1-\cos\Theta\cos\theta-\sin\Theta\sin\theta\cos\phi)}\left(\frac{1}{2}\cos\Theta\sin(2\theta)\sin\phi\right.$$
$$\left.+\frac{1}{4}\sin\Theta\,(1-\cos(2\theta))\,\sin(2\phi)\right). \tag{F.2d}$$

The integrals for $\Gamma^L_{y\phi}(\Theta)$ and $\Gamma^L_{y\phi}(\Theta)$ in eqs. (F.1a) and (F.1b) may be evaluated in the same way as those for $\Gamma^{+,\times}_{x\theta}(\Theta)$ and $\Gamma^{+,\times}_{y\phi}(\Theta)$ in Appendix B to give the results presented in Section 5.1.4 of the main text,

$$\Gamma^L_{x\theta}(\Theta) = -\frac{10\pi}{3}+\frac{8\pi}{3}\sin^2(\Theta/2)-2\pi\frac{\ln(\sin(\Theta/2))}{1-\sin^2(\Theta/2)}, \tag{5.26a}$$

$$\Gamma^L_{y\phi}(\Theta) = -\frac{4\pi}{3}-2\pi\frac{\ln(\sin(\Theta/2))}{1-\sin^2(\Theta/2)}. \tag{5.26b}$$

As evident from Fig. 5.7, where these two curves are plotted, they diverge at $\Theta=0$. Obviously, this implies that in the context of the scalar longitudinal mode, the method for calculating the overlap reduction function is inapplicable. Below is presented a modified approach which solves the issue of the divergent curves.

F.1 Numerical Correlation Integrals on the Sphere

The cause of the divergence in eqs. (5.26a) and (5.26b) is the use of the distant-source version of the astrometric response in eq. (3.20). If the full astrometric response in eq. (3.19) is used instead the resulting spatial correlation is always finite (although no longer analytically tractable). All of the general discussion of the spatial correlation in Section 5.1 proceeds

exactly as before, except eq. (5.4) now becomes the distance dependent expression

$$\begin{aligned}\Delta_i^{\ jk}(\mathbf{n},\mathbf{q},d) = &\left(\left\{1+\frac{\mathrm{i}(2-q^r n_r)}{d(1-q^\ell n_\ell)}\left(1-\exp\left(-\mathrm{i}d(1-q^s n_s)\right)\right)\right\} n_{\hat{\imath}}\right.\\ &\left.-\left\{1+\frac{\mathrm{i}}{d(1-q^\ell n_\ell)}\left(1-\exp\left(-\mathrm{i}d(1-q^s n_s)\right)\right)\right\} q_{\hat{\imath}}\right)\frac{n^j n^k}{2(1-q^\ell n_\ell)}\\ &-\left\{\frac{1}{2}+\frac{\mathrm{i}}{d(1-q^\ell n_\ell)}\left(1-\exp\left(-\mathrm{i}d(1-q^s n_s)\right)\right)\right\}\delta_i^{\ j} n^k\,,\end{aligned} \tag{F.4}$$

where $d=\omega\lambda_s\Omega$ is a measure of the distance to the star (in gravitational wavelengths). With this form of $\Delta_i^{\ jk}$, the integral becomes regular for all relevant values of Θ. The correlation curve is now a 3-parameter function of the angle on the sky Θ and the distances to both stars, d_n and d_m:

$$\begin{aligned}\Gamma^L_{x\theta}(\Theta,d_n,d_m) &= \int_{S^2}\mathrm{d}\Omega_{\mathbf{q}}\;\delta n^L_x(\mathbf{q},d_n)\,\delta m^L_\theta(\mathbf{q},d_m)\\ &= \int_0^{2\pi}\mathrm{d}\phi\int_0^{\pi}\mathrm{d}\theta\,\sin\theta\,\delta n^L_x(\theta,\phi,d_n)\,\delta m^L_\theta(\theta,\phi,d_m)\,,\end{aligned} \tag{F.5a}$$

$$\begin{aligned}\Gamma^L_{y\phi}(\Theta,d_n,d_m) &= \int_{S^2}\mathrm{d}\Omega_{\mathbf{q}}\;\delta n^L_y(\mathbf{q},d_n)\,\delta m^L_\phi(\mathbf{q},d_m)\\ &= \int_0^{2\pi}\mathrm{d}\phi\int_0^{\pi}\mathrm{d}\theta\,\sin\theta\,\delta n^L_y(\theta,\phi,d_n)\,\delta m^L_\phi(\theta,\phi,d_m)\,.\end{aligned} \tag{F.5b}$$

The vector $\mathbf{q}=(\sin\theta\cos\phi,\sin\theta\sin\phi,\cos\theta)$ is the direction on the sky from which the GW originates. The components of the astrometric deflections may be evaluated from the definitions in eqs. (5.16a), (5.17a), (5.16b), and (5.17b), using the formula for the astrometric deflection in eq. (3.19), the expression for the GW basis tensor in eq. (3.24f), and the expressions for the basis vectors tangent to the sphere in eqs. (5.11a), (5.12a), (5.11b), and (5.12b). Unfortunately, the integrals in eqs. (F.5a) and (F.5b) can no longer be solved using the same method as above, and need to be evaluated numerically. Let $\mathscr{L}_{x\theta}(\Theta)$ be the result of numerically evaluating $\Gamma^L_{x\theta}(\Theta)$ and $\mathscr{L}_{y\phi}(\Theta)$ be the result of numerically evaluating $\Gamma^L_{y\phi}(\Theta)$. In Fig. 5.7 two curves $\mathscr{L}_{x\theta}(\Theta)$ and $\mathscr{L}_{y\phi}(\Theta)$ are shown as examples of these integrals for $(d_n,d_m)=(100,200)$. It becomes evident that the numerical curves tend to the two analytic functions (5.26a) and (5.26b) for large Θ.

F.2 Correlation integrals for stars in the same direction on the sky

Integrals (F.5a) and (F.5b) can be solved analytically for the case $\Theta = 0$ (and also for $\Theta = \pi$) to give a 2-parameter family of functions which quantifies the correlation between the astrometric deflections of stars with the same position on the sky but located at different distances,

$$\begin{aligned}\Sigma^L(d_{\mathbf{n}}, d_{\mathbf{m}}) &= \int_0^{2\pi} \mathrm{d}\phi \int_0^{\pi} \mathrm{d}\theta\, \sin\theta\, \delta n_x^L(d_{\mathbf{n}}, \theta, \phi)\, \delta m_\theta^L(d_{\mathbf{m}}, \theta, \phi)\Big|_{\Theta=0} \\ &= \int_0^{2\pi} \mathrm{d}\phi \int_0^{\pi} \mathrm{d}\theta\, \sin\theta\, \delta n_x^L(d_{\mathbf{n}}, \theta, \phi)\, \delta n_x^L(d_{\mathbf{m}}, \theta, \phi).\end{aligned} \tag{F.6}$$

The derivation involves a simple azimuthal integral which yields another straightforward polar integral. The components of the astrometric deflections (at $\Theta = 0$) may be evaluated from the definitions in eqs. (5.16a), (5.17a), (5.16b), and (5.17b), using the formula for the astrometric deflection in eq. (3.19), the expression for the GW basis tensor in eq. (3.24f), and the expressions for the basis vectors tangent to the sphere in eqs. (5.11a), (5.12a), (5.11b), and (5.12b):

$$\begin{aligned}\delta n_x^L(d,\theta,\phi) = \delta n_y^L(d,\theta,\phi) &= -\frac{1}{\sqrt{2}}\left(\frac{\cos^3(\theta/2)}{\sin(\theta/2)} - \sin(\theta/2)\cos(\theta/2)\right)\cos\phi \\ &+ \frac{1}{2\sqrt{2}\,d}\left(3 - 2\cos^2(\theta/2)\right)\left(\frac{\cos^3(\theta/2)}{\sin^3(\theta/2)} - \frac{\cos(\theta/2)}{\sin(\theta/2)}\right)\sin\left(2d\sin^2(\theta/2)\right)\cos\phi\,.\end{aligned} \tag{F.7}$$

The integral for $\Sigma^L(d_{\mathbf{n}}, d_{\mathbf{m}})$ in eq. (F.6) may be evaluated using a computer algebra package to give

$$\begin{aligned}\Sigma^L(d_{\mathbf{n}}, d_{\mathbf{m}}) &= \pi\gamma + \pi\ln(2) - \frac{29\pi}{30} + \frac{33\pi}{d_{\mathbf{n}}^4} + \frac{33\pi}{d_{\mathbf{m}}^4} + \frac{11\pi}{2\,d_{\mathbf{n}}^2} + \frac{11\pi}{2\,d_{\mathbf{m}}^2} - \frac{90\pi}{\left(d_{\mathbf{n}}^2 - d_{\mathbf{m}}^2\right)^2} + \pi\ln(d_{\mathbf{n}} d_{\mathbf{m}}) \\ &- \pi\,\frac{(d_{\mathbf{n}} + d_{\mathbf{m}} - 2)\,(d_{\mathbf{n}} + d_{\mathbf{m}} + 2)}{4\,d_{\mathbf{n}} d_{\mathbf{m}}}\ln(d_{\mathbf{n}} + d_{\mathbf{m}}) \\ &+ \pi\,\frac{(d_{\mathbf{n}} - d_{\mathbf{m}} - 2)\,(d_{\mathbf{n}} - d_{\mathbf{m}} + 2)}{4\,d_{\mathbf{n}} d_{\mathbf{m}}}\ln|d_{\mathbf{n}} - d_{\mathbf{m}}| \\ &- \pi\,\mathrm{Ci}(2d_{\mathbf{n}}) - \pi\,\mathrm{Ci}(2d_{\mathbf{m}}) - \frac{9\pi}{2\,d_{\mathbf{n}}}\,\mathrm{Si}(2d_{\mathbf{n}}) - \frac{9\pi}{2\,d_{\mathbf{m}}}\,\mathrm{Si}(2d_{\mathbf{m}}) \\ &+ \pi\,\frac{(d_{\mathbf{n}} + d_{\mathbf{m}} - 2)\,(d_{\mathbf{n}} + d_{\mathbf{m}} + 2)}{4\,d_{\mathbf{n}} d_{\mathbf{m}}}\,\mathrm{Ci}(2(d_{\mathbf{n}} + d_{\mathbf{m}}))\end{aligned}$$

$$
\begin{aligned}
&- \pi \frac{(d_{\mathbf{n}} - d_{\mathbf{m}} - 2)(d_{\mathbf{n}} + d_{\mathbf{m}} + 2)}{4 d_{\mathbf{n}} d_{\mathbf{m}}} \mathrm{Ci}(2|d_{\mathbf{n}} - d_{\mathbf{m}}|) \\
&+ \frac{15\pi (d_{\mathbf{n}} + d_{\mathbf{m}})}{4 d_{\mathbf{n}} d_{\mathbf{m}}} \mathrm{Si}(2(d_{\mathbf{n}} + d_{\mathbf{m}})) - \frac{15\pi (d_{\mathbf{n}} - d_{\mathbf{m}})}{4 d_{\mathbf{n}} d_{\mathbf{m}}} \mathrm{Si}(2|d_{\mathbf{n}} - d_{\mathbf{m}}|)\big) \\
&- \pi \frac{5 d_{\mathbf{n}}^2 - 54}{2 d_{\mathbf{n}}^4} \cos(2d_{\mathbf{n}}) - \pi \frac{5 d_{\mathbf{m}}^2 - 54}{2 d_{\mathbf{m}}^4} \cos(2d_{\mathbf{m}}) + \pi \frac{d_{\mathbf{n}}^4 + 11 d_{\mathbf{n}}^2 - 60}{2 d_{\mathbf{n}}^5} \sin(2d_{\mathbf{n}}) \\
&+ \pi \frac{d_{\mathbf{m}}^4 + 11 d_{\mathbf{m}}^2 - 60}{2 d_{\mathbf{m}}^5} \sin(2d_{\mathbf{m}}) \\
&- \frac{10\pi}{\left(d_{\mathbf{n}}^2 - d_{\mathbf{m}}^2\right)^2} \cos(2d_{\mathbf{n}}) \cos(2d_{\mathbf{m}}) \\
&- \pi \frac{\left(d_{\mathbf{n}}^2 - d_{\mathbf{m}}^2\right)^3 - 12\left(d_{\mathbf{n}}^2 - d_{\mathbf{m}}^2\right)^2 + 100\left(d_{\mathbf{n}}^2 + 3 d_{\mathbf{m}}^2\right)}{4\left(d_{\mathbf{n}}^2 - d_{\mathbf{m}}^2\right)^3 d_{\mathbf{m}}} \cos(2d_{\mathbf{n}}) \sin(2d_{\mathbf{m}}) \\
&+ \pi \frac{\left(d_{\mathbf{n}}^2 - d_{\mathbf{m}}^2\right)^3 + 12\left(d_{\mathbf{n}}^2 - d_{\mathbf{m}}^2\right)^2 - 100\left(d_{\mathbf{n}}^2 + 3 d_{\mathbf{m}}^2\right)}{4\left(d_{\mathbf{n}}^2 - d_{\mathbf{m}}^2\right)^3 d_{\mathbf{n}}} \sin(2d_{\mathbf{n}}) \cos(2d_{\mathbf{m}}) \\
&+ \frac{\pi}{8 d_{\mathbf{n}} d_{\mathbf{m}}} \left(\frac{20}{(d_{\mathbf{n}} + d_{\mathbf{m}})^2} + \frac{20}{(d_{\mathbf{n}} - d_{\mathbf{m}})^2} + 31 \right) \sin(2d_{\mathbf{n}}) \sin(2d_{\mathbf{m}}) \,. \qquad \text{(F.8)}
\end{aligned}
$$

Here, $\gamma = 0.57722$ is the Eüler-Mascheroni constant, and $\mathrm{Ci}(\bullet)$ and $\mathrm{Si}(\bullet)$ are the cosine and sine integrals, respectively.

Appendix G

Kerr space-time

Since the background we consider in this part of the dissertation is exclusively the Kerr space-time, it is worth providing a summary of the metric for a rotating non-charged black hole. Alternatively, a charged and spinning black hole is described by the Kerr-Newman metric, while a non-rotating charged black hole solution is given by the Reissner-Nordstöm background. The Kerr metric, in Boyer-Lindquist coordinates [142] (t, r, θ, ϕ), is given by:

$$\begin{aligned} \mathrm{d}s^2 = &-\frac{\Delta - a^2 \sin^2\theta}{\Sigma}\mathrm{d}t^2 - 2a\sin^2\theta\frac{r^2+a^2-\Delta}{\Sigma}\mathrm{d}t\mathrm{d}\phi \\ &+ \frac{\left(r^2+a^2\right)^2 - \Delta a^2\sin^2\theta}{\Sigma}\sin^2\theta\mathrm{d}\phi^2 + \frac{\Sigma}{\Delta}\mathrm{d}r^2 + \Sigma\mathrm{d}\theta^2 \end{aligned} \tag{G.1a}$$

where

$$\Delta(r) = r^2 - 2Mr + a^2 \,, \tag{G.1b}$$

$$\Sigma(r,\theta) = r^2 + a^2\cos^2\theta \,, \tag{G.1c}$$

and $a = \mathscr{L}_z/M$ is the specific black hole spin parameter. This metric is singular at the points where $\theta = \{0, \pi\}$, however these are the usual coordinate singularities associated with the spherical polar system, remedied by the introduction of a second coordinate system. Further, we encounter coordinate singularities at the points where $\Delta(r) = 0$, i.e., for values of the radial coordinate $r_\pm = M \pm \sqrt{M^2 + a^2}$. To demonstrate that these are merely coordinate singularities (and not an inherent curvature singularity of the metric), it is customary to make the change to Kerr coordinates (v, r, θ, χ), given by [143]:

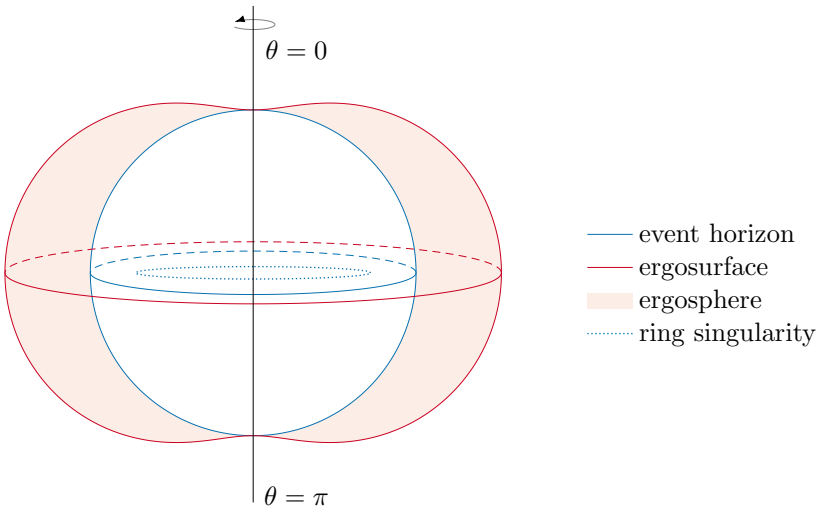

Fig. G.1 Visualisation of the Kerr space-time for $a/M = 0.95$. Figure appeared in [1].

$$\mathrm{d}v = \mathrm{d}t + \frac{r^2 + a^2}{\Delta}\mathrm{d}r\,, \tag{G.2a}$$

$$\mathrm{d}\chi = \mathrm{d}\phi + \frac{a}{\Delta}\mathrm{d}r\,. \tag{G.2b}$$

This shows that the metric could be analytically continued through the surface $r_\pm$ to the region $0 < r < r_+$:

$$\begin{aligned}\mathrm{d}s^2 = &-\frac{\Delta - a^2\sin^2\theta}{\Sigma}\mathrm{d}v^2 + 2\mathrm{d}v\mathrm{d}r - 2a\sin^2\theta\,\frac{r^2 + a^2 - \Delta}{\Sigma}\mathrm{d}v\mathrm{d}\chi \\ &- 2a\sin^2\theta\mathrm{d}\chi\mathrm{d}r + \frac{\left(r^2 + a^2\right)^2 - \Delta a^2\sin^2\theta}{\Sigma}\sin^2\theta\mathrm{d}\chi^2 + \Sigma\mathrm{d}\theta^2.\end{aligned} \tag{G.3}$$

The surface $r = r_+ = M + \sqrt{M^2 - a^2}$ is a null hypersurface with normal 4-vector given by

$$\xi^a = \left(\frac{\partial}{\partial v}\right)^a + \frac{a}{a^2 + r_+^2}\left(\frac{\partial}{\partial\chi}\right)^a = \left(\frac{\partial}{\partial v}\right)^a + \Omega_{\mathrm{Kerr}}\left(\frac{\partial}{\partial\chi}\right)^a \tag{G.4}$$

and the region $r \leq r_+$ is (part of) the black hole region. Ω is the angular velocity of the black hole with respect to an observer at infinity. There are several important surfaces in the Kerr space-time. Firstly, the curvature singularity $r = 0$ is in fact a ring singularity, which can be explained as follows. A rotating black hole would not be spherically symmetric, as matter would bulge around the equator, the effect quantified by the spin parameter a.

Since a point singularity cannot support angular momentum, the lowest-dimensional shape required is a ring. This is evidenced by substituting $t \equiv const.$, $r = 0$, $\theta = \pi/2$ (i.e., the singularity associated with $\Sigma(r,\theta) = 0$) in eq. (G.1a), obtaining $\mathrm{d}s^2 = a^2\mathrm{d}\phi^2$, i.e., a ring of radius a. Another important surface is the event horizon $r_+ = M + \sqrt{M^2 - a^2}$. To understand the final feature of interest, we consider the norm of the Killing vector field $(\partial/\partial t)^a$ in Boyer-Lindquist coordinates:

$$\left(\frac{\partial}{\partial t}\right)^2 = -\frac{\Delta - a^2\sin^2\theta}{\Sigma} = -1 + \frac{2Mr}{r^2 + a^2\sin^2\theta} \tag{G.5}$$

and notice that it is space-like ($(\partial/\partial t)^2 < 0$) in the following region outside the event horizon $r = r_+$:

$$M + \sqrt{M^2 - a^2} < r < M + \sqrt{M^2 - a^2\cos^2\theta}. \tag{G.6}$$

This region is called the ergosphere, and its outside surface is named the ergosurface, which intersects the event horizon at the poles $\theta = 0, \pi$. These surfaces are illustrated on the Kerr black-hole schematic on Fig. G.1.

Appendix H

Geodesic constants

One immediately notices that the Kerr metric does not depend on the time coordinate, t, or the azimuthal angle, ϕ. Therefore, using the Euler-Lagrange equations, it can be shown that the conjugate momenta $p_\mu = \partial\mathscr{L}/\partial\dot{q}^\mu$ associated to those coordinates are constant with respect to the affine parameter of the geodesic:

$$\frac{\mathrm{d}}{\mathrm{d}\tau}\left(\frac{\partial\mathscr{L}}{\partial\dot{q}^\mu}\right) = \frac{\partial\mathscr{L}}{\partial q^\mu} \quad \Leftrightarrow \quad \frac{\mathrm{d}p_\mu}{\mathrm{d}\tau} = \frac{\partial\mathscr{L}}{\partial q^\mu} = 0 \quad \Leftrightarrow \quad \begin{cases} p_t \equiv const. \\ p_\phi \equiv const.\,, \end{cases} \tag{H.1}$$

where in general relativity, the Lagrangian is formally given by $\mathscr{L}(q,\dot{q}) = {}^1\!/_2\, g_{\mu\nu}\dot{q}^\mu\dot{q}^\nu$. Thus we have identified 2 quantities which are constant along geodesics of the Kerr space-time. These are related to the energy of the orbit $\mathscr{E}$, and the axial component of the angular momentum $\mathscr{L}_z$, respectively:

$$\mathscr{E} = -p_t = -g_{t\nu}\dot{q}^\nu = \frac{\Delta - a^2\sin^2\theta}{\Sigma}\,\dot{t} + a\sin^2\theta\,\frac{r^2+a^2-\Delta}{\Sigma}\,\dot{\phi} \tag{H.2}$$

$$\mathscr{L}_3 = p_\phi = g_{\phi\nu}\dot{q}^\nu = -a\sin^2\theta\,\frac{r^2+a^2-\Delta}{\Sigma}\,\dot{t} + \frac{\left(r^2+a^2\right)^2 - \Delta a^2\sin^2\theta}{\Sigma}\,\sin^2\theta\,\dot{\phi} \tag{H.3}$$

For equatorial geodesics ($\theta = {}^\pi\!/_2$), these two constants are sufficient to uniquely determine a given geodesic. However, for general geodesics with 3 spatial degrees of freedom, we can identify a third constant of the motion, which is not associated with a linear symmetry of the background space-time.

Apart from the two Killing vectors associated with the Kerr metric, there exists a second-order Killing tensor for this background, $Q_{\mu\nu}$. This Killing tensor gives rise to another conserved quantity, which was originally discovered in 1968 as a consequence of the sep-

arable Hamilton-Jacobi equation. This quantity is called the Carter's constant, and can be written as [117]:

$$\mathscr{Q} = Q^{\mu\nu} p_\mu p_\nu = p_\theta^2 + \cos^2\theta \left(a^2 \left(m^2 - \mathscr{E}^2 \right) + \left(\frac{\mathscr{L}_z}{\sin\theta} \right)^2 \right). \tag{H.4}$$

Appendix I

Geodesics of the Kerr metric

The equatorial geodesics of the Kerr metric can be characterised by the constants $\mathscr{E}$ and $\mathscr{L}_z$, combined with the Hamiltonian, which is an additional integral of motion. General 3-dimensional geodesics, however, require the introduction of a further integral of motion, Carter's constant, discussed in Appendix H. The equations of motion for a massless particle, as per [13], are given by

$$\frac{\mathrm{d}t}{\mathrm{d}\tau} = \frac{1}{\Delta}\left(\left(r^2 + a^2\,\frac{2Ma^2}{r}\right)\mathscr{E} - \frac{2Ma}{r}\,\mathscr{L}_z^2\right) \tag{I.1a}$$

$$\frac{\mathrm{d}r}{\mathrm{d}\tau} = \pm\frac{1}{\Sigma}\sqrt{\Big(\mathscr{E}\big(r^2+a^2\big) - a\,\mathscr{L}_z\Big)^2 - \Delta\Big(\mathscr{Q} + (\mathscr{L}_z - a\mathscr{E})^2\Big)} \tag{I.1b}$$

$$\frac{\mathrm{d}\theta}{\mathrm{d}\tau} = \pm\frac{1}{\Sigma}\sqrt{\mathscr{Q} + \cos^2\theta\left(a^2\mathscr{E}^2 - \frac{\mathscr{L}_z}{\sin^2\theta}\right)} \tag{I.1c}$$

$$\frac{\mathrm{d}\phi}{\mathrm{d}\tau} = \frac{1}{\Delta}\left(\left(1 - \frac{2M}{r}\right)\mathscr{L}_z + \frac{2Ma}{r}\,\mathscr{E}\right) \tag{I.1d}$$

In the general case, these equation cannot be solved analytically to find a closed form of the shape of the geodesic. However, it is possible to integrate the equations numerically to find an approximate shape for a Kerr geodesic, and one possible solutions is shown in Fig. I.1. The Kerr geodesics are not closed, but rather fill the entire parameter space $r_{\mathrm{MIN}} < r < r_{\mathrm{MAX}}$, $\theta_{\mathrm{MIN}} < \theta < \theta_{\mathrm{MAX}}$, $0 < \phi < 2\pi$ (which has the shape of a torus) before returning to the starting (r, θ, ϕ). Moreover, the plane of inclination of the orbit is not stationary, but precesses around the black hole. In the case of a resonance, when two of the frequencies become commensurate,

this configuration breaks down and the geodesic becomes a (simpler) closed curve around the black hole, defined only by 2 parameters.

(a) Projections of the geodesic on the principal planes.

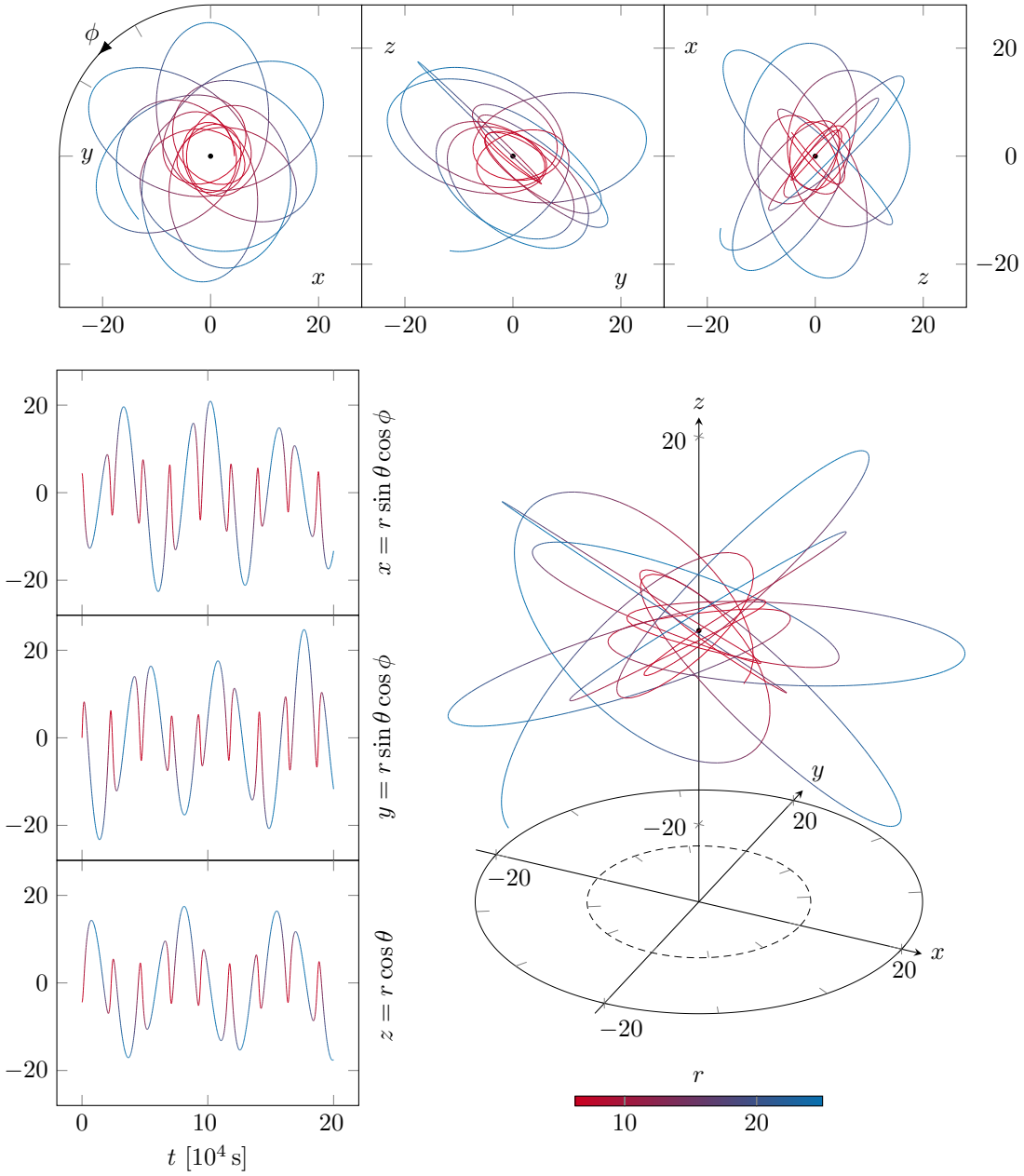

(b) Evolution of the coordinates x, y and z with physical time t.

(c) A 3-dimensional view of the geodesic in Cartesian and cylindrical coordinate systems.

Fig. I.1 A geodesic of the Kerr metric, and several projections, evolved for a period of 2×10^5 s ≈ 5.56 hours. The orbit has eccentricity $e = 0.6$ and semi-latus rectum $10M$, while the central black hole has mass $M = 10^6 M_\odot$ and spin $0.9M^2$. All distances are in units of the black-hole mass M. The angle of inclination is $\iota = 45°$, and the plane of inclination precesses. Figure appeared in [1].

Appendix J

Fresnel integrals

In the course of solving the phase resonance equations, as well as in the presentation of the frequency resonance solution, we encounter integrals of trigonometric functions with quadratic arguments:

$$\int_0^x \mathrm{d}y \sin\left(\frac{\pi y^2}{2}\right) \quad \text{and} \quad \int_0^x \mathrm{d}y \cos\left(\frac{\pi y^2}{2}\right). \tag{J.1}$$

These are known as the Fresnel integrals, after the French engineer and physicist Augustin-Jean Fresnel, who used them in optics. Here, we have adopted the notation where the argument of the integrand is premultiplied by $\pi/2$. Please note that this definition is equivalent to the one used in [114]:

$$C(x) = \frac{\sqrt{2}}{\sqrt{\pi}} \int_0^x \mathrm{d}y \cos\left(y^2\right). \tag{J.2}$$

These integrals are not directly solvable analytically, and therefore other methods for integration must be used. One approach to finding the two integrals in (J.1) is by expanding the integrands in converging Taylor series:

$$\begin{aligned} S(x) &= \int_0^x \mathrm{d}y \sin\left(\frac{\pi y^2}{2}\right) \\ &= \sum_{n=0}^{\infty} \frac{(-1)^n}{(2n+1)!} \int_0^x \mathrm{d}y \left(\frac{\pi y^2}{2}\right)^{2n+1} = \sum_{n=0}^{\infty} \frac{(-1)^n \pi^{2n+1}}{(2n+1)!\,(4n+3)\,2^{2n+1}} x^{4n+3}, \end{aligned} \tag{J.3a}$$

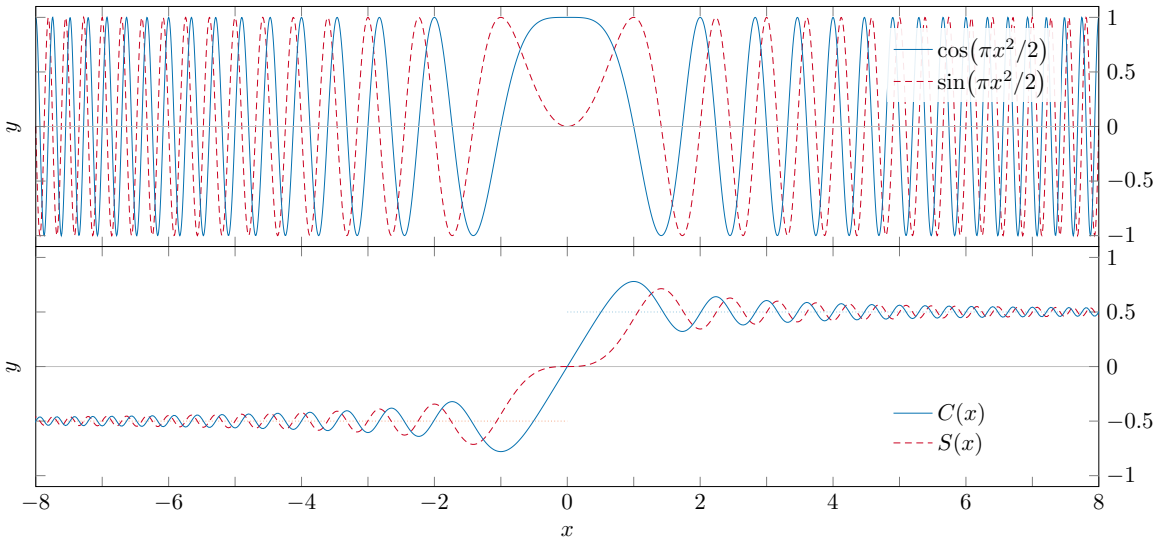

Fig. J.1 *Upper panel:* the integrands of the two Fresnel integrals, the functions $\cos\left(\pi x^2/2\right)$ and $\sin\left(\pi x^2/2\right)$, and the axis $y=0$ around which they oscillate. The frequency of oscillation increases with the absolute value of x. *Lower panel:* numerical integration of the functions above gives the desired graphs of $C(x)$ and $S(x)$. They converge towards the line $y=\pm 1/2$. Figure appeared in [1].

$$\begin{aligned} C(x) &= \int_0^x \mathrm{d}y \cos\left(\frac{\pi y^2}{2}\right) \\ &= \sum_{n=0}^{\infty} \frac{(-1)^n}{(2n)!} \int_0^x \mathrm{d}y \left(\frac{\pi y^2}{2}\right)^{2n} = \sum_{n=0}^{\infty} \frac{(-1)^n \pi^{2n}}{(2n)!\,(4n+1)\,2^{2n}} x^{4n+1}. \end{aligned} \tag{J.3b}$$

Often, a symbol like the ones appearing on the left-hand sides of eqs. (J.3) are used in lieu of the actual series solutions. Hence, it is useful to know the first few terms of the series for each of the integrals:

$$S(x) = \frac{\pi}{6}x^3 - \frac{\pi^3}{336}x^7 + \mathscr{O}\left(x^{11}\right), \tag{J.4a}$$

$$C(x) = x - \frac{\pi^2}{40}x^5 + \mathscr{O}\left(x^9\right). \tag{J.4b}$$

The integrands and the integral functions are plotted in Fig. J.1. I make note of several features: at $x=0$, $S(x)$ starts flat, and progresses as $\sim x^3$, while $C(x)$ is linear. For positive or negative infinity, both functions tend to $\pm 1/2$, and can be represented by an asymptotic expansion for large absolute values of x:

$$S(x) = \frac{\operatorname{sgn}(x)}{2} - \frac{1}{\pi x}\cos\left(\frac{\pi x^2}{2}\right) - \frac{1}{\pi^2 x^3}\sin\left(\frac{\pi x^2}{2}\right) + \frac{3}{\pi^3 x^5}\cos\left(\frac{\pi x^2}{2}\right) + \mathscr{O}\left(x^{-6}\right), \tag{J.5a}$$

$$C(x) = \frac{\operatorname{sgn}(x)}{2} + \frac{1}{\pi x}\sin\left(\frac{\pi x^2}{2}\right) - \frac{1}{\pi^2 x^3}\cos\left(\frac{\pi x^2}{2}\right) - \frac{3}{\pi^3 x^5}\sin\left(\frac{\pi x^2}{2}\right) + \mathscr{O}\left(x^{-6}\right). \quad \text{(J.5b)}$$

Appendix K

Shorthand trigonometric notation

In eqs. (9.20) we define the following to make the discussion regarding the frequency mode equation easier to read:

$$S_n(x) \equiv \sin\left[n\left(ax+(1+b)x^2\right)\right] \quad \text{(9.20a)} \quad C_n(x) \equiv \cos\left[n\left(ax+(1+b)x^2\right)\right]. \quad \text{(9.20b)}$$

for some arbitrary constants a and b.

Please note that these are different from the Fresnel integrals, denoted by the same letters, but without subscripts, discussed in Appendix J. These functions are plotted for several representative values of n in Fig. K.1. It is worth noting several identities which we make use of, but do not derive explicitly. These follow directly from the product-to-sum formulae and the double angle formulae in trigonometry.

$$S_n(x)S_m(x) = \frac{1}{2}\left(C_{(n-m)}(x) - C_{(n+m)}(x)\right) \tag{K.2a}$$

$$S_n(x)C_m(x) = \frac{1}{2}\left(S_{(n+m)}(x) - S_{(n-m)}(x)\right) \tag{K.2b}$$

$$C_n(x)C_m(x) = \frac{1}{2}\left(C_{(n-m)}(x) + C_{(n+m)}(x)\right) \tag{K.2c}$$

$$S_n^2(x) = \frac{1}{2}\left(1 - C_{2n}(x)\right) \tag{K.2d}$$

$$C_n^2(x) = \frac{1}{2}\left(1 + C_{2n}(x)\right) \tag{K.2e}$$

I only consider positive values of the subscripts, with the following rules for negative values: $S_{-n}(x) = -S_n(x)$ and $C_{-n}(x) = C_n(x)$. It is important to note that these functions are linearly independent, i.e., they form a basis in functional space. This is most easily verified

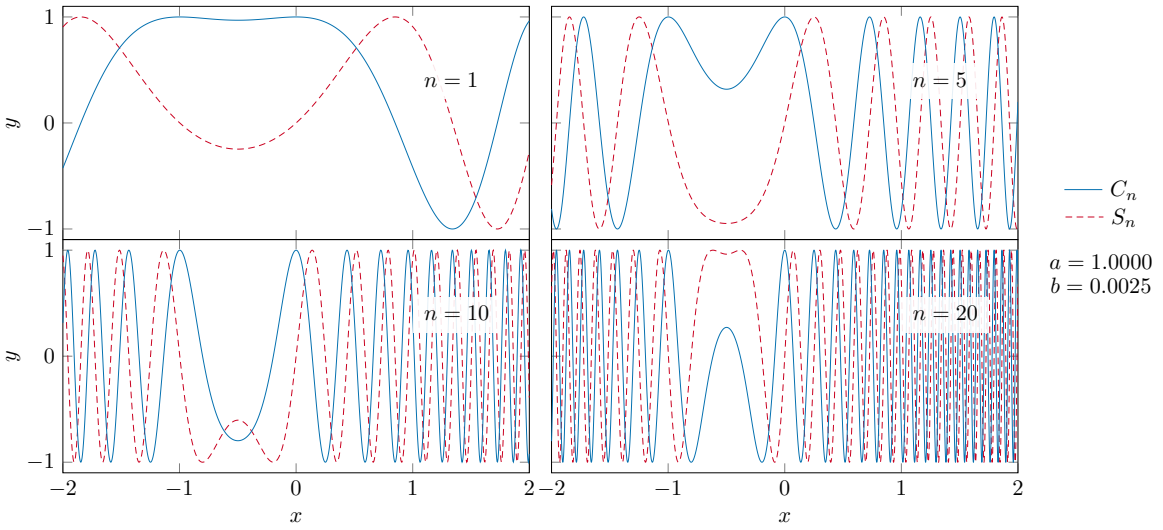

Fig. K.1 The functions $S_n(x)$ and $C_n(x)$ for several values of n. As we can see, the functions oscillate (away from the region around $x = 0$) more rapidly as n increases. I have used values of $a = 1$ and $b = 0.0025$ for the constants. Figure appeared in [1].

by considering the Wronskian for the sequence of functions

$$f_0(x) = 1, \quad f_1(x) = S_1(x), \quad f_2(x) = C_1(x), \quad f_3(x) = S_2(x), \quad f_4(x) = C_2(x) \text{ and so on.} \tag{K.3}$$

For $\{f_0(x), f_1(x), f_2(x)\}$, the Wronskian is $-(a+2(1+b)x)^3$, while for the first 5 functions in the series, it is $72(a+2(1+b)x)^{10}$, both of which do not vanish in the general case. Since their Wronskian does not vanish, we can conclude that these functions are linearly independent over $\mathbb{R}\setminus\{0\}$:

$$W(f_0, f_1, f_2, \ldots)(x) = \det \begin{vmatrix} f_0(x) & f_1(x) & f_2(x) & f_3(x) & f_4(x) & \\ f_0'(x) & f_1'(x) & f_2'(x) & f_3'(x) & f_4'(x) & \cdots \\ f_0''(x) & f_1''(x) & f_2''(x) & f_3''(x) & f_4''(x) & \\ & & \vdots & & & \ddots \end{vmatrix} \neq 0. \tag{K.4}$$

It should be noted that these functions are not orthogonal. First, we show how to integrate a single factor of $S_n(x)$:

$$\int_{-\infty}^{\infty} \mathrm{d}x\, S_n(x) = \lim_{\substack{L_1\to-\infty \\ L_2\to+\infty}} \int_{L_1}^{L_2} \mathrm{d}x \sin\left[\frac{\pi}{2}\left(\sqrt{\frac{2n(1+b)}{\pi}}\left(x+\frac{a}{2(1+b)}\right)\right)^2 - \frac{na^2}{4(1+b)}\right]$$

$$= \lim_{\substack{L_1\to-\infty \\ L_2\to+\infty}} \sqrt{\frac{\pi}{2n(1+b)}} \left(\cos\left[\frac{na^2}{4(1+b)}\right] \big(S(L_2) - S(L_1)\big) - \sin\left[\frac{na^2}{4(1+b)}\right] \big(C(L_2) - C(L_1)\big) \right)$$
$$= \sqrt{\frac{\pi}{n(1+b)}} \cos\left[\frac{na^2}{4(1+b)} + \frac{\pi}{4}\right]$$

or similarly, a single factor of $C_n(x)$:

$$\int_{-\infty}^{\infty} \mathrm{d}x C_n(x)$$
$$= \lim_{\substack{L_1\to-\infty \\ L_2\to+\infty}} \sqrt{\frac{\pi}{2n(1+b)}} \left(\cos\left[\frac{na^2}{4(1+b)}\right] \big(C(L_2) - C(L_1)\big) - \sin\left[\frac{na^2}{4(1+b)}\right] \big(S(L_2) - S(L_1)\big) \right)$$
$$= \sqrt{\frac{\pi}{n(1+b)}} \sin\left[\frac{na^2}{4(1+b)} + \frac{\pi}{4}\right].$$

Here, $S(x)$ and $C(x)$ are the Fresnel integrals, whose properties and limits are discussed in Appendix J. Using these results, we can easily demonstrate that these functions do not form an orthogonal basis:

$$\int_{-\infty}^{\infty} \mathrm{d}x S_n(x) S_m(x) = \frac{1}{2} \int_{-\infty}^{\infty} \mathrm{d}x \left(C_{(n-m)}(x) - C_{(n+m)}(x) \right) =$$
$$= \frac{1}{2} \sqrt{\frac{\pi}{1+b}} \left(\frac{1}{\sqrt{|n-m|}} \sin\left[\frac{|n-m|\,a^2}{4(1+b)} + \frac{\pi}{4}\right] - \frac{1}{\sqrt{n+m}} \sin\left[\frac{(n+m)a^2}{4(1+b)} + \frac{\pi}{4}\right] \right), \tag{K.5}$$

which does not vanish in general. Similar expressions can be obtained for integrals of $S_n(x) C_m(x)$ and $C_n(x) C_m(x)$.

Appendix L

Solutions to the Frequency resonance equation

L.1 Third-order solution

In the body of the dissertation we derived in detail the solution to the single-mode frequency resonance equation (9.1) up to second order in the parameter κ. Here we extend the same solution method to derive the behaviour of $\omega(x)$ to $\mathscr{O}\left(\kappa^3\right)$. Building onto our previous ansätze, eqs. (9.16) and (9.28), we suggest the third-order function

$$\omega_3(x) = a + (1+b_3)\,x + c_1\frac{S_1(x)}{x} + c_2\frac{S_2(x)}{x} + c_3\frac{S_3(x)}{x} + d_1\frac{S_1(x)}{x^2} + d_2\frac{S_2(x)}{x^2} + l\ln|x|. \tag{9.35}$$

where $S_3(x) = \sin\left[3\left(ax+(1+b)x^2\right)\right]$ and we assume that $c_3 \sim \mathscr{O}\left(\kappa^3\right)$, since it needs to match terms of $\mathscr{O}\left(\kappa^3\right)$ in eq. (9.30). I substitute this proposed solution into our governing equation (9.1), and following rearrangement of both sides using familiar techniques, but this time keeping terms $\mathscr{O}\left(x^{-1}\right)$, we find

$$\begin{aligned} &b + 2(1+b_3)\,c_1 C_1(x) + 4(1+b_3)\,c_2 C_2(x) + 6(1+b_3)\,c_3 C_3(x) + \frac{l}{x} \\ &\quad + \left(c_1 a_3 + 2(1+b_3)\,d_1\right)\frac{C_1(x)}{x} + \left(2c_2 a_3 + 4(1+b_3)\,d_2\right)\frac{C_2(x)}{x} \\ &\qquad + \left(3c_3 a_3 + 6(1+b_3)\,d_3\right)\frac{C_3(x)}{x} + \mathscr{O}\left(x^{-2}\right) \sim \\ &\sim -\frac{\kappa c_1}{2} + \left(\kappa - \frac{\kappa c_1^2}{8} - \frac{\kappa c_2}{2}\right)C_1(x) + \frac{\kappa c_1}{2}C_2(x) + \left(\frac{\kappa c_1^2}{8} + \frac{\kappa c_2}{2}\right)C_3(x) \end{aligned}$$

$$-\frac{\kappa d_1}{2}\frac{1}{x}+\left(-\frac{\kappa c_1 d_1}{2}-\frac{\kappa d_2}{2}\right)\frac{C_1(x)}{x}+\frac{\kappa d_1}{2}\frac{C_2(x)}{x}+\frac{\kappa d_2}{2}\frac{C_3(x)}{x}+\mathscr{O}\left(\kappa^4\right). \tag{L.1}$$

Matching terms on both sides yields a system of coupled equations, which determines the coefficients:

$$\begin{aligned}
&b\sim-\frac{\kappa c_1}{2}\,,\ 2(1+b)\,c_1\sim\kappa-\frac{\kappa c_1^2}{8}-\frac{\kappa c_2}{2}\,,\ 4(1+b)\,c_2\sim\frac{\kappa c_1}{2}\,,\\
&6(1+b)\,c_3\sim\frac{\kappa c_1^2}{8}+\frac{\kappa c_2}{2}\,,\ l\sim-\frac{\kappa d_1}{2}\,,\ c_1a_3+2(1+b_3)\,d_1\sim-\frac{\kappa c_1 d_1}{2}-\frac{\kappa d_2}{2}\,,\\
&2c_2a_3+4(1+b_3)\,d_2\sim\frac{\kappa d_1}{2}\,,\ 3c_3a_3+6(1+b_3)\,d_3\sim\frac{\kappa d_2}{2}.
\end{aligned} \tag{L.2}$$

These yield the following expressions for the undetermined coefficients of the anzats, eq. (9.35):

$$\begin{aligned}
&b\sim-\frac{1}{4}\,\kappa^2\,,\ c_1\sim\frac{1}{2}\,\kappa+\frac{3}{32}\,\kappa^3\,,\ c_2\sim\frac{1}{16}\,\kappa^2\,,\ c_3\sim\frac{1}{96}\,\kappa^3\,,\\
&d_1\sim\mp\frac{\sqrt{2\pi}}{16}\,\kappa^2\pm\frac{\sqrt{\pi}}{64}\,\kappa^3\,,\ d_2\sim\mp\frac{\sqrt{2\pi}}{64}\,\kappa^3\,,\ l\sim\pm\frac{\sqrt{2\pi}}{32}\,\kappa^3
\end{aligned}$$

and the solution to third order in κ can be written as

$$\begin{aligned}
\omega_3(x)=a&+\left(1-\frac{\kappa^2}{4}\right)x+\kappa\frac{1}{2}\frac{1}{x}\sin\left[\left(\pm\frac{\sqrt{2\pi}}{4}\,\kappa\mp\frac{\sqrt{\pi}}{16}\,\kappa^2\right)x+\left(1-\frac{\kappa^2}{4}\right)x^2\right]\\
&+\kappa^2\frac{1}{16}\frac{1}{x}\sin\left[2\left(\left(\pm\frac{\sqrt{2\pi}}{4}\,\kappa\right)x+x^2\right)\right]+\kappa^3\frac{1}{x}\left(\frac{3}{32}\sin\left(x^2\right)+\frac{1}{96}\sin\left(3x^2\right)\right)\\
&\mp\kappa^2\frac{\sqrt{2\pi}}{16}\frac{1}{x^2}\sin\left[\left(\pm\frac{\sqrt{2\pi}}{4}\,\kappa\right)x+x^2\right]\\
&\pm\kappa^3\left(\frac{\sqrt{\pi}}{64}\frac{1}{x^2}\sin\left(x^2\right)-\frac{\sqrt{2\pi}}{64}\frac{1}{x^2}\sin\left(2x^2\right)+\frac{\sqrt{2\pi}}{32}\ln|x|\right)
\end{aligned} \tag{9.40}$$

The value of the initial value parameter a_3 is determined in the main body of the thesis.

L.2 Frequency resonance equation with $\mathbf{n} \neq \mathbf{1}$

In Section 9.2 we solved the single-mode frequency resonance equation to obtain the solution (9.26). Instead of including the first oscillatory mode $n = 1$, we now solve this equation for $n = r$:

$$\omega'(x) = 1 + \kappa_r \cos(rx\omega). \tag{L.3}$$

I propose a version of the ansatz (9.16), with a modified oscillating term, reflecting the modified governing equation:

$$\begin{aligned} \omega_r(x) &= a + (1+b)x + c_1^{(r)} \frac{\sin\left(r\left(ax + (1+b)x^2\right)\right)}{x} + \mathscr{O}\left(x^{-1}\right) \\ &= a + (1+b)x + c_1^{(r)} \frac{S_r(x)}{x} + \mathscr{O}\left(x^{-1}\right). \end{aligned} \tag{L.4}$$

Upon substitution and carrying out the derivative and the Taylor expansion (valid since $r\kappa_r \sim 1/r^{\alpha-1}$), we obtain:

$$b + 2r(1+b)\, c_1^{(r)} C_r(x) \sim -\frac{1}{2} r\kappa_r c_1^{(r)} + \kappa_r C_r(x) + \text{TERM INVOLVING } C_{2r}(x) \tag{L.5}$$

Matching the respective coefficients in the manner already familiar from above, we obtain the following expressions:

$$b \sim -\frac{\kappa_r^2}{4}, \tag{L.6a}$$

$$c_1^{(r)} \sim \frac{\kappa_r}{2r}. \tag{L.6b}$$

I have shown that $b \sim \mathscr{O}\left(\kappa_r^2\right)$ and ${c_1}^{(r)} \sim \mathscr{O}(\kappa_r/r)$ for the r^{th} oscillating mode. Note that since [108] propose a value of $\alpha \gtrsim 2$, the series ${c_1}^{(n)}$ converge, and our use of the Taylor expansion is valid.

L.3 Frequency resonance equation with two distinct modes

If we investigate the same equation with two distinct modes on the right-hand side, say $n = \{r, s\}$, with $r < s$:

$$\omega' = 1 + \kappa_r \cos(rx\omega) + \kappa_s \cos(sx\omega), \tag{L.7}$$

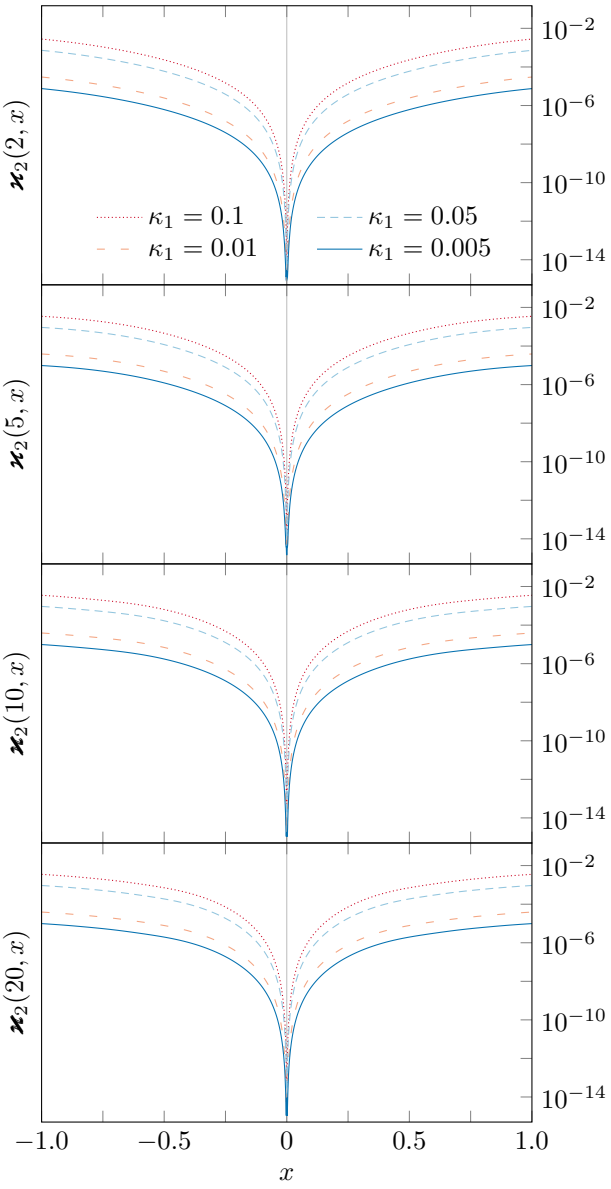

Fig. L.1 Graphical demonstration of the validity of solution (9.46) for different number of terms on the right-hand side. The coefficients $\{\kappa_n\}$ follow the power law $\kappa_1/n^{2.5}$. It is evident that the fractional errors scale with the value of the primary resonance modification κ_1. Figure appeared in [1].

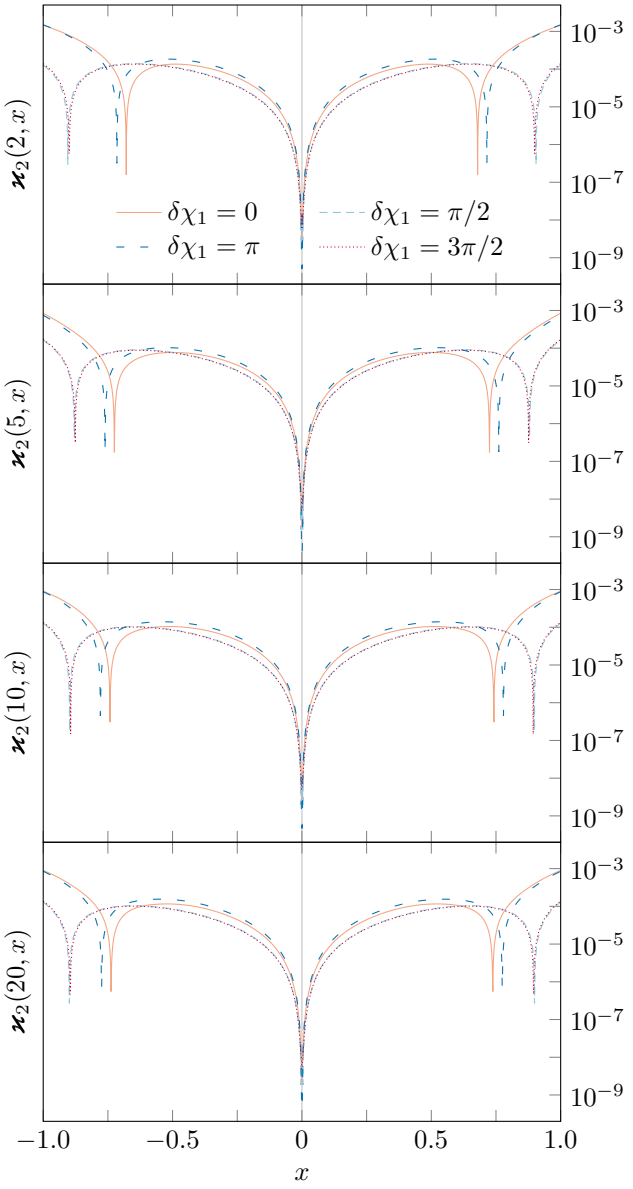

Fig. L.2 Graphical demonstration of the validity of solution (9.92) for different number of oscillating terms and for values of $\{\delta\chi_n\}$ given by eq. (9.96). In all panels we have used $\kappa_1 = 0.1$ with consecutive values given by $\kappa_n = \kappa_1/n^{2.5}$. Figure appeared in [1].

then the solution would include two leading-order terms associated with each of the two separate oscillating terms, with corrections at sub-leading order due to cross-terms between these. Specifically, we find ${c_1}^{(r)} \sim \kappa_r/2r(1+b)$ and ${c_1}^{(s)} \sim \kappa_s/2s(1+b)$, which implies that the coefficient b is given by the expression

$$b \sim -\frac{1}{2}\, r\, \kappa_r\, c_1^{(r)} - \frac{1}{2}\, s\, \kappa_s\, c_1^{(s)} \sim -\frac{\kappa_r^2 + \kappa_s^2}{4}\,, \tag{L.8}$$

and consequently

$$c_1^{(r)} \sim \frac{\kappa_r}{2r}, \tag{L.9a}$$

$$c_1^{(s)} \sim \frac{\kappa_s}{2s}, \tag{L.9b}$$

where each expression also includes sub-leading terms of order $\mathscr{O}(\kappa_r \kappa_s)$. This proves the important result that for the frequency equation with 2 distinct modes, all mixed terms (which depend on both κ_r and κ_s) are of sub-leading order compared to the quadratic contributions originating from the individual modes as found earlier.

L.4 Frequency equation with a non-vanishing phase term

Let us consider the frequency equation with a single oscillating mode but with a non-vanishing phase term $\delta\chi$:

$$\omega'(x) = 1 + \kappa \cos(x\omega - \delta\chi)\,, \tag{9.69}$$

and let us expand the cosine term on the right-hand side to obtain the following differential equation:

$$\omega'(x) = 1 + \kappa \cos(\delta\chi)\cos(x\omega) + \kappa \sin(\delta\chi)\sin(x\omega)\,. \tag{L.10}$$

I may naively try the ansatz which previously proved suitable for the zero-phase version of the equation, given by eq. (9.16), however it will not work this time, as there will be unmatched terms left on the right-hand side. Instead, we suggest the following alternative ansatz, including an extra term proportional to $C_1(x)$

$$\omega_1(x) = a + (1+b)\,x + c_1 \frac{S_1(x)}{x} + d_1 \frac{C_1(x)}{x}. \tag{L.11}$$

Upon differentiating and substituting on both sides of eq. (9.69), we obtain a more involved relation than before:

$$\begin{aligned} b+2(1+b)c_1C_1(x)-2(1+b)d_1S_1(x) \sim &-\frac{1}{2}\,\kappa c_1\cos(\delta\chi)-\frac{1}{2}\,\kappa d_1\sin(\delta\chi) \\ &+\kappa\cos(\delta\chi)\,C_1(x)-\kappa\sin(\delta\chi)\,S_1(x). \end{aligned} \tag{L.12}$$

Making the informed assumption that $b \sim \mathscr{O}(\kappa)$, we find the constants c_1 and d_1 by matching terms on both sides:

$$c_1 \sim \frac{\kappa}{2}\cos(\delta\chi)\,, \tag{L.13a}$$

$$d_1 \sim -\frac{\kappa}{2}\sin(\delta\chi)\,, \tag{L.13b}$$

which is different from the previously found value of c_1. These yield the same value of the slope correction b as before:

$$b \sim -\frac{1}{2}\,\kappa c_1\cos(\delta\chi)+\frac{1}{2}\,\kappa d_1\sin(\delta\chi) = -\frac{\kappa^2}{2}\left(\cos^2(\delta\chi)+\sin^2(\delta\chi)\right) = -\frac{\kappa^2}{2}. \tag{L.14}$$

If we substitute these into our proposed ansatz, we see that we recover the proposed alternative ansatz:

$$\begin{aligned} \omega_1(x) &= a+x+\frac{\kappa}{2}\,\frac{1}{x}\left(S_1(x)\cos(\delta\chi)-C_1(x)\sin(\delta\chi)\right) \\ &\equiv a+x+\frac{\kappa}{2}\,\frac{1}{x}\sin\left[ax+\left(1-\frac{\kappa^2}{2}\right)x^2-\delta\chi\right], \end{aligned} \tag{L.15}$$

where the sine factor in the last term is identical to $\mathscr{S}_1(x)$, as defined in eq. (9.80a).

Appendix M

Solutions to the phase resonance equation

In Section 9.3, we explain our algorithm for finding iterative solutions to the phase resonance equation, and present the solutions to third order in the parameter λ. However, we omit the details of finding these solutions, since these are often too tedious and irrelevant to our discussion. Here, we present these solutions in more detail. The zeroth-order equation (9.99) is straightforward to solve, by integrating both sides twice.

M.1 Phase equation with a single mode and zero phase

We source the first-order correction from the zeroth-order solution, and arrive at eq. (9.103). Integrating both sides between 0 and x, making use of the Fresnel integrals, with initial

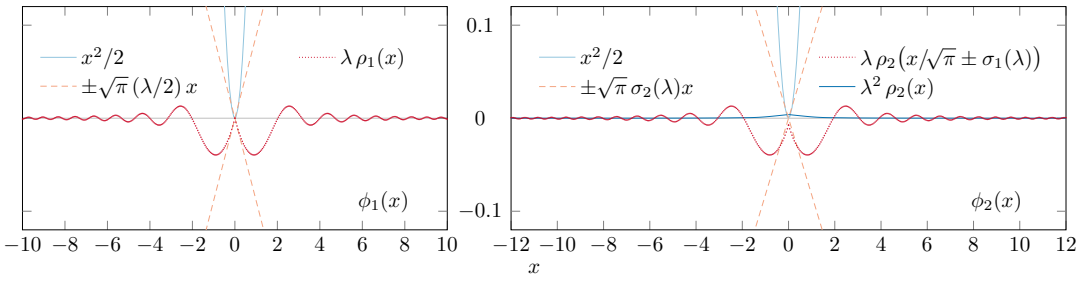

Fig. M.1 Graphical comparison of the terms in the argument on the right-hand side of eq. (M.6). Evidently the term $\lambda\,\rho_1$ stays close to 0 for all positive x. Figure appeared in [1].

Fig. M.2 Graphical comparison of the terms in the argument on the right-hand side of eq. (M.19). We can see that both terms, $\lambda\,\rho_1$ and $\lambda^2\rho_2$, are small compared to the other terms in the argument. Figure appeared in [1].

condition $\phi'(0) = 0$, we find:

$$\phi'_{(1)}(x) = \lambda \int_0^x \mathrm{d}y \cos\left(\frac{y^2}{2}\right) = \sqrt{\pi}\,\lambda\, C\left(\frac{x}{\sqrt{\pi}}\right). \tag{M.1}$$

Integrating once again, using the method of integration by parts, we obtain an initial form of the first-order correction:

$$\phi_{(1)}(x) = \sqrt{\pi}\,\lambda \int_0^x \mathrm{d}y\, C\left(\frac{y}{\sqrt{\pi}}\right) = \sqrt{\pi}\,\lambda \left[x C\left(\frac{x}{\sqrt{\pi}}\right) - \frac{1}{\sqrt{\pi}} \sin\left(\frac{x^2}{2}\right)\right]. \tag{M.2}$$

While this is indeed a valid result, we prefer to re-arrange it in a form which is more useful for our tasks. If we look at the graph of this result for $\lambda = 0.1$ (Fig. M.4), we can notice several features. First of all, since there are no constants dependant on λ in eq. (M.2), it vanishes at $x = 0$. Furthermore, we immediately notice that the solution is a linear function which is modified by a decaying oscillating function. Therefore, we split the solution into two parts: a linear part, whose coefficient is a function of λ, and another part, a collection of periodic and quasi-periodic functions (trigonometric functions and Fresnel integrals) that collectively oscillates around $\phi = 0$, and whose magnitude is small compared to the linear term. Since the graph is symmetric relative to the vertical axis, it is necessary to write down solutions for both cases $x > 0$ and $x < 0$. The Fresnel integrals oscillate around the value $\pm 1/2$ (instead of 0) for large $\pm x$, so we subtract this value from each of them in the rapidly oscillating terms. Finally, we note of an emerging pattern: the argument of the Fresnel integral is $x/\sqrt{\pi}$, therefore we express the linear term and the remaining factors of x in terms of this scaled variable. The upper sign is for positive x, while the lower sign is for $x < 0$.

$$\phi_{(1)}(x) = \underbrace{\pm\pi\left[\frac{1}{2}\lambda\right]\left(\frac{x}{\sqrt{\pi}}\right)}_{\text{LINEAR TERM}} + \underbrace{\lambda\left[\pi\left(\frac{x}{\sqrt{\pi}}\right)\left(C\left(\frac{x}{\sqrt{\pi}}\right) \mp \frac{1}{2}\right) - \sin\left[\frac{\pi}{2}\left(\frac{x}{\sqrt{\pi}}\right)^2\right]\right]}_{\text{OSCILLATING TERM PROPORTIONAL TO } \lambda}. \tag{M.3}$$

We note that this result is strictly first order in the mode parameter λ. To construct the complete solution of the phase resonance equation to first order in λ, eq. (9.105), we combine

eq. (M.3) with the zeroth-order function (9.100):

$$\phi_1(x) = \frac{\pi}{2}\left(\frac{x}{\sqrt{\pi}} \pm \frac{1}{2}\lambda\right)^2 + \lambda\left[\pi\left(\frac{x}{\sqrt{\pi}}\right)\left(C\left(\frac{x}{\sqrt{\pi}}\right) \mp \frac{1}{2}\right) - \sin\left[\frac{\pi}{2}\left(\frac{x}{\sqrt{\pi}}\right)^2\right]\right] + \mathscr{O}(\lambda^2)\,. \tag{9.105}$$

We have combined the quadratic and linear terms into a single quadratic term, by implicitly adding the constant term $(\pi\lambda^2/8)$, which is nevertheless ignored at linear order in the mode parameter, thus obtaining the form (9.105):

$$\frac{\pi}{2}\left(\frac{x}{\sqrt{\pi}}\right)^2 \pm \frac{\pi}{2}\lambda\left(\frac{x}{\sqrt{\pi}}\right) + \mathscr{O}(\lambda^2) = \frac{\pi}{2}\left(\frac{x}{\sqrt{\pi}} \pm \frac{1}{2}\lambda\right)^2 + \mathscr{O}(\lambda^2)\,. \tag{M.4}$$

Finally, we make note of the functional form of the oscillating term, which will be investigated in detail later together with the functions incurred at higher order (let $X = x/\sqrt{\pi}$ and see Appendix M.2 for plots and discussion):

$$\rho_1(X) = \pi X\left(C(X) \mp \frac{1}{2}\right) - \sin\left(\frac{\pi}{2}X^2\right) \tag{M.5}$$

The above result allows us to solve the equation at the next higher order, which is discussed below.

Finding the solution up to second order in λ involves substituting $\phi_1(x) = \phi_0(x) + \phi_{(1)}(x)$ on the right-hand side of the source equation (9.98), and solving for $\phi_{(2)}(x)$. Explicitly, eq. (9.106) is (we use the variant (M.2) of $\phi_{(1)}(x)$):

$$\phi''_{(2)}(x) = \lambda\cos\left[\frac{x^2}{2} \pm \frac{\sqrt{\pi}}{2}\lambda\, x + \lambda\left[\sqrt{\pi}x\left(C\left(\frac{x}{\sqrt{\pi}}\right) \mp \frac{1}{2}\right) - \sin\left(\frac{x^2}{2}\right)\right]\right]. \tag{M.6}$$

We write the last term in the argument of the cosine as $\lambda\,\rho_1\left(x/\sqrt{\pi}\right)$ and invoke our knowledge of trigonometric identities to write the right-hand side as:

$$\phi''_{(2)}(x) = \lambda\cos\left(\frac{x^2}{2} \pm \frac{\sqrt{\pi}}{2}\lambda\, x\right)\cos\left(\lambda\,\rho_1\left(\frac{x}{\sqrt{\pi}}\right)\right) - \lambda\sin\left(\frac{x^2}{2} \pm \frac{\sqrt{\pi}}{2}\lambda\, x\right)\sin\left(\lambda\,\rho_1\left(\frac{x}{\sqrt{\pi}}\right)\right) \tag{M.7}$$

The function $\rho_1\left(x/\sqrt{\pi}\right)$ oscillates around 0, and further, is pre-multiplied by the coefficient $\lambda \ll 1$, hence we can assume that it is always small (compared to the quadratic and linear x-terms, see Figure M.1 for comparison of the relative magnitude of the terms), and use this fact to substitute the trigonometric functions involving ρ_1 for Taylor series to leading order in λ. We ignore all terms of $\mathscr{O}\left(\lambda^3\right)$ and higher, since they are not included at the current order.

$$\phi''_{(2)}(x) = \lambda \cos\left(\frac{x^2}{2} \pm \frac{\sqrt{\pi}}{2}\lambda x\right)\left(1+\mathscr{O}\left(\lambda^2\right)\right) - \lambda \sin\left(\frac{x^2}{2} \pm \frac{\sqrt{\pi}}{2}\lambda x\right)\left(\lambda\,\rho_1\left(\frac{x}{\sqrt{\pi}}\right)+\mathscr{O}\left(\lambda^3\right)\right) \tag{M.8}$$

We carry out the same procedure with the term multiplied by λ^2, and neglect resulting terms proportional to λ^3:

$$\lambda^2 \sin\left(\frac{x^2}{2} \pm \frac{\sqrt{\pi}}{2}\lambda x\right)\rho_1\left(\frac{x}{\sqrt{\pi}}\right) = \lambda^2 \sin\left(\frac{x^2}{2}\right)\rho_1\left(\frac{x}{\sqrt{\pi}}\right) + \mathscr{O}\left(\lambda^3\right). \tag{M.9}$$

Thus, we are left with the integral below, which can be easily performed using standard techniques, integration by parts and utilising the Fresnel integrals notation. We keep in mind to throw out terms of $\mathscr{O}\left(\lambda^3\right)$ and higher.

$$\phi'_{(2)}(x) = \int_0^x \mathrm{d}y \left[\lambda \cos\left(\frac{y^2}{2} \pm \frac{\sqrt{\pi}}{2}\lambda y\right) - \sqrt{\pi}\lambda^2 \sin\left(\frac{y^2}{2}\right) y \left(C\left(\frac{y}{\sqrt{\pi}}\right) \mp \frac{1}{2}\right) - \sin\left(\frac{y^2}{2}\right)\right] \tag{M.10}$$

$$\begin{aligned} &= \sqrt{\pi}\lambda\left[C\left(\frac{x}{\sqrt{\pi}} \pm \frac{\lambda}{2}\right) \mp C\left(\frac{\lambda}{2}\right)\right] \\ &\quad + \sqrt{\pi}\lambda^2\left[\cos\left(\frac{x^2}{2}\right) C\left(\frac{x}{\sqrt{\pi}}\right) - \frac{1}{\sqrt{2}} C\left(\frac{\sqrt{2}x}{\sqrt{\pi}}\right) \mp \frac{1}{2}\cos\left(\frac{x^2}{2}\right) \pm \frac{1}{2}\right]. \end{aligned} \tag{M.11}$$

We need to integrate this further once again, keeping track of the initial condition, $\phi(0) = 0$. We obtain the following expression for the correction, where again the upper sign is valid for

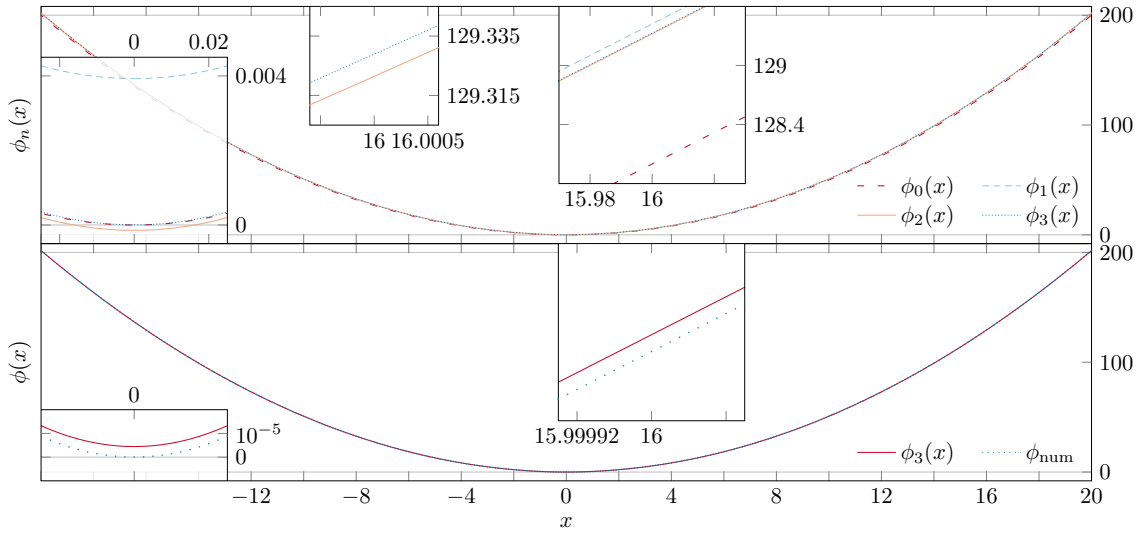

Fig. M.3 *Upper panel:* All four solutions (9.100) – (9.110) represented on the same plot. Evidently, they are all very close to each other, and cannot be easily distinguished in this manner. The three insets show features of the plot. At the origin, the solutions vanish up to a small deviation of magnitude comparable with the next respective order. Upon zooming in closer, one can distinguish the graphs from each other. *Lower panel:* Visual comparison of the highest-order solution, $\phi_3(x)$, and the numerical solution of the phase resonance equation. In all calculations and simulations we have used value of $\lambda = 0.1$. Figure appeared in [1].

$x > 0$ and the lower for $x < 0$:

$$\begin{aligned}\phi_{(2)}(x) = \sqrt{\pi}\lambda\left[xC\left(\frac{x}{\sqrt{\pi}} \pm \frac{\lambda}{2}\right) - \frac{1}{\sqrt{\pi}}\sin\left[\frac{\pi}{2}\left(\frac{x}{\sqrt{\pi}} \pm \frac{1}{2}\lambda\right)^2\right] \mp C\left(\frac{\lambda}{2}\right)x\right] \\ + \sqrt{\pi}\lambda^2\left[\frac{\sqrt{\pi}}{2}C^2\left(\frac{x}{\sqrt{\pi}}\right) \mp \frac{\sqrt{\pi}}{2}C\left(\frac{x}{\sqrt{\pi}}\right) \pm \frac{\sqrt{\pi}}{2}C\left(\frac{x}{\sqrt{\pi}} \pm \frac{\lambda}{2}\right)\right. \\ \left. - \frac{1}{\sqrt{2}}xC\left(\frac{\sqrt{2}x}{\sqrt{\pi}}\right) + \frac{1}{2\sqrt{\pi}}\sin\left(x^2\right) \pm \frac{x}{2}\right]\end{aligned} \tag{M.12}$$

We have obtained an expression which gives the correction to the quadratic term to second order in λ, which can be seen plotted in Figure M.4. Again, we seek to express this in a modified form where the linear term is explicit, and all the oscillating terms are grouped by order of the parameter λ, which allows for better understanding of the solution.

$$\phi_{(2)}(x) = \underbrace{\pm\sqrt{\pi}\left[\frac{\lambda}{2} - \lambda\, C\left(\frac{\lambda}{2}\right) + \frac{\sqrt{2}-1}{2\sqrt{2}}\lambda^2\right]x}_{\text{LINEAR TERM}} + \underbrace{\frac{\pi}{8}\lambda^2}_{\text{CONSTANT}}$$

$$\underbrace{+\lambda\left[\pi\left(\frac{x}{\sqrt{\pi}} \pm \frac{1}{2}\lambda\right)\left(C\left(\frac{x}{\sqrt{\pi}} \pm \frac{1}{2}\lambda\right) \mp \frac{1}{2}\right) - \sin\left[\frac{\pi}{2}\left(\frac{x}{\sqrt{\pi}} \pm \frac{1}{2}\lambda\right)^2\right]\right]}_{\text{OSCILLATING TERM PROPORTIONAL TO } \lambda}$$

$$\underbrace{+\lambda^2\left[\frac{\pi}{2}\left(C\left(\frac{x}{\sqrt{\pi}}\right) \mp \frac{1}{2}\right)^2 - \frac{\pi}{2}\left(\sqrt{2}\left[\frac{x}{\sqrt{\pi}}\right]\right)\left(C\left(\sqrt{2}\left[\frac{x}{\sqrt{\pi}}\right]\right) \mp \frac{1}{2}\right) + \frac{1}{2}\sin\left[\frac{\pi}{2}\left(\sqrt{2}\left[\frac{x}{\sqrt{\pi}}\right]\right)^2\right]\right]}_{\text{OSCILLATING TERM PROPORTIONAL TO } \lambda^2} \tag{M.13}$$

We note that some of these terms, if expanded, would be $\mathcal{O}(\lambda^3)$ or higher, but we leave them in for presentational purposes. We simplify the coefficient of the linear term (the slope of the derivative $\phi_2'(x)$), by writing the Fresnel integral in power series, and retaining only its linear term (the next higher-order term is of fifth order):

$$\frac{\lambda}{2} - \lambda\, C\left(\frac{\lambda}{2}\right) + \frac{\sqrt{2}-1}{2\sqrt{2}}\lambda^2 = \frac{\lambda}{2} - \frac{\lambda^2}{2} + \frac{\sqrt{2}-1}{2\sqrt{2}}\lambda^2 + \mathcal{O}\left(\lambda^6\right) \approx \frac{1}{2}\lambda - \frac{\sqrt{2}}{4}\lambda^2. \tag{M.14}$$

When we combine this with the zeroth-order function $\phi_0(x) = x^2/2$, we find the complete second-order solution, given by eq. (9.108). Specifically, we can complete the square with the quadratic, linear, and constant terms, to obtain

$$\frac{x^2}{2} \pm \sqrt{\pi}\left[\frac{1}{2}\lambda - \frac{\sqrt{2}}{4}\lambda^2\right]x + \frac{\pi}{8}\lambda^2 = \frac{\pi}{2}\left(\frac{x}{\sqrt{\pi}} \pm \left[\frac{1}{2}\lambda - \frac{\sqrt{2}}{4}\lambda^2\right]\right)^2 + \mathcal{O}\left(\lambda^3\right). \tag{M.15}$$

In deriving this solution, we have used familiar integration techniques, and the definition of the Fresnel integrals, however it is useful to quote one of the “tricks" for the benefit of the reader who wishes to replicate these results:

$$\int_{\pm f(\lambda)}^{x/\sqrt{\pi} \pm f(\lambda)} \mathrm{d}y \cos\left(\frac{\pi}{2}y^2\right) = C\left(\frac{x}{\sqrt{\pi}} \pm f(\lambda)\right) \mp C\left(f(\lambda)\right). \tag{M.16}$$

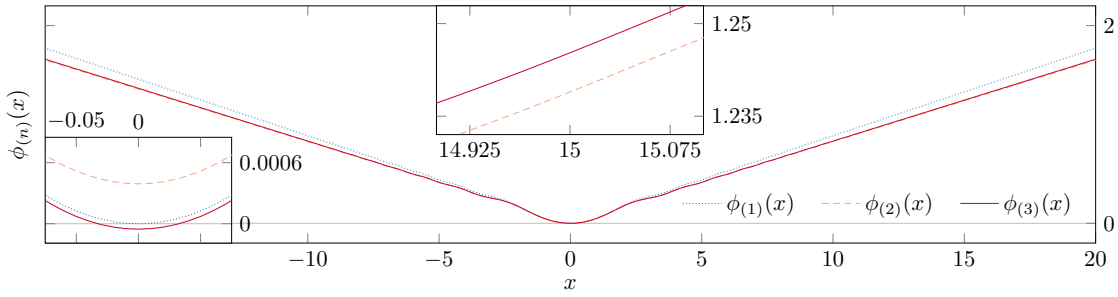

Fig. M.4 Graphical comparison of the three corrections $\phi_{(1)}(x)$, $\phi_{(2)}(x)$, and $\phi_{(3)}(x)$ for $\lambda = 0.1$. At the origin, $\phi_{(1)}(0) = 0$ as it does not involve a constant term, while $\phi_{(2)}(0)$ and $\phi_{(3)}(0)$ do not vanish, but rather obey the condition to $\mathscr{O}(\lambda^3)$ and $\mathscr{O}(\lambda^4)$, respectively, which is within their errors: $|\phi_{(2)}(0)| < \lambda^3$ and $|\phi_{(3)}(0)| < \lambda^4$. Figure appeared in [1].

It is important to pay attention to the two oscillating terms in eq. (M.13): the first one, has the same functional form as the oscillating term in eq. (M.3), and can in fact be related to $\rho_1(X)$ in the following way:

$$\text{OSCILLATING TERM PROPORTIONAL TO } \lambda = \rho_1\left(\frac{x}{\sqrt{\pi}} \pm \frac{1}{2}\lambda\right). \tag{M.17}$$

The second oscillating term has not been encountered before, and will be investigated in detail in Appendix M.2:

$$\rho_2(X) = \frac{\pi}{2}\left(C(X) \mp \frac{1}{2}\right)^2 - \frac{\pi}{2}\left(\sqrt{2}X\right)\left(C\left(\sqrt{2}X\right) \mp \frac{1}{2}\right) + \frac{1}{2}\sin\left[\frac{\pi}{2}\left(\sqrt{2}X\right)^2\right]. \tag{M.18}$$

As we can see, the second-order solution $\phi_2(x) = \phi_0(x) + \phi_{(2)}(x)$ is already heavily involved. Extending the results in [114], we use this function to source the third-order solution, see below for details.

Substituting the expression (9.110) for $\phi_2(x)$ into eq. (9.109) gives the equation we need to solve at third order:

$$\phi''_{(3)}(x) = \lambda \cos\left[\frac{x^2}{2} \pm \sqrt{\pi}\left(\frac{1}{2}\lambda - \frac{\sqrt{2}}{4}\lambda^2\right)x + \frac{\pi}{8}\lambda^2 + \lambda\,\rho_1\left(\frac{x}{\sqrt{\pi}} \pm \frac{1}{2}\lambda\right) + \lambda^2\rho_2\left(\frac{x}{\sqrt{\pi}}\right)\right], \tag{M.19}$$

$$\text{where } \rho_1\left(\frac{x}{\sqrt{\pi}} \pm \frac{1}{2}\lambda\right) = \pi\left(\frac{x}{\sqrt{\pi}} \pm \frac{1}{2}\lambda\right)\left(C\left(\frac{x}{\sqrt{\pi}} \pm \frac{1}{2}\lambda\right) \mp \frac{1}{2}\right) - \sin\left[\frac{\pi}{2}\left(\frac{x}{\sqrt{\pi}} \pm \frac{1}{2}\lambda\right)^2\right] \tag{M.20}$$

$$\begin{aligned}\text{and } \rho_2\left(\frac{x}{\sqrt{\pi}}\right) = \frac{\pi}{2}\left(C\left(\frac{x}{\sqrt{\pi}}\right) \mp \frac{1}{2}\right)^2 - \frac{\pi}{2}\left(\sqrt{2}\left[\frac{x}{\sqrt{\pi}}\right]\right)\left(C\left(\sqrt{2}\left[\frac{x}{\sqrt{\pi}}\right]\right) \mp \frac{1}{2}\right) \\ + \frac{1}{2}\sin\left[\frac{\pi}{2}\left(\sqrt{2}\left[\frac{x}{\sqrt{\pi}}\right]\right)^2\right].\end{aligned} \tag{M.21}$$

It is important to realise that $\lambda\,\rho_1(\bullet)$ and $\lambda^2\rho_2(\bullet)$ are small in magnitude compared to the other terms, as is obvious when these are plotted on the same graph, see Figure M.2. Hence we can treat these as a perturbation to the rest of the argument. This becomes obvious when the functions are plotted on the same graph, see Figure M.2. This prompts us to expand the cosine term using the sum-to-product formulae, and expand the terms containing the perturbation:

$$\lambda\,\cos\left[\frac{x^2}{2} \pm \sqrt{\pi}\left(\frac{1}{2}\lambda - \frac{\sqrt{2}}{4}\lambda^2\right)x + \frac{\pi}{8}\lambda^2 + \lambda\,\rho_1\left(\frac{x}{\sqrt{\pi}} \pm \frac{1}{2}\lambda\right) + \lambda^2\rho_2\left(\frac{x}{\sqrt{\pi}}\right)\right] \tag{M.22}$$

$$\begin{aligned}&= \lambda\,\cos\left[\frac{x^2}{2} \pm \sqrt{\pi}\left(\frac{1}{2}\lambda - \frac{\sqrt{2}}{4}\lambda^2\right)x + \frac{\pi}{8}\lambda^2\right] \times \cos\left(\lambda\,\rho_1\left(\frac{x}{\sqrt{\pi}} \pm \frac{1}{2}\lambda\right) + \lambda^2\rho_2\left(\frac{x}{\sqrt{\pi}}\right)\right) \\ &\quad - \lambda\,\sin\left[\frac{x^2}{2} \pm \sqrt{\pi}\left(\frac{1}{2}\lambda - \frac{\sqrt{2}}{4}\lambda^2\right)x + \frac{\pi}{8}\lambda^2\right] \times \sin\left(\lambda\,\rho_1\left(\frac{x}{\sqrt{\pi}} \pm \frac{1}{2}\lambda\right) + \lambda^2\rho_2\left(\frac{x}{\sqrt{\pi}}\right)\right)\end{aligned} \tag{M.23}$$

$$\begin{aligned}&= \lambda\,\cos\left[\frac{x^2}{2} \pm \sqrt{\pi}\left(\frac{1}{2}\lambda - \frac{\sqrt{2}}{4}\lambda^2\right)x + \frac{\pi}{8}\lambda^2\right] - \lambda^2\sin\left(\frac{x^2}{2} \pm \frac{\sqrt{\pi}}{2}\lambda\,x\right)\rho_1\left(\frac{x}{\sqrt{\pi}} \pm \frac{1}{2}\lambda\right) \\ &\quad - \frac{1}{2}\lambda^3\left(\cos\left(\frac{x^2}{2}\right)\rho_1^2\left(\frac{x}{\sqrt{\pi}} \pm \frac{1}{2}\lambda\right) + 2\sin\left(\frac{x^2}{2}\right)\rho_2\left(\frac{x}{\sqrt{\pi}}\right)\right) + \mathscr{O}\left(\lambda^4\right).\end{aligned} \tag{M.24}$$

We have combined both third-order terms together, since it makes the integration more straightforward. Integrating the expression (M.24), subject to the boundary condition $\phi'(0) =$

0 gives the derivative of the third-order correction:

$$\begin{aligned}\phi'_{(3)}(x) = \sqrt{\pi}\lambda &\left[C\left(\frac{x}{\sqrt{\pi}} \pm \left[\frac{1}{2}\lambda - \frac{\sqrt{2}}{4}\lambda^2\right]\right) \mp C\left(\frac{1}{2}\lambda - \frac{\sqrt{2}}{4}\lambda^2\right)\right] \\ &+ \sqrt{\pi}\lambda^2 \left[\cos\left(\frac{x^2}{2} \pm \frac{\sqrt{\pi}}{2}\lambda x\right) C\left(\frac{x}{\sqrt{\pi}} \pm \frac{\lambda}{2}\right) \mp \frac{1}{2}\cos\left(\frac{x^2}{2} \pm \frac{\sqrt{\pi}}{2}\lambda x\right)\right. \\ &\left. - \frac{1}{\sqrt{2}} C\left(\frac{\sqrt{2}x}{\sqrt{\pi}} \pm \frac{\lambda}{\sqrt{2}}\right) \pm \frac{1}{\sqrt{2}} C\left(\frac{\lambda}{\sqrt{2}}\right) \mp C\left(\frac{\lambda}{2}\right) \pm \frac{1}{2}\right] \\ &- \sqrt{\pi}\lambda^3 \left[\frac{\sqrt{\pi}}{2} x \sin\left(\frac{x^2}{2}\right)\left[C^2\left(\frac{x}{\sqrt{\pi}}\right) \mp C\left(\frac{x}{\sqrt{\pi}}\right) + \frac{1}{4}\right] - \frac{3}{8} C\left(\frac{x}{\sqrt{\pi}}\right) - \frac{3\sqrt{3}}{8} C\left(\frac{\sqrt{3}x}{\sqrt{\pi}}\right)\right. \\ &\left. + \frac{1}{2}\cos(x^2)\left[C\left(\frac{x}{\sqrt{\pi}}\right) \mp \frac{1}{2}\right] + \frac{1}{\sqrt{2}}\cos\left(\frac{x^2}{2}\right)\left[C\left(\frac{\sqrt{2}x}{\sqrt{\pi}}\right) \mp \frac{1}{2}\right] \pm \frac{\sqrt{2}}{4} \pm \frac{1}{4}\right].\end{aligned} \tag{M.25}$$

Integrating this again, using a combination of integration by parts, substitution, double-angle formulae and other trigonometric identities, finally applying the current boundary condition $\phi(0) = 0$, we arrive at an expression for the third-order correction to the solution (9.100). Below is given an initial form of the solution, and as before the upper sign holds for positive x, while the lower sign is valid for negative x (see Figure M.4 for a plot of this function):

$$\begin{aligned}\phi_{(3)}(x) = \sqrt{\pi}\lambda &\left[xC\left(\frac{x}{\sqrt{\pi}} \pm \left[\frac{1}{2}\lambda - \frac{\sqrt{2}}{4}\lambda^2\right]\right) - \frac{1}{\sqrt{\pi}} \sin\left[\frac{\pi}{2}\left(\frac{x}{\sqrt{\pi}} \pm \left[\frac{1}{2}\lambda - \frac{\sqrt{2}}{4}\lambda^2\right]\right)^2\right]\right. \\ &+ \frac{\sqrt{\pi}}{2}\left(\frac{1}{2}\lambda - \frac{\sqrt{2}}{4}\lambda^2\right)^2 \pm \sqrt{\pi}\left(\frac{1}{2}\lambda - \frac{\sqrt{2}}{4}\lambda^2\right) C\left(\frac{x}{\sqrt{\pi}} \pm \left[\frac{1}{2}\lambda - \frac{\sqrt{2}}{4}\lambda^2\right]\right) \\ &\left. - \frac{\sqrt{\pi}}{2}\lambda C\left(\frac{1}{2}\lambda - \frac{\sqrt{2}}{4}\lambda^2\right) \mp C\left(\frac{1}{2}\lambda - \frac{\sqrt{2}}{4}\lambda^2\right) x\right]\end{aligned}$$

$$
\begin{aligned}
&+\sqrt{\pi}\lambda^2\left[\frac{\sqrt{\pi}}{2}C^2\left(\frac{x}{\sqrt{\pi}}\pm\frac{1}{2}\lambda\right)\mp\frac{\sqrt{\pi}}{2}C\left(\frac{x}{\sqrt{\pi}}\pm\frac{1}{2}\lambda\right)\right.\\
&\quad+\frac{1}{2\sqrt{\pi}}\sin\left[\frac{\pi}{2}\left(\sqrt{2}\left[\frac{x}{\sqrt{\pi}}\pm\frac{1}{2}\lambda\right]\right)^2\right]\mp C\left(\frac{\lambda}{2}\right)x-\frac{1}{\sqrt{2}}xC\left(\sqrt{2}\left[\frac{x}{\sqrt{\pi}}\pm\frac{1}{2}\lambda\right]\right)\\
&\quad\left.\mp\frac{\sqrt{\pi}}{2\sqrt{2}}\lambda C\left(\frac{\sqrt{2}x}{\sqrt{\pi}}\right)\pm\frac{1}{2}x+\frac{\sqrt{\pi}}{2}C\left(\frac{\lambda}{2}\right)\pm\frac{1}{\sqrt{2}}C\left(\frac{\lambda}{\sqrt{2}}\right)x\right]\\
&+\sqrt{\pi}\lambda^3\left[\frac{\sqrt{\pi}}{2}\cos\left(\frac{x^2}{2}\right)\left[C^2\left(\frac{x}{\sqrt{\pi}}\right)\mp C\left(\frac{x}{\sqrt{\pi}}\right)+\frac{1}{4}\right]-\frac{\sqrt{\pi}}{\sqrt{2}}C\left(\frac{\sqrt{2}x}{\sqrt{\pi}}\right)C\left(\frac{x}{\sqrt{\pi}}\right)\right.\\
&\quad+\frac{3\sqrt{3}}{8}xC\left(\frac{\sqrt{3}x}{\sqrt{\pi}}\right)-\frac{x}{8}C\left(\frac{x}{\sqrt{\pi}}\right)\pm\frac{\sqrt{\pi}}{2\sqrt{2}}C\left(\frac{\sqrt{2}x}{\sqrt{\pi}}\right)\pm\frac{\sqrt{\pi}}{2\sqrt{2}}C\left(\frac{x}{\sqrt{\pi}}\right)\\
&\quad\left.-\frac{3}{8\sqrt{\pi}}\sin\left(\frac{3x^2}{2}\right)+\frac{1}{8\sqrt{\pi}}\sin\left(\frac{x^2}{2}\right)\mp\frac{x}{2\sqrt{2}}-\frac{\sqrt{\pi}}{8}\right]. \qquad \text{(M.26)}
\end{aligned}
$$

As before, we re-arrange this form of the solution to obtain groups of terms which oscillate around 0 (both for negative and positive x) and beside them, terms which are either linear or constant with x, but are otherwise functions of λ.

$$
\begin{aligned}
&\phi_{(3)}(x)=\phi_3(x)-\phi_0(x)=\\
&=\pm\sqrt{\pi}\left[\frac{\lambda}{2}-\lambda C\left(\frac{\lambda}{2}-\frac{\lambda^2}{2\sqrt{2}}\right)+\frac{\lambda^2}{2}-\lambda^2 C\left(\frac{\lambda}{2}\right)\right.
\end{aligned}
$$

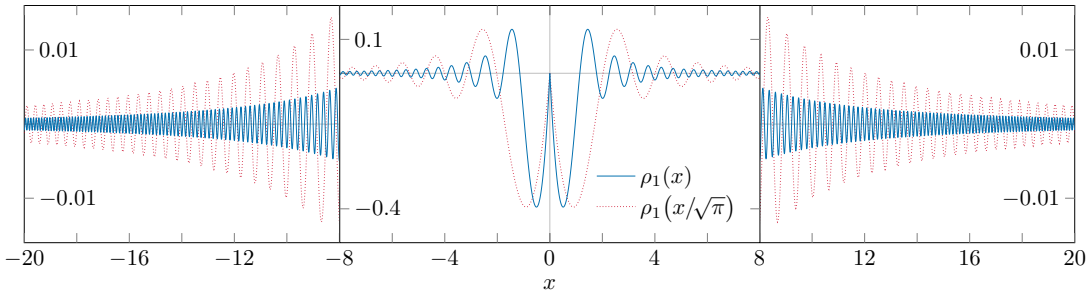

Fig. M.5 Plots of the two functions $\rho_{(1)}(x)$ and $\rho_1\left(x/\sqrt{\pi}\right)$. We see that both branches (for positive and negative x) are comprised of oscillations which peter out as we increase distance from the origin. Figure appeared in [1].

$$
\underbrace{\left.-\frac{\lambda^2}{2\sqrt{2}}+\frac{\lambda^2}{\sqrt{2}}C\left(\frac{\lambda}{\sqrt{2}}\right)-\frac{\lambda^3}{16}-\frac{\lambda^3}{2\sqrt{2}}+\frac{3\sqrt{3}}{16}\lambda^3\right]x}_{\text{LINEAR TERM}}
$$

$$
\underbrace{\begin{aligned}&+\lambda\sin\left[\frac{\pi}{2}\left(\frac{\lambda}{2}-\frac{\lambda^2}{2\sqrt{2}}\right)^2\right]+\frac{\pi}{2}\lambda\left(\frac{\lambda}{2}-\frac{\lambda^2}{2\sqrt{2}}\right)-\pi\lambda\,\frac{\lambda}{2}C\left(\frac{\lambda}{2}\right)\\&\qquad-\frac{\pi}{8}\lambda^2+\frac{\pi}{2}\lambda^2C\left(\frac{\lambda}{2}\right)-\frac{\pi}{4\sqrt{2}}\lambda^3+\frac{\pi}{4\sqrt{2}}\lambda^3-\frac{\pi}{8}\lambda^3\end{aligned}}_{\text{CONSTANT TERM}}
$$

$$
\underbrace{\begin{aligned}&+\lambda\left[\pi\left(\frac{x}{\sqrt{\pi}}\pm\left[\frac{1}{2}\lambda-\frac{\sqrt{2}}{4}\lambda^2\right]\right)\left(C\left(\frac{x}{\sqrt{\pi}}\pm\left[\frac{1}{2}\lambda-\frac{\sqrt{2}}{4}\lambda^2\right]\right)\mp\frac{1}{2}\right)\right.\\&\qquad\left.-\sin\left[\frac{\pi}{2}\left(\frac{x}{\sqrt{\pi}}\pm\left[\frac{1}{2}\lambda-\frac{\sqrt{2}}{4}\lambda^2\right]\right)^2\right]\right]\end{aligned}}_{\text{OSCILLATING TERM PROPORTIONAL TO }\lambda}
$$

$$
\underbrace{\begin{aligned}&+\lambda^2\left[\frac{\pi}{2}\left(C\left(\frac{x}{\sqrt{\pi}}\pm\frac{1}{2}\lambda\right)\mp\frac{1}{2}\right)^2-\frac{\pi}{2}\left(\sqrt{2}\left[\frac{x}{\sqrt{\pi}}\pm\frac{1}{2}\lambda\right]\right)\left(C\left(\sqrt{2}\left[\frac{x}{\sqrt{\pi}}\pm\frac{1}{2}\lambda\right]\right)\mp\frac{1}{2}\right)\right.\\&\qquad\left.+\frac{1}{2}\sin\left[\frac{\pi}{2}\left(\sqrt{2}\left[\frac{x}{\sqrt{\pi}}\pm\frac{1}{2}\lambda\right]\right)^2\right]\right]\end{aligned}}_{\text{OSCILLATING TERM PROPORTIONAL TO }\lambda^2}
$$

$$
\underbrace{\begin{aligned}&+\lambda^3\left[\frac{\pi}{2}\cos\left[\frac{\pi}{2}\left(\frac{x}{\sqrt{\pi}}\right)^2\right]\left(C\left(\frac{x}{\sqrt{\pi}}\right)\mp\frac{1}{2}\right)^2-\frac{\pi}{\sqrt{2}}\left(C\left(\sqrt{2}\left[\frac{x}{\sqrt{\pi}}\right]\right)\mp\frac{1}{2}\right)\left(C\left(\frac{x}{\sqrt{\pi}}\right)\mp\frac{1}{2}\right)\right.\\&\qquad-\frac{\pi}{4}\left(\frac{x}{\sqrt{\pi}}\right)\left(C\left(\frac{x}{\sqrt{\pi}}\right)\mp\frac{1}{2}\right)+\frac{3\pi}{8}\left(\sqrt{3}\left[\frac{x}{\sqrt{\pi}}\right]\right)\left(C\left(\sqrt{3}\left[\frac{x}{\sqrt{\pi}}\right]\right)\mp\frac{1}{2}\right)\\&\qquad\left.+\frac{1}{8}\sin\left[\frac{\pi}{2}\left(\frac{x}{\sqrt{\pi}}\right)^2\right]-\frac{3}{8}\sin\left[\frac{\pi}{2}\left(\sqrt{3}\left[\frac{x}{\sqrt{\pi}}\right]\right)^2\right]\right]+\mathscr{O}(\lambda^4)\end{aligned}}_{\text{OSCILLATING TERM PROPORTIONAL TO }\lambda^3}
$$

(M.27)

A useful trick that we use in evaluating these integrals is the following: if $f \sim \mathscr{O}(\lambda)$ is a polynomial function of the mode parameter, we can establish which terms are relevant at each order of the solution:

$$\begin{aligned} C\left(\frac{x}{\sqrt{\pi}} \pm f(\lambda)\right) &= \int_0^{x/\sqrt{\pi}} \mathrm{d}y \cos\left(\frac{\pi}{2} y^2\right) + \int_{x/\sqrt{\pi}}^{x/\sqrt{\pi} \pm f(\lambda)} \mathrm{d}y \cos\left(\frac{\pi}{2} y^2\right) = \\ &= C\left(\frac{x}{\sqrt{\pi}}\right) \pm f(\lambda) \times \cos\left[\frac{\pi}{2}\left(\frac{x}{\sqrt{\pi}}\right)^2\right] = C\left(\frac{x}{\sqrt{\pi}}\right) + \mathscr{O}(\lambda)\,. \end{aligned} \tag{M.28}$$

The linear and constant terms can be simplified by expanding the sine function and the Fresnel integral (see eq. (J.4b)):

$$\begin{aligned} &\pm\sqrt{\pi}\left[\frac{\lambda}{2} - \lambda C\left(\frac{\lambda}{2} - \frac{\lambda^2}{2\sqrt{2}}\right) + \frac{\lambda^2}{2} - \lambda^2 C\left(\frac{\lambda}{2}\right)\right. \\ &\qquad \left. - \frac{\lambda^2}{2\sqrt{2}} + \frac{\lambda^2}{\sqrt{2}} C\left(\frac{\lambda}{\sqrt{2}}\right) - \frac{\lambda^3}{16} - \frac{\lambda^3}{2\sqrt{2}} + \frac{3\sqrt{3}}{16}\lambda^3\right] x \\ &+ \lambda \sin\left[\frac{\pi}{2}\left(\frac{\lambda}{2} - \frac{\lambda^2}{2\sqrt{2}}\right)^2\right] + \frac{\pi}{2}\lambda\left(\frac{\lambda}{2} - \frac{\lambda^2}{2\sqrt{2}}\right) - \pi\lambda\frac{\lambda}{2} C\left(\frac{\lambda}{2}\right) \\ &\qquad - \frac{\pi}{8}\lambda^2 + \frac{\pi}{2}\lambda^2 C\left(\frac{\lambda}{2}\right) - \frac{\pi}{4\sqrt{2}}\lambda^3 + \frac{\pi}{4\sqrt{2}}\lambda^3 - \frac{\pi}{8}\lambda^3 = \\ &= \pm\pi\left[\frac{1}{2}\lambda - \frac{\sqrt{2}}{4}\lambda^2 + \frac{3\sqrt{3}-1}{16}\lambda^3\right]\left(\frac{x}{\sqrt{\pi}}\right) + \pi\left[\frac{1}{8}\lambda^2 - \frac{\sqrt{2}}{8}\lambda^3\right] + \mathscr{O}(\lambda^4) \end{aligned} \tag{M.29}$$

Combining eq. (M.27) with $\phi_{(0)}(x) = x^2/2$, we obtain the complete solution to third order in λ, eq. (9.110). In particular, we have combined the quadratic, linear, and constant terms into a single quadratic term:

$$\begin{aligned} &\frac{x^2}{2} \pm \pi\left[\frac{1}{2}\lambda - \frac{\sqrt{2}}{4}\lambda^2 + \frac{3\sqrt{3}-1}{16}\lambda^3\right]\left(\frac{x}{\sqrt{\pi}}\right) + \pi\left[\frac{\lambda^2}{8} - \frac{\lambda^3}{4\sqrt{2}}\right] \\ &\qquad = \frac{\pi}{2}\left(\frac{x}{\sqrt{\pi}} \pm \left[\frac{1}{2}\lambda - \frac{\sqrt{2}}{4}\lambda^2 + \frac{3\sqrt{3}-1}{16}\lambda^3\right]\right)^2 + \mathscr{O}(\lambda^4)\,. \end{aligned} \tag{M.30}$$

Finally, we pay attention to the form of the oscillating terms. If we compare eq. (M.27) to eqs. (M.3) and (M.13), we can immediately notice how the oscillating terms proportional to λ and λ^2 are related to previous results:

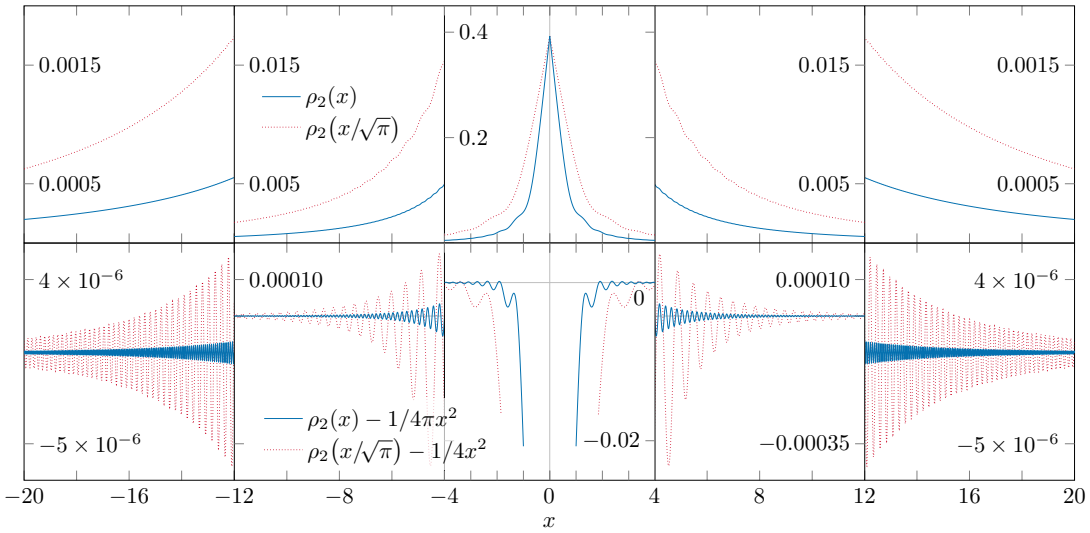

Fig. M.6 *Upper pannel*: Graphical representation of the two functions $\rho_2(x)$ and $\rho_2\left(x/\sqrt{\pi}\right)$. *Lower panel*: The same functions, however here the highest-order guide function is removed to reveal the oscillations. It is evident from the deviation from $y = 0$, especially around the origin, that there are lower-order contributions to the guide function. From both panels, however, we see that the function $\rho_2(X)$ oscillates more rapidly and decreases in magnitude away from the origin. Figure appeared in [1].

$$\begin{aligned} &\text{OSCILLATING TERM} \\ &\text{PROPORTIONAL TO } \lambda \end{aligned} = \rho_1\left(\frac{x}{\sqrt{\pi}} \pm \left[\frac{1}{2}\lambda - \frac{\sqrt{2}}{4}\lambda^2\right]\right), \tag{M.31a}$$

$$\begin{aligned} &\text{OSCILLATING TERM} \\ &\text{PROPORTIONAL TO } \lambda^2 \end{aligned} = \rho_2\left(\frac{x}{\sqrt{\pi}} \pm \frac{1}{2}\lambda\right). \tag{M.31b}$$

We are in a position to establish the functional form of the third-order oscillating term, $\rho_{(3)}(X)$:

$$\begin{aligned} \rho_3(X) = \frac{\pi}{2}\cos\left[\frac{\pi}{2}X^2\right]\left(C(X) \mp \frac{1}{2}\right)^2 - \frac{\pi}{\sqrt{2}}\left(C\left(\sqrt{2}X\right) \mp \frac{1}{2}\right)\left(C(X) \mp \frac{1}{2}\right) - \frac{\pi}{8}X\left(C(X) \mp \frac{1}{2}\right) \\ + \frac{3\pi}{8}\left(\sqrt{3}X\right)\left(C\left(\sqrt{3}X\right) \mp \frac{1}{2}\right) + \frac{1}{8}\sin\left[\frac{\pi}{2}X^2\right] - \frac{3}{8}\sin\left[\frac{\pi}{2}\left(\sqrt{3}X\right)^2\right]. \end{aligned} \tag{M.32}$$

M.2 Supplementary plots and remarks

The corrections have been plotted in Figure M.4 for value of $\lambda = 0.1$. Interesting is their behaviour around the origin: even though we have imposed the condition $\phi(0) = 0$ at each order of the solution, it is important to note that they have corrections of the next-higher order of λ: $\phi_{(1)}(x)$ is accurate up to $\mathscr{O}(\lambda^2)$, $\phi_{(2)}(x)$ to $\mathscr{O}(\lambda^3)$, and so on. Therefore, at the origin $x = 0$, $\phi_{(1)}(x)$ satisfies the initial condition and goes through (0,0), since it does not contain any constant terms in λ (cf. eq. (M.3)). The next-order correction, $\phi_{(2)}(x)$, however, does not go through the origin: we can see this both from eq. (M.13) and from Figure M.4. Note that this is not only due to the constant term $\pi\lambda^2/8$, but also because the oscillating term proportional to λ in eq. (M.13) does not go through the origin. Similarly, $|\phi_{(3)}(0)| \sim \mathscr{O}(\lambda^4)$, and the third-order correction is also valid.

As we can see, certain function emerge in the arguments of the phase functions: the coefficients of the linear x term in each of the phase corrections can be written as $\pm\sqrt{\pi}\,\sigma_{\{1,2,3\}}(\lambda)$, where the functions are given by:

$$\sigma_1(\lambda) = \frac{1}{2}\lambda, \tag{M.33}$$

$$\sigma_2(\lambda) = \frac{1}{2}\lambda - \frac{\sqrt{2}}{4}\lambda^2, \tag{M.34}$$

$$\sigma_3(\lambda) = \frac{1}{2}\lambda - \frac{\sqrt{2}}{4}\lambda^2 + \frac{3\sqrt{3}-1}{16}\lambda^3. \tag{9.111}$$

These have been plotted (for $\lambda = 0.1$) in Fig. 9.15, and discussed in more detail in Section 9.3.

The last issue we will discuss in this section is the functional form of the oscillating terms $\rho_{\{1,2,3\}}(X)$, given by eqs. (M.5), (M.18), and (M.32). These represent the functions which arise as the oscillating terms at first, second, and third orders, respectively. Two of

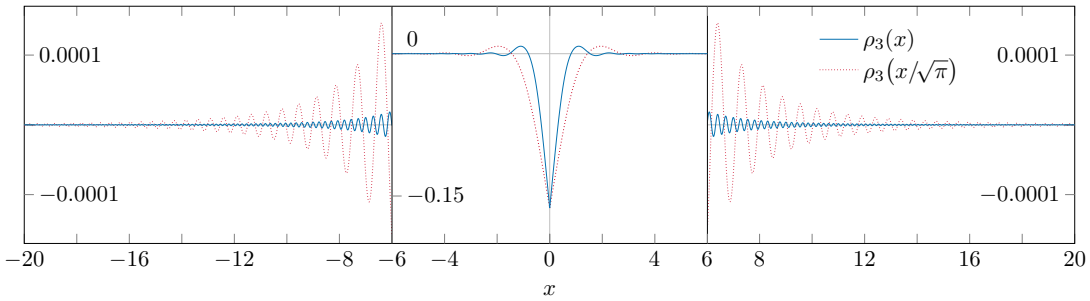

Fig. M.7 Plots of the two functions $\rho_3(x)$ and $\rho_3(x/\sqrt{\pi})$. We see that both branches (for positive and negative x) are comprised of oscillations which peter out as the distance from the origin increases. Figure appeared in [1].

them, $\rho_1(X)$ and $\rho_3(X)$, oscillate around the abscissa, and are depicted in Figure M.5 and Figure M.7. The magnitude of the oscillations decreases with $|X|$, while their frequency increases, which means that they can safely be treated as perturbations to terms which grow quadratically or linearly with X. The function $\rho_2(X)$ differs slightly from the others in that it does not oscillate around the abscissa, but rather around the curve $1/4\pi X^2$, as can be seen from analytically expanding the function for large values of $|X|$ (i.e., $|X| > 1$):

$$\begin{aligned}\rho_2(X) &= \frac{\pi}{2}\left(C(X) \mp \frac{1}{2}\right)^2 - \frac{\pi}{\sqrt{2}} X\left(C\left(\sqrt{2}X\right) \mp \frac{1}{2}\right) + \frac{1}{2}\sin\left(\pi X^2\right) \\ &\sim \frac{1}{4\pi X^2}\left(1 - \cos\left(\pi X^2\right)\right) + \mathscr{O}\left(X^{-3}\right)\end{aligned} \tag{M.35}$$

The details about $\rho_2(X)$ are plotted on Figure M.6, and we can see that despite the dissimilarities to the other two functions, it still decreases in magnitude with increasing $|X|$, and can be treated as a perturbation to the other terms.

M.3 Phase resonance equation with $\mathbf{n \neq 1}$

If we consider the source equation (7.17b) in the single-mode version again, however this time instead of keeping the mode with $n = 1$, we include only the r^{th} mode, then we need to solve the following differential equation:

$$\left(\phi^{(r)}(x)\right)'' = 1 + \lambda_r \cos\left(r\phi^{(r)}\right). \tag{M.36}$$

The algorithm for solution is identical to the one presented above for the case with $r = 1$, hence we only quote the results at each order. The zeroth-order correction is left unchanged, given by eq. (9.100). The first-order correction is:

$$\begin{aligned}\phi^{(r)}_{(1)}(x) = \pm\pi\left[\frac{1}{2}\frac{\lambda_r}{\sqrt{r}}\right]\left(\frac{x}{\sqrt{\pi}}\right) + \frac{\lambda_r}{r}\Bigg[\pi\left(\sqrt{r}\left[\frac{x}{\sqrt{\pi}}\right]\right)\left(C\left(\sqrt{r}\left[\frac{x}{\sqrt{\pi}}\right]\right) \mp \frac{1}{2}\right) \\ - \sin\left[\frac{\pi}{2}\left(\sqrt{r}\left[\frac{x}{\sqrt{\pi}}\right]\right)^2\right]\Bigg] + \mathscr{O}\left(\lambda_r^2\right).\end{aligned} \tag{M.37}$$

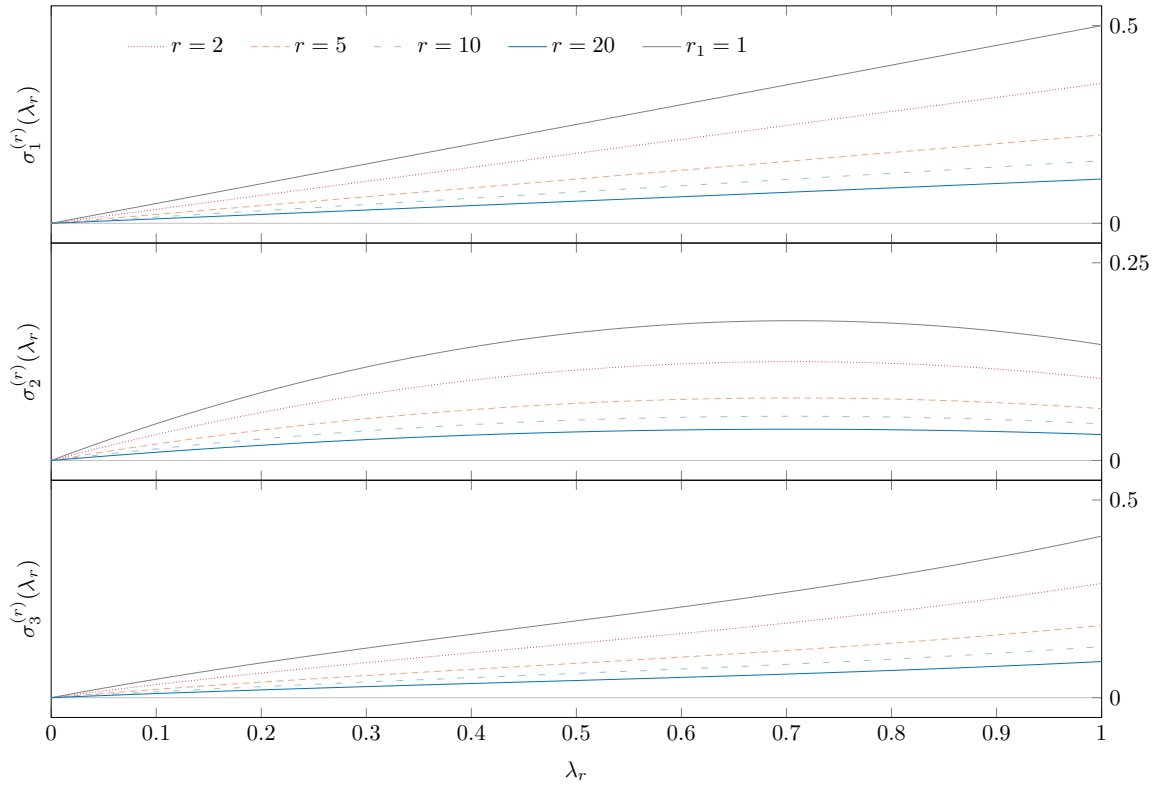

Fig. M.8 Evolution of the slope of the phase resonance solution (for large $|x|$) with changing number of the mode $n = r$. Figure appeared in [1].

In the second-order correction we begin to notice the evolution of the terms from the original solution eq. (M.13):

$$\begin{aligned}\phi_{(2)}^{(r)}(x) = \pm\pi\left[\frac{1}{2}\frac{\lambda_r}{\sqrt{r}} - \frac{\sqrt{2}}{4}\frac{\lambda_r^2}{\sqrt{r}}\right]\left(\frac{x}{\sqrt{\pi}}\right) + \pi\left[\frac{1}{8}\frac{\lambda_r^2}{r}\right] \\ + \frac{\lambda_r}{r}\left[\pi\left(\sqrt{r}\left[\frac{x}{\sqrt{\pi}} \pm \frac{1}{2}\frac{\lambda_r}{\sqrt{r}}\right]\right)\left(C\left(\sqrt{r}\left[\frac{x}{\sqrt{\pi}} \pm \frac{1}{2}\frac{\lambda_r}{\sqrt{r}}\right]\right) \mp \frac{1}{2}\right)\right. \\ \left. - \sin\left[\frac{\pi}{2}\left(\sqrt{r}\left[\frac{x}{\sqrt{\pi}} \pm \frac{1}{2}\frac{\lambda_r}{\sqrt{r}}\right]\right)^2\right]\right] \\ + \frac{\lambda_r^2}{r}\left[\frac{\pi}{2}\left(C\left(\sqrt{r}\left[\frac{x}{\sqrt{\pi}}\right]\right) \mp \frac{1}{2}\right)^2 - \frac{\pi}{2}\left(\sqrt{2r}\left[\frac{x}{\sqrt{\pi}}\right]\right)\left(C\left(\sqrt{2r}\left[\frac{x}{\sqrt{\pi}}\right]\right) \mp \frac{1}{2}\right)\right.\end{aligned}$$

$$+\frac{1}{2}\sin\left[\frac{\pi}{2}\left(\sqrt{2r}\left[\frac{x}{\sqrt{\pi}}\right]\right)^2\right]\Bigg] + \mathscr{O}\left(\lambda_r^3\right). \qquad \text{(M.38)}$$

We can already notice some ways in which this result differs from the second-order correction with $r = 1$, for instance the change of variables from $x/\sqrt{\pi}$ to $\sqrt{r}x/\sqrt{\pi}$, and the factor of $1/r$ added to the multipliers of the oscillating terms. Before we explain how this arises from the governing equation, we present the third-order result:

$$\begin{aligned}
\phi_{(3)}^{(r)}(x) = \pm\pi\left[\frac{1}{2}\frac{\lambda_r}{\sqrt{r}} - \frac{\sqrt{2}}{4}\frac{\lambda_r^2}{\sqrt{r}} + \frac{3\sqrt{3}-1}{16}\frac{\lambda_r^3}{\sqrt{r}}\right]\left(\frac{x}{\sqrt{\pi}}\right) + \pi\left[\frac{1}{8}\frac{\lambda_r^2}{r} - \frac{\sqrt{2}}{8}\frac{\lambda_r^3}{r}\right] \\
+\frac{\lambda_r}{r}\Bigg[\pi\left(\sqrt{r}\left[\frac{x}{\sqrt{\pi}} \pm \sigma_2^{(r)}(\lambda_r)\right]\right)\left(C\left(\sqrt{r}\left[\frac{x}{\sqrt{\pi}} \pm \sigma_2^{(r)}(\lambda_r)\right]\right) \mp \frac{1}{2}\right) \\
- \sin\left[\frac{\pi}{2}\left(\sqrt{r}\left[\frac{x}{\sqrt{\pi}} \pm \sigma_2^{(r)}(\lambda_r)\right]\right)^2\right]\Bigg] \\
+\frac{\lambda_r^2}{r}\Bigg[\frac{\pi}{2}\left(C\left(\sqrt{r}\left[\frac{x}{\sqrt{\pi}} \pm \frac{1}{2}\frac{\lambda_r}{\sqrt{r}}\right]\right) \mp \frac{1}{2}\right)^2 + \frac{1}{2}\sin\left[\frac{\pi}{2}\left(\sqrt{2r}\left[\frac{x}{\sqrt{\pi}} \pm \frac{1}{2}\frac{\lambda_r}{\sqrt{r}}\right]\right)^2\right] \\
- \frac{\pi}{2}\left(\sqrt{2r}\left[\frac{x}{\sqrt{\pi}} \pm \frac{1}{2}\frac{\lambda_r}{\sqrt{r}}\right]\right)\left(C\left(\sqrt{2r}\left[\frac{x}{\sqrt{\pi}} \pm \frac{1}{2}\frac{\lambda_r}{\sqrt{r}}\right]\right) \mp \frac{1}{2}\right)\Bigg] \\
+\frac{\lambda_r^3}{r}\Bigg[\frac{\pi}{2}\cos\left[\frac{\pi}{2}\left(\sqrt{r}\left[\frac{x}{\sqrt{\pi}}\right]\right)^2\right]\left(C\left(\sqrt{r}\left[\frac{x}{\sqrt{\pi}}\right]\right) \mp \frac{1}{2}\right)^2 \\
- \frac{\pi}{\sqrt{2}}\left(C\left(\sqrt{2r}\left[\frac{x}{\sqrt{\pi}}\right]\right) \mp \frac{1}{2}\right)\left(C\left(\sqrt{r}\left[\frac{x}{\sqrt{\pi}}\right]\right) \mp \frac{1}{2}\right) \\
+ \frac{3\pi}{8}\left(\sqrt{3r}\left[\frac{x}{\sqrt{\pi}}\right]\right)\left(C\left(\sqrt{3r}\left[\frac{x}{\sqrt{\pi}}\right]\right) \mp \frac{1}{2}\right) \\
- \frac{\pi}{8}\left(\sqrt{r}\left[\frac{x}{\sqrt{\pi}}\right]\right)\left(C\left(\sqrt{r}\left[\frac{x}{\sqrt{\pi}}\right]\right) \mp \frac{1}{2}\right) - \frac{3}{8}\sin\left[\frac{\pi}{2}\left(\sqrt{3r}\left[\frac{x}{\sqrt{\pi}}\right]\right)^2\right]
\end{aligned}$$

$$+\frac{1}{8}\sin\left[\frac{\pi}{2}\left(\sqrt{r}\left[\frac{x}{\sqrt{\pi}}\right]\right)^2\right]\Bigg]+\mathscr{O}\left(\lambda_r^4\right). \tag{M.39}$$

These results can be obtained from the ones involving $\lambda_1 \equiv \lambda$ by transforming eq. (9.98) with a change of variables:

$$\phi \quad \mapsto \quad \phi^{(r)} = r\phi \tag{M.40a}$$

$$x \quad \mapsto \quad \sqrt{r}x, \tag{M.40b}$$

which yields eq. (M.36), hence the solutions to this equation can be found from eq. (9.98) by applying a change of variables. It is interesting to see how the number of the mode r affects the graphical behaviour of the solution. In Figure 9.18 we have plotted the effect of the mode number r on the correction ${\phi_3}^{(r)}(x)$, and in Figure M.8 we see the effect of r on the slope of the solution. The validity of solutions (M.37) – (M.39) is confirmed graphically in Figure M.9.

M.4 Phase resonance equation with two distinct modes

As an interlude to solving the multi-mode version of the phase resonance equation, we present the solution for two modes on the right-hand side, labelled by integers r and s. Without loss of generality, we can let let $r < s$.

$$\left(\phi^{(r,s)}(x)\right)'' = 1 + \lambda_r \cos(r\phi) + \lambda_s \cos(s\phi). \tag{9.119}$$

The zeroth-order solution remains unchanged, $\phi_0^{(r,s)} = x^2/2$. The first-order correction can be written in the form:

$$\phi_{(1)}^{(r,s)}(x) = \sum_{l\in\{r,s\}} \Bigg\{ \pm\frac{\pi}{2}\frac{\lambda_l}{\sqrt{l}}\left(\frac{x}{\sqrt{\pi}}\right) + \frac{\lambda_l}{l}\Bigg[\pi\left(\sqrt{l}\left[\frac{x}{\sqrt{\pi}}\right]\right)\left(C\left(\sqrt{l}\left[\frac{x}{\sqrt{\pi}}\right]\right)\mp\frac{1}{2}\right) - \sin\left[\frac{\pi}{2}\left(\sqrt{l}\left[\frac{x}{\sqrt{\pi}}\right]\right)^2\right]\Bigg]\Bigg\}, \tag{M.41}$$

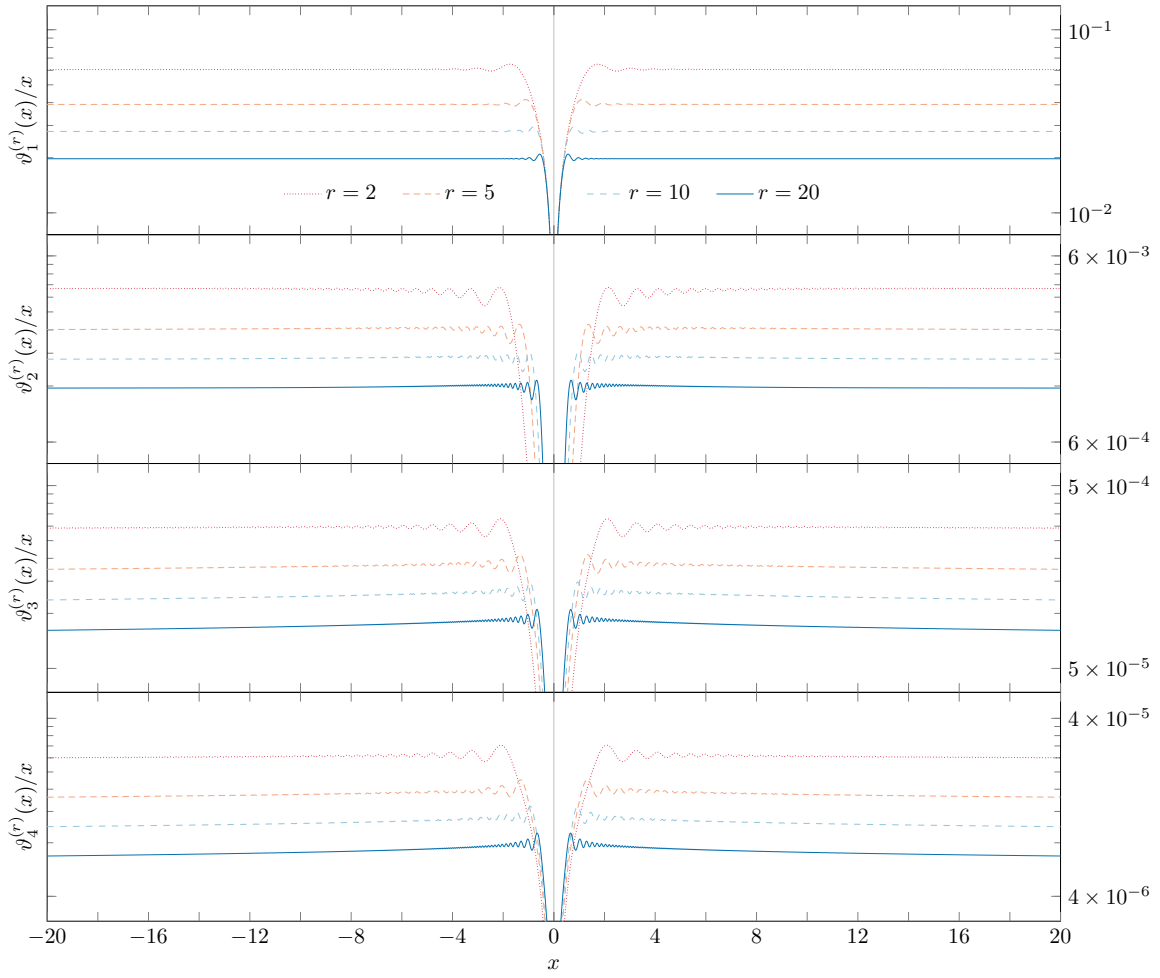

Fig. M.9 Graphical validation of the phase resonance equation with a single $n \neq 1$ mode: solutions (M.37) – (M.39). Figure appeared in [1].

i.e., the two separate solutions do not mix at first order, and effectively $\phi_{(1)}^{(r,s)}(x) = \phi_{(1)}^{(r)}(x) + \phi_{(1)}^{(s)}(x)$.

At next order, however, mixing occurs, since we need to substitute the above expression (M.41) in both terms on the right-hand side of eq. (9.119). The second-order correction to the original solution can be found to be a combination of (modified) single-mode corrections plus a new mixing term at second order.

$$\phi_{(2)}^{(r,s)}(x) = \pm\pi\left[\frac{1}{2}\left(\frac{\lambda_r}{\sqrt{r}}+\frac{\lambda_s}{\sqrt{s}}\right) - \frac{\sqrt{2}}{4}\left(\frac{\lambda_r^2}{\sqrt{r}}+\frac{\lambda_s^2}{\sqrt{s}}\right) + \frac{1}{4}\left((s-r)^{3/2}-(r+s)^{3/2}\right)\frac{\lambda_r}{r}\frac{\lambda_s}{s}\right]\left(\frac{x}{\sqrt{\pi}}\right) + \frac{\pi}{8}\left(\frac{\lambda_r}{\sqrt{r}}+\frac{\lambda_s}{\sqrt{s}}\right)^2$$

$$+\frac{\lambda_r}{r}\left[\pi\left(\sqrt{r}\left[\frac{x}{\sqrt{\pi}}\pm\frac{1}{2}\left(\frac{\lambda_r}{\sqrt{r}}+\frac{\lambda_s}{\sqrt{s}}\right)\right]\right)\left(C\left(\sqrt{r}\left[\frac{x}{\sqrt{\pi}}\pm\frac{1}{2}\left(\frac{\lambda_r}{\sqrt{r}}+\frac{\lambda_s}{\sqrt{s}}\right)\right]\right)\mp\frac{1}{2}\right)\right.$$

$$\left.-\sin\left[\frac{\pi}{2}\left(\sqrt{r}\left[\frac{x}{\sqrt{\pi}}\pm\frac{1}{2}\left(\frac{\lambda_r}{\sqrt{r}}+\frac{\lambda_s}{\sqrt{s}}\right)\right]\right)^2\right]\right]$$

$$+\frac{\lambda_s}{s}\left[\pi\left(\sqrt{s}\left[\frac{x}{\sqrt{\pi}}\pm\frac{1}{2}\left(\frac{\lambda_r}{\sqrt{r}}+\frac{\lambda_s}{\sqrt{s}}\right)\right]\right)\left(C\left(\sqrt{s}\left[\frac{x}{\sqrt{\pi}}\pm\frac{1}{2}\left(\frac{\lambda_r}{\sqrt{r}}+\frac{\lambda_s}{\sqrt{s}}\right)\right]\right)\mp\frac{1}{2}\right)\right.$$

$$\left.-\sin\left[\frac{\pi}{2}\left(\sqrt{s}\left[\frac{x}{\sqrt{\pi}}\pm\frac{1}{2}\left(\frac{\lambda_r}{\sqrt{r}}+\frac{\lambda_s}{\sqrt{s}}\right)\right]\right)^2\right]\right]$$

$$+\frac{\pi}{2}\left(\frac{\lambda_r}{\sqrt{r}}\left(C\left(\sqrt{r}\left[\frac{x}{\sqrt{\pi}}\right]\right)\mp\frac{1}{2}\right)+\frac{\lambda_s}{\sqrt{s}}\left(C\left(\sqrt{s}\left[\frac{x}{\sqrt{\pi}}\right]\right)\mp\frac{1}{2}\right)\right)^2$$

$$+\frac{\pi}{2}\frac{\lambda_r}{r}\frac{\lambda_s}{s}\left((s-r)\left(\sqrt{s-r}\left[\frac{x}{\sqrt{\pi}}\right]\right)\left(C\left(\sqrt{s-r}\left[\frac{x}{\sqrt{\pi}}\right]\right)\mp\frac{1}{2}\right)\right.$$

$$\left.-(r+s)\left(\sqrt{r+s}\left[\frac{x}{\sqrt{\pi}}\right]\right)\left(C\left(\sqrt{r+s}\left[\frac{x}{\sqrt{\pi}}\right]\right)\mp\frac{1}{2}\right)\right)$$

$$-\frac{\pi}{2}\left(\frac{\lambda_r^2}{r}\left(\sqrt{2r}\left[\frac{x}{\sqrt{\pi}}\right]\right)\left(C\left(\sqrt{2r}\left[\frac{x}{\sqrt{\pi}}\right]\right)\mp\frac{1}{2}\right)\right.$$

$$\left.+\frac{\lambda_s^2}{s}\left(\sqrt{2s}\left[\frac{x}{\sqrt{\pi}}\right]\right)\left(C\left(\sqrt{2s}\left[\frac{x}{\sqrt{\pi}}\right]\right)\mp\frac{1}{2}\right)\right)$$

$$-\frac{1}{2}\frac{\lambda_r}{r}\frac{\lambda_s}{s}\left((s-r)\sin\left[\frac{\pi}{2}\left(\sqrt{s-r}\left[\frac{x}{\sqrt{\pi}}\right]\right)^2\right]-(r+s)\sin\left[\frac{\pi}{2}\left(\sqrt{r+s}\left[\frac{x}{\sqrt{\pi}}\right]\right)^2\right]\right)$$

$$+\frac{1}{2}\left(\frac{\lambda_r^2}{r}\sin\left[\frac{\pi}{2}\left(\sqrt{2r}\left[\frac{x}{\sqrt{\pi}}\right]\right)^2\right]+\frac{\lambda_s^2}{s}\sin\left[\frac{\pi}{2}\left(\sqrt{2s}\left[\frac{x}{\sqrt{\pi}}\right]\right)^2\right]\right)= \tag{M.42}$$

$$=\sum_{l\in\{r,s\}}\Bigg\{\pm\pi\left[\frac{1}{2}\frac{\lambda_l}{l}-\frac{\sqrt{2}}{4}\frac{\lambda_l^2}{l}\right]\left(\sqrt{l}\left[\frac{x}{\sqrt{\pi}}\right]\right)+\pi\left[\frac{1}{8}\frac{\lambda_l^2}{l}\right]$$

$$+\frac{\lambda_l}{l}\Bigg[\pi\left(\sqrt{l}\left[\frac{x}{\sqrt{\pi}}\pm\frac{1}{2}\left(\frac{\lambda_l}{\sqrt{l}}+\frac{\lambda_{\bar{l}}}{\sqrt{\bar{l}}}\right)\right]\right)\left(C\left(\sqrt{l}\left[\frac{x}{\sqrt{\pi}}\pm\frac{1}{2}\left(\frac{\lambda_l}{\sqrt{l}}+\frac{\lambda_{\bar{l}}}{\sqrt{\bar{l}}}\right)\right]\right)\mp\frac{1}{2}\right)$$

$$-\sin\left[\frac{\pi}{2}\left(\sqrt{l}\left[\frac{x}{\sqrt{\pi}}\pm\frac{1}{2}\left(\frac{\lambda_l}{\sqrt{l}}+\frac{\lambda_{\bar{l}}}{\sqrt{\bar{l}}}\right)\right]\right)^2\right]\Bigg]$$

$$+\frac{\lambda_l^2}{l}\Bigg[\frac{\pi}{2}\left(C\left(\sqrt{l}\left[\frac{x}{\sqrt{\pi}}\right]\right)\mp\frac{1}{2}\right)^2-\frac{\pi}{2}\left(\sqrt{2l}\left[\frac{x}{\sqrt{\pi}}\right]\right)\left(C\left(\sqrt{2l}\left[\frac{x}{\sqrt{\pi}}\right]\right)\mp\frac{1}{2}\right)$$

$$+\frac{1}{2}\sin\left[\frac{\pi}{2}\left(\sqrt{2l}\left[\frac{x}{\sqrt{\pi}}\right]\right)^2\right]\Bigg]\Bigg\}$$

$$\pm\frac{\pi}{4}\frac{\lambda_r}{r}\frac{\lambda_s}{s}\left[(s-r)\left(\sqrt{s-r}\left[\frac{x}{\sqrt{\pi}}\right]\right)-(r+s)\left(\sqrt{r+s}\left[\frac{x}{\sqrt{\pi}}\right]\right)\right]+\frac{\pi}{4}\frac{\lambda_r}{\sqrt{r}}\frac{\lambda_s}{\sqrt{s}}$$

$$+\frac{\lambda_r}{\sqrt{r}}\frac{\lambda_s}{\sqrt{s}}\Bigg[\pi\left(C\left(\sqrt{r}\left[\frac{x}{\sqrt{\pi}}\right]\right)\mp\frac{1}{2}\right)\left(C\left(\sqrt{s}\left[\frac{x}{\sqrt{\pi}}\right]\right)\mp\frac{1}{2}\right)$$

$$+\frac{\pi}{2}\frac{s-r}{\sqrt{rs}}\left(\sqrt{s-r}\left[\frac{x}{\sqrt{\pi}}\right]\right)\left(C\left(\sqrt{s-r}\left[\frac{x}{\sqrt{\pi}}\right]\right)\mp\frac{1}{2}\right)$$

$$-\frac{\pi}{2}\frac{r+s}{\sqrt{rs}}\left(\sqrt{r+s}\left[\frac{x}{\sqrt{\pi}}\right]\right)\left(C\left(\sqrt{r+s}\left[\frac{x}{\sqrt{\pi}}\right]\right)\mp\frac{1}{2}\right)$$

$$+\frac{1}{2}\frac{r+s}{\sqrt{rs}}\sin\left[\frac{\pi}{2}\left(\sqrt{r+s}\left[\frac{x}{\sqrt{\pi}}\right]\right)^2\right]-\frac{1}{2}\frac{s-r}{\sqrt{rs}}\sin\left[\frac{\pi}{2}\left(\sqrt{s-r}\left[\frac{x}{\sqrt{\pi}}\right]\right)^2\right]\Bigg] \tag{M.43}$$

Here, $\bar{l}$ denotes the element of the set $\{r,s\}$ which is currently not l. It is best to interpret these results graphically.

Finally, we present the third-order solution for a source equation with two distinct modes.

$$\begin{aligned}
\phi_{(3)}^{(r,s)}(x) = \pm\pi\Bigg[&\frac{1}{2}\left(\frac{\lambda_r}{\sqrt{r}}+\frac{\lambda_s}{\sqrt{s}}\right)-\frac{\sqrt{2}}{4}\left(\frac{\lambda_r^2}{\sqrt{r}}+\frac{\lambda_s^2}{\sqrt{s}}\right)+\frac{1}{4}\Big((s-r)^{3/2}-(r+s)^{3/2}\Big)\frac{\lambda_r}{r}\frac{\lambda_s}{s}\\
&+\frac{3\sqrt{3}-1}{16}\left(\frac{\lambda_r^3}{\sqrt{r}}+\frac{\lambda_s^3}{\sqrt{s}}\right)+\frac{1}{16}\Big((2r+s)^{5/2}-\operatorname{sgn}(2r-s)|2r-s|^{5/2}-2s^{5/2}\Big)\frac{\lambda_r^2}{r^2}\frac{\lambda_s}{s}\\
&+\frac{1}{16}\Big((2s+r)^{5/2}-(2s-r)^{5/2}-2r^{5/2}\Big)\frac{\lambda_r}{r}\frac{\lambda_s^2}{s^2}\Bigg]\left(\frac{x}{\sqrt{\pi}}\right)\\
&+\pi\Bigg[\frac{1}{8}\left(\frac{\lambda_r}{\sqrt{r}}+\frac{\lambda_s}{\sqrt{s}}\right)^2-\frac{\sqrt{2}}{8}\left(\frac{\lambda_r}{\sqrt{r}}+\frac{\lambda_s}{\sqrt{s}}\right)\left(\frac{\lambda_r^2}{\sqrt{r}}+\frac{\lambda_s^2}{\sqrt{s}}\right)\\
&+\frac{1}{8}\left(\frac{\lambda_r}{\sqrt{r}}+\frac{\lambda_s}{\sqrt{s}}\right)\Big((s-r)^{3/2}-(r+s)^{3/2}\Big)\frac{\lambda_r}{r}\frac{\lambda_s}{s}\Bigg]\\
&+\pi\left(\frac{\lambda_r}{r}\left(\sqrt{r}\left[\frac{x}{\sqrt{\pi}}\pm\sigma_2^{(r,s)}\right]\right)\left(C\left(\sqrt{r}\left[\frac{x}{\sqrt{\pi}}\pm\sigma_2^{(r,s)}\right]\right)\mp\frac{1}{2}\right)\right.\\
&\left.+\frac{\lambda_s}{s}\left(\sqrt{s}\left[\frac{x}{\sqrt{\pi}}\pm\sigma_2^{(r,s)}\right]\right)\left(C\left(\sqrt{s}\left[\frac{x}{\sqrt{\pi}}\pm\sigma_2^{(r,s)}\right]\right)\mp\frac{1}{2}\right)\right)\\
&-\frac{\lambda_r}{r}\sin\left[\frac{\pi}{2}\left(\sqrt{r}\left[\frac{x}{\sqrt{\pi}}\pm\sigma_2^{(r,s)}\right]\right)^2\right]-\frac{\lambda_s}{s}\sin\left[\frac{\pi}{2}\left(\sqrt{s}\left[\frac{x}{\sqrt{\pi}}\pm\sigma_2^{(r,s)}\right]\right)^2\right]\\
&+\frac{\pi}{2}\left(\frac{\lambda_r}{\sqrt{r}}\left(C\left(\sqrt{r}\left[\frac{x}{\sqrt{\pi}}\pm\sigma_1^{(r,s)}\right]\right)\mp\frac{1}{2}\right)+\frac{\lambda_s}{\sqrt{s}}\left(C\left(\sqrt{s}\left[\frac{x}{\sqrt{\pi}}\pm\sigma_1^{(r,s)}\right]\right)\mp\frac{1}{2}\right)\right)^2
\end{aligned}$$

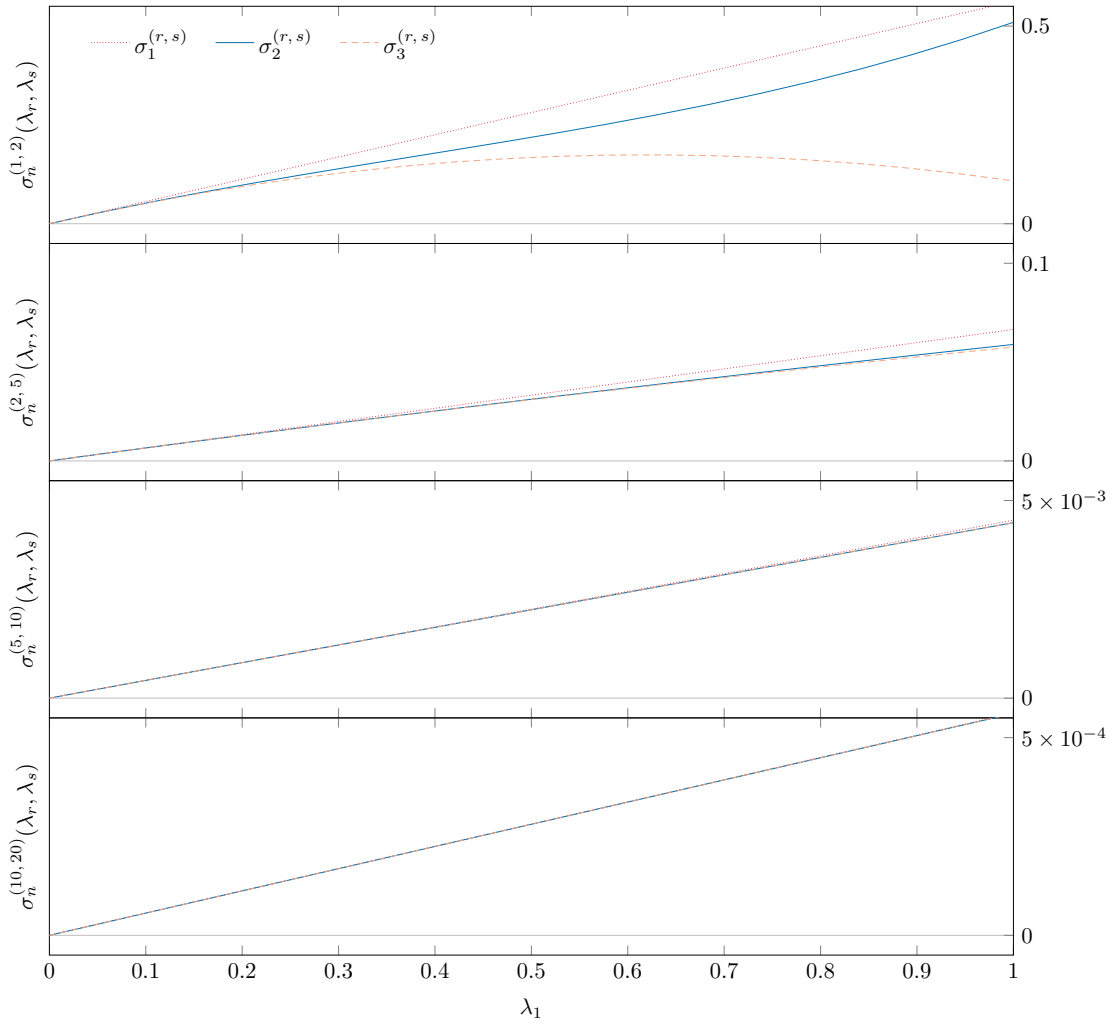

Fig. M.10 Slope of the phase solution with two different oscillating modes, r and s, for several different combinations of the mode numbers, and for $0 \leq \lambda_r, \lambda_s \leq 1$. Figure appeared in [1].

$$
\begin{aligned}
&+\frac{\pi}{2}\frac{\lambda_r}{r}\frac{\lambda_s}{s}\left((s-r)\left(\sqrt{s-r}\left[\frac{x}{\sqrt{\pi}}\pm\sigma_1^{(r,s)}\right]\right)\left(C\left(\sqrt{s-r}\left[\frac{x}{\sqrt{\pi}}\pm\sigma_1^{(r,s)}\right]\right)\mp\frac{1}{2}\right)\right.\\
&\qquad\left.-(r+s)\left(\sqrt{r+s}\left[\frac{x}{\sqrt{\pi}}\pm\sigma_1^{(r,s)}\right]\right)\left(C\left(\sqrt{r+s}\left[\frac{x}{\sqrt{\pi}}\pm\sigma_1^{(r,s)}\right]\right)\mp\frac{1}{2}\right)\right)\\
&-\frac{\pi}{2}\left(\frac{\lambda_r^2}{r}\left(\sqrt{2r}\left[\frac{x}{\sqrt{\pi}}\pm\sigma_1^{(r,s)}\right]\right)\left(C\left(\sqrt{2r}\left[\frac{x}{\sqrt{\pi}}\pm\sigma_1^{(r,s)}\right]\right)\mp\frac{1}{2}\right)\right.\\
&\qquad\left.+\frac{\lambda_s^2}{s}\left(\sqrt{2s}\left[\frac{x}{\sqrt{\pi}}\pm\sigma_1^{(r,s)}\right]\right)\left(C\left(\sqrt{2s}\left[\frac{x}{\sqrt{\pi}}\pm\sigma_1^{(r,s)}\right]\right)\mp\frac{1}{2}\right)\right)\\
&-\frac{1}{2}\frac{\lambda_r}{r}\frac{\lambda_s}{s}\left((s-r)\sin\left[\frac{\pi}{2}\left(\sqrt{s-r}\left[\frac{x}{\sqrt{\pi}}\pm\sigma_1^{(r,s)}\right]\right)^2\right]\right.\\
&\qquad\left.-(r+s)\sin\left[\frac{\pi}{2}\left(\sqrt{r+s}\left[\frac{x}{\sqrt{\pi}}\pm\sigma_1^{(r,s)}\right]\right)^2\right]\right)\\
&+\frac{1}{2}\left(\frac{\lambda_r^2}{r}\sin\left[\frac{\pi}{2}\left(\sqrt{2r}\left[\frac{x}{\sqrt{\pi}}\pm\sigma_1^{(r,s)}\right]\right)^2\right]+\frac{\lambda_s^2}{s}\sin\left[\frac{\pi}{2}\left(\sqrt{2s}\left[\frac{x}{\sqrt{\pi}}\pm\sigma_1^{(r,s)}\right]\right)^2\right]\right)\\
&+\frac{\pi}{2}\left(\lambda_r\cos\left[\frac{\pi}{2}\left(\sqrt{r}\left[\frac{x}{\sqrt{\pi}}\right]\right)^2\right]+\lambda_s\cos\left[\frac{\pi}{2}\left(\sqrt{s}\left[\frac{x}{\sqrt{\pi}}\right]\right)^2\right]\right)\times\\
&\qquad\times\left(\frac{\lambda_r}{\sqrt{r}}\left(C\left(\sqrt{r}\left[\frac{x}{\sqrt{\pi}}\right]\right)\mp\frac{1}{2}\right)+\frac{\lambda_s}{\sqrt{s}}\left(C\left(\sqrt{s}\left[\frac{x}{\sqrt{\pi}}\right]\right)\mp\frac{1}{2}\right)\right)^2\\
&+\frac{\pi}{2}\frac{\lambda_r}{r}\frac{\lambda_s}{s}\left((s-r)^{3/2}\left(C\left(\sqrt{s-r}\left[\frac{x}{\sqrt{\pi}}\right]\right)\mp\frac{1}{2}\right)-(r+s)^{3/2}\left(C\left(\sqrt{r+s}\left[\frac{x}{\sqrt{\pi}}\right]\right)\mp\frac{1}{2}\right)\right)\times\\
&\qquad\times\left(\frac{\lambda_r}{\sqrt{r}}\left(C\left(\sqrt{r}\left[\frac{x}{\sqrt{\pi}}\right]\right)\mp\frac{1}{2}\right)+\frac{\lambda_s}{\sqrt{s}}\left(C\left(\sqrt{s}\left[\frac{x}{\sqrt{\pi}}\right]\right)\mp\frac{1}{2}\right)\right)
\end{aligned}
$$

$$
\begin{aligned}
&-\frac{\pi}{\sqrt{2}}\left(\frac{\lambda_r^2}{\sqrt{r}}\left(C\left(\sqrt{2r}\left[\frac{x}{\sqrt{\pi}}\right]\right)\mp\frac{1}{2}\right)+\frac{\lambda_s^2}{\sqrt{s}}\left(C\left(\sqrt{2s}\left[\frac{x}{\sqrt{\pi}}\right]\right)\mp\frac{1}{2}\right)\right)\times\\
&\qquad\times\left(\frac{\lambda_r}{\sqrt{r}}\left(C\left(\sqrt{r}\left[\frac{x}{\sqrt{\pi}}\right]\right)\mp\frac{1}{2}\right)+\frac{\lambda_s}{\sqrt{s}}\left(C\left(\sqrt{s}\left[\frac{x}{\sqrt{\pi}}\right]\right)\mp\frac{1}{2}\right)\right)\\
&+\frac{3\pi}{8}\left(\frac{\lambda_r^3}{r}\left(\sqrt{3r}\left[\frac{x}{\sqrt{\pi}}\right]\right)\left(C\left(\sqrt{3r}\left[\frac{x}{\sqrt{\pi}}\right]\right)\mp\frac{1}{2}\right)\right.\\
&\qquad\left.+\frac{\lambda_s^3}{s}\left(\sqrt{3s}\left[\frac{x}{\sqrt{\pi}}\right]\right)\left(C\left(\sqrt{3s}\left[\frac{x}{\sqrt{\pi}}\right]\right)\mp\frac{1}{2}\right)\right)\\
&+\frac{\pi}{8}\frac{\lambda_r}{r}\frac{\lambda_s}{s}\left(\frac{\lambda_r}{r}(2r+s)^2\left(\sqrt{2r+s}\left[\frac{x}{\sqrt{\pi}}\right]\right)\left(C\left(\sqrt{2r+s}\left[\frac{x}{\sqrt{\pi}}\right]\right)\mp\frac{1}{2}\right)\right.\\
&\qquad\left.+\frac{\lambda_s}{s}(2s+r)^2\left(\sqrt{2s+r}\left[\frac{x}{\sqrt{\pi}}\right]\right)\left(C\left(\sqrt{2s+r}\left[\frac{x}{\sqrt{\pi}}\right]\right)\mp\frac{1}{2}\right)\right)\\
&-\frac{\pi}{8}\frac{\lambda_r}{r}\frac{\lambda_s}{s}\left(\frac{\lambda_r}{r}\operatorname{sgn}(2r-s)(2r-s)^2\left(\sqrt{|2r-s|}\left[\frac{x}{\sqrt{\pi}}\right]\right)\left(C\left(\sqrt{|2r-s|}\left[\frac{x}{\sqrt{\pi}}\right]\right)\mp\frac{1}{2}\right)\right.\\
&\qquad\left.+\frac{\lambda_s}{s}(2s-r)^2\left(\sqrt{2s-r}\left[\frac{x}{\sqrt{\pi}}\right]\right)\left(C\left(\sqrt{2s-r}\left[\frac{x}{\sqrt{\pi}}\right]\right)\mp\frac{1}{2}\right)\right)\\
&-\frac{\pi}{8}\left(\frac{\lambda_r^3}{r}\left(\sqrt{r}\left[\frac{x}{\sqrt{\pi}}\right]\right)\left(C\left(\sqrt{r}\left[\frac{x}{\sqrt{\pi}}\right]\right)\mp\frac{1}{2}\right)\right.\\
&\qquad\left.+\frac{\lambda_s^3}{s}\left(\sqrt{s}\left[\frac{x}{\sqrt{\pi}}\right]\right)\left(C\left(\sqrt{s}\left[\frac{x}{\sqrt{\pi}}\right]\right)\mp\frac{1}{2}\right)\right)\\
&-\frac{\pi}{4}\frac{\lambda_r}{r}\frac{\lambda_s}{s}\left(\frac{\lambda_r}{r}s^2\left(\sqrt{s}\left[\frac{x}{\sqrt{\pi}}\right]\right)\left(C\left(\sqrt{s}\left[\frac{x}{\sqrt{\pi}}\right]\right)\mp\frac{1}{2}\right)\right.
\end{aligned}
$$

$$
\begin{aligned}
&\qquad\qquad + \frac{\lambda_s}{s} r^2 \left(\sqrt{r}\left[\frac{x}{\sqrt{\pi}}\right]\right)\left(C\left(\sqrt{r}\left[\frac{x}{\sqrt{\pi}}\right]\right) \mp \frac{1}{2}\right)\Bigg) \\
&- \frac{3}{8}\left(\frac{\lambda_r^3}{r}\sin\left[\frac{\pi}{2}\left(\sqrt{3r}\left[\frac{x}{\sqrt{\pi}}\right]\right)^2\right] + \frac{\lambda_s^3}{s}\sin\left[\frac{\pi}{2}\left(\sqrt{3s}\left[\frac{x}{\sqrt{\pi}}\right]\right)^2\right]\right) \\
&- \frac{1}{8}\frac{\lambda_r}{r}\frac{\lambda_s}{s}\left(\frac{\lambda_r}{r}(2r+s)^2\sin\left[\frac{\pi}{2}\left(\sqrt{2r+s}\left[\frac{x}{\sqrt{\pi}}\right]\right)^2\right]\right. \\
&\qquad\qquad \left. + \frac{\lambda_s}{s}(2s+r)^2\sin\left[\frac{\pi}{2}\left(\sqrt{2s+r}\left[\frac{x}{\sqrt{\pi}}\right]\right)^2\right]\right) \\
&+ \frac{1}{8}\frac{\lambda_r}{r}\frac{\lambda_s}{s}\left(\frac{\lambda_r}{r}\operatorname{sgn}(2r-s)(2r-s)^2\sin\left[\frac{\pi}{2}\left(\sqrt{|2r-s|}\left[\frac{x}{\sqrt{\pi}}\right]\right)^2\right]\right. \\
&\qquad\qquad \left. + \frac{\lambda_s}{s}(2s-r)^2\sin\left[\frac{\pi}{2}\left(\sqrt{2s-r}\left[\frac{x}{\sqrt{\pi}}\right]\right)^2\right]\right) \\
&+ \frac{1}{8}\left(\frac{\lambda_r^3}{r}\sin\left[\frac{\pi}{2}\left(\sqrt{r}\left[\frac{x}{\sqrt{\pi}}\right]\right)^2\right] + \frac{\lambda_s^3}{s}\sin\left[\frac{\pi}{2}\left(\sqrt{s}\left[\frac{x}{\sqrt{\pi}}\right]\right)^2\right]\right) \\
&+ \frac{1}{4}\frac{\lambda_r}{r}\frac{\lambda_s}{s}\left(\frac{\lambda_r}{s}r^2\sin\left[\frac{\pi}{2}\left(\sqrt{r}\left[\frac{x}{\sqrt{\pi}}\right]\right)^2\right] + \frac{\lambda_s}{r}s^2\sin\left[\frac{\pi}{2}\left(\sqrt{s}\left[\frac{x}{\sqrt{\pi}}\right]\right)^2\right]\right) \qquad \text{(M.44)}
\end{aligned}
$$

M.5 Multi-mode phase equation

We know by designation that the correction $\boldsymbol{\phi}_{(1)}(x)$ will be of first order in the $\{\lambda_n\}$. Therefore, we ignore any terms of second or higher order when solving the differential equation (9.123), as they belong to higher-order corrections:

$$\boldsymbol{\phi}''_{(1)}(x) = \sum_n \lambda_n \cos(n\boldsymbol{\phi}_0)\,. \qquad (9.123)$$

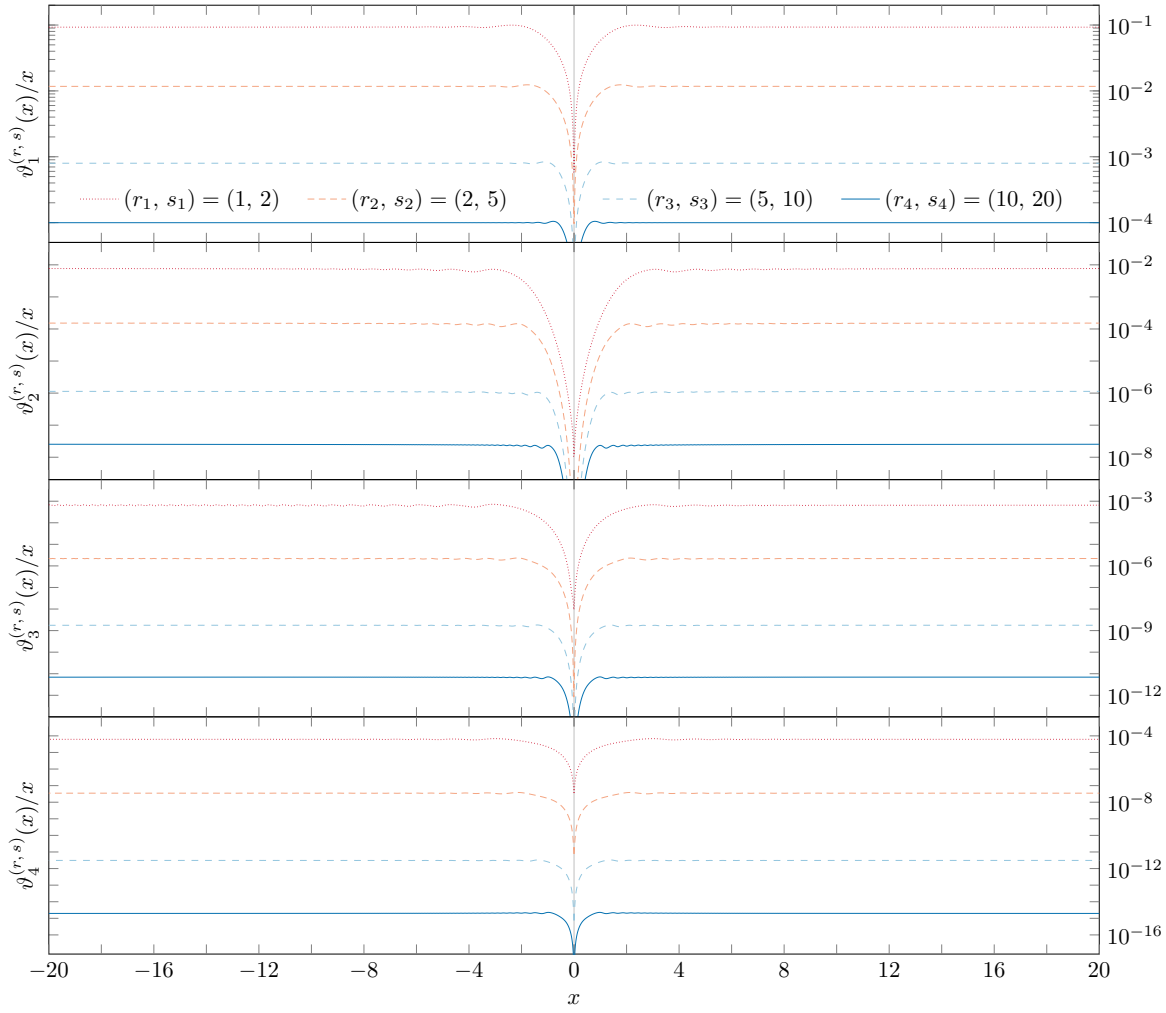

Fig. M.11 Graphical demonstration of the validity of the solutions to the phase resonance equation with two distinct modes r and s, for several different number combinations. In all these cases, we use $\lambda_1 = 0.1$, and then consecutive coefficients are calculated by $\lambda_n = \lambda_1/n^{2.5}$. We can see that in all cases, the remainder is an order of magnitude smaller than the larger coefficient λ_r. Figure appeared in [1].

Substituting for $\boldsymbol{\phi}_0(x)$ from eq. (9.121), we obtain the differential equation whose solution is the first-order correction:

$$\boldsymbol{\phi}''_{(1)}(x) = \sum_n \lambda_n \cos\left(\frac{nx^2}{2}\right). \tag{M.45}$$

We integrate once to find the first derivative (we have to apply the appropriate boundary condition $\boldsymbol{\phi}'(0) = 0$), keeping in mind that the integral of a sum is simply a sum of the integrals. We obtain the following result:

$$\boldsymbol{\phi}'_{(1)}(x) = \sqrt{\pi} \sum_n \frac{\lambda_n}{\sqrt{n}} C\left(\frac{\sqrt{n}x}{\sqrt{\pi}}\right). \tag{M.46}$$

Integrating this once again, and keeping track of the boundary condition $\boldsymbol{\phi}(0) = 0$ yields the first-order correction:

$$\begin{aligned}\boldsymbol{\phi}_{(1)}(x) = \sum_n \Bigg\{ &\pm \frac{\pi}{2}\frac{\lambda_n}{n}\left(\sqrt{n}\left[\frac{x}{\sqrt{\pi}}\right]\right) \\ &+ \frac{\lambda_n}{n}\left[\pi\left(\sqrt{n}\left[\frac{x}{\sqrt{\pi}}\right]\right)\left(C\left(\sqrt{n}\left[\frac{x}{\sqrt{\pi}}\right]\right) \mp \frac{1}{2}\right) - \sin\left[\frac{\pi}{2}\left(\sqrt{n}\left[\frac{x}{\sqrt{\pi}}\right]\right)^2\right]\right]\Bigg\} = \sum_n \phi^{(n)}_{(1)}.\end{aligned} \tag{M.47}$$

As we can see, in exactly the same way as solution (M.41), this first-order result exhibits no mixing between the solutions for different values of n, which means it can be expressed as a sum over many single-mode solutions of the form (M.37). Combining this with the zeroth-order solution, eq. (9.121), we can write down the complete solution of the phase equation to first order in the case of an infinite number of Fourier-like coefficients $\{\lambda_n\}$. As before, it is beneficial to combine the terms proportional to x^2 and x into a single term, again

retaining only terms linear in $\{\lambda_n\}$:

$$\begin{aligned}\boldsymbol{\phi}_1(x) = \frac{\pi}{2}&\left(\frac{x}{\sqrt{\pi}} \pm \frac{1}{2}\sum_n \frac{\lambda_n}{\sqrt{n}}\right)^2 \\ &+ \sum_n \frac{\lambda_n}{n}\left[\pi\left(\sqrt{n}\left[\frac{x}{\sqrt{\pi}}\right]\right)\left(C\left(\sqrt{n}\left[\frac{x}{\sqrt{\pi}}\right]\right) \mp \frac{1}{2}\right) - \sin\left[\frac{\pi}{2}\left(\sqrt{n}\left[\frac{x}{\sqrt{\pi}}\right]\right)^2\right]\right].\end{aligned} \tag{9.124}$$

The second-order correction to eq. (9.120) requires us to solve eq. (9.126). The argument of the trigonometric function on the right-hand side is given by the first-order correction, eq. (M.47) combined with the zeroth-order solution:

$$\boldsymbol{\phi}''_{(2)}(x) = \sum_n \lambda_n \cos\left[n\left(\frac{x^2}{2} \pm \sum_m \frac{\pi}{2}\frac{\lambda_m}{m}\left(\frac{\sqrt{m}x}{\sqrt{\pi}}\right)\right.\right. \tag{M.48}$$

$$\left.\left. + \sum_m \frac{\lambda_m}{m}\left(\pi\left(\frac{\sqrt{m}x}{\sqrt{\pi}}\right)\left(C\left(\frac{\sqrt{m}x}{\sqrt{\pi}}\right) \mp \frac{1}{2}\right) - \sin\left[\frac{\pi}{2}\left(\frac{\sqrt{m}x}{\sqrt{\pi}}\right)^2\right]\right)\right)\right]. \tag{M.49}$$

Even though the process is more involved than before, the method of solution here is the same: consecutively integrating the right-hand side twice, while observing the boundary conditions. After the first integration, we obtain

$$\begin{aligned}\boldsymbol{\phi}'_{(2)}(x) = \sqrt{\pi}&\sum_n \frac{\lambda_n}{\sqrt{n}}\left(C\left(\frac{\sqrt{n}x}{\sqrt{\pi}} \pm \frac{\sqrt{n}}{2}\sum_m \frac{\lambda_m}{\sqrt{m}}\right) \mp C\left(\frac{\sqrt{n}}{2}\sum_m \frac{\lambda_m}{\sqrt{m}}\right)\right) \\ &+ \sqrt{\pi}\sum_{n,m}\lambda_n\lambda_m\left[\frac{1}{\sqrt{m}}\cos\left(\frac{nx^2}{2}\right)C\left(\frac{\sqrt{m}x}{\sqrt{\pi}}\right) \mp \frac{1}{2\sqrt{m}}\cos\left(\frac{nx^2}{2}\right) \pm \frac{1}{2\sqrt{m}}\right. \\ &\left. + \frac{1}{2m}\frac{n-m}{\sqrt{|n-m|}}C\left(\frac{\sqrt{|n-m|}x}{\sqrt{\pi}}\right) - \frac{1}{2m}\sqrt{n+m}\,C\left(\frac{\sqrt{n+m}x}{\sqrt{\pi}}\right)\right].\end{aligned} \tag{M.50}$$

While performing this integration, we encounter some unusual integrals, hence we quote the results here:

$$\begin{aligned} -\int_0^x \mathrm{d}y \cos\left(\frac{ny^2}{2}\right)\cos\left(\frac{my^2}{2}\right) + \frac{n}{m}\int_0^x \mathrm{d}y \sin\left(\frac{ny^2}{2}\right)\sin\left(\frac{my^2}{2}\right) = \\ = \frac{\sqrt{\pi}}{2}\left(\mathrm{sgn}(n-m)\,\frac{\sqrt{|n-m|}}{m}\,C\left(\frac{\sqrt{|n-m|}\,x}{\sqrt{\pi}}\right) - \frac{\sqrt{n+m}}{m}\,C\left(\frac{\sqrt{n+m}\,x}{\sqrt{\pi}}\right)\right). \end{aligned} \tag{M.51}$$

Similarly, when we integrate the expression (M.50), we encounter the following integral, whose solution is made possible by the fact that we are summing over both indices n and m, and hence we can re-label them interchangeably.

$$\sqrt{\pi}\sum_{n,m}\lambda_n\frac{\lambda_m}{\sqrt{m}}\int_0^x \mathrm{d}y \cos\left(\frac{ny^2}{2}\right) C\left(\frac{\sqrt{m}\,x}{\sqrt{\pi}}\right) = \frac{\pi}{2}\sum_{n,m}\frac{\lambda_n}{\sqrt{n}}\frac{\lambda_m}{\sqrt{m}}\,C\left(\frac{\sqrt{n}\,x}{\sqrt{\pi}}\right)C\left(\frac{\sqrt{m}\,x}{\sqrt{\pi}}\right) \tag{M.52}$$

Using this, the second-order correction is found to be as follows (remember that we are using $\boldsymbol{\phi}'(0) = \boldsymbol{\phi}(0) = 0$).

$$\begin{aligned} \boldsymbol{\phi}_{(2)}(x) = \pm\,\pi\left[\frac{1}{2}\sum_n\frac{\lambda_n}{\sqrt{n}} + \sum_{n,m}\frac{1}{8}\left(|n-m|^{3/2} - (n+m)^{3/2}\right)\frac{\lambda_n}{n}\frac{\lambda_m}{m}\right]\left(\frac{x}{\sqrt{\pi}}\right) + \frac{\pi}{8}\sum_{n,m}\frac{\lambda_n}{\sqrt{n}}\frac{\lambda_m}{\sqrt{m}} \\ + \sum_n\frac{\lambda_n}{n}\left[\pi\left(\sqrt{n}\left[\frac{x}{\sqrt{\pi}} \pm \frac{1}{2}\sum_m\frac{\lambda_m}{\sqrt{m}}\right]\right)\left(C\left(\sqrt{n}\left[\frac{x}{\sqrt{\pi}} \pm \frac{1}{2}\sum_m\frac{\lambda_m}{\sqrt{m}}\right]\right) \mp \frac{1}{2}\right)\right. \\ \left. - \sin\left[\frac{\pi}{2}\left(\sqrt{n}\left[\frac{x}{\sqrt{\pi}} \pm \frac{1}{2}\sum_m\frac{\lambda_m}{\sqrt{m}}\right]\right)^2\right]\right] \\ + \sum_{n,m}\frac{\lambda_n}{\sqrt{n}}\frac{\lambda_m}{\sqrt{m}}\left[\frac{\pi}{2}\left(C\left(\sqrt{n}\left[\frac{x}{\sqrt{\pi}}\right]\right) \mp \frac{1}{2}\right)\left(C\left(\sqrt{m}\left[\frac{x}{\sqrt{\pi}}\right]\right) \mp \frac{1}{2}\right)\right. \end{aligned}$$

$$
\begin{aligned}
&-\frac{\pi}{2}\frac{\sqrt{n}}{\sqrt{m}}\left(\sqrt{n+m}\left[\frac{x}{\sqrt{\pi}}\right]\right)\left(C\left(\sqrt{n+m}\left[\frac{x}{\sqrt{\pi}}\right]\right)\mp\frac{1}{2}\right)\\
&+\frac{\pi}{2}\frac{\sqrt{n}}{\sqrt{m}}\operatorname{sgn}(n-m)\left(\sqrt{|n-m|}\left[\frac{x}{\sqrt{\pi}}\right]\right)\left(C\left(\sqrt{|n-m|}\left[\frac{x}{\sqrt{\pi}}\right]\right)\mp\frac{1}{2}\right)\\
&-\frac{1}{2}\frac{\sqrt{n}}{\sqrt{m}}\left(\operatorname{sgn}(n-m)\sin\left[\frac{\pi}{2}\left(\sqrt{|n-m|}\left[\frac{x}{\sqrt{\pi}}\right]\right)^2\right]-\sin\left[\frac{\pi}{2}\left(\sqrt{n+m}\left[\frac{x}{\sqrt{\pi}}\right]\right)^2\right]\right)\Bigg]
\end{aligned}
\tag{M.53}
$$

It is important to note that this is consistent with our previous results. For $n=m=1$, we retrieve the second-order single-mode solution, eq. (M.13) while if we choose $n,m=\{r,s\}$, we find the second-order solution for an equation with 2 distinct modes, namely the voluminous eq. (M.42). Moreover, we recognise that the oscillating terms here have similar form to the ones in the single-mode solution, hence we can introduce the notation $\{\boldsymbol{\sigma}_n\}$ and $\{\boldsymbol{\rho}_n^m(x)\}$.

To obtain the third-order correction, we need to solve the following multi-mode second-order differential equation:

$$
\begin{aligned}
\boldsymbol{\phi}''_{(3)}(x)=&\sum_n\lambda_n\cos\left[\frac{\pi}{2}\left(\sqrt{n}\left[\frac{x}{\sqrt{\pi}}\pm\boldsymbol{\sigma}_2\right]\right)^2\right]-\sum_{n,m}\frac{n}{m}\lambda_n\lambda_m\sin\left[\frac{\pi}{2}\left(\sqrt{n}\left[\frac{x}{\sqrt{\pi}}\pm\boldsymbol{\sigma}_1\right]\right)^2\right]\boldsymbol{\rho}_1^m(x)\\
&-\sum_{n,m,p}\lambda_n\lambda_m\lambda_p\left(\frac{1}{2}\frac{n^2}{mp}\cos\left[\frac{\pi}{2}\left(\sqrt{n}\left[\frac{x}{\sqrt{\pi}}\right]\right)^2\right]\boldsymbol{\rho}_1^m(x)\,\boldsymbol{\rho}_1^p(x)\right.\\
&\qquad\left.+\frac{n}{\sqrt{m}\sqrt{p}}\sin\left[\frac{\pi}{2}\left(\sqrt{n}\left[\frac{x}{\sqrt{\pi}}\right]\right)^2\right]\boldsymbol{\rho}_2^{mp}(x)\right).
\end{aligned}
\tag{M.54}
$$

Following through with two rounds of integration yields the following solution for the third-order correction:

$$
\boldsymbol{\phi}_{(3)}(x)=\pm\pi\left[\sum_n\frac{1}{2}\frac{\lambda_n}{\sqrt{n}}+\sum_{n,m}\frac{1}{8}\left(|n-m|^{3/2}-(n+m)^{3/2}\right)\frac{\lambda_n}{n}\frac{\lambda_m}{m}\right.
$$

$$+\sum_{n,m,p}\frac{1}{16}\left((n+m+p)^{3/2}-|n-m+p|^{3/2}-|n+m-p|^{3/2}+|n-m-p|^{3/2}\right)\lambda_n\frac{\lambda_m}{m}\frac{\lambda_p}{p}\Bigg]\left(\frac{x}{\sqrt{\pi}}\right)$$

$$+\pi\Bigg[\sum_{n,m}\frac{1}{8}\frac{\lambda_n}{\sqrt{n}}\frac{\lambda_m}{\sqrt{m}}$$

$$+\sum_{n,m,p}\frac{1}{16}\left(\operatorname{sgn}(n-m)\frac{\sqrt{|n-m|}}{\sqrt{m}}+\operatorname{sgn}(n-p)\frac{\sqrt{|n-p|}}{\sqrt{p}}-\frac{\sqrt{n+m}}{\sqrt{m}}-\frac{\sqrt{n+p}}{\sqrt{p}}\right)\lambda_n\frac{\lambda_m}{\sqrt{m}}\frac{\lambda_p}{\sqrt{p}}\Bigg]$$

$$+\sum_{n}\frac{\lambda_n}{n}\left[\pi\left(\sqrt{n}\left[\frac{x}{\sqrt{\pi}}\pm\boldsymbol{\sigma}_2\right]\right)\left(C\left(\sqrt{n}\left[\frac{x}{\sqrt{\pi}}\pm\boldsymbol{\sigma}_2\right]\right)\mp\frac{1}{2}\right)-\sin\left[\frac{\pi}{2}\left(\sqrt{n}\left[\frac{x}{\sqrt{\pi}}\pm\boldsymbol{\sigma}_2\right]\right)^2\right]\right]$$

$$+\sum_{n,m}\frac{\lambda_n}{\sqrt{n}}\frac{\lambda_m}{\sqrt{m}}\Bigg[\frac{\pi}{2}\left(C\left(\sqrt{n}\left[\frac{x}{\sqrt{\pi}}\pm\boldsymbol{\sigma}_1\right]\right)\mp\frac{1}{2}\right)\left(C\left(\sqrt{m}\left[\frac{x}{\sqrt{\pi}}\pm\boldsymbol{\sigma}_1\right]\right)\mp\frac{1}{2}\right)$$

$$+\frac{\pi}{2}\frac{\sqrt{n}}{\sqrt{m}}\operatorname{sgn}(n-m)\left(\sqrt{|n-m|}\left[\frac{x}{\sqrt{\pi}}\pm\boldsymbol{\sigma}_1\right]\right)\left(C\left(\sqrt{|n-m|}\left[\frac{x}{\sqrt{\pi}}\pm\boldsymbol{\sigma}_1\right]\right)\mp\frac{1}{2}\right)$$

$$-\frac{\pi}{2}\frac{\sqrt{n}}{\sqrt{m}}\left(\sqrt{n+m}\left[\frac{x}{\sqrt{\pi}}\pm\boldsymbol{\sigma}_1\right]\right)\left(C\left(\sqrt{n+m}\left[\frac{x}{\sqrt{\pi}}\pm\boldsymbol{\sigma}_1\right]\right)\mp\frac{1}{2}\right)$$

$$-\frac{1}{2}\frac{\sqrt{n}}{\sqrt{m}}\Bigg(\sin\left[\frac{\pi}{2}\operatorname{sgn}(n-m)\left(\sqrt{|n-m|}\left[\frac{x}{\sqrt{\pi}}\pm\boldsymbol{\sigma}_1\right]\right)^2\right]$$

$$-\sin\left[\frac{\pi}{2}\left(\sqrt{n+m}\left[\frac{x}{\sqrt{\pi}}\pm\boldsymbol{\sigma}_1\right]\right)^2\right]\Bigg)\Bigg]$$

$$+\sum_{n,m,p}\lambda_n\frac{\lambda_m}{\sqrt{m}}\frac{\lambda_p}{\sqrt{p}}\Bigg[\frac{\pi}{2}\cos\left[\frac{\pi}{2}\left(\sqrt{n}\left[\frac{x}{\sqrt{\pi}}\right]\right)^2\right]\left(C\left(\sqrt{m}\left[\frac{x}{\sqrt{\pi}}\right]\right)\mp\frac{1}{2}\right)\left(C\left(\sqrt{p}\left[\frac{x}{\sqrt{\pi}}\right]\right)\mp\frac{1}{2}\right)$$

$$+\frac{\pi}{4}\left(\operatorname{sgn}(n-m)\frac{\sqrt{|n-m|}}{\sqrt{m}}\left(C\left(\sqrt{|n-m|}\left[\frac{x}{\sqrt{\pi}}\right]\right)\mp\frac{1}{2}\right)\right.$$

$$
\begin{aligned}
&- \frac{\sqrt{n+m}}{\sqrt{m}} \left(C\left(\sqrt{n+m} \left[\frac{x}{\sqrt{\pi}} \right] \right) \mp \frac{1}{2} \right) \Bigg) \left(C\left(\sqrt{p} \left[\frac{x}{\sqrt{\pi}} \right] \right) \mp \frac{1}{2} \right) \\
&+ \frac{\pi}{4} \Bigg(\operatorname{sgn}(n-p) \frac{\sqrt{|n-p|}}{\sqrt{p}} \left(C\left(\sqrt{|n-p|} \left[\frac{x}{\sqrt{\pi}} \right] \right) \mp \frac{1}{2} \right) \\
&\qquad - \frac{\sqrt{n+p}}{\sqrt{p}} \left(C\left(\sqrt{n+p} \left[\frac{x}{\sqrt{\pi}} \right] \right) \mp \frac{1}{2} \right) \Bigg) \left(C\left(\sqrt{m} \left[\frac{x}{\sqrt{\pi}} \right] \right) \mp \frac{1}{2} \right) \\
&+ \frac{\pi}{8} \frac{(n+m+p)}{\sqrt{m}\sqrt{p}} \left(\sqrt{n+m+p} \left[\frac{x}{\sqrt{\pi}} \right] \right) \left(C\left(\sqrt{n+m+p} \left[\frac{x}{\sqrt{\pi}} \right] \right) \mp \frac{1}{2} \right) \\
&\quad - \frac{\pi}{8} \frac{|n-m+p|}{\sqrt{m}\sqrt{p}} \left(\sqrt{|n-m+p|} \left[\frac{x}{\sqrt{\pi}} \right] \right) \left(C\left(\sqrt{|n-m+p|} \left[\frac{x}{\sqrt{\pi}} \right] \right) \mp \frac{1}{2} \right) \\
&\quad - \frac{\pi}{8} \frac{|n+m-p|}{\sqrt{m}\sqrt{p}} \left(\sqrt{|n+m-p|} \left[\frac{x}{\sqrt{\pi}} \right] \right) \left(C\left(\sqrt{|n+m-p|} \left[\frac{x}{\sqrt{\pi}} \right] \right) \mp \frac{1}{2} \right) \\
&\quad + \frac{\pi}{8} \frac{|n-m-p|}{\sqrt{m}\sqrt{p}} \left(\sqrt{|n-m-p|} \left[\frac{x}{\sqrt{\pi}} \right] \right) \left(C\left(\sqrt{|n-m-p|} \left[\frac{x}{\sqrt{\pi}} \right] \right) \mp \frac{1}{2} \right) \\
&- \frac{1}{8} \frac{(n+m+p)}{\sqrt{m}\sqrt{p}} \sin\left[\frac{\pi}{2} \left(\sqrt{n+m+p} \left[\frac{x}{\sqrt{\pi}} \right] \right)^2 \right] \\
&\qquad + \frac{1}{8} \frac{|n-m+p|}{\sqrt{m}\sqrt{p}} \sin\left[\frac{\pi}{2} \left(\sqrt{|n-m+p|} \left[\frac{x}{\sqrt{\pi}} \right] \right)^2 \right] \\
&+ \frac{1}{8} \frac{|n+m-p|}{\sqrt{m}\sqrt{p}} \sin\left[\frac{\pi}{2} \left(\sqrt{|n+m-p|} \left[\frac{x}{\sqrt{\pi}} \right] \right)^2 \right] \\
&\qquad - \frac{1}{8} \frac{|n-m-p|}{\sqrt{m}\sqrt{p}} \sin\left[\frac{\pi}{2} \left(\sqrt{|n-m-p|} \left[\frac{x}{\sqrt{\pi}} \right] \right)^2 \right] \Bigg] . \qquad \text{(M.55)}
\end{aligned}
$$

As with the second-order result, this one reduces to the appropriate previous expressions for $n = m = p = 1$, or for $n = m = p = \{r, s\}$. Moreover, it is easy to recognise the generalised form of the terms proportional to λ^n and how they reduce to their single-mode counterparts.

A more detailed discussion about the features and validity of these solutions for different mode counts is presented in the main text.

M.6 Phase equation with a single mode and non-zero phase

Having considered the multi-mode zero-phase equation, we revert back to the single mode case and introduce a non-zero phase $\delta\psi$:

$$\varphi''(x) = 1 + \lambda \cos\big(\varphi(x) - \delta\psi\big). \tag{9.133}$$

The first-order solution is $\varphi_0 = x^2/2$, and we substitute it into eq. (9.133) to obtain the differential equation for $\varphi_{(1)}$:

$$\varphi''_{(1)}(x) = \lambda \cos\left(\varphi_0 - \delta\psi\right). \tag{M.56}$$

The method of solution is identical to expand the trigonometric function on the right-hand side:

$$\varphi''_{(1)}(x) = \lambda \cos(\delta\psi)\cos(\varphi_0) + \lambda \sin(\delta\psi)\sin(\varphi_0). \tag{M.57}$$

We now proceed to integrate this exactly as before, only this time there are twice as many terms that need to be integrated. The final solution can be presented in a fashion similar to before, however this time we have $\delta\psi$-dependence both in the slope and in the oscillating terms.

$$\begin{aligned}\varphi_1(x) = {} & \frac{\pi}{2}\left(\frac{x}{\sqrt{\pi}} \pm \frac{1}{2}\big(\cos(\delta\psi) + \sin(\delta\psi)\big)\lambda\right)^2 \\ & + \lambda\left[\pi\left(\frac{x}{\sqrt{\pi}}\right)\left(\cos(\delta\psi)\left(C\left(\frac{x}{\sqrt{\pi}}\right) \mp \frac{1}{2}\right) + \sin(\delta\psi)\left(S\left(\frac{x}{\sqrt{\pi}}\right) \mp \frac{1}{2}\right)\right)\right. \\ & \left. - \left(\sin\left[\frac{\pi}{2}\left(\frac{x}{\sqrt{\pi}}\right)^2 - \delta\psi\right] + \sin(\delta\psi)\right)\right]\end{aligned} \tag{M.58}$$

This solution can be used again in the source equation to find the second-order correction:

$$
\begin{aligned}
\varphi_{(2)}(x) = \pm\pi \Bigg[& \frac{1}{2}\big(\cos(\delta\psi)+\sin(\delta\psi)\big)\lambda \\
& -\left(\frac{\sqrt{2}}{4}\big(\cos(2\delta\psi)+\sin(2\delta\psi)\big)-\frac{1}{2}\big(\cos(\delta\psi)-\sin(\delta\psi)\big)\sin(\delta\psi)\right)\lambda^2\Bigg]\left(\frac{x}{\sqrt{\pi}}\right) \\
& +\frac{\pi}{8}\big(\cos(\delta\psi)+\sin(\delta\psi)\big)^2\lambda^2 \\
+\lambda\Bigg[& \pi\left(\frac{x}{\sqrt{\pi}}\pm\frac{1}{2}\big(\cos(\delta\psi)+\sin(\delta\psi)\big)\lambda\right)\times \\
& \times\left(\cos(\delta\psi)\left(C\left(\frac{x}{\sqrt{\pi}}\pm\frac{1}{2}\big(\cos(\delta\psi)+\sin(\delta\psi)\big)\lambda\right)\mp\frac{1}{2}\right)\right. \\
& \left.+\sin(\delta\psi)\left(S\left(\frac{x}{\sqrt{\pi}}\pm\frac{1}{2}\big(\cos(\delta\psi)+\sin(\delta\psi)\big)\lambda\right)\mp\frac{1}{2}\right)\right) \\
& -\left(\sin\left[\frac{\pi}{2}\left(\frac{x}{\sqrt{\pi}}\pm\frac{1}{2}\big(\cos(\delta\psi)+\sin(\delta\psi)\big)\lambda\right)^2-\delta\psi\right]+\sin(\delta\psi)\right)\Bigg] \\
+\lambda^2\Bigg[& \frac{\pi}{2}\left(\cos(\delta\psi)\left(C\left(\frac{x}{\sqrt{\pi}}\right)\mp\frac{1}{2}\right)+\sin(\delta\psi)\left(S\left(\frac{x}{\sqrt{\pi}}\right)\mp\frac{1}{2}\right)\right)^2 \\
& -\frac{\pi}{2}\left(\sqrt{2}\left[\frac{x}{\sqrt{\pi}}\right]\right)\left(\cos(2\delta\psi)\left(C\left(\sqrt{2}\left[\frac{x}{\sqrt{\pi}}\right]\right)\mp\frac{1}{2}\right)+\sin(2\delta\psi)\left(S\left(\sqrt{2}\left[\frac{x}{\sqrt{\pi}}\right]\right)\mp\frac{1}{2}\right)\right) \\
& -\pi\left(\frac{x}{\sqrt{\pi}}\right)\left(\sin(\delta\psi)\left(C\left(\frac{x}{\sqrt{\pi}}\right)\mp\frac{1}{2}\right)-\cos(\delta\psi)\left(S\left(\frac{x}{\sqrt{\pi}}\right)\mp\frac{1}{2}\right)\right)\sin(\delta\psi) \\
& +\frac{1}{2}\left(\sin\left[\frac{\pi}{2}\left(\sqrt{2}\left[\frac{x}{\sqrt{\pi}}\right]\right)^2-2\delta\psi\right]+\sin(2\delta\psi)\right)
\end{aligned}
$$

$$+\left(\cos\left[\frac{\pi}{2}\left(\frac{x}{\sqrt{\pi}}\right)^2-\delta\psi\right]-\cos(\delta\psi)\right)\sin(\delta\psi)\Bigg] \tag{M.59}$$

We can apply the same technique to find the third-order solution. The third-order correction is given below.

$$\begin{aligned}
\varphi_{(3)}(x) = \pm\pi\Bigg[&\frac{1}{2}\big(\cos(\delta\psi)+\sin(\delta\psi)\big)\lambda \\
&-\left(\frac{\sqrt{2}}{4}\big(\cos(2\delta\psi)+\sin(2\delta\psi)\big)-\frac{1}{2}\big(\cos(\delta\psi)-\sin(\delta\psi)\big)\sin(\delta\psi)\right)\lambda^2 \\
&+\Bigg(\frac{3\sqrt{3}}{16}\big(\cos(3\delta\psi)+\sin(3\delta\psi)\big)-\frac{\sqrt{2}}{2}\sin(\delta\psi)\big(\cos(2\delta\psi)-\sin(2\delta\psi)\big) \\
&\qquad-\frac{3}{16}\big(\cos(\delta\psi)+\sin(\delta\psi)\big)+\frac{1}{8}\cos(2\delta\psi)\big(\cos(\delta\psi)+\sin(\delta\psi)\big)\Bigg)\lambda^3\Bigg]\left(\frac{x}{\sqrt{\pi}}\right) \\
&+\pi\Bigg[\frac{1}{8}\big(\cos(\delta\psi)+\sin(\delta\psi)\big)^2\lambda^2 \\
&-\left(\frac{\sqrt{2}}{8}\big(\cos(2\delta\psi)+\sin(2\delta\psi)\big)\big(\cos(\delta\psi)+\sin(\delta\psi)\big)-\frac{1}{4}\cos(2\delta\psi)\sin(\delta\psi)\right)\lambda^3\Bigg] \\
&+\lambda\Bigg[\pi\left(\frac{x}{\sqrt{\pi}}\pm\varsigma_2\right)\left(\cos(\delta\psi)\left(C\left(\frac{x}{\sqrt{\pi}}\pm\varsigma_2\right)\mp\frac{1}{2}\right)+\sin(\delta\psi)\left(S\left(\frac{x}{\sqrt{\pi}}\pm\varsigma_2\right)\mp\frac{1}{2}\right)\right) \\
&\qquad-\left(\sin\left[\frac{\pi}{2}\left(\frac{x}{\sqrt{\pi}}\pm\varsigma_2\right)^2-\delta\psi\right]+\sin(\delta\psi)\right)\Bigg] \\
&+\lambda^2\Bigg[\frac{\pi}{2}\left(\cos(\delta\psi)\left(C\left(\frac{x}{\sqrt{\pi}}\pm\varsigma_1\right)\mp\frac{1}{2}\right)+\sin(\delta\psi)\left(S\left(\frac{x}{\sqrt{\pi}}\pm\varsigma_1\right)\mp\frac{1}{2}\right)\right)^2
\end{aligned}$$

$$
\begin{aligned}
&-\frac{\pi}{2}\left(\sqrt{2}\left[\frac{x}{\sqrt{\pi}}\pm\varsigma_1\right]\right)\left(\cos(2\delta\psi)\left(C\left(\sqrt{2}\left[\frac{x}{\sqrt{\pi}}\pm\varsigma_1\right]\right)\mp\frac{1}{2}\right)\right.\\
&\qquad\left.+\sin(2\delta\psi)\left(S\left(\sqrt{2}\left[\frac{x}{\sqrt{\pi}}\pm\varsigma_1\right]\right)\mp\frac{1}{2}\right)\right)\\
&-\pi\left(\frac{x}{\sqrt{\pi}}\pm\varsigma_1\right)\left(\sin(\delta\psi)\left(C\left(\frac{x}{\sqrt{\pi}}\pm\varsigma_1\right)\mp\frac{1}{2}\right)-\cos(\delta\psi)\left(S\left(\frac{x}{\sqrt{\pi}}\pm\varsigma_1\right)\mp\frac{1}{2}\right)\right)\sin(\delta\psi)\\
&\qquad+\frac{1}{2}\sin\left[\frac{\pi}{2}\left(\sqrt{2}\left[\frac{x}{\sqrt{\pi}}\pm\varsigma_1\right]\right)^2-2\delta\psi\right]+\cos\left[\frac{\pi}{2}\left(\frac{x}{\sqrt{\pi}}\pm\varsigma_1\right)^2-\delta\psi\right]\sin(\delta\psi)\Bigg]\\
&+\lambda^3\left[\frac{\pi}{2}\cos\left[\frac{\pi}{2}\left(\frac{x}{\sqrt{\pi}}\right)^2-\delta\psi\right]\left(\cos(\delta\psi)\left(C\left(\frac{x}{\sqrt{\pi}}\right)\mp\frac{1}{2}\right)+\sin(\delta\psi)\left(S\left(\frac{x}{\sqrt{\pi}}\right)\mp\frac{1}{2}\right)\right)^2\right.\\
&-\frac{\pi}{\sqrt{2}}\left(\cos(2\delta\psi)\left(C\left(\sqrt{2}\left[\frac{x}{\sqrt{\pi}}\right]\right)\mp\frac{1}{2}\right)+\sin(2\delta\psi)\left(S\left(\sqrt{2}\left[\frac{x}{\sqrt{\pi}}\right]\right)\mp\frac{1}{2}\right)\right)\times\\
&\qquad\times\left(\cos(\delta\psi)\left(C\left(\frac{x}{\sqrt{\pi}}\right)\mp\frac{1}{2}\right)+\sin(\delta\psi)\left(S\left(\frac{x}{\sqrt{\pi}}\right)\mp\frac{1}{2}\right)\right)\\
&-\pi\left(\sin(\delta\psi)\left(C\left(\frac{x}{\sqrt{\pi}}\right)\mp\frac{1}{2}\right)-\cos(\delta\psi)\left(S\left(\frac{x}{\sqrt{\pi}}\right)\mp\frac{1}{2}\right)\right)\times\\
&\qquad\times\left(\cos(\delta\psi)\left(C\left(\frac{x}{\sqrt{\pi}}\right)\mp\frac{1}{2}\right)+\sin(\delta\psi)\left(S\left(\frac{x}{\sqrt{\pi}}\right)\mp\frac{1}{2}\right)\right)\sin(\delta\psi)\\
&+\frac{3\pi}{8}\left(\sqrt{3}\left[\frac{x}{\sqrt{\pi}}\right]\right)\left(\cos(3\delta\psi)\left(C\left(\sqrt{3}\left[\frac{x}{\sqrt{\pi}}\right]\right)\mp\frac{1}{2}\right)+\sin(3\delta\psi)\left(S\left(\sqrt{3}\left[\frac{x}{\sqrt{\pi}}\right]\right)\mp\frac{1}{2}\right)\right)\\
&+\pi\left(\sqrt{2}\left[\frac{x}{\sqrt{\pi}}\right]\right)\left(\sin(2\delta\psi)\left(C\left(\sqrt{2}\left[\frac{x}{\sqrt{\pi}}\right]\right)\mp\frac{1}{2}\right)\right.
\end{aligned}
$$

$$
\begin{aligned}
&\qquad\qquad\qquad\qquad\qquad\qquad - \cos(2\delta\psi)\left(S\left(\sqrt{2}\left[\frac{x}{\sqrt{\pi}}\right]\right) \mp \frac{1}{2}\right)\Bigg)\sin(\delta\psi) \\
&+ \frac{\pi}{8}\left(\frac{x}{\sqrt{\pi}}\right)\Bigg(\cos(\delta\psi)\left(C\left(\frac{x}{\sqrt{\pi}}\right) \mp \frac{1}{2}\right) + \sin(\delta\psi)\left(S\left(\frac{x}{\sqrt{\pi}}\right) \mp \frac{1}{2}\right)\Bigg)\left(2\cos(2\delta\psi) - 3\right) \\
&- \frac{3}{8}\sin\left[\frac{\pi}{2}\left(\sqrt{3}\left[\frac{x}{\sqrt{\pi}}\right]\right)^2 - 3\delta\psi\right] - \cos\left[\frac{\pi}{2}\left(\sqrt{2}\left[\frac{x}{\sqrt{\pi}}\right]\right)^2 - 2\delta\psi\right]\sin(\delta\psi) \\
&\qquad\qquad\qquad\qquad\qquad\qquad - \frac{1}{8}\sin\left[\frac{\pi}{2}\left(\frac{x}{\sqrt{\pi}}\right)^2 - \delta\psi\right]\left(2\cos(2\delta\psi) - 3\right)\Bigg]
\end{aligned}
\tag{M.60}
$$

Details about these solutions are discussed in the main text. We can now address the final problem, namely that of a phase equation with many oscillating modes, each with an independent initial phase.

M.7 Multi-mode phase equation with non-zero phase

The solutions to the phase resonance equation with an infinite number of modes and non-zero phases

$$
\boldsymbol{\varphi}''(x) = 1 + \sum_{n>1} \lambda_n \cos\left(n\,\boldsymbol{\varphi}(x) - \delta\psi_n\right). \tag{7.17b}
$$

can be found using the established algorithm. Note this is the most complete solution to the phase resonance equation. The first-order correction to the zeroth-order solutions is given by the expression below.

$$
\begin{aligned}
\boldsymbol{\varphi}_{(1)}(x) &= \pm\pi\left[\sum_n \frac{1}{2}\left(\cos(\delta\psi_n) + \sin(\delta\psi_n)\right)\frac{\lambda_n}{\sqrt{n}}\right]\left(\frac{x}{\sqrt{\pi}}\right) \\
&+ \sum_n \frac{\lambda_n}{n}\Bigg[\pi\left(\sqrt{n}\left[\frac{x}{\sqrt{\pi}}\right]\right)\Bigg(\cos(\delta\psi_n)\left(C\left(\sqrt{n}\left[\frac{x}{\sqrt{\pi}}\right]\right) \mp \frac{1}{2}\right)
\end{aligned}
$$

$$+\sin(\delta\psi_n)\left(S\left(\sqrt{n}\left[\frac{x}{\sqrt{\pi}}\right]\right)\mp\frac{1}{2}\right)\Bigg)-\left(\sin\left[\frac{\pi}{2}\left(\sqrt{n}\left[\frac{x}{\sqrt{\pi}}\right]\right)^2-\delta\psi_n\right]+\sin(\delta\psi_n)\right)\Bigg] \tag{M.61}$$

Similarly, we can find the second-order correction, given here.

$$\begin{aligned}
\boldsymbol{\varphi}_{(2)}(x) = \pm\pi\Bigg[&\sum_n \frac{1}{2}\big(\cos(\delta\psi_n)+\sin(\delta\psi_n)\big)\frac{\lambda_n}{\sqrt{n}} \\
&+\sum_{n,m}\Bigg(\frac{1}{8}\frac{|n-m|^{3/2}}{\sqrt{n}\sqrt{m}}\big(\cos(\delta\psi_n-\delta\psi_m)+\operatorname{sgn}(n-m)\sin(\delta\psi_n-\delta\psi_m)\big) \\
&\quad-\frac{1}{8}\frac{(n+m)^{3/2}}{\sqrt{n}\sqrt{m}}\big(\cos(\delta\psi_n+\delta\psi_m)+\sin(\delta\psi_n+\delta\psi_m)\big) \\
&\quad+\frac{1}{4}\frac{n}{\sqrt{m}}\big(\cos(\delta\psi_n)-\sin(\delta\psi_n)\big)\sin(\delta\psi_m) \\
&\quad+\frac{1}{4}\frac{m}{\sqrt{n}}\sin(\delta\psi_n)\big(\cos(\delta\psi_m)-\sin(\delta\psi_m)\big)\Bigg)\frac{\lambda_n}{\sqrt{n}}\frac{\lambda_m}{\sqrt{m}}\Bigg]\left(\frac{x}{\sqrt{\pi}}\right) \\
&+\frac{\pi}{8}\sum_{n,m}\big(\cos(\delta\psi_n)+\sin(\delta\psi_n)\big)\big(\cos(\delta\psi_m)+\sin(\delta\psi_m)\big)\frac{\lambda_n}{\sqrt{n}}\frac{\lambda_m}{\sqrt{m}} \\
&+\sum_n\frac{\lambda_n}{n}\Bigg[\pi\left(\sqrt{n}\left[\frac{x}{\sqrt{\pi}}\pm\boldsymbol{\varsigma}_1\right]\right)\Bigg(\cos(\delta\psi_n)\left(C\left(\sqrt{n}\left[\frac{x}{\sqrt{\pi}}\pm\boldsymbol{\varsigma}_1\right]\right)\mp\frac{1}{2}\right) \\
&\qquad+\sin(\delta\psi_n)\left(S\left(\sqrt{n}\left[\frac{x}{\sqrt{\pi}}\pm\boldsymbol{\varsigma}_1\right]\right)\mp\frac{1}{2}\right)\Bigg) \\
&\qquad-\left(\sin\left[\frac{\pi}{2}\left(\sqrt{n}\left[\frac{x}{\sqrt{\pi}}\pm\boldsymbol{\varsigma}_1\right]\right)^2-\delta\psi_n\right]+\sin(\delta\psi_n)\right)\Bigg] \\
&+\sum_{n,m}\frac{\lambda_n}{\sqrt{n}}\frac{\lambda_m}{\sqrt{m}}\Bigg[\frac{\pi}{2}\left(\cos(\delta\psi_n)\left(C\left(\sqrt{n}\left[\frac{x}{\sqrt{\pi}}\right]\right)\mp\frac{1}{2}\right)+\sin(\delta\psi_n)\left(S\left(\sqrt{n}\left[\frac{x}{\sqrt{\pi}}\right]\right)\mp\frac{1}{2}\right)\right)\times
\end{aligned}$$

$$
\begin{aligned}
&\times\left(\cos(\delta\psi_m)\left(C\left(\sqrt{m}\left[\frac{x}{\sqrt{\pi}}\right]\right)\mp\frac{1}{2}\right)+\sin(\delta\psi_m)\left(S\left(\sqrt{m}\left[\frac{x}{\sqrt{\pi}}\right]\right)\mp\frac{1}{2}\right)\right)\\
&+\frac{\pi}{2}\frac{\sqrt{n}}{\sqrt{m}}\left(\sqrt{|n-m|}\left[\frac{x}{\sqrt{\pi}}\right]\right)\times\\
&\quad\times\left(\operatorname{sgn}(n-m)\cos(\delta\psi_n-\delta\psi_m)\left(C\left(\sqrt{|n-m|}\left[\frac{x}{\sqrt{\pi}}\right]\right)\mp\frac{1}{2}\right)\right.\\
&\qquad\left.+\sin(\delta\psi_n-\delta\psi_m)\left(S\left(\sqrt{|n-m|}\left[\frac{x}{\sqrt{\pi}}\right]\right)\mp\frac{1}{2}\right)\right)\\
&-\frac{\pi}{2}\frac{\sqrt{n}}{\sqrt{m}}\left(\sqrt{n+m}\left[\frac{x}{\sqrt{\pi}}\right]\right)\times\\
&\quad\times\left(\cos(\delta\psi_n+\delta\psi_m)\left(C\left(\sqrt{n+m}\left[\frac{x}{\sqrt{\pi}}\right]\right)\mp\frac{1}{2}\right)\right.\\
&\qquad\left.+\sin(\delta\psi_n+\delta\psi_m)\left(S\left(\sqrt{n+m}\left[\frac{x}{\sqrt{\pi}}\right]\right)\mp\frac{1}{2}\right)\right)\\
&+\pi\frac{\sqrt{n}}{\sqrt{m}}\left(\sqrt{n}\left[\frac{x}{\sqrt{\pi}}\right]\right)\times\\
&\quad\times\left(\cos(\delta\psi_n)\left(S\left(\sqrt{n}\left[\frac{x}{\sqrt{\pi}}\right]\right)\mp\frac{1}{2}\right)-\sin(\delta\psi_n)\left(C\left(\sqrt{n}\left[\frac{x}{\sqrt{\pi}}\right]\right)\mp\frac{1}{2}\right)\right)\sin(\delta\psi_m)\\
&-\frac{1}{2}\frac{\sqrt{n}}{\sqrt{m}}\sin\left[\frac{\pi}{2}\operatorname{sgn}(n-m)\left(\sqrt{|n-m|}\left[\frac{x}{\sqrt{\pi}}\right]\right)^2-(\delta\psi_n-\delta\psi_m)\right]\\
&\quad+\frac{1}{2}\frac{\sqrt{n}}{\sqrt{m}}\sin\left[\frac{\pi}{2}\left(\sqrt{n+m}\left[\frac{x}{\sqrt{\pi}}\right]\right)^2-(\delta\psi_n+\delta\psi_m)\right]\\
&\qquad+\frac{\sqrt{n}}{\sqrt{m}}\cos\left[\frac{\pi}{2}\left(\sqrt{n}\left[\frac{x}{\sqrt{\pi}}\right]\right)^2-\delta\psi_n\right]\sin(\delta\psi_m)\Bigg] \qquad \text{(M.62)}
\end{aligned}
$$

Finally, we get to the point where we can derive the most complete solution to the problem we are considering in this work. The third-order solution in this case is given by eq. (9.137).

$$\begin{aligned}\boldsymbol{\varphi}_3(x) = \frac{\pi}{2}\left(\frac{x}{\sqrt{\pi}} \pm \boldsymbol{\varsigma}_3\right)^2 + \sum_n \frac{\lambda_n}{n}\boldsymbol{\rho}_1^n\left(\frac{x}{\sqrt{\pi}} \pm \boldsymbol{\varsigma}_2\right) \\ + \sum_{n,m}\frac{\lambda_n}{\sqrt{n}}\frac{\lambda_m}{\sqrt{m}}\boldsymbol{\rho}_2^{nm}\left(\frac{x}{\sqrt{\pi}} \pm \boldsymbol{\varsigma}_1\right) + \sum_{n,m,p}\lambda_n\frac{\lambda_m}{\sqrt{m}}\frac{\lambda_p}{\sqrt{p}}\boldsymbol{\rho}_3^{nmp}\left(\frac{x}{\sqrt{\pi}}\right)\end{aligned} \tag{9.137}$$

In this solution, $\boldsymbol{\varsigma}_3$ is the third-order slope function, dependent on the resonance flux parameters $\{\lambda_n\}$ and the mode numbers $\{n\}$ (this solutions does not require the mode numbers to be consecutive). The lower-order functions $\boldsymbol{\varsigma}_1$ and $\boldsymbol{\varsigma}_2$ are given as part of the corrections $\boldsymbol{\varphi}_{(1)}$ and $\boldsymbol{\varphi}_{(2)}$, respectively.

$$\begin{aligned}\boldsymbol{\varsigma}_3 = &\sum_n \frac{1}{2}\big(\cos(\delta\psi_n) + \sin(\delta\psi_n)\big)\frac{\lambda_n}{\sqrt{n}} \\ &+ \sum_{n,m}\left(\frac{1}{8}\frac{|n-m|^{3/2}}{\sqrt{n}\sqrt{m}}\big(\cos(\delta\psi_n - \delta\psi_m) + \operatorname{sgn}(n-m)\sin(\delta\psi_n - \delta\psi_m)\big)\right. \\ &\quad - \frac{1}{8}\frac{(n+m)^{3/2}}{\sqrt{n}\sqrt{m}}\big(\cos(\delta\psi_n + \delta\psi_m) + \sin(\delta\psi_n + \delta\psi_m)\big) \\ &\quad + \frac{1}{4}\frac{n}{\sqrt{m}}\big(\cos(\delta\psi_n) - \sin(\delta\psi_n)\big)\sin(\delta\psi_m) \\ &\quad \left. + \frac{1}{4}\frac{m}{\sqrt{n}}\sin(\delta\psi_n)\big(\cos(\delta\psi_m) - \sin(\delta\psi_m)\big)\right)\frac{\lambda_n}{\sqrt{n}}\frac{\lambda_m}{\sqrt{m}} \\ &+ \sum_{n,m,p}\left(\frac{1}{16}\frac{(n+m+p)^{3/2}}{\sqrt{m}\sqrt{p}}\big(\cos(\delta\psi_n + \delta\psi_m + \delta\psi_p) + \sin(\delta\psi_n + \delta\psi_m + \delta\psi_p)\big)\right. \\ &\quad - \frac{1}{16}\frac{|n-m+p|^{3/2}}{\sqrt{m}\sqrt{p}}\big(\cos(\delta\psi_n - \delta\psi_m + \delta\psi_p) + \operatorname{sgn}(n-m+p)\sin(\delta\psi_n - \delta\psi_m + \delta\psi_p)\big) \\ &\quad - \frac{1}{16}\frac{|n+m-p|^{3/2}}{\sqrt{m}\sqrt{p}}\big(\cos(\delta\psi_n + \delta\psi_m - \delta\psi_p) + \operatorname{sgn}(n+m-p)\sin(\delta\psi_n + \delta\psi_m - \delta\psi_p)\big) \\ &\quad + \frac{1}{16}\frac{|n-m-p|^{3/2}}{\sqrt{m}\sqrt{p}}\big(\cos(\delta\psi_n - \delta\psi_m - \delta\psi_p) + \operatorname{sgn}(n-m-p)\sin(\delta\psi_n - \delta\psi_m - \delta\psi_p)\big) \\ &\quad + \frac{1}{8}\frac{|n-m|^{3/2}}{\sqrt{m}\sqrt{p}}\big(\operatorname{sgn}(n-m)\cos(\delta\psi_n - \delta\psi_m) - \sin(\delta\psi_n - \delta\psi_m)\big)\sin(\delta\psi_p) \\ &\quad \left. - \frac{1}{8}\frac{(n+m)^{3/2}}{\sqrt{m}\sqrt{p}}\big(\cos(\delta\psi_n + \delta\psi_m) - \sin(\delta\psi_n + \delta\psi_m)\big)\sin(\delta\psi_p)\right)\end{aligned}$$

$$
\begin{aligned}
&+\frac{1}{8}\frac{|n-p|^{3/2}}{\sqrt{m}\sqrt{p}}\left(\operatorname{sgn}(n-p)\cos(\delta\psi_n-\delta\psi_p)-\sin(\delta\psi_n-\delta\psi_p)\right)\sin(\delta\psi_m)\\
&-\frac{1}{8}\frac{(n+p)^{3/2}}{\sqrt{m}\sqrt{p}}\left(\cos(\delta\psi_n+\delta\psi_p)-\sin(\delta\psi_n+\delta\psi_p)\right)\sin(\delta\psi_m)\\
&-\frac{1}{8}\frac{(n-m)}{\sqrt{m}}\cos(\delta\psi_n-\delta\psi_m)\left(\cos(\delta\psi_p)+\sin(\delta\psi_p)\right)\\
&+\frac{1}{8}\frac{(n+m)}{\sqrt{m}}\cos(\delta\psi_n+\delta\psi_m)\left(\cos(\delta\psi_p)+\sin(\delta\psi_p)\right)\\
&-\frac{1}{8}\frac{(n-p)}{\sqrt{p}}\cos(\delta\psi_n-\delta\psi_p)\left(\cos(\delta\psi_m)+\sin(\delta\psi_m)\right)\\
&+\frac{1}{8}\frac{(n+p)}{\sqrt{p}}\cos(\delta\psi_n+\delta\psi_p)\left(\cos(\delta\psi_m)+\sin(\delta\psi_m)\right)\\
&-\frac{1}{4}\frac{n^{3/2}}{\sqrt{m}\sqrt{p}}\left(\cos(\delta\psi_n)+\sin(\delta\psi_n)\right)\sin(\delta\psi_m)\sin(\delta\psi_p)\\
&+\frac{1}{4}\frac{n}{\sqrt{m}}\sin(\delta\psi_n)\sin(\delta\psi_m)\left(\cos(\delta\psi_p)+\sin(\delta\psi_p)\right)\\
&+\frac{1}{4}\frac{n}{\sqrt{p}}\sin(\delta\psi_n)\left(\cos(\delta\psi_m)+\sin(\delta\psi_m)\right)\sin(\delta\psi_p)\\
&-\frac{1}{4}\sqrt{m}\cos(\delta\psi_n)\cos(\delta\psi_m)\left(\cos(\delta\psi_p)+\sin(\delta\psi_p)\right)\\
&-\frac{1}{4}\sqrt{p}\cos(\delta\psi_n)\left(\cos(\delta\psi_m)+\sin(\delta\psi_m)\right)\cos(\delta\psi_p)\Bigg)\lambda_n\frac{\lambda_m}{\sqrt{m}}\frac{\lambda_p}{\sqrt{p}}
\end{aligned}
\tag{M.63}
$$

The three oscillating functions $\{\boldsymbol{\rho}_i\}$ are given below.

$$
\begin{aligned}
\boldsymbol{\rho}_1^n(x) = \pi&\left(\sqrt{n}\left[\frac{x}{\sqrt{\pi}}\pm\boldsymbol{\varsigma}_2\right]\right)\times\\
&\times\Bigg(\cos(\delta\psi_n)\left(C\left(\sqrt{n}\left[\frac{x}{\sqrt{\pi}}\pm\boldsymbol{\varsigma}_2\right]\right)\mp\frac{1}{2}\right)+\sin(\delta\psi_n)\left(S\left(\sqrt{n}\left[\frac{x}{\sqrt{\pi}}\pm\boldsymbol{\varsigma}_2\right]\right)\mp\frac{1}{2}\right)\Bigg)\\
&-\left(\sin\left[\frac{\pi}{2}\left(\sqrt{n}\left[\frac{x}{\sqrt{\pi}}\pm\boldsymbol{\varsigma}_2\right]\right)^2-\delta\psi_n\right]+\sin(\delta\psi_n)\right),
\end{aligned}
\tag{M.64}
$$

$$
\boldsymbol{\rho}_2^{nm}(x)=\frac{\pi}{2}\left(\cos(\delta\psi_n)\left(C\left(\sqrt{n}\left[\frac{x}{\sqrt{\pi}}\pm\boldsymbol{\varsigma}_1\right]\right)\mp\frac{1}{2}\right)+\sin(\delta\psi_n)\left(S\left(\sqrt{n}\left[\frac{x}{\sqrt{\pi}}\pm\boldsymbol{\varsigma}_1\right]\right)\mp\frac{1}{2}\right)\right)
$$

$$
\begin{aligned}
&\times\left(\cos(\delta\psi_m)\left(C\left(\sqrt{m}\left[\frac{x}{\sqrt{\pi}}\pm\varsigma_1\right]\right)\mp\frac{1}{2}\right)+\sin(\delta\psi_m)\left(S\left(\sqrt{m}\left[\frac{x}{\sqrt{\pi}}\pm\varsigma_1\right]\right)\mp\frac{1}{2}\right)\right)\\
&+\frac{\pi}{2}\frac{\sqrt{n}}{\sqrt{m}}\left(\sqrt{|n-m|}\left[\frac{x}{\sqrt{\pi}}\pm\varsigma_1\right]\right)\times\\
&\quad\times\left(\operatorname{sgn}(n-m)\cos(\delta\psi_n-\delta\psi_m)\left(C\left(\sqrt{|n-m|}\left[\frac{x}{\sqrt{\pi}}\pm\varsigma_1\right]\right)\mp\frac{1}{2}\right)\right.\\
&\qquad\left.+\sin(\delta\psi_n-\delta\psi_m)\left(S\left(\sqrt{|n-m|}\left[\frac{x}{\sqrt{\pi}}\pm\varsigma_1\right]\right)\mp\frac{1}{2}\right)\right)\\
&-\frac{\pi}{2}\frac{\sqrt{n}}{\sqrt{m}}\left(\sqrt{n+m}\left[\frac{x}{\sqrt{\pi}}\pm\varsigma_1\right]\right)\times\\
&\quad\times\left(\cos(\delta\psi_n+\delta\psi_m)\left(C\left(\sqrt{n+m}\left[\frac{x}{\sqrt{\pi}}\pm\varsigma_1\right]\right)\mp\frac{1}{2}\right)\right.\\
&\qquad\left.+\sin(\delta\psi_n+\delta\psi_m)\left(S\left(\sqrt{n+m}\left[\frac{x}{\sqrt{\pi}}\pm\varsigma_1\right]\right)\mp\frac{1}{2}\right)\right)\\
&+\pi\frac{\sqrt{n}}{\sqrt{m}}\left(\sqrt{n}\left[\frac{x}{\sqrt{\pi}}\pm\varsigma_1\right]\right)\left(\cos(\delta\psi_n)\left(S\left(\sqrt{n}\left[\frac{x}{\sqrt{\pi}}\pm\varsigma_1\right]\right)\mp\frac{1}{2}\right)\right.\\
&\qquad\left.-\sin(\delta\psi_n)\left(C\left(\sqrt{n}\left[\frac{x}{\sqrt{\pi}}\pm\varsigma_1\right]\right)\mp\frac{1}{2}\right)\right)\sin(\delta\psi_m)\\
&-\frac{1}{2}\frac{\sqrt{n}}{\sqrt{m}}\sin\left[\frac{\pi}{2}\operatorname{sgn}(n-m)\left(\sqrt{|n-m|}\left[\frac{x}{\sqrt{\pi}}\pm\varsigma_1\right]\right)^2-(\delta\psi_n-\delta\psi_m)\right]\\
&+\frac{1}{2}\frac{\sqrt{n}}{\sqrt{m}}\sin\left[\frac{\pi}{2}\left(\sqrt{n+m}\left[\frac{x}{\sqrt{\pi}}\pm\varsigma_1\right]\right)^2-(\delta\psi_n+\delta\psi_m)\right]\\
&+\frac{\sqrt{n}}{\sqrt{m}}\cos\left[\frac{\pi}{2}\left(\sqrt{n}\left[\frac{x}{\sqrt{\pi}}\pm\varsigma_1\right]\right)^2-\delta\psi_n\right]\sin(\delta\psi_m),
\end{aligned}
\tag{M.65}
$$

and

$$\begin{aligned}
\boldsymbol{\rho}_3^{nmp}(x) = \frac{\pi}{2}\cos\left[\frac{\pi}{2}\left(\sqrt{n}\left[\frac{x}{\sqrt{\pi}}\right]\right)^2 - \delta\psi_n\right]\times \\
\times\left(\cos(\delta\psi_m)\left(C\left(\sqrt{m}\left[\frac{x}{\sqrt{\pi}}\right]\right)\mp\frac{1}{2}\right)+\sin(\delta\psi_m)\left(S\left(\sqrt{m}\left[\frac{x}{\sqrt{\pi}}\right]\right)\mp\frac{1}{2}\right)\right)\times \\
\times\left(\cos(\delta\psi_p)\left(C\left(\sqrt{p}\left[\frac{x}{\sqrt{\pi}}\right]\right)\mp\frac{1}{2}\right)+\sin(\delta\psi_p)\left(S\left(\sqrt{p}\left[\frac{x}{\sqrt{\pi}}\right]\right)\mp\frac{1}{2}\right)\right) \\
+\frac{\pi}{4}\left(\frac{\sqrt{|n-m|}}{\sqrt{m}}\left(\operatorname{sgn}(n-m)\cos(\delta\psi_n-\delta\psi_m)\left(C\left(\sqrt{|n-m|}\left[\frac{x}{\sqrt{\pi}}\right]\right)\mp\frac{1}{2}\right)\right.\right. \\
\left.+\sin(\delta\psi_n-\delta\psi_m)\left(S\left(\sqrt{|n-m|}\left[\frac{x}{\sqrt{\pi}}\right]\right)\mp\frac{1}{2}\right)\right) \\
-\frac{\sqrt{n+m}}{\sqrt{m}}\left(\cos(\delta\psi_n+\delta\psi_m)\left(C\left(\sqrt{n+m}\left[\frac{x}{\sqrt{\pi}}\right]\right)\mp\frac{1}{2}\right)\right. \\
\left.\left.+\sin(\delta\psi_n+\delta\psi_m)\left(S\left(\sqrt{n+m}\left[\frac{x}{\sqrt{\pi}}\right]\right)\mp\frac{1}{2}\right)\right)\right)\times \\
\times\left(\cos(\delta\psi_p)\left(C\left(\sqrt{p}\left[\frac{x}{\sqrt{\pi}}\right]\right)\mp\frac{1}{2}\right)+\sin(\delta\psi_p)\left(S\left(\sqrt{p}\left[\frac{x}{\sqrt{\pi}}\right]\right)\mp\frac{1}{2}\right)\right) \\
+\frac{\pi}{4}\left(\frac{\sqrt{|n-p|}}{\sqrt{p}}\left(\operatorname{sgn}(n-p)\cos(\delta\psi_n-\delta\psi_p)\left(C\left(\sqrt{|n-p|}\left[\frac{x}{\sqrt{\pi}}\right]\right)\mp\frac{1}{2}\right)\right.\right. \\
\left.\left.+\sin(\delta\psi_n-\delta\psi_p)\left(S\left(\sqrt{|n-p|}\left[\frac{x}{\sqrt{\pi}}\right]\right)\mp\frac{1}{2}\right)\right)\right)
\end{aligned}$$

$$
\begin{aligned}
&- \frac{\sqrt{n+p}}{\sqrt{p}} \left(\cos(\delta\psi_n + \delta\psi_p) \left(C\left(\sqrt{n+p}\left[\frac{x}{\sqrt{\pi}}\right]\right) \mp \frac{1}{2} \right) \right. \\
&\qquad \left. + \sin(\delta\psi_n + \delta\psi_p) \left(S\left(\sqrt{n+p}\left[\frac{x}{\sqrt{\pi}}\right]\right) \mp \frac{1}{2} \right) \right) \times \\
&\qquad \times \left(\cos(\delta\psi_m) \left(C\left(\sqrt{m}\left[\frac{x}{\sqrt{\pi}}\right]\right) \mp \frac{1}{2} \right) + \sin(\delta\psi_m) \left(S\left(\sqrt{m}\left[\frac{x}{\sqrt{\pi}}\right]\right) \mp \frac{1}{2} \right) \right) \\
&+ \frac{\pi}{2} \frac{\sqrt{n}}{\sqrt{m}} \left(\cos(\delta\psi_n) \left(S\left(\sqrt{n}\left[\frac{x}{\sqrt{\pi}}\right]\right) \mp \frac{1}{2} \right) - \sin(\delta\psi_n) \left(C\left(\sqrt{n}\left[\frac{x}{\sqrt{\pi}}\right]\right) \mp \frac{1}{2} \right) \right) \sin(\delta\psi_m) \\
&\qquad \times \left(\cos(\delta\psi_p) \left(C\left(\sqrt{p}\left[\frac{x}{\sqrt{\pi}}\right]\right) \mp \frac{1}{2} \right) + \sin(\delta\psi_p) \left(S\left(\sqrt{p}\left[\frac{x}{\sqrt{\pi}}\right]\right) \mp \frac{1}{2} \right) \right) \\
&+ \frac{\pi}{2} \frac{\sqrt{n}}{\sqrt{p}} \left(\cos(\delta\psi_n) \left(S\left(\sqrt{n}\left[\frac{x}{\sqrt{\pi}}\right]\right) \mp \frac{1}{2} \right) - \sin(\delta\psi_n) \left(C\left(\sqrt{n}\left[\frac{x}{\sqrt{\pi}}\right]\right) \mp \frac{1}{2} \right) \right) \times \\
&\qquad \times \left(\cos(\delta\psi_m) \left(C\left(\sqrt{m}\left[\frac{x}{\sqrt{\pi}}\right]\right) \mp \frac{1}{2} \right) + \sin(\delta\psi_m) \left(S\left(\sqrt{m}\left[\frac{x}{\sqrt{\pi}}\right]\right) \mp \frac{1}{2} \right) \right) \sin(\delta\psi_p) \\
&+ \frac{\pi}{8} \frac{(n+m+p)}{\sqrt{m}\sqrt{p}} \left(\sqrt{n+m+p}\left[\frac{x}{\sqrt{\pi}}\right] \right) \times \\
&\qquad \times \left(\cos(\delta\psi_n + \delta\psi_m + \delta\psi_p) \left(C\left(\sqrt{n+m+p}\left[\frac{x}{\sqrt{\pi}}\right]\right) \mp \frac{1}{2} \right) \right. \\
&\qquad \left. + \sin(\delta\psi_n + \delta\psi_m + \delta\psi_p) \left(S\left(\sqrt{n+m+p}\left[\frac{x}{\sqrt{\pi}}\right]\right) \mp \frac{1}{2} \right) \right) \\
&- \frac{\pi}{8} \frac{|n-m+p|}{\sqrt{m}\sqrt{p}} \left(\sqrt{|n-m+p|}\left[\frac{x}{\sqrt{\pi}}\right] \right) \times \\
&\qquad \times \left(\cos(\delta\psi_n - \delta\psi_m + \delta\psi_p) \left(C\left(\sqrt{|n-m+p|}\left[\frac{x}{\sqrt{\pi}}\right]\right) \mp \frac{1}{2} \right) \right.
\end{aligned}
$$

$$+\operatorname{sgn}(n-m+p)\sin(\delta\psi_n-\delta\psi_m+\delta\psi_p)\left(S\left(\sqrt{|n-m+p|}\left[\frac{x}{\sqrt{\pi}}\right]\right)\mp\frac{1}{2}\right)\Bigg)$$

$$-\frac{\pi}{8}\frac{|n+m-p|}{\sqrt{m}\sqrt{p}}\left(\sqrt{|n+m-p|}\left[\frac{x}{\sqrt{\pi}}\right]\right)\times$$

$$\times\Bigg(\cos(\delta\psi_n+\delta\psi_m-\delta\psi_p)\left(C\left(\sqrt{|n+m-p|}\left[\frac{x}{\sqrt{\pi}}\right]\right)\mp\frac{1}{2}\right)$$

$$+\operatorname{sgn}(n+m-p)\sin(\delta\psi_n+\delta\psi_m-\delta\psi_p)\left(S\left(\sqrt{|n+m-p|}\left[\frac{x}{\sqrt{\pi}}\right]\right)\mp\frac{1}{2}\right)\Bigg)$$

$$+\frac{\pi}{8}\frac{|n-m-p|}{\sqrt{m}\sqrt{p}}\left(\sqrt{|n-m-p|}\left[\frac{x}{\sqrt{\pi}}\right]\right)\times$$

$$\times\Bigg(\cos(\delta\psi_n-\delta\psi_m-\delta\psi_p)\left(C\left(\sqrt{|n-m-p|}\left[\frac{x}{\sqrt{\pi}}\right]\right)\mp\frac{1}{2}\right)$$

$$+\operatorname{sgn}(n-m-p)\sin(\delta\psi_n-\delta\psi_m-\delta\psi_p)\left(S\left(\sqrt{|n-m-p|}\left[\frac{x}{\sqrt{\pi}}\right]\right)\mp\frac{1}{2}\right)\Bigg)$$

$$-\frac{\pi}{4}\frac{|n-m|}{\sqrt{m}\sqrt{p}}\left(\sqrt{|n-m|}\left[\frac{x}{\sqrt{\pi}}\right]\right)\sin(\delta\psi_p)\times$$

$$\times\Bigg(\sin(\delta\psi_n-\delta\psi_m)\left(C\left(\sqrt{|n-m|}\left[\frac{x}{\sqrt{\pi}}\right]\right)\mp\frac{1}{2}\right)$$

$$-\operatorname{sgn}(n-m)\cos(\delta\psi_n-\delta\psi_m)\left(S\left(\sqrt{|n-m|}\left[\frac{x}{\sqrt{\pi}}\right]\right)\mp\frac{1}{2}\right)\Bigg)$$

$$+\frac{\pi}{4}\frac{(n+m)}{\sqrt{m}\sqrt{p}}\left(\sqrt{n+m}\left[\frac{x}{\sqrt{\pi}}\right]\right)\sin(\delta\psi_p)\times$$

$$\times\Bigg(\sin(\delta\psi_n+\delta\psi_m)\left(C\left(\sqrt{n+m}\left[\frac{x}{\sqrt{\pi}}\right]\right)\mp\frac{1}{2}\right)$$

$$-\cos(\delta\psi_n+\delta\psi_m)\left(S\left(\sqrt{n+m}\left[\frac{x}{\sqrt{\pi}}\right]\right)\mp\frac{1}{2}\right)\Bigg)$$

$$
\begin{aligned}
&-\frac{\pi}{4}\frac{|n-p|}{\sqrt{m}\sqrt{p}}\left(\sqrt{|n-p|}\left[\frac{x}{\sqrt{\pi}}\right]\right)\sin(\delta\psi_m)\times \\
&\quad\times\left(\sin(\delta\psi_n-\delta\psi_p)\left(C\left(\sqrt{|n-p|}\left[\frac{x}{\sqrt{\pi}}\right]\right)\mp\frac{1}{2}\right)\right. \\
&\qquad\left.-\operatorname{sgn}(n-p)\cos(\delta\psi_n-\delta\psi_p)\left(S\left(\sqrt{|n-p|}\left[\frac{x}{\sqrt{\pi}}\right]\right)\mp\frac{1}{2}\right)\right) \\
&+\frac{\pi}{4}\frac{(n+p)}{\sqrt{m}\sqrt{p}}\left(\sqrt{n+p}\left[\frac{x}{\sqrt{\pi}}\right]\right)\sin(\delta\psi_m)\times \\
&\quad\times\left(\sin(\delta\psi_n+\delta\psi_p)\left(C\left(\sqrt{n+p}\left[\frac{x}{\sqrt{\pi}}\right]\right)\mp\frac{1}{2}\right)\right. \\
&\qquad\left.-\cos(\delta\psi_n+\delta\psi_p)\left(S\left(\sqrt{n+p}\left[\frac{x}{\sqrt{\pi}}\right]\right)\mp\frac{1}{2}\right)\right) \\
&-\frac{\pi}{2}\frac{n}{\sqrt{m}\sqrt{p}}\left(\sqrt{n}\left[\frac{x}{\sqrt{\pi}}\right]\right)\left(\cos(\delta\psi_n)\left(C\left(\sqrt{n}\left[\frac{x}{\sqrt{\pi}}\right]\right)\mp\frac{1}{2}\right)\right. \\
&\qquad\left.+\sin(\delta\psi_n)\left(S\left(\sqrt{n}\left[\frac{x}{\sqrt{\pi}}\right]\right)\mp\frac{1}{2}\right)\right)\sin(\delta\psi_m)\sin(\delta\psi_p) \\
&-\frac{1}{8}\frac{(n+m+p)}{\sqrt{m}\sqrt{p}}\sin\left[\frac{\pi}{2}\left(\sqrt{n+m+p}\left[\frac{x}{\sqrt{\pi}}\right]\right)^2-(\delta\psi_n+\delta\psi_m+\delta\psi_p)\right] \\
&+\frac{1}{8}\frac{(n-m+p)}{\sqrt{m}\sqrt{p}}\sin\left[\frac{\pi}{2}\operatorname{sgn}(n-m+p)\left(\sqrt{n-m+p}\left[\frac{x}{\sqrt{\pi}}\right]\right)^2-(\delta\psi_n-\delta\psi_m+\delta\psi_p)\right] \\
&+\frac{1}{8}\frac{(n+m-p)}{\sqrt{m}\sqrt{p}}\sin\left[\frac{\pi}{2}\operatorname{sgn}(n+m-p)\left(\sqrt{n+m-p}\left[\frac{x}{\sqrt{\pi}}\right]\right)^2-(\delta\psi_n+\delta\psi_m-\delta\psi_p)\right] \\
&-\frac{1}{8}\frac{(n-m-p)}{\sqrt{m}\sqrt{p}}\sin\left[\frac{\pi}{2}\operatorname{sgn}(n-m-p)\left(\sqrt{n-m-p}\left[\frac{x}{\sqrt{\pi}}\right]\right)^2-(\delta\psi_n-\delta\psi_m-\delta\psi_p)\right] \\
&+\frac{1}{4}\frac{(n-m)}{\sqrt{m}\sqrt{p}}\cos\left[\frac{\pi}{2}\operatorname{sgn}(n-m)\left(\sqrt{|n-m|}\left[\frac{x}{\sqrt{\pi}}\right]\right)^2-(\delta\psi_n-\delta\psi_m)\right]\sin(\delta\psi_p)
\end{aligned}
$$

$$
\begin{aligned}
&-\frac{1}{4}\frac{(n+m)}{\sqrt{m}\sqrt{p}}\cos\left[\frac{\pi}{2}\left(\sqrt{n+m}\left[\frac{x}{\sqrt{\pi}}\right]\right)^2-(\delta\psi_n+\delta\psi_m)\right]\sin(\delta\psi_p)\\
&+\frac{1}{4}\frac{(n-p)}{\sqrt{m}\sqrt{p}}\cos\left[\frac{\pi}{2}\operatorname{sgn}(n-p)\left(\sqrt{|n-p|}\left[\frac{x}{\sqrt{\pi}}\right]\right)^2-(\delta\psi_n-\delta\psi_p)\right]\sin(\delta\psi_m)\\
&-\frac{1}{4}\frac{(n+p)}{\sqrt{m}\sqrt{p}}\cos\left[\frac{\pi}{2}\left(\sqrt{n+p}\left[\frac{x}{\sqrt{\pi}}\right]\right)^2-(\delta\psi_n+\delta\psi_p)\right]\sin(\delta\psi_m)\\
&+\frac{1}{2}\frac{n}{\sqrt{m}\sqrt{p}}\sin\left[\frac{\pi}{2}\left(\sqrt{n}\left[\frac{x}{\sqrt{\pi}}\right]\right)^2-(\delta\psi_n)\right]\sin(\delta\psi_m)\sin(\delta\psi_p)
\end{aligned}
\tag{M.66}
$$